High-Temperature Long-Wavelength Vertical-Cavity Lasers

by

Near M. Margalit

ECE Techincal Report #98-15

Department of Electrical and Computer Engineering
University of California, at Santa Barbara
June 1998

UNIVERSITY OF CALIFORNIA

Santa Barbara

High-Temperature Long-Wavelength Vertical-Cavity Lasers

A Dissertation submitted in partial satisfaction of the requiremments for the degree of

Doctor of Philosophy

in

Electrical and Computer Engineering

by

Near M. Margalit

Committee in charge:

Professor John E. Bowers, Chairperson

Professor Evelyn L. Hu

Professor Larry A. Coldren

Professor Michael Melliar-Smith

The dissertation of Near M. Margalit

is approved:

_____

Professor Larry A. Coldren

_____

Professor Michael Melliar-Smith

_____

Professor Evelyn L. Hu

_____

Professor John E. Bowers, Chairperson

June 1998

High-Temperature Long-Wavelength

Vertical-Cavity Lasers

June 1998

Electrical and Computer Engineering Department

University of California, Santa Barbara

Santa Barbara, CA 93106

Acknowledgments

The development of long-wavelength vertical-cavity lasers is a project that cannot be undertaken by one person. This project requires high quality growth, fabrication, fusion, and analysis. Thus, a great of collaboration is required to excel in an otherwise very difficult field. It is in this respect that I would first like to thank my advisor Professor John E. Bowers. He has put together the environment necessary for success. You could always count on his support for whatever was best for his students and the research. In addition, he also proved to be extremely unselfish in allowing me to present our research results in places like Israel, England, Japan, Canada, and Snowbird(Utah). Over the past four years he has been an excellent teacher, collaborator, and friend.

The other members of my committee were also very helpful through my graduate career. I would like to thank Professor Evelyn L. Hu for all her help in the analysis and understanding of our devices. Her emphasis on material issues was a great help to our effort. I would also like to thank Professor Larry A. Coldren. It is under his guidance that I started understanding the intricacies of lasers, and especially

vertical-cavity lasers. His contribution to vertical-cavity laser research has greatly enhanced the field as well as my research. In addition, I would like to thank Professor Michael Melliar-Smith for being on my committee.

There are many other people that helped me along the way. Dubravko Babic brought me from knowing nothing to a position of some competency. I greatly appreciate his patience and his dedication. It was on the shoulders of his work that we were able to achieve our success. There are countless other people who aided in this research. Especially important are the crystal grower that worked may hours at a time to get their growths just right. I would like to thank Klaus Struebel and Patrick Abraham for all their effort in InP active region growth. In addition our project required very difficult GaAs DBR mirror growths. There growth require very high precision thickness and very thick growth structures. In this respect I would like to thank both Eric Hegblom and Yi-Jen Chiu for their tireless effort. Rich Mirin, Ryan Naone, and Hong Ho also contributed important mirror growths. Sheng Zhang did a remarkable job with the many of the transmission experiments. In addition to mirror growth, Eric Hegblom directly contributed to the understanding of our devices, with great work on current spreading and scattering losses. Finally on the technical side I would like to thank Alexis Black for all the hard work you contributed. Your commitment to fundamental understanding of the subject will serve you well in continuing this research. There are also countless others that I would like to thank for contributing their time and effort.

Besides technical help, there are many people I would like to thank for their involvement in my life: my wife Michelle that brings me happiness every day, my mother that was always there for me, and my father for giving me ambition and direction. Also I would like to thank my two bothers Erez and Alon whom you can always count on. My grandmother, Haya, is a very important person in my life, and I thank her for all her support. Finally I would like to thank all my friends at UCSB which were always fun to be around, with specially thanks to Amber, Greg, Eric, Duane, Beck, and Ola.

This dissertation is dedicated to

my wife, Michelle

and my family,

who are always there for me

Vita

November 2, 1972:	Born in Haifa, Israel
June 1994:	B.S., Applied Physics, Caltech
December 1995:	M.S., Electrical Engineering, UC Santa Barbara
October 1994-June 1998:	Research Assistant, UC Santa Barbara
June 1998:	Ph. D., Electrical Engineering, UC Santa Barbara

Publications in Technical Journals

1. N. M. Margalit, S. Z. Zhang, and J. E. Bowers, "Vertical cavity lasers for telecom applications.", IEEE Communications Magazine, vol.35, 164 (1997).(**invited**)

2. N. M. Margalit, K. A. Black, Y. J. Chiu, E. R. Hegblom, K. Streubel, P. Abraham, M. Anzlowar, J. E. Bowers, and E. L. Hu, "Top-emitting double-fused 1.5 mu m vertical cavity lasers.", Elect. Lett., vol.34, 285 (1998).

3. N. M. Margalit, J. Piprek, S. Zhang, D. I. Babic, K. Streubel, R. P. Mirin, J. R. Wesselmann, and J. E. Bowers, "64 degrees C continuous-wave operation of 1.5- mu m vertical-cavity laser.", IEEE Journal of Selected Topics in Quantum Electronics, vol.3, 359 (1997).

4. N. M. Margalit, D. I. Babic, K. Streubel, R. P. Mirin, R. L. Naone, J. E. Bowers, and E. L. Hu, "Submilliamp long wavelength vertical cavity lasers.", Elect. Lett., vol.32, 1675 (1997).

5. N. M. Margalit, D. I. Babic, K. Streubel, R. P. Mirin, D. E. Mars, J. E. Bowers, and E. L. Hu, "Laterally oxidized long wavelength cw vertical-cavity lasers.", Appl. Phys. Lett., vol.69, 471 (1996).

6. D. I. Babic, J. Piprek, K. Streubel, R. P. Mirin, N. M. Margalit, D. E. Mars, J. E. Bowers, and E. L. Hu, "Design and analysis of double-fused 1.55- mu m vertical-cavity lasers.", IEEE J. Quant. Elect., vol.33, 1369 (1997).

7. A. Black, A. R. Hawkins, N. M. Margalit, D. I. Babic, A. L. Holmes Jr., Y.-L. Chang, P. Abraham, J. E. Bowers, and E. L. Hu, "Wafer fusion: materials issues and device results.", IEEE Journal of Selected Topics in Quantum Electronics, vol.3, 943 (1997)(**invited**).

8. D. I. Babic, K. Streubel, R. P. Mirin, N. M. Margalit, M. G. Peters, J. E. Bowers, and E. L. Hu, "Fabrication and characteristics of double-fused vertical-cavity lasers.", Optical and Quantum Electronics, vol.28, 475 (1996).

9. D. I. Babic, K. Streubel, R. P. Mirin, N. M. Margalit, J. E. Bowers, E. L. Hu, D. E. Mars, Y. a. n. g. Long, and K. Carey, "Room-temperature continuous-wave operation of 1.54- mu m vertical-cavity lasers.", IEEE Photonics Technology Letters, vol.7, 1225 (1995).

10. D. I. Babic, K. Streubel, R. P. Mirin, N. M. Margalit, J. E. Bowers, and E. L. Hu, "Transverse-mode and polarisation characteristics of double-fused 1.52 mu m vertical-cavity lasers", Elect. Lett., vol.31, 653 (1995).

11. S. Z. Zhang, N. M. Margalit, T. E. Reynolds, and J. E. Bowers, "1.54- mu m vertical-cavity surface-emitting laser transmission at 2.5 Gb/s.", IEEE Photonics Technology Letters, vol.9, 374 (1997).

12. J. R. Wesselmann, N. M. Margalit, and J. E. Bowers, "Analog measurements of long wavelength vertical-cavity lasers.", Appl. Phys. Lett., vol.72, 2084 (1997).

13. S. Z. Zhang, N. M. Margalit, T. E. Reynolds, and J. E. Bowers, "1.55 mu m vertical cavity laser transmission over 200 km at 622 Mbit/s.", Elect. Lett., vol.32, 1597 (1997).

14. P. Blixt, D. I. Babic, N. M. Margalit, K. Streubel, and J. E. Bowers, "Multimode fiber transmission using room temperature double-fused 1.54-mu m vertical-cavity lasers.", IEEE Photonics Technology Letters, vol.8, 1564 (1996).

15. P. Blixt, D. I. Babic, K. Streubel, N. M. Margalit, T. E. Reynolds, and J. E. Bowers, "Single-mode, 1 Gb/s operation of double-fused vertical-cavity lasers at 1.54 mu m.", IEEE Photonics Technology Letters, vol.8, 700 (1996).

16. J. Ko, E. R. Hegblom, Y. Akulova, N. M. Margalit, and L. A. Coldren, "AlInGaAs/AlGaAs strained-layer 850 nm vertical-cavity lasers with very low thresholds.", Elect. Lett., vol.33, 1550 (1998).

Conference Presentations

1. N. M. Margalit, K. A. Black, A. Hawkins, B. Liu, A. Shakouri, P. Abraham, J. E. Bowers, E. L. Hu, “Fused Optoelectronic Devices”, Integrated Photonic Research, Victoria, B. C., (1998).(**invited**)

2. N. Margalit, Y-J. Chiu, E. Hegblom, P. Abraham, A. Black, J. Wesselmann, J. E. Bowers, E. L. Hu, and K. Streubel, "120 degrees C pulsed operation from a 1.55 mu m vertical-cavity laser.", 1997 Digest of the IEEE/LEOS Summer Topical Meetings: Vertical-Cavity Lasers Materials, Processing, and Devices (Cat. No.97TH8276), 43 (1997).(**invited**)

3. N. M. Margalit, Y-J. Chiu, J. E. Bowers, and E. L. Hu, “Long-Wavelength Vertical-Cavity Lasers Through Wafer Fusion,” CLEO Pacific Rim ‘97, Chiba, Japan, July 14-18, (1997). (**invited**)

4. N. M. Margalit, K. Streubel, Y-J. Chiu, E. R. Hegblom, H. Q. Hou, J. E. Bowers, and E. L. Hu, "High-temperature 1.55 mu m vertical-cavity lasers through wafer fusion.", Proceedings of the SPIE - The International Society for Optical Engineering, vol.3003 169 (1997)(**invited**).

5. N. M. Margalit, Y-J. Chiu,E. Hegblom, P. Abraham, A. Black, J. Wesselmann, J. E. Bowers, and E. L. Hu, “Vertical Cavity Surface Emitting Lasers Operating at 1550 nm,” Mini-Symposium on Devices and Systems fro Optical Interconnects and Data Links, Grasmere, England, Sept. 1-4 (1997).(**invited**).

6. N. M. Margalit, D. I. Babic, K. Streubel, R. P. Mirin, J. E. Bowers, and E. L. Hu, “Laterally Oxidized Long-Wavelength Vertical Cavity Lasers,” High Speed Optoelectronics Devices and Systems, Snowbird, UT, Aug 8-15 (1996). (**invited**)

7. N. M. Margalit, D. I. Babic, K. Streubel, R. P. Mirin, J. E. Bowers, and E. L. Hu, "Submilliamp long wavelength vertical cavity lasers.", Conference Digest. 15th IEEE International Semiconductor Laser Conference (Cat. No.96CH35896), Haifa,Israel (1996).

8. N. M. Margalit, D. I. Babic, K. Streubel, R. P. Mirin, D. E. Mars, S. Zhang, J. E. Bowers, and E. L. Hu, "Laterally oxidized long wavelength CW vertical-cavity lasers", OFC '96. Optical Fiber Communication. Vol.2. 1996 Technical Digest Series. Postconference Edition (IEEE Cat. No.CH35901), 368 (1996)(**postdeadline**).

9. E. R. Hegblom, N. M. Margalit, B. J. Thibeault, L. A. Coldren, and J. E. Bowers, "Current spreading in apertured vertical cavity lasers.", Proceedings of the SPIE - The International Society for Optical Engineering, vol.3003 176 (1997).

10. J. Piprek, D. I. Babic, N. M. Margalit, and J. E. Bowers, "Loss analysis of 1.55 mu m vertical cavity lasers", Conference Digest. 15th IEEE International Semiconductor Laser Conference (Cat. No.96CH35896), 25 (1996).

11. V. Jayaraman, N. M. Margalit, K. Streubel, M. E. Heimbuch, R. P. Mirin, B. J. Thibeault, J. E. Bowers, E. L. Hu, and S. Denbaars, "Long-wavelength vertical-cavity surface-emitting laser diodes.", Compound Semiconductor Electronics and Photonics Symposium, 63 (1996).

12. E. R. Hegblom, R. L. Naone, N. M. Margalit, and L. A. Coldren, "Comparison of tapered apertures in vertical cavity lasers.", Conference Proceedings. LEOS '97, 10th Annual Meeting. IEEE Lasers and Electro-Optics Society 1997 Annual Meeting (Cat. No.97CH36057, 350 (1996).

13. P. Blixt, D. I. Babic, N. M. Margalit, T. E. Reynolds, and J. E. Bowers, "1-Gbit/s, single-mode operation of vertical cavity lasers emitting at 1.54 mu m.", OFC'96. Optical Fiber Communication. Vol.2. 1996 Technical Digest Series. Conference Edition (IEEE Cat. No.96CH35901), 12 (1996).

14. P. Blixt, D. I. Babic, N. M. Margalit, K. Streubel, and J. E. Bowers, "Multimode fibre transmission using room temperature double-fused 1.54 mu m vertical-cavity lasers", ECOC '96. 22nd European Conference on Optical Communication (IEEE Cat. No.96TH8217), 97 (1996).

15. D. I. Babic, K. Streubel, R. P. Mirin, J. Piprek, N. M. Margalit, J. E. Bower, E. L. Hu, D. E. Mars, L. Yang, and K. Carey, "Room-temperature performance of double-fused 1.54 mu m vertical-cavity laser.", IPRM 1996. Eighth International Conference on Indium Phosphide and Related Materials (Cat. No.96CH35930), 719 (1996).

Abstract

Vertical cavity lasers(VCLs) have recently been the subject of much research effort around the world. These lasers hold the promise of inexpensive, low threshold, high speed sources for optical communication. Short wavelength lasers have many applications, including free space optical interconnects and short distance datacom, but have limited potential for longer distances due to the absorption and dispersion spectrum of standard optical fiber. The longer wavelength sources near 1.3 or 1.5 μm are ideally suited for medium and long distance applications. Interoperability as well as compatibility with existing fiber optic infrastructure also call for longer wavelength sources. However, large volume commercialization of such devices, for applications such as FTTH(fiber to the home), requires a wide temperature range of operation(-40°C to 85°C). Historically, the realization of such high performance long-wavelength vertical cavity-lasers has been difficult. Nonetheless, advances in fabrication techniques, such as wafer fusion, have allowed for ever increasing device performance. In this thesis, we present recent results that include devices with multigigahetz frequency responses, hundred of microwatts of cw output powers, as well as 65°C continuous-wave operating temperatures. In addition, these devices have now been demonstrated as sources in link transmission experiment at 2.5 Gb/s over 200 km of optical fiber, far surpassing the record distance-bandwidth products of any other VCL experiment. We analyze here the design and fabrication of these record performance devices. Further advancements may soon lead to commercial level performance.

Table of Contents

Chapter 1

Introduction to Vertical-Cavity Lasers

This thesis examines the design, fabrication, and characterization of 1.5 μm vertical-cavity lasers. In this chapter, I introduce the basic constructs and issues for vertical-cavity lasers. I begin with a general discussion of the applications and requirements for commercial devices. Section 1.02 establishes the need for inexpensive long-wavelength sources for fiber communications. Section 1.03 then elaborates upon the device requirements necessary for widespread commercialization of long-wavelength vertical-cavity lasers. The most difficult of these requirements is the need for high-temperature operation. Section 1.04 describes some of the advantages inherent in VCLs. Section 1.05 presents the different device structures available for high-temperature design. Finally in Section 1.06 I describe the history and current state of long-wavelength vertical-cavity lasers. The use of wafer fusion, along with lateral oxidation, has allowed for the highest performance to date, from our devices, of any long-wavelength vertical-cavity lasers. We have demonstrated the highest temperature cw operation, lowest threshold currents, and largest modulation bandwidth. In addition, these devices have been demonstrated in direct link

experiments at 2.5 Gb/s. Design, fabrication, and analysis of such high-performance devices is the focus of this dissertation. Specifically, we address issues related to: a) incorporation of an oxide aperture, b) low loss mirror design, c) characterization of the fused junction, and d) analysis of device scaling. After the introductory chapter, the next two chapters will focus on the analysis of the fused junctions as well as general fabrication of the double-fused top-emitting VCL structure. Chapters 5 and 6 examine the analysis and performance of several generations of devices. The final chapter will be devoted to future work that may improve device performance further.

1.01 What is a Vertical-Cavity Laser?

Vertical-cavity (surface-emitting) lasers are a promising new class of semiconductor lasers. They have come a long way from the research curiosity they were in the late seventies. The basic concept of the "vertical-cavity laser" arose from the simple interest in having a semiconductor laser with the lasing direction perpendicular rather than parallel to the wafer surface. Figure 1.01 shows this basic difference between an in-plane semiconductor laser and a vertical-cavity laser. This concept evolved over the years to the rather complex designs and analysis of today's structures. Over the years, the research effort on the development of such devices has grown exponentially, with over 350

publications or conference presentations in 1997 alone. The great bulk of the work was done on lasers with wavelength between 850-980 nm, which I will call the GaAs regime(based on the substrate upon which it is grown). However, it is interesting to note that the first work on such devices was actually on InP based design lasing at 1.3 μm[1]. The reason for the focus on GaAs based VCLs was due not so much to the demand for this wavelength, but rather to its natural structures that lent themselves better to the Ga(Al)As material system. Particularly, the use of expitaxial GaAs/Al(Ga)As mirrors greatly improved the structures. With the use of such mirrors, performance of InP and GaAs based lasers quickly diverged so that by 1995 the highest temperature operation of InP based VCLs was only 15°C, while GaAs based VCLs were achieving record-breaking performance even when compared to in-plane lasers.

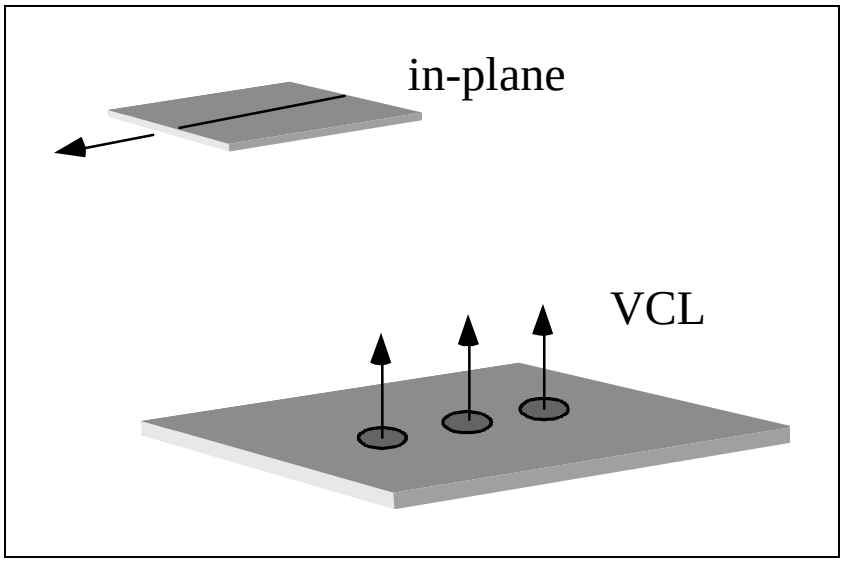

Figure 1.01. Fundamental geometries of in-plane and vertical- cavity lasers.

As of 1998, GaAs based VCLs have achieved very impressive results such as sub 100 μA threshold currents as well as 50%+ power conversion efficiencies[2,3]. In the last couple of years, though, there has been renewed effort and success in the long-wavelength regime, with at least four groups achieving above room-temperature cw operation[4,5,6,7]. This new success has renewed the possibility of achieving commercial level long-wavelength VCLs in the near future.

1.02 Demand for Vertical-Cavity Lasers

The great technical success of GaAs based VCLs opened up several potential applications of the devices. Two primary areas of interest became apparent quite early. These were: 1) datacom through fiber and 2) board-to-board computer interconnects. The primary reason VCLs were and are still attractive for computer interconnects is that VCLs can easily be fabricated into two-dimensional arrays. In addition, the very low-power consumption and low threshold of such lasers enable the possibility of directly driving the VCL with standard chip voltage logic levels. To this end, an effort was made to reduce the threshold current and improve the power conversion efficiency of the lasers. This optimization continues to this day with remarkable success. These advantages have placed GaAs based VCLs as the dominant technology for the next generation of optical interconnects, including board-to-board or even chip-to-chip.

The datacom application also arose quite early from a very simple problem: the need for increased data rates in inexpensive fiber links. These links traditionally use light-emitting diodes(LEDs) as sources. In fact, very cheap links are almost defined by the use of a LED rather than a laser. These devices can easily be tested on wafer, and coupling into multi-mode fiber offers a wide alignment tolerance. Mass production of such devices can be

implemented without the need for specialized human labor. However, a problem arises with the use of LEDs for the next generation of datacom links. Today, the fastest data rate reliably transmitted using LEDs is about 622 Mb/s. With the advent of the internet and multimedia applications, newer generation communication systems require much higher data rates. The vertical-cavity laser was perceived as a possible inexpensive high-speed source to replace LEDs. One can design a circular output beam with a low-divergence angle for ease of coupling. In addition, VCLs can be tested directly on wafer just like an LED. For many practical purposes the VCLs could be considered the new high-speed LEDs.

There remained, nonetheless, a problem with VCLs in that they could not be fabricated to work well at the traditional wavelengths for fiber communication of 1.3-μm and 1.55-μm. In fact, it was only in 1995 that Dubravko Babic reported the first room-temperature cw operation of any long-wavelength VCL[4]. Whereas the shorter wavelength GaAs based VCL were setting record performances for semiconductor lasers, long-wavelength lasers were struggling even to operate at room temperature. In order to use vertical-cavity lasers for fiber links, a new standard for fiber communication for short distances was set up to work at 850 nm(IEEE802.3z-Gigabit Ethernet). Thus

VCLs became the first choice for inexpensive high-speed, short-distance fiber communications.

Not surprisingly, with the new shorter wavelength laser, tradeoffs in certain performance criteria were made, the most important being the maximum transmission distance. This limitation still left a very strong demand for long-wavelength VCLs. One reason for the limitation was that short-distance links were to run on inexpensive multi-mode fiber. Multi-mode fiber has an inherent transmission distance limitation due to intermodal dispersion. For standard 62.5 μm fiber the maximum distance one can transmit 1.25 Gb/s is 800 m due to the distance bandwidth product of the fiber. In reality, certain imperfections in installed fiber limit the distance to 200 m(IEEE 802.3z). At longer wavelengths, there is reduced dispersion so greater distances can be connected. For example, at 1.25 Gb/s with the same imperfect fiber one can go 500 m with a 1.3 μm laser versus 200 m using a 0.85 μm source. The distance difference between these two cases may make a strong marketing difference if the costs were similar. To further increase the maximum distance of transmission, one can use single-mode fiber which addresses the modal dispersion problem. This, of course, significantly increases device packaging, connector, and fiber costs. Despite this, with the ever increasing need for bandwidth, it is very likely that single-mode fiber will become the standard choice for new generation networks.

The implementation of single-mode fiber gives rise to another problem with the use of 850 nm sources. Standard telecommunications single-mode glass fiber(SMF) is designed for long-wavelength lasers so that it is no longer single-mode for 850 nm lasers. In fact, there are actually two modes for 850 nm light in standard SMF. 980 nm VCLs, which can be fabricated as easily as 850 nm VCLs, would be much better in this respect, but require InGaAs versus Si detectors. One has to use specially designed fiber if it is to be truly single-mode at these wavelength. Using the shorter wavelengths for high-speed transmission, the distance bandwidth product of the link is severely degraded. The possible use of two different types of single-mode fiber results in issues of interoperability. Long-distance applications such as telecom or wide-area networks(WANs) will always use standard SMF fiber. Even if dispersion was not an issue, the transmission distance of 850 nm light in fiber is limited by the material loss so that it cannot be used for very long distances at any data rate. With 2 dB/km loss for 850 nm light versus 0.2 dB/km loss for 1.5 μm light, the minimum repeater distance for a long-wavelength link is an order of magnitude more than using a short-wavelength link. In addition, fiber amplifiers are also commercially available at 1.3 μm and 1.5 μm allowing the transmission distance to be increased by at least another order of magnitude. This leaves local area networks(LANs) with the choice of either installing 850 nm SMF fiber or

standard SMF, when upgrading from MMF. With a strict definition of what is LAN versus a WAN(Wide Area Network), either is a reasonable choice. But a problem arises when the boundary between LAN and WAN is unclear. System design becomes much simpler when all components are interoperable regardless of application. Thus the interoperability with existing fiber and components may become an important consideration when deciding on GaAs versus InP based lasers for LANs.

Although the LAN market offers great opportunity for long-wavelength VCLs, an even bigger possible market for vertical-cavity lasers is the so-called fiber-to-the home(FTTH) or fiber-to-the-curb(FTTC) applications(also known as the access market). In such applications a transmitter-receiver pair is placed in every home of every subscriber. Such systems would allow private residences to have very high-speed internet access, as well as CATV and telephone service, delivered on a single fiber or fiber pair. There have been, however, many roadblocks to the implementation of such systems. Among them is the cost sensitivity of this application. The 1997 OITDA(Optoelectronic Industry and Technology Development Association) report stated that the goal for the complete ONU(Optical Network Unit) with transmitter, receiver, power supply, and package should be around $125 for FTTH applications. One great roadblock to this price target has been the high cost of the fiber-optic

transmitters. In addition, due to the potentially large distances involved in such applications, SMF is necessary, increasing the components costs of the system. With the use of SMF, packaging of the lasers becomes a significant part of the transmitter cost. These costs must be minimized in order to allow for the mass production of such systems. To reduce costs some performance standards can be sacrificed, as long as some minimum standards are met so that the system can work reliably. These minimum standards must be meet in order for the devices to be considered commercially viable.

1.03 Requirements for Commercial Devices

One of the important requirements to making commercial devices is cost. The key consideration when choosing an emitter source for a transmitter package is not only the chip cost of the device, but the expense of the complete fiber-coupled transmitter package using such a device. As discussed earlier, VCLs have some potential benefits that may lead to cost cutting not in the chip cost, but rather in the complete transmitter package. To evaluate such benefits, one must have a point of reference as to what is currently available for such applications. If one wants to buy a high-data rate, single-mode, long-wavelength source for a fiber link, the *de facto* choice is the distributed feedback laser(DFB). DFB lasers offer high-power single-frequency lasing

light, as well as reasonable direct modulation response rates(~2.5 Gb/s). The technology of DFB lasers is well established and commercially available. Still, mass production of such devices is limited by some production issues. The cost of such sources is still much too high to reach the price goal necessary for FTTH. Yet, one major price reduction in the production of DFB lasers is already being implemented. This is the elimination of the thermoelectric cooler. Coolerless DFB lasers are significantly cheaper for several reasons. One reason is the elimination of the cost of the cooler itself, as well as the power supply and driving electronics to control it. Another reason is the reduction of package size as well as complexity. This difference can clearly be seen in the selling price of cooled($1500) versus uncooled DFB lasers($300). The elimination of the thermoelectric coolers means the laser must be able to perform to a minimum standard over a very wide temperature range. For reasons to be discussed in later chapters, the design and fabrication of a long-wavelength laser with good high-temperature performance is difficult. For in-plane DFB lasers these problems have primarily been overcome so that it is possible to purchase lasers with very wide temperature range of operation(-40°C to 100°C). The temperature range required differs depending on application. Applications are usually classified into “outdoor” for telecom application, with a required temperature range of -40°C to 85°C, or “indoor” for datacom, with a required

temperature range of 0°C to 70°C. These temperatures, at first glance, appear to be far in excess of any possible temperature range that can occur, but it is important to remember that these sources are placed in boxes that can heat up to high temperatures. The DFB laser story tells us that if the VCL is to compete in the total transmitter package cost, then it too must be able to operate in an uncooled package. Consequently, the major focus of long-wavelength vertical-cavity laser research has been on the improvement of the maximum continuous-wave operating temperature.

Of course, once the temperature range of operation is set there are several minimum performance criteria it must also meet at those temperatures. The simplest performance criteria is that the device must still be lasing throughout the temperature range. The highest maximum cw operating temperature reported in this thesis is 65°C, close to the datacom specification. The next important parameter it must satisfy is a minimum output power coupled into a fiber. One benefit with a VCL is that the circular output beam improves the coupling efficiencies without expensive aspherical lenses. Depending on what applications is intended, different amounts of output power are required. One can easily approximate the output required of 1.5 μm lasers through the receiver sensitivity and the loss in fiber(0.2 dB/km). Suppose one wanted a medium distance link of 20 km and had a receiver with sensitivity of -

30 dBm(@2.5 Gb/s). The minimum amount of power required would be -26 dBm(-30 dBm + .2 dB/km * 20 km) which is only 3 μW. This is an incredibly low amount of power to go 20 km. In a real system, you need a margin of error, and you want to use an inexpensive receiver with lesser sensitivities. In a more practical example, let us take a -20 dBm receiver, 2 dB fiber loss, 3 dB connector loss, and a margin of 5 dB to insure low bit-error rates. Calculating the power budget, one sees the necessary power from the laser is -10 dBm(100 μW). Thus even in a real system, the required laser power is very low ~100 μW for a long-wavelength laser. Granted, this is for a point-to-point application. For distribution systems where the power is divided over many users, the more power, the better. In long-distance applications or distribution systems where a lot of power is required, it is unlikely the VCL can complete with the DFB laser. There are applications, nonetheless, where only a very modest amount of power is required over a wide temperature range.

In low-cost transmitters, the laser light must be directly modulated by the bias of the laser. The maximum modulation frequency response of the laser becomes an issue in this case. Since it is expensive to use external modulators to impart the data onto the power, one has to be able to directly modulate the laser power at high rates. At least a gigahetz of bandwidth is required for most applications, with some applications requiring much higher values. The

important aspect to remember is that this bandwidth must be available at the high end of the temperature range, not just at room temperature. This is important because the laser bandwidth degrades significantly with increasing temperatures. However, if one looks at the problem more carefully it is clear that if the laser has significant output power at the higher temperatures, it will also have the multigigahetz modulation response.

For effective modulation and transmission at high bit rates over long distances, the laser spectrum must be very narrow. This means that the laser should only be lasing in a single mode. If a laser has more than one mode, the spectral content of pulses from the laser will be very broad. This is because the relative spectral width of a single mode is much smaller that the spacing between adjacent modes. Due to fiber dispersion, the difference in group velocity for different wavelengths, large spectral width implies pulse broadening through propagation in fiber. Over long distances this difference in velocity means narrow pulses will be spread out to very broad pulses. If the pulses are spaced closely, as is necessary in a high data rate transmission system, then the smeared pulses will make 1's and 0's indistinguishable in a digital system. Furthermore, multilateral mode lasers cannot be modulated as quickly as single-mode lasers due to intermodal competition. Thus for high data rate transmission, it is important that the laser source have only a single lasing mode.

There are also more basic concerns when choosing a laser source. One of these issues is the reliability of the source. Typically, one wants laser sources to have a mean lifetime of about 10 years, but longer lifetimes such as 100 years are much preferred. The reason for such long lifetime demands is the statistical variations in the devices. Even if the mean lifetime is much greater than is required there will be a small portion that will die well before the mean. Device reliability is one of the key concerns when it comes to the production of fused vertical-cavity lasers. There has yet to be a definitive study on the reliability of fused lasers, but such a study would be required before one could seriously consider commercial devices.

Assuming one has a device that meets the performance criteria, it still does not guarantee a lower cost VCL versus DFB laser. To achieve the low-cost objective one has to have a device that is simple to package into a transmitter. Packaging brings up the issue of top-emitting devices versus bottom-emitting devices. One advantage top-emitting VCL have over bottom-emitting is the elimination of the flip-chip bonding process. The latter process involves taking a bottom-emitting structure and mounting it with the epi side down onto a substrate. Placing individual dies onto submounts can slow the production significantly. If not done carefully, this process may induce stresses in the devices, affecting device reliability. Finally, on-wafer testing with

bottom-emitting devices is considerably more complicated. For top-emitting devices, a fiber can be directly placed above the device to measure its power and wavelength. With bottom-emitting devices, one needs to couple the light into a fiber through the use of a lens. To avoid the flip-chip bonding process our packaged devices were of the top-emitting variety. We will see in a later chapters that there may be other performance advantages to using such a structure.

1.04 Advantages of VCLs--Fact or Fiction?

As VCL performance has reached the level of in-plane lasers, at least in the GaAs regime, many arguments have been offered as to the a superiority of VCLs over in-plane lasers. These claims range from 1) better fiber coupling, to 2) 2D arrays, to 3) lower threshold currents. Some characteristics of VCLs do allow for a competitive advantage over in-plane lasers while others are unsubstantiated suppositions. I will evaluate the substantiality of these assertions, focusing on the application of data transmission through fiber. Some beneficial characteristics may only be pertinent to other applications, so to maintain focus they will not be included in this discussion. Advantages can typically be classified as either related to cost savings or to better performance.

One of the most noticeable features of VCLs is the high density of devices one can have on a wafer. One can easily see this in Fig 1.02. In fact, in Babic's work he quotes some 10,000 devices on a 8x8 mm sample. Imagine, on a two-inch wafer one can have over 300,000 devices. This is clearly an attractive proposition in that a few wafers could supply the entire world demand. There is, of course, a fatal flaw in this argument. One cannot separate or package devices that are 30 μm apart.

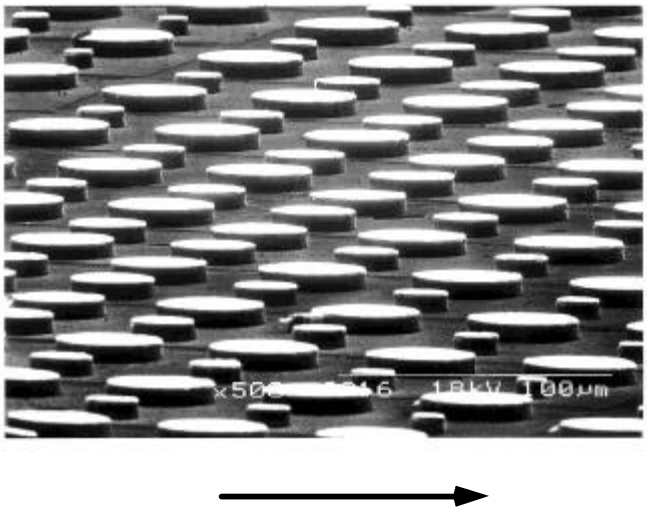

Figure 1.02. SEM of VCL wafer showing very high packing density of devices.

In fact, if one wants to handle individual chips, there is some minimum practical size to the chips. The minimum chip size is usually quoted between 150-300 μm per side. In-plane laser chips are usually 300x300 μm in size. This means

that there is no real advantage to having a higher density of devices since they cannot be separated. One can then argue not to separate the devices, but rather to have an array of devices going into an array of fibers. Yet once again there is a problem in that the minimum spacing between fiber cores is usually about 150 μm.

This means there is no point in placing the lasers any closer than this dimension. So, in terms of fiber-optic applications, there is no real difference in the packing density of in-plane lasers over vertical-cavity lasers. However, one could again argue that VCLs can be arranged in two dimensional arrays whereas in-plane laser are limited to one dimensional arrays. This is in fact true, but there is no practical need for two dimensional arrays in fiber applications. A 1-D fiber ribbon cable has become the standard for parallel optical links. There are no foreseeable plans to go to 2-D fiber ribbon bundles. For other applications such as laser printing, allowing for 2-D arrays creates a significant competitive advantage. In printing applications where one wants very large number of elements, the packing density also becomes a critical advantage for VCLs. This is a good example as to how different applications may imply different requirements for the devices. For long-wavelength VCLs, though, the primary applications is communication through fiber cable.

Another highly touted advantage of VCLs is their circular output beam. Astigmatism in output beams require very expensive optics to allow for high-efficient coupling to single-mode fiber. For standard in-plane lasers one can usually only achieve 50% coupling with a single lens element. If one wants to couple directly without a lens element this coupling becomes much worse ~ 10%. Many times mode converters are fabricated on the end of the in-plane lasers to give better coupling efficiencies and to reduce the tolerance for error in alignment[8]. The ultimate goal of the use of mode-converters is to be able to align the laser to fiber without active feedback. Active alignment is time consuming and expensive. However, the problem with mode converters is that they have traditionally been difficult to fabricate reliably in high volume. Vertical-cavity lasers can have a natural circular output beam that can be matched directly to a single-mode fiber. Since both fiber and VCL have similar mode shapes and similar mode sizes, high-efficient coupling may be expected even without lens elements or special mode converters. The fiber must be placed very close to the active device if such coupling is to be efficient. In effect, the fiber must be placed in very close proximity to the output mirror (<3 μm). The fact that fiber placement is much simpler in the top-emitting devices grants them an advantage. If one wanted to use bottom-emitting devices, either a hole must be etched through the substrate[9], or an integrated lens element

can be etched on the back of wafer[10]. It is unclear how effective each of these coupling schemes may be, but we have done our own measurements and found that 70% coupling into a single-mode fiber using a single lens element can be achieved. This coupling will be discussed in the later chapters. This issue is a bit misleading, though, since in-plane lasers inherently have higher maximum output powers than do VCLs. This comes from the smaller dimensions of VCLs over in-plane lasers. Larger VCLs can be designed, but most of the other advantages that come with VCLs diminish at larger dimensions. Given this fact, it is likely that it is better to have a 15 mW in-plane laser with 20% coupling than a 2 mW VCL with 90% coupling. Admittedly, it takes much more electrical power to generate 15 mW of output power from an in-plane laser than 2 mW of output power from a VCLs. Coupling issues may therefore still play an important role in device choice.

This naturally brings us to the issue of power consumption of VCLs. One of the defining feature of VCLs is their small active region volume. A low-threshold vertical-cavity laser usually has an active region of 6 μm in diameter or smaller. This translates into an active region area of about 30 μm^2, whereas a typical in-plane laser has an active region area of 900 μm^2 (3 μm width x 300 μm length). This is over an order of magnitude difference in area. This small active region area has some very nice properties. One of these properties is the

very low-threshold currents achievable in VCLs. The reason for the low-threshold currents is very simple. A certain current density is needed into the active region to achieve lasing. A small area translates directly into a small threshold current level, assuming a constant current density for lasing. For very small sizes the threshold current density may start to increase with smaller dimensions. As will be examined in great detail in Chapter 4, over a large range of device dimensions, the threshold current is proportional to the area. The much lower threshold currents allow VCLs to operate at much lower current levels than in-plane lasers. An above average performance VCL has a threshold current around 0.5 mA, whereas an average in-plane laser has a threshold current of 10 mA. This comes directly from the large difference in active region area as discussed.

Clearly, threshold is only one aspect of the operating current for a laser. To achieve a certain output power level as well as modulation frequency, a laser needs to be biased above threshold. For very high-power operation the in-plane laser is better due to its larger size, allowing for better heat dissipation, but what about for low-power applications(<1 mW)? In this case, the in-plane has already one strike against it with the higher threshold current. All the current used to reach threshold does not contribute to the output power, so one could consider it as wasted. The other important factor is the differential efficiency

above threshold. This determines the amount of power one gets for a certain current about threshold. Both devices can be designed to have very high efficiencies, and VCLs with up to 95% efficiencies have been demonstrated[3]. For low-power applications both devices can achieve the necessary power level with only a few milliamps above threshold.

The final important factor is the modulation response at a given bias current. If one wants to be able to modulate the laser directly at high data rates then there is also a requirement for a certain current above threshold. Equation 1.01 show the dependence for semiconductor lasers of modulation frequency versus bias current. Before heating takes effects, there is a wide range of which the modulation bandwidth is proportional to the square root of the current above threshold. The proportionality factor is usually called the modulation current enhancement factor(MCEF).

$$f_r = MCEF\sqrt{I - I_{th}} = \frac{1}{2p}\sqrt{\frac{g_o \Gamma h_i v_g (I - I_{th})}{eV_{active}}} \qquad (1.01)$$

In this equation g_o is the differential gain, Γ is the total confinement factor, η_i is the injection efficiency, v_g is the group velocity, and V_{active} is the active region volume. The important thing to note in comparing MCEFs between in-plane and VCLs is the factor of the active region volume in Equation 1.01. Since the active region volume in a VCL is smaller by an order of magnitude, its MCEFs

should have much larger values. Recent reports on VCLs have shown MCEFs on the order of 20 GHz/mA$^{1/2}$, much larger than anything reported from an in-plane lasers[11]. This naturally suggests that VCLs are capable of much higher absolute speeds than in-plane lasers. In fact, this has not been demonstrated experimentally. In general, a good MCEF for an in-plane laser may be 1 GHz/mA$^{1/2}$, whereas a good MCEF for a VCL may be 5 GHz/mA$^{1/2}$. This means to achieve 5 GHz modulation response one would need to take the in-plane laser to 25 mA above threshold, whereas one would only need to take the VCL to only 1 mA above threshold. This translates into a huge difference in operating currents. Although a bit exaggerated in this example, to get multi-GHz operation, one would only need a couple of milliamps from an VCL and as much as 50 mA from an in-plane laser. The voltage at 2 mA for a VCL versus 50 mA for in-plane is very similar so that the power consumption for the same frequency operation can be more than 10 times less in a VCL. It is important to note that these are only typical values for in-plane lasers. There have been experimental demonstrations of submilliamp threshold currents[12] and high MCEFs[13] from in-plane lasers using very small active regions(very short narrow stripes). However, the mass fabrication of such lasers is questionable. Overall, the low-power consumption is an important advantage VCLs have for many low-power, high-frequency applications.

Another factor touted about VCLs since their inception is the ease of packaging. Arguably, having surface normal emission allows for a simpler package. For most applications, though, this is not the case (with the notable exception of CD player read heads). For fiber-coupled applications there is no reason why surface normal emission is an advantage. Indeed, most manufactures of VCLs actually have packages that redirect the emitted power from the surface normal direction to the in-plane direction, either using a 45° mirror or a waveguide. In addition, in-plane lasers have the advantage that they can be integrated with Si V-grooves for self-alignment to single-mode fiber. These hybrid packaging techniques called Photonic Lightwave Circuits(PLC) offer potentially much more efficient laser packaging involving SMF. Most PLC platform require laser with spot size converters, so that there may still be barriers to large volume production. On the whole, though, on the issue of ease of packaging, VCL are at best even with in-plane lasers.

Finally, there is the issue of on-wafer testing. This is a critical issue in the comparison of VCLs and in-plane lasers. Since the light coming from a VCL is perpendicular to the wafer surface, there is no need to separate individual lasers before they are tested. An automated process can probe each device on a wafer and determine if the laser is suitable for use. In the case of an in-plane laser, individual bars must be cleaved before any testing can occur.

This makes it very difficult to have a completely automated process. With a VCL, on-wafer testing can be done with a simple fiber probe and electrical probes coming down and sending the data to either a power meter or a spectrometer. Dies that do not match the criteria can either be stored in a computer as bad, or can be injected in the form of an inkblot onto bad dies as in LED processing. Since on-wafer testing can be done on wafer, the dicing process as well as the wire-bonding process can also be automated. This allows the possibility of testing, dicing, and wire-bonding the devices to a package without any human labor. It is important to note that this could only be done with a top-emitting structure. With a bottom-emitting structure, it is necessary to flip-chip bond the devices individually before they are tested so the whole advantage is negated. If one could find a self aligned technique to align the fiber and the devices, then VCL testing and packaging could proceed very rapidly, allowing for low-cost, high-volume production. On-wafer testing may be one of the most fundamental advantages VCLs have over their in-plane counterparts. In the next section some of the specifics of the device structures will be analyzed in light of these advantages of VCLs.

1.05 Device Structures

To get a better feel for different device structures one has to understand some of the basic issues in VCLs. As discussed earlier, the defining feature of VCLs is lasing emission perpendicular to the semiconductor surface. This, in turn, limits the gain region of this laser to very short lengths. Typically, these lengths are less than 0.1 μm compared to hundreds of microns for in-plane lasers. The very short gain region allows for very little amplification for a round-trip of an optical mode. To achieve the gain-equal-to-loss condition necessary for lasing, the small amount of gain must be matched with an equally small amount of loss. This requires very high reflectivity mirrors and short optical cavities. To attain some perspective on how reflective these mirrors need to be, we present a simple example. Consider the seemingly innocent case of two 99% reflectivity mirrors; even without any other optical losses, two 99.0% mirrors would have a round-trip loss of 2%. Assuming three 8 nm quantum wells, this loss would require a very high 2000/cm of material gain(taking into account the gain enhancement factor of a standing wave discussed later). This demonstrates one of the two basic requirements for realizing high-performance VCLs, namely a good active region and high reflectivity mirrors.

1.05.1 Current Confinement

There are several other issues that must be addressed before the different mirror systems can be compared. Two of these issues are intimately related in the VCL geometry; these are current confinement and optical confinement. The current confinement method, critical in device scaling, is often considered the defining element in the VCL. Fig. 1.03,1.05,1.06,1.07 show the four basic methods to achieve current confinement: proton implantation, etched mesa, dielectric/oxide aperture, and buried-heterostructure. Each has its advantages and disadvantages which will be discussed.

Possibly the simplest VCL structure to fabricate is the proton-implanted structure depicted in Figure 1.03. It is fabricated by a masked ion implantation, which defines the active region by funneling current from the non-conducting region into the lasing region. Typically, the implantation is carefully tailored so as to avoid going through the active region and avoid the nonradiative recombination that would accompany the implant. This type of GaAs based VCLs is commercially available and has been shown to be very reliable, with lifetimes exceeding one million hours.

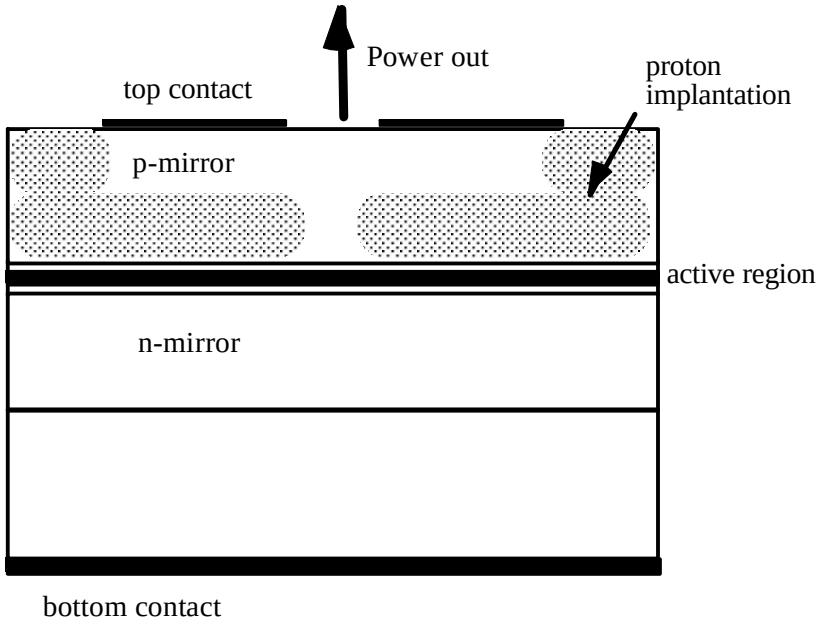

Figure 1.03. Typical proton implanted VCL.

The primary drawback to this structure is the lack of stable optical confinement. Optical guiding is achieved through a process known as thermal lensing. Thermal lensing relies on the change of the refractive index of a semiconductor as it is heated up. Current flow through the device forms a natural thermal gradient from the center to the edge of the device. This gradient causes a gradient in the refractive index, providing some optical confinement. However, the thermal profile in the device tends to be unstable under modulation. This leads to near-field patterns that are many times dependent on the patterns of data being sent. For most applications, this can be corrected by simply coding

data to be sent such that there are nearly equal ones and zeros. In this way, the average power through the device is constant over thermal time scales(microseconds).

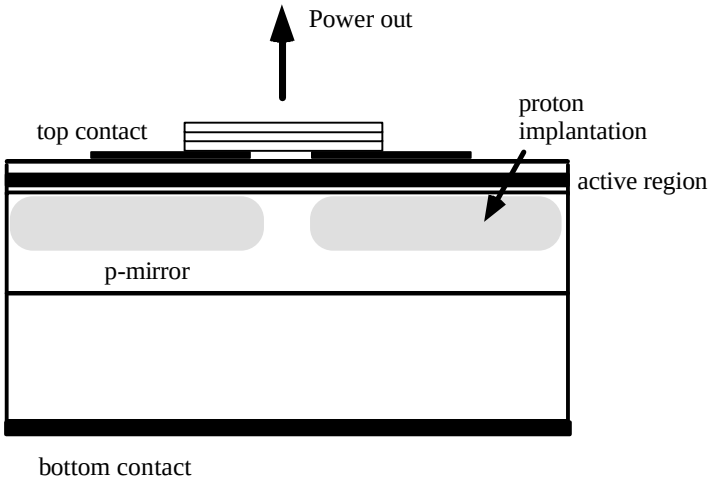

Figure 1.04. Oxygen implanted 1.3 μm VCL.

The other problem with lack of strong optical guiding is that diffraction losses prevent the devices from being scaled down to small dimensions. We shall see that the scaling of devices becomes an important issue in all the structures presented. Figure 1.04 shows a possible alternative structure for long-wavelength VCLs, using oxygen implantation as well as fusion. Lo *et al.* have investigated such a structure and have achieved a record performance for a 1.3 μm laser, with submilliamp threshold currents and up to 40°C cw operation.

Another simple VCL structure is the etched pillar. In this structure, current confinement is achieved through the etching of the top mirror to define the active region. An example of such a structure is shown in Fig. 1.05. As with most in-plane (ridge) lasers, the etching usually stops above the active region so as to avoid surface recombination. In contrast to a proton implanted device, strong optical guiding is naturally provided by the air-semiconductor interface, allowing for stable optical modes. In addition, etched mesa structures allow for uniform injection of current into the active region, maximizing gain mode overlap.

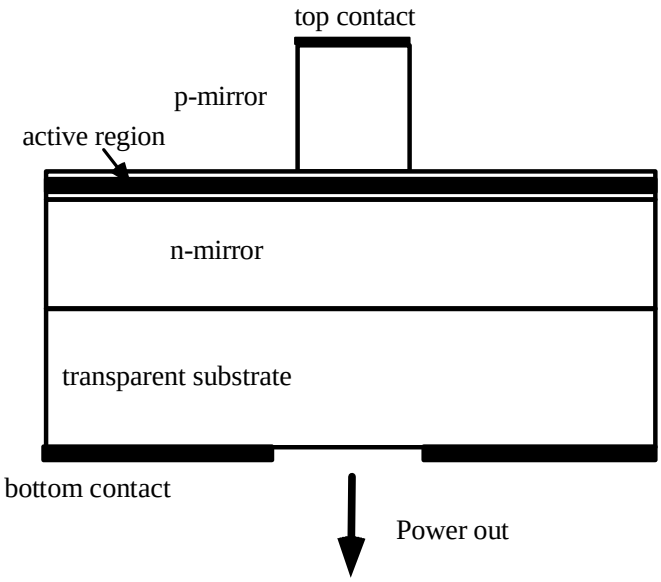

Figure 1.05. Bottom-emitting etch pillar structure.

The most serious drawback to this structure is the inability to scale the devices to very small dimensions. The optical loss at the etched semiconductor/air interface increases dramatically for device diameters below 8 μm[14]. This increased loss leads to increased thresholds currents and dramatically reduced efficiencies for smaller devices. Ultimately this reduces the attractiveness of such a structure, because many of the benefits of VCLs are realized only when devices are quite small.

An alternative to the etch pillar structure is the dielectrically-apertured VCL, referred to as oxide-confined VCLs. This type of structure has produced the highest performance results in both GaAs[2,3] and long-wavelength VCLs[15]. Fig. 1.06 shows the double-fused laterally-oxidized 1.5-μm VCL using this current constriction.

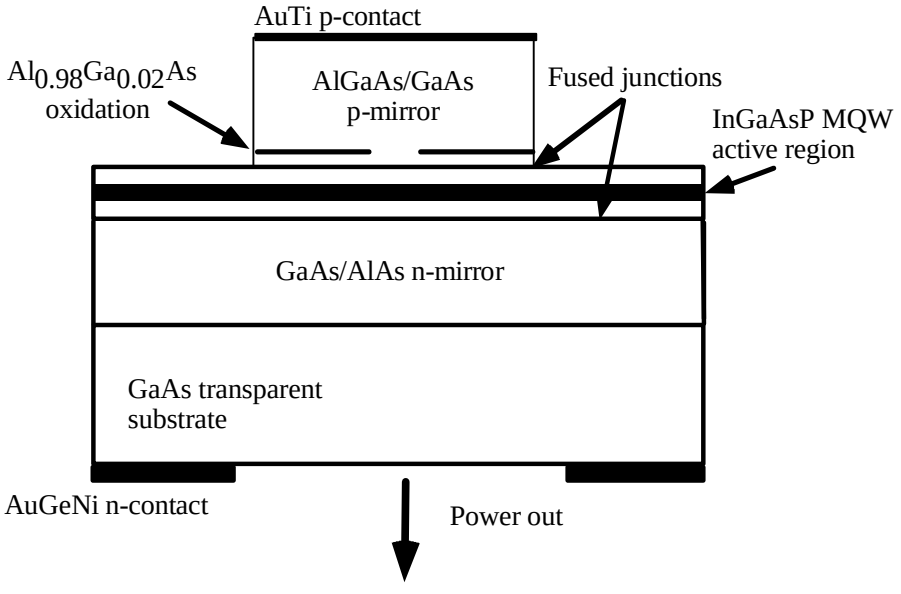

Figure 1.06. Bottom-emitting, double-fused, oxide confined VCL.

The dielectrically-apertured structures rely on selective lateral oxidation or etching to form a current blocking aperture over the active region. Designed properly, these types of apertured structures have also shown very good optical confinement. The index difference at the aperture forms an effective waveguide for the structure. However, unlike the etched pillar structure, these types of devices can be scaled to much smaller dimensions. In addition, it has been shown theoretically that by tailoring the aperture to a tapered lens-like shape, optical losses can be even further reduced for small device diameters[16]. These type of tapered oxide apertures in the AlGaAs system can be fabricated through specific layer composition designs[17]. In the case of wafer-fused AlGaAs/GaAs based mirrors, these designs can be directly incorporated into a long-wavelength VCL.

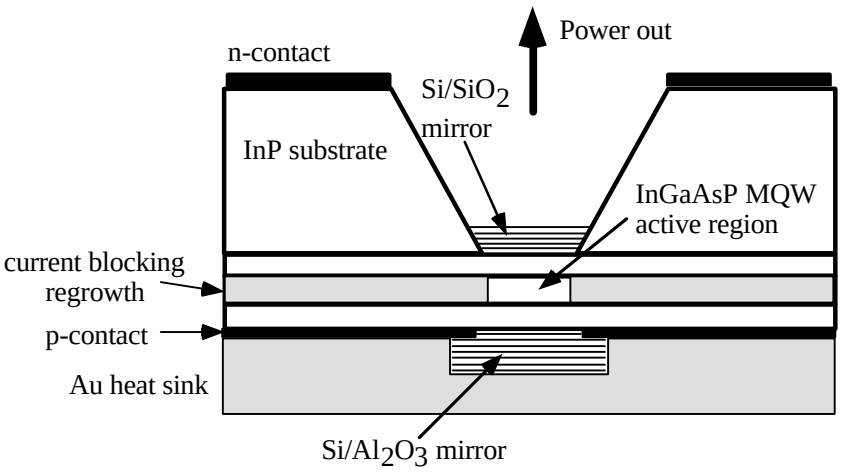

Figure 1.07. Buried-heterostructure, long-wavelength VCL.

Dielectrically-apertured structures can also be used in the long-wavelength regime with other type mirrors. These include using InAlAs oxidation[18] or selective etching of InGaAsP over InP[19]. This confinement scheme solves many of the problems associated with the other two designs discussed, but still does not prevent carrier diffusion out of the active region.

The only structure to eliminate both carrier diffusion and surface recombination is the buried-heterostructure. This type of structure is fabricated by an etch through the active region and then regrowing current blocking layers in the etched regions, as in a buried-heterostructure in-plane laser. Fig. 1.07 shows a long-wavelength VCL with two dielectric mirrors and a buried-heterostructure confinement scheme. Usually, the regrown material is of higher

bandgap than the active material, effectively confining carriers in the active region. The higher bandgap material is also of lower refractive index which provides optical guiding. In contrast to the oxide aperture structure, this guiding profile is fixed by the current blocking scheme, limiting the flexibility in design. In terms of optical loss, there are no reports as of now on the significance of the problem in such structures. Yet one might speculate the losses would be small due to the small index difference between the guiding layers and the active layers. The real difficulty in this structure is the proper regrowth of the current blocking layers, and the integration with epitaxial or fused mirrors. Even though regrowth techniques are significantly more developed in the InP based system than the (Al)GaAs, there still may be some problems with circular instead of square active regions. The many crystal planes exposed in a circular geometry causes havoc for uniform regrowth. However, overall, the buried-heterostructure is a promising structure that should allow for high-performance devices if one can integrate this confinement scheme with good mirrors. In the future work section of Chapter 7, I will discuss a possible double-fused, buried-heterostructure VCL for carrier and optical confinement.

1.05.2 Mirror Requirements

The type of mirror system used in the long-wavelength VCL is of critical importance. There are several important parameters to consider when comparing different mirror systems, the most important being the maximum achievable reflectivity. As seen in the earlier example, even 99% mirror reflectivities are not enough for high-performance operation. Two parameters determine the reflectivity of a given mirror; these are transmission and absorptive losses. Transmission through the mirror can always be decreased by adding more periods to the quarter wave stack. Thus it is really the loss in the mirror that determines the *maximum* reflectivity available. In the case of high reflectivity mirrors, this loss is, to first order, independent of the number of periods. It is determined by two factors: the material absorption in the layers, and the penetration depth of the optical wave($\%Loss \approx 100 \bullet 2aL_{penetration}$). An approximate formula for this penetration depth is $L_{penetration} \approx \frac{l}{4\Delta n}$, where n is the index difference. The origin of these formulas will be described in the next chapter. Clearly, one would want high index-difference mirrors to reduce the penetration depth and thereby reduce the amount of loss in the mirror.

There are also a couple of other benefits to having high index-contrast mirrors. The first is that the reduced penetration depth can result in reduced diffraction loss because of the shorter effective cavity. This means less optical

confinement is necessary to scale devices to smaller diameters. The other advantage of high-contrast mirrors is that they have a larger optical bandwidth over which they have high reflectivity. This allows for reduced growth tolerances to achieve high reflectivity; however, this does not reduce the growth tolerance for the lasing mode position. Unlike simple single-interface mirrors, quarter-wave stacks have a different phase of reflection at different wavelengths. This means that if a cavity mode is tuned exactly to 1.30 μm and the mirrors are slightly mistuned, then the lasing mode will not be exactly at 1.30 μm. The amount the mirrors affect the final lasing wavelength is directly proportional to their phase penetration depths. The percentage error in the final lasing wavelength is simply the weighted average of the percentage growth error in each mirror and the active region:

$$l_{lase} = \frac{\Delta l_{m1} \times L_{m1} + \Delta l_{m2} \times L_{m2} + \Delta l_{c} \times L_{c}}{L_{m1} + L_{m2} + L_{c}} \qquad (1.02)$$

Since, typically, the penetration depths of the mirrors are significantly larger than the active region cavity length, the error in the final cavity mode is more determined by the growth error in the mirrors than the active region cavity. When choosing a mirror system, all these considerations must be taken into account. In certain types of structures, the thermal impedance of the mirror plays an important role in device heating. Finally, one must also consider the

practicality and manufacturability of different structures in choosing a mirror system.

1.05.3 Mirror Systems

There are many different mirror schemes that have been proposed for long-wavelength VCLs. One can generally classify them into three main categories. These are the epitaxially-grown(InP/InGaAsP) , dielectric-deposited(Si/SiO_x), and wafer-fused (AlAs/GaAs), where in parenthesis I have put the most common materials used. Each mirror system has its advantages and disadvantages, and a combination of two schemes may in some situations be advantageous.

Let us start with the direct epitaxially-grown mirrors. These mirrors have the distinct advantage that they are directly integrated into the device as with standard GaAs based VCLs. This allows for easy manufacturability and device processing. The most work has been done on the InP/InGaAsP epitaxial mirror. However, there have been some promising results in Sb based mirrors lattice matched to InP[20]. The problem with the InP/InGaAsP system is the small index difference between InP and InGaAsP. This is especially true for 1.3 μm lasers where the composition choice for the InGaAsP layer is even further reduced. A very large number of periods is required to reach any reasonable

reflectivity(40-60 periods). Figure 1.08 shows a typical plot of reflectivity of three different mirror systems versus the number of periods in the mirror. This small index difference also results in large penetration depth into the mirrors, increasing diffractive and absorptive losses. Furthermore, the thermal conductivity of InGaAsP material is very low due to alloy scattering of phonons from quaternary material. This results in a thick mirror(>10μm) with a very low thermal conductivity.

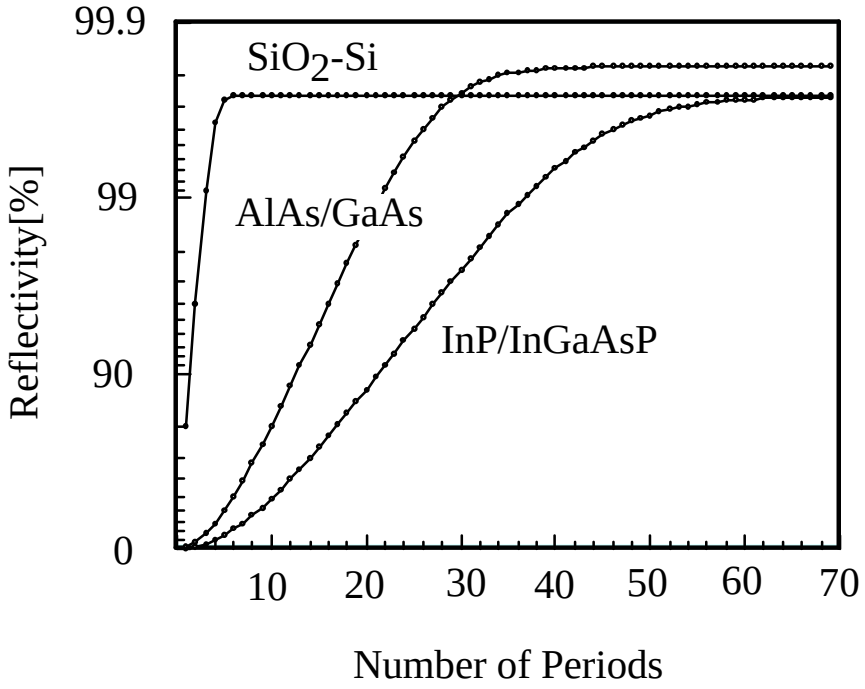

Figure 1.08. Typical comparison of long-wavelength mirror systems.

Heating in such a device is very pronounced and limits the maximum operating temperature. With these problems, it seems very unlikely that a device with two epitaxial InP/InGaAsP mirrors will work effectively, but there is still some possibility for a single epitaxial mirror with another type mirror for effective heat removal. For Sb based mirrors there is plenty of index contrast, but there are many problems with the growth of such materials. There have been only very meager laser results using such a system, but improvements in growth techniques may change that[21].

The second type of mirror system developed for long-wavelength VCLs is the dielectric-deposited mirror. This mirror system typically consists of an oxide layer as one material and a semiconductor, such as Si/SiO_2, as the other. This mirror system has the distinct advantage of having a very high index difference due to the very low index of oxides and very high index of semiconductors. Less than eight periods are usually required to reach peak reflectivity. The small penetration depth reduces diffractive losses allowing for smaller devices to be fabricated. Unfortunately, the small penetration depth does not always translate directly into very high peak. This is because the reduction in penetration depth is accompanied by a very large absorption coefficient in the amorphous Si layers; this loss can be as high as 400 - 1000/cm[22]. To avoid this problem, structures can and have been fabricated

that replace the Si with TiO_2, but in doing so, significantly reduces the index contrast. The second problem with this mirror system is the very poor thermal conductivity of amorphous oxide layers such as SiO_2. This can result in excessive self-heating under continuous-wave operation. Finally, there is great difficulty in integrating such mirrors as the bottom mirror in a device. To do so, a deep hole must be etched in the substrate to reach the active region, as shown in 1.07. The top of the device must then be mounted on a supporting substrate, most often a heat sink, to maintain mechanical stability of the thin epitaxial layers. Clearly, this type of mirror is better suited as a top rather than a bottom mirror, but has been used effectively as both.

The final mirror system to produce working lasers is the wafer-fused AlAs/GaAs mirror. Wafer fusion allows for the use of non-lattice matched materials such as InP and GaAs to be combined into a single device[23]. Epitaxial wafers of each material are grown separately and combined under high temperature and pressure. The resultant interface is electrically conductive and optically transparent. GaAs/AlAs mirrors provide a high index contrast as well as the uniformity and reproducibility that comes with epitaxial growth. Furthermore, the successful technique of lateral oxidation has been directly employed for current constriction, producing record results. On the negative side, intervalance band absorption in p-doped GaAs becomes more pronounced

at longer wavelengths, limiting the maximum reflectivity of the mirrors. This absorption is significantly worse at 1.55 μm than at 1.3 μm, but still allows for very high maximum reflectivities. In terms of manufacturability, wafer fusion has been commercialized by Hewlett Packard, Inc. in the production of high efficiency LEDs, so that the final overriding question concerning wafer-fused devices remains reliability. There is no data on the reliability of such junctions at the high-current densities that laser operate at, but, encouragingly, fused junctions have been found to be very reliable at the lower current levels of LEDs[24]. This thesis will examine many of the issues involved in fabricating wafer-fused VCLs.

1.05.4 Quantum Well Active Region

The final important ingredient to making high-performance, long-wavelength VCLs is a good quantum well active region. Due to high Auger coefficients and smaller conduction band discontinuities, the high-temperature, InP based active regions are more difficult to achieve than GaAs based ones. Fortunately, the basic active region designs for in-plane lasers and VCLs are very similar. Using this, one can utilize the years of experience accumulated in making high temperature 1.3 μm and 1.55 μm in-plane lasers. Such lasers have been fabricated that operate well above 120°C continuos-wave[25]. These

lasers employ strained quantum wells to reduce the effects of Auger recombination. Many such strained wells can be used without material degradation if one strain-compensates(puts opposite strain in barriers and wells), such that the net strain per well/barrier is small. All the high-temperature cw VCL results discussed in the introduction use strain-compensated wells with 7, 9, and 12 wells, respectively, for the UCSB[4], NTT[7], and Furakawa[26] devices. Moreover, VCLs do not need any vertical optical guiding layer incorporated into the active region growth since this is accomplished by the mirrors. This allows for further flexibility in terms of carrier confinement, eliminating the need for the optical separate confinement heterostructure.

If in-plane lasers operate to such high temperatures and VCLs have these same active regions, one might ask the question why long-wavelength VCLs have only operated to 65°C and below. To answer this one must look at which point on the gain curve the active regions are operated at in both cases. If in both cases the quantum wells required the same amount of material gain to lase, then indeed both lasers would operate to the same temperature. The key is that VCLs fabricated until now have much higher losses than their in-plane counterparts. This requires more material gain to lase, which the active region cannot supply at the higher temperatures. To make higher temperature VCLs,

one comes to the obvious conclusion that one needs to reduce the round-trip loss in the structures, i.e. make better mirrors. Of course, this simple argument ignores heating in the laser due to dissipated power. The thermal resistances of VCLs are much higher than in-plane lasers(in-plane lasers have more area to dissipate heat). If, however, one makes low-threshold, low-voltage lasers, this heating becomes insignificant at threshold. As a simple example, if one has a 1 mA threshold VCL with 3 Volt bias the total dissipated power is 3 mW. If one takes a very high value of thermal resistance of 2000°C/W, the total temperature rise at threshold is 6°C(.003 W * 2000 °C/W). The point is that if one makes good lasers in terms of threshold currents, through better mirrors for example, self-heating in the laser will be greatly reduced. The final conclusion seems to be that there is no *inherent* reason why VCLs should not operate to the same temperatures as their in-plane counterparts. In Chapter 4 we will show in great detail some of the limitation on our VCLs.

A rather new concept in long-wavelength VCL research that has recently evolved is the attempt to make long-wavelength active regions lattice matched to GaAs. In this case, one would not need to fuse mirrors, but would grow them just as one would do a GaAs VCL. One possible way to accomplish this is to incorporate Nitrogen into an InGaAs active region. The Nitrogen lowers the lattice constant of the crystal so that it can be lattice matched to

GaAs. Normally, one would expect a reduction in lattice constant to decrease the bandedge of emission. But surprisingly, due to the bowing parameter of Nitrogen in InGaAs, incorporation of Nitrogen actually *lowers* the bandgap of emission. This means one can have lattice matched active regions to GaAs to emit at long wavelength. The growth of such material is only in its infant stages, and thus results have not been outstanding as of yet. The longer the wavelength of emission, the more difficult the material is to grow. There have been some promising results at 1.2 μm with in-plane lasers[27]. With VCL, only optical-pumped lasers have been achieved at 1.3 μm[28]. It seems likely, though, that for 1.3 μm VCLs that this is an attractive scheme for devices. The growth of such material is a very long way away from making practical 1.55 μm lasers.

1.06 State-Of-The-Art Long-Wavelength VCLs

Given the basic structures, it is worthwhile to discuss the evolution of the device structures in long-wavelength VCLs. Figure 1.09 shows the dramatic decrease in pulsed threshold currents of device in the last several years. Before we delve into the recent history of the long-wavelength vertical-cavity laser, I will briefly discuss the early history of the device.

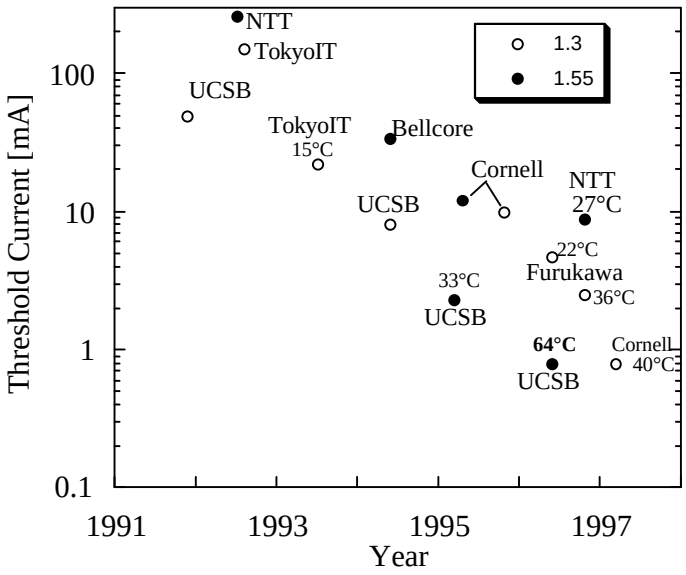

Figure 1.09 - Recent progress on long-wavelength VCL research.

In 1979, Keniichi Iga *et al.* first reported a semiconductor laser which emitted light perpendicular to the substrate[1]. The structure was a InGaAsP double-heterostructure active region, with a 90 μm long cavity and two metal mirrors. It lased under pulsed conditions at 77 K with a threshold current of 0.9 A. For the next ten years, only Iga's group from the Tokyo Institute of Technology reported on long-wavelength VCLs. During this decade, several improvements on their initial device structure were implemented. A shorter cavity was implemented by etching through the back of the substrate[9], and dielectric mirrors were developed for higher reflectivity[29]. In addition, there was some work on the use of expitaxial InP/InGaAsP mirrors[30].

Meanwhile, UCSB began its long-wavelength VCL effort. The first device attempted was similar to the two dielectric mirror structure developed by Iga *et al.* It achieved a record-high optically-pumped temperature of 66°C[31]. A year after this result was the first publication of the use of wafer fusion for long-wavelength vertical-cavity lasers by Dudley *et al.*[32]. This first use of wafer fusion for this purpose lead to our devices reported in this thesis. At the time, the single-fused 1.3 μm VCL by Dudley gave a record-low pulsed threshold of 8 mA. Recently, further improvements on the dielectric mirror structure were giving results. Baba *et al.* from the Tokyo I. T. reported on a near room-temperature(15°C) 1.3 μm VCL[6]. This near room-temperature result would be the highest temperature cw result for several years. Soon Dubravko Babic at UCSB began to work on the first double-fused VCL. The final structure from this work used an etch-pillar aperture structure described above. In mid 1995 Babic reported on a 33°C cw result, representing the first true room-temperature operation of a long-wavelength VCL[4].

In the last couple of years there has been significant effort from other groups on the use of wafer fusion for long-wavelength VCLs. Successful results have come from a group at NTT[7] as well as Cornell[5] using single-fused structures similar to the ones used by Dudley. Moreover, further optimization of the Baba structure by a group at Furakawa yielded above room-

temperature cw performance of 37°C[26]. Our efforts at UCSB continued to be successful with the use of the double-fused structure. Using these structures, for the first time system experiments were conducted using long-wavelength VCLs.

1.07 Summary

Vertical-cavity lasers are an important new class of semiconductor lasers. They offer the potential for inexpensive and reliable sources for many applications. For extended distance fiber-optic applications, long-wavelength sources at 1.3 μm or 1.55 μm are preferred. These communications wavelengths are compatible with the existing fiber infrastructure and allow for much longer distance transmission as compared with GaAs based lasers. However, to achieve very inexpensive transceivers, the lasers must operate over a wide temperature range. The wide temperature range operation allows for elimination of the thermoelectric cooler along with the high-power driving electronics that go along with it. Until recently, long-wavelength vertical-cavity lasers performed very poorly at elevated temperature. Only in the last couple of year have researchers been able to achieve even room-temperature cw operation. Our effort in the last couple years, have resulted in great strides in

device performance. The use of the wafer-fusion process, enabling high reflectivity mirrors, along with the oxide aperture current constriction have allowed for record- high cw operation from our lasers. This record-high performance operation enabled us to use the devices in real link experiments at 2.5 Gb/s, demonstrating the potential of such devices for high-speed fiber optic communications.

In the rest of the thesis we will elaborate upon the design and fabrication of the high-temperature long-wavelength VCLs. We begin in Chapter 2 with the basic design issues associated with such devices. Chapter 3 is fully dedicated to the characterization of the fused junction interface. Chapter 4 describes the fabrication of the rather complicated structures we have designed. Chapter 5 will focus on the characteristics of the several generations of devices including limiting factors affecting such devices. Chapter 6 will describe both the dynamic behavior and the high-speed link experiments conducted using our devices. The conclusion will then overview the thesis while providing possible directions for future research.

1.08 References

[1] H. Soda, K. Iga, C. Kitahara, and Y. Suematsu, "GaInAsP/InP surface emitting injection lasers.", Jpn. J. Appl. Phys., vol.18, 2329 (1979).

[2] D. L. Huffaker, L. A. Graham, H. Deng, and D. G. Deppe, "Sub-40 µA continuous-wave lasing in an oxidized vertical-cavity surface-emitting laser with dielectric mirrors.", IEEE Photonics Technology Letters, vol.8, 974 (1996).

[3] R. Jager, M. Grabherr, C. Jung, R. Michalzik, G. Reiner, B. Weigl, and K. J. Ebeling, "57% wallplug efficiency oxide-confined 850 nm wavelength GaAs VCSELs.", Elect. Lett., vol.33, 330 (1997).

[4] D. I. Babic, K. Streubel, R. P. Mirin, N. M. Margalit, J. E. Bowers, E. L. Hu, D. E. Mars, L. Yang, and K. Carey, "Room-temperature continuous-wave operation of 1.54- mu m vertical-cavity lasers.", IEEE Photonics Technology Letters, vol.7, 1225 (1995).

[5] Y. Qian, Z. H. Zhu, Y. H. Lo, D. L. Huffaker, D. G. Deppe, H. Q. Hou, B. E. Hammons, W. Lin, and Y. K. Tu, "Long wavelength (1.3 µm) vertical-cavity surface-emitting lasers with a wafer-bonded mirror and an oxygen-implanted confinement region.", Appl. Phys. Lett., vol.71, 25 (1997).

[6] T. Baba, Y. Yogo, K. Suzuki, F. Koyama, and K. Iga, "Near room temperature continuous wave lasing characteristics of GaInAsP/InP surface emitting laser.", Elect. Lett., vol.29, 913 (1993).

[7] Y. Ohiso, C. Amano, Y. Itoh, K. Tateno, T. Tadokoro, H. Takenouchi, and T. Kurokawa, "1.55 mu m vertical-cavity surface-emitting lasers

with wafer-fused InGaAsP/lnP-GaAs/AlAs DBRs", Elect. Lett., vol.32, 1483 (1996).

[8] B. Hubner, G. Vollrath, et al., "Laser diodes with integrated spot-size transformer as low-cost optical transmitter elements for telecommunications.", IEEE Journal of Selected Topics in Quantum Electronics, vol.3, 1372 (1997).

[9] Y. Motegi, H. Soda, and K. Iga, "Surface-emitting GaInAsP/InP injection laser with short cavity length.", Elect. Lett., vol.18, 461 (1982).

[10] E. M. Strzelecka, G. D. Robinson, M. G. Peters, F. H. Peters, and L. A. Coldren, "Monolithic integration of vertical-cavity laser diodes with refractive GaAs microlenses.", Elect. Lett., vol.31, 724 (1995).

[11] K. L. Lear, A. Mar, K. D. Choquette, S. P. Kilcoyne, R. P. Schneider Jr., and K. M. Geib, "High-frequency modulation of oxide-confined vertical cavity surface emitting lasers.", Elect. Lett., vol.32, 457 (1996).

[12] T. Tsuchiya, M. Komori, A. Oka, T. Kawano, and A. Oishi, "Ultralow threshold 1.3- mu m InGaAsP-InP compressive-strained multiquantum-well monolithic laser array for parallel high-density optical interconnects.", IEEE Journal of Selected Topics in Quantum Electronics, vol.1, 203 (1995).

[13] R. Nagarajan, D. Tauber, and J. E. Bowers, "High speed semiconductor lasers.", International Journal of High Speed Electronics and Systems, vol.5, 1 (1994).

[14] P. D. Floyd, B. J. Thibeault, E. R. Hegblom, J. Ko, L. A. Coldren, and J. L. Merz, "Comparison of optical losses in dielectric-apertured vertical-cavity lasers.", IEEE Photonics Technology Letters, vol.8, 590 (1996).

[15] N. M. Margalit, J. Piprek, S. Zhang, D. I. Babic, K. Streubel, R. P. Mirin, J. R. Wesselmann, and J. E. Bowers, "64 degrees C continuous-wave operation of 1.5- μm vertical-cavity laser.", IEEE Journal of Selected Topics in Quantum Electronics, vol.3, 359 (1997).

[16] E. R. Hegblom, D. I. Babic, B. J. Thibeault, and L. A. Coldren, "Scattering losses from dielectric apertures in vertical-cavity lasers.", IEEE Journal of Selected Topics in Quantum Electronics, vol.3, 379 (1997).

[17] R. L. Naone, E. R. Hegblom, B. J. Thibeault, and L. A. Coldren, "Oxidation of AlGaAs layers for tapered apertures in vertical-cavity lasers.", Elect. Lett., vol.33, 300 (1997).

[18] H. Gebretsadik, K. Kamath, W.-D. Zhou, P. Bhattacharyaa, C. Caneau, and R. Bhat, "Lateral oxidation of InAlAs in InP-based heterostructures for long wavelength vertical cavity surface emitting laser applications.", Appl. Phys. Lett., vol.72, 135 (1998).

[19] A. Tsigopoulos, V. Paschos, C. Caroubalos, P. Salet, and J. Jacquet, "Numerical modeling of undercut ridge VCSELs designed for CW operation at 1.3 mu m: design optimization.", IEEE J. Quant. Elect., vol.33, 2221 (1997).

[20] H. Shimomura, T. Anan, and S. Sugou, "Growth of AlPSb and GaPSb on InP by gas-source molecular beam epitaxy.", J. Cryst. Growth, vol.162, 121 (1996).

[21] O. Blum, J. F. Klem, K. L. Lear, G. A. Vawter, and S. R. Kurtz, "Optically pumped, monolithic, all-epitaxial 1.56 mu m vertical cavity surface emitting laser using Sb-based reflectors.", Elect. Lett., vol.33, 1878 (1997).

[22] Dudley, J. J., “Wafer-fused long-wavelength vertical-cavity lasers”, Ph.D. dissertation, University of California, Santa Barbara, unpublished(1994).

[23] R. J. Ram, J. J. Dudley, J. E. Bowers, L. Yang, K. Carey, S. J. Rosner, and K. Nauka, "GaAs to InP wafer fusion.", J. Appl. Phys., vol.78 4227 (1995).

[24] F. A. Kish, D. A. Vanderwater, D. C. DeFevere, D. A. Steigerwald, G. E. Hofler, K. G. Park, and F. M. Steranka, "Highly reliable and efficient semiconductor wafer-bonded AlGaInP/GaP light-emitting diodes", Elect. Lett., vol.32, 132 (1996).

[25] C. E. Zah, R. Bhat, and T. P. Lee, "High-temperature operation of AlGaInAs/InP lasers 1994.", Optical and Quantum Electronics, vol.28, 463 (1996).

[26] S. Uchiyama, N. Yokouchi, and T. Ninomiya, "Continuous-wave operation up to 36 degrees C of 1.3- mu m GaInAsP-InP vertical-cavity surface-emitting lasers.", IEEE Photonics Technology Letters, vol.9, 141 (1997).

[27] K. Nakahara, M. Kondow, T. Kitatani, M. C. Larson, and K. Uomi, "1.3- mu m continuous-wave lasing operation in GaInNAs quantum-well lasers.", IEEE Photonics Technology Letters, vol.10, 487 (1998).

[28] M. C. Larson, M. Kondow, T. Kitatani, K. Tamura, and M. Okai, "Photopumped lasing at 1.25 mu m of GaInNAs-GaAs multiple-quantum-well vertical-cavity surface-emitting lasers.", IEEE Photonics Technology Letters, vol.9, 1549 (1997).

[29] K. Iga and S. Uchiyama, "GaInAsP/InP surface-emitting laser diode.", Optical and Quantum Electronics, vol.18, 403 (1986).

[30] A. Chailertvanitkul, K. Iga, and K. Moriki, "GaInAsP/InP surface emitting laser (lambda =1.4 mu m, 77K) with heteromultilayer Bragg reflector.", Elect. Lett., vol.21, 303 (1985).

[31] H. Wada, D. I. Babic, et al., "Low-threshold, high-temperature pulsed operation of InGaAsP/InP vertical cavity surface emitting lasers", IEEE Photonics Technology Letters, vol.3, 977 (1991).

[32] J. J. Dudley, D. I. Babic, R. Mirin, L. Yang, B. I. Miller, R. J. Ram, T. Reynolds, E. L. Hu, and J. E. Bowers, "Low threshold, wafer fused long wavelength vertical cavity lasers.", Appl. Phys. Lett., vol.64, 1463 (1994).

Chapter 2

VCL Design

In making a vertical-cavity laser, at least two separate area of designs need to be considered: 1) the transverse 1-D structure and 2) the lateral structure of the device. In many cases tradeoffs arise from the design of the transverse structure and the lateral structure. In these two categories lie the issues of gain, loss, resistance, and heating, among others. This chapter will examine many of these design issues. We begin with a simple 1-D analysis of device design. The terminology of round-trip gain or loss is introduced, as well as an examination of the standing wave in a VCL. Section 2.02 deals with the issue of reflectivity from lossless quarter-wave stack mirrors. Simple formulas

are examined for the reflectivity of such mirrors. Section 2.03 introduces absorptive loss into the VCL design. These losses greatly impact the performance of the final devices. Section 2.04 described some of the grading and doping techniques used in designing the p-mirror, which try simultaneously to reduce absorptive loss as well as limit device resistance. In the following sections the 2-D design of the VCL is examined. The role of the oxide-aperture in limiting electrical and thermal resistance is evaluated. In Section 2.06 I discuss the general scaling laws in oxide VCLs. This section reveals the importance of realizing proper scaling of device to small dimensions. Finally in Section 2.07 a general analytical model is presented, which describes the role of current spreading. This current spreading plays a critical role in limiting the device scaling described in Section 2.06. All the issues described in this chapter play an important role in device performance as analyzed in Chapter 5 and 6.

2.01 Simple Transverse-Structure Design

Figure 2.01 shows the basic components of the transverse structure in a VCL. As with any laser, the two fundamental elements necessary are mirrors and a gain region. In the case of a VCL, the mirrors and the active(gain) region are stacked vertically on one another, perpendicular to the semiconductor

surface. A general condition for lasing occurs when the gain from the active region plus the spontaneous emission equals the loss. As discussed in Chapter 1, to have an efficient VCL one has to have both very low loss and very high gain. In an electrically-pumped structure, electrons and holes are injected into the active region to provide that gain. However, in the case of a vertical structure, the active region can only provide so much gain due to its short interaction length with the mode. This means that the losses must be very small.

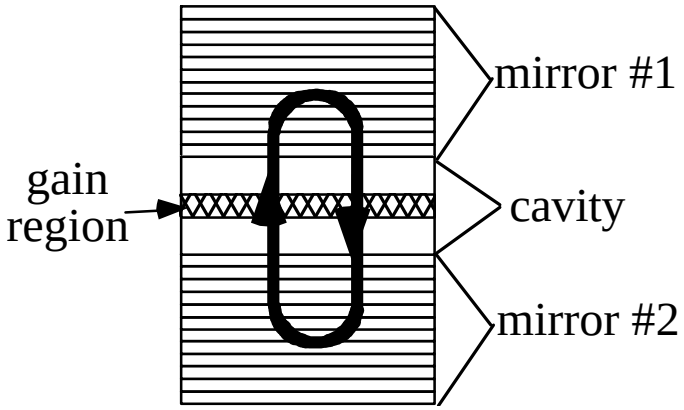

Figure 2.01. Simple schematic of transverse VCL structure.

Before one discusses the exact amount of loss in mirrors and cavity, it is important to familiarize oneself with the terminology of round-trip loss or gain used in analyzing VCLs. To understand this terminology, one has to discern that one can view the optical as a standing wave between two mirrors or as a

traveling wave bouncing between the mirrors. These two pictures can both be correct as long as one takes all the factors into account. In the traveling wave picture, the power in the mode is amplified as it passes through the active region. The power bounces off a mirror and gets sent back into the active region where it gets amplified again, bounces off the second mirror, and repeats the process. As the mode bounces back and forth, there are several effects that contribute to its loss of power including absorptive material loss, diffractive losses, scattering losses, and transmission through the mirror. Lasing occurs where the net gain/loss through the structure is zero such that any additional gain provided would indefinitely increase the power in the optical mode. With additional gain, the power in the mode obviously cannot go to infinity, so there must be some limit to this process. When the gain is larger than the loss, the optical mode starts to increase in power exponentially. As the power gets larger, the amplification process(stimulated emission) cannot support such power levels so that the gain starts to saturate(the carriers are getting depleted due to the fast recombination of stimulated emission). In steady state the active region cannot support a carrier density in which the gain is larger than the loss. Any additional carriers injected into the active region to provide additional gain are quickly recombined through stimulated emission due to the increased power traveling through the active region. Thus any additional carriers injected into

the active region above threshold recombine through stimulated emission giving the characteristic L-I curve of a laser.

To quantify the optical loss of a mode, it is many times useful to consider the traveling wave picture so that one can talk about round-trip(or single pass) loss or gain through a structure. Technically, the loss or gain adds exponentially with each pass through different structures. This can be seen in Equation 2.01.

$$P = P_o \exp(-a_1 l_1 - a_2 l_2 - a_3 l_3)$$
$$P = P_o \exp(gl) \qquad (2.01)$$

P is final power, P_o is initial power, a is loss, g is gain, and l is the length of interaction. In a VCL, it is very convenient to make an approximation that allows one to add the gain or loss linearly. Since the thicknesses of the layer for which the optical mode passes through are very thin, the net effect of any section on the optical mode is very small. In this case, one can approximate very accurately the effect of passing through a segment by using exp(x) =1+x for x<<1. For example, gl, which is the single pass gain through an active region, is rarely over 1%. This means the error in using the approximation exp(gl)=1+ gl is only 0.5% of the correct one pass gain value. The gain values are not known to nearly such accuracies, so using such an approximation does not create additional uncertainty. Hence for VCLs it is very useful and accurate

to use the linear version of the gain-equals-loss condition rather than the exponential one used in in-plane lasers. So one can use the very simple formula for threshold of $G=L+T$, where G is the round-trip loss in the structure, L is the total round-trip loss in the structure, and T is the transmission through both mirrors.

The problem with this simple traveling wave picture is that it does not convey the whole story, if one uses the obvious formulas of $G=2g_{act}l_{act}$ and $L=2al_{tot}$. The forward-traveling wave and the backward-traveling wave can constructively or destructively interfere with one another through a coherent interaction between the two waves. If one was considering an incoherent source, then the formulas above would be correct as stated above. However, in the case of a VCL, the light is indeed coherent on the length scale of the cavity, forming a standing wave in the cavity. Figure 2.02 shows a typical standing-wave pattern in a VCL cavity.

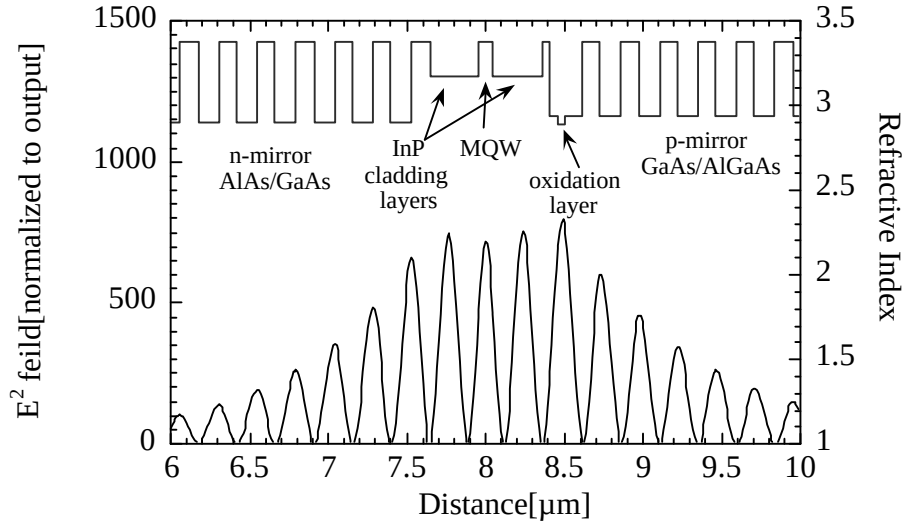

Figure 2.02. Standing-wave pattern in long-wavelength VCL.

The formation of such a standing can be derived from basic electromagnetic theory. Let us consider the case of two counterpropagating complex plane waves of equal amplitude incident on a medium, as in Equation 2.02 where x is the complex electric field, w is the frequency of the wave, f is the phase of the wave, k is the wave vector, and P is the power.

$$x_1 = E_o \exp(-iw_1 t + ikz + f_1); x_2 = E_o \exp(-iw_2 t - ikz + f_2)$$
$$P_{tpt} \propto xx^* = 2E_o^2 + 2E_o^2 \cos(2kz + (w_2 - w_1)t + f_2 - f_1) \qquad (2.02)$$

The power is proportional to the magnitude of the electric field vector squared. These simple equations can convey many of the aspects in a laser cavity. For instance, if w_1 and w_2 are not equal, then the cosine term averages over time to zero so that the total power is simply the sum of the individual

powers, i.e. incoherent interaction. If, however, w_1 and w_2 are equal, then what forms is a standing wave with a spatial period of $l/2n$, where l/n is the wavelength of the light in the material with refractive index n. In the case of coherent interaction, the power of the standing-wave peaks is actually double the power of the case of incoherent interaction.

This interaction is very important in that this forces the active region to the standing-wave peak for optimal operation. In this case, the power incident on the active region is almost twice as high as in the traveling wave picture. Since the gain depends on the power incident on the medium, the gain is actually twice as high as in the traveling wave picture. In order to make the traveling wave picture accurate, one needs to multiply the gain or loss in each region by the standing wave factor in that region. For example, if one wants to consider the gain or loss from a thin layer, then one needs to get the average value of the electric field at that segment- i.e. integrate the field and divide by the length of the segment. This average value is called the gain enhancement factor and is expressed in Equation 2.03 below,

$$x = \frac{2}{\ell} \int_{x_o - \ell/2}^{x_o - \ell/2} Cos\left[\frac{2pn}{l} x\right]^2 dx \qquad (2.03)$$

where x_o is the distance away from the standing-wave peak, and l is the length of the segment. This formula is usually only used in the active region, but it can

be used in other regions. For this region, I include the factor x_o where it is usually not included since the active region is normally centered in the standing-wave peak. This integral has a analytical solution expressed in Equation 2.04.

$$x = \frac{Sin\left[\frac{2pn}{l}\left(l + 2x_o\right)\right] + Sin\left[\frac{2pn}{l}\left(l - 2x_o\right)\right]}{2pnl/l} \qquad (2.04)$$

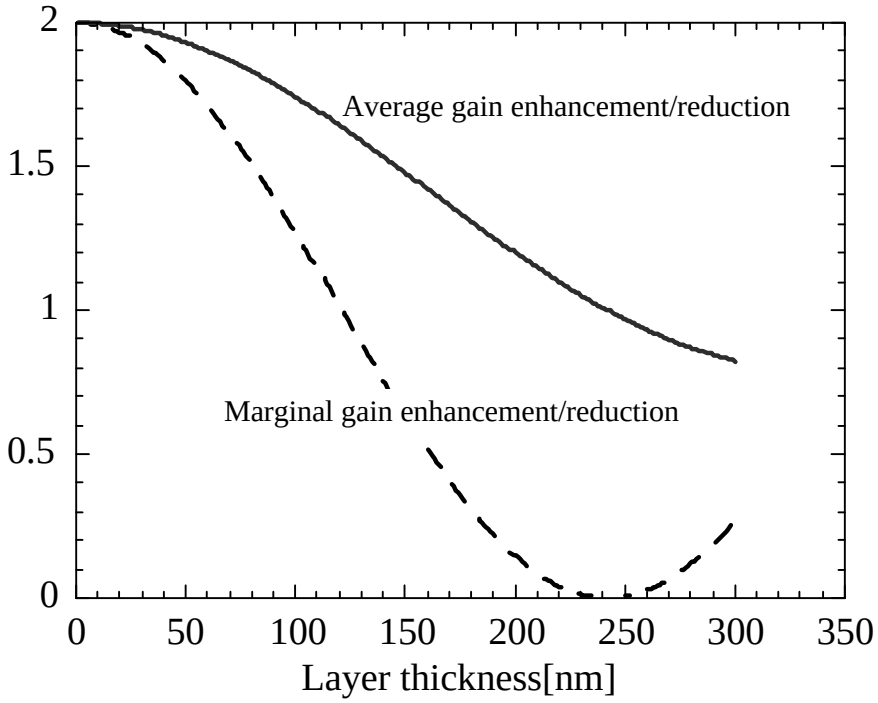

Figure 2.03 - Gain enhancement factor and standing wave for active region of thickness l .

Figure 2.03 shows a plot of the standing wave and also the gain enhancement factor assuming a centered active region of thickness l, a

wavelength of 1.55 μm, and a refractive index of 3.2. If one looks at the standing-wave curve, one can see the decreasing marginal benefit of making the active region thicker(for example by adding more quantum wells). One can see that if the active region is 100 nm thick(as is the case in the real double-fused structure) the quantum well at the edge of the active region is only giving half the benefit of the quantum well in the center. The average gain enhancement from all the wells can be read of this graph as 1.75 for an active region 100 nm thick.

Due to practical issues such as growth errors, many times the quantum wells in double-fused VCLs may not be centered exactly at the standing-wave peak. How much is the gain from the wells is decreased by misplacing the active region? This is an especially critical question to consider when one is making adjustments to the active region thickness so as to get the correct cavity mode. If one trims the thickness on one-half of the active region on but not the other half, then the quantum wells will be off-center. This reduction in gain effectively acts as an increase in loss for the same pumping level. Figure 2.04 shows the reduction in gain if one misplaces the quantum wells normalized to the quantum wells being centered.

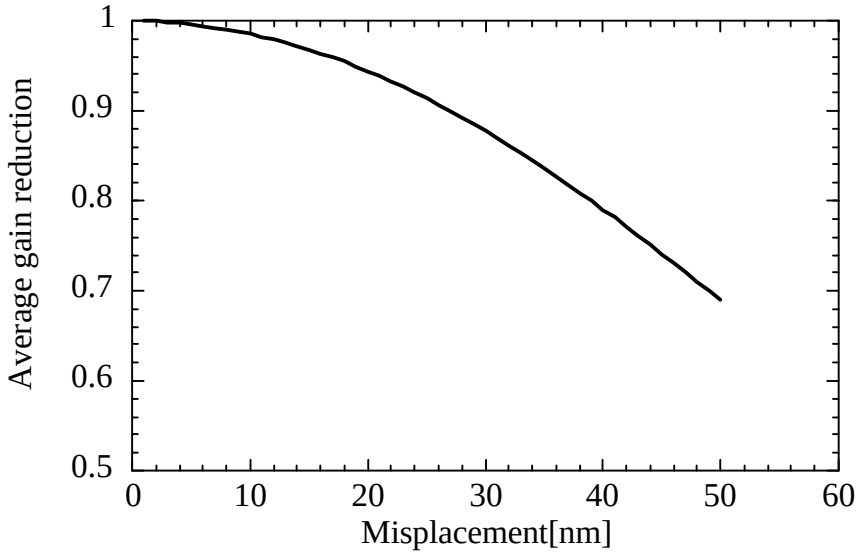

Figure 2.04 - Reduction in effective gain by misplacing the quantum wells away form standing-wave peak for typical parameters used in fused VCL.

The standing-wave factors are clearly very important in much of the design of the VCL. One can also use the standing-wave nulls for ones advantage. For instance, the fused junction can potentially introduce a lot of loss to a laser, but correct placement of the junction may reduce the effect of this loss dramatically. In addition, high-doped layers in the mirrors may have drastically different amounts of effective loss if they are at the standing-wave peak or null. We can introduce a new term called the “loss-reduction factor” which is very similar to the gain enhancement for sections close to the standing-wave null. Equations 2.05 define the loss-reduction factor.

$$a_{eff} = \frac{a_{material}}{x_{loss}}$$
$$x_{loss} = 1 \Big/ (2 - x) \qquad (2.05)$$

Figure 2.05 plots the loss-reduction factor versus misplacement from the standing-wave null. Three thicknesses of interaction lengths are considered of 10 nm, 20 nm, and 40 nm. The thinner the layer, and the closer to the null, the greater the reduction in loss. However, even for a misplacement of 10 nm and an interaction thickness of 20 nm, the loss reduction is greater than a factor of 10. For a layer precisely at a null, with a thickness of 20 nm, the loss reduction may be almost a factor of 100. In the original double-fused structure by Babic, the fused junctions were positioned 30 nm and 50 nm away from the null. This means that the loss-reduction factor was not very large for such a case. It is not exactly clear what the interaction length is between the fused junction and the optical wave, or, for that matter, how much optical loss, if any, is at the junction. In Chapter 3, this loss will be estimated.

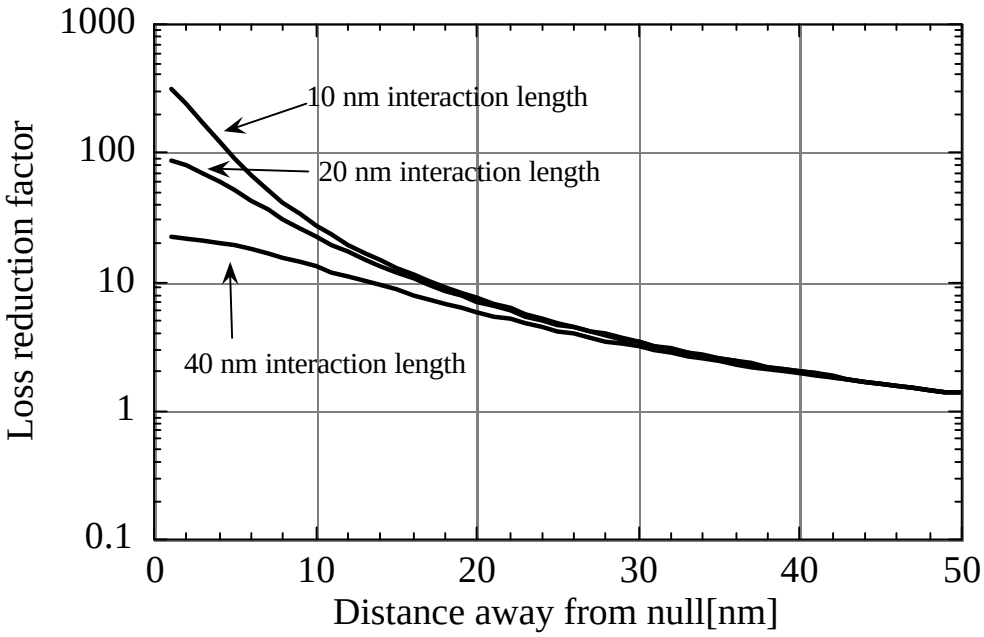

Figure 2.05- Loss-reduction factor near a standing-wave null.

Thus with the gain enhancement and loss-reduction factors we can maintain the very simple formula for threshold in a VCL, namely $G=L+T$. Yet, now instead of $G= 2gl$, it is equal to $2\Psi gl$. Equivalently, if there is a layer that extends less than a standing-wave period, the loss in that section must be multiplied by its standing-wave factor. It is important to note that this scheme assumes that the presence of loss or gain in any one region does not perturb the standing-wave pattern itself. However, this is almost always the case in a VCL. With this basic information one can start to investigate specifics of VCL structures.

2.02 Reflectivity of GaAs/AlGaAs DBR Mirrors

The principles and workings of DBR mirrors have been thoroughly investigated, and many different method of analyzing such structures have been devised, including transmission matrix, analytical formulas, and adiabatic approximations[1,2,3] Whichever way one analyzes DBR stacks, the basic principle of operations is a series of dielectric interfaces that provide a reflection that is in phase with the rest of the stack. The DBR layers are typically quarter-wave stacks in that a quarter wavelength of material is required to keep all the reflections in phase. Actually 3/4, 5/4, 7/4 layers can also be used for such a mirror, but require more material for the same peak reflection.

It is many times useful to separate out the loss and transmission through a mirror so that reflectivity is equal to one minus transmission plus loss($R=1-(T+L)$). One obviously cannot separate out these two factors for a general quarter wave stack, but there are many conditions where this separation remains relatively accurate. These conditions will later be presented. So, assuming this separation can be done, we can first look at the transmission through different mirror stacks. An analytical formula has been developed by Babic[4] for the

peak reflection from a lossless quarter-wave stack. The formula is expressed in Equation 2.06 below.

$$q = \frac{n_i}{n_H} : p = \frac{n_L}{n_H}; a = \frac{n_e}{n_H}$$
$$R = \left(\frac{1 - qap^{m-1}}{1 + qap^{m-1}} \right)^2 \qquad (2.06)$$

Here, n_i is the refractive index of the incident medium, n_H is the refractive index of the high index material, n_L is the refractive index of the low-index material, n_e is the refractive index of the exiting material, and m is the number of layer(NOT the number of periods). The formula assumes that all the interfaces are phase matched so as to increase the reflection. Figure 2.06 shows 1-R or the transmission through several quarter wave stacks versus number of periods in the stack. One can clearly see that as the index difference between the two materials is decreased, through reduced Al concentration, larger numbers of period are need to achieve the same reflectivity.

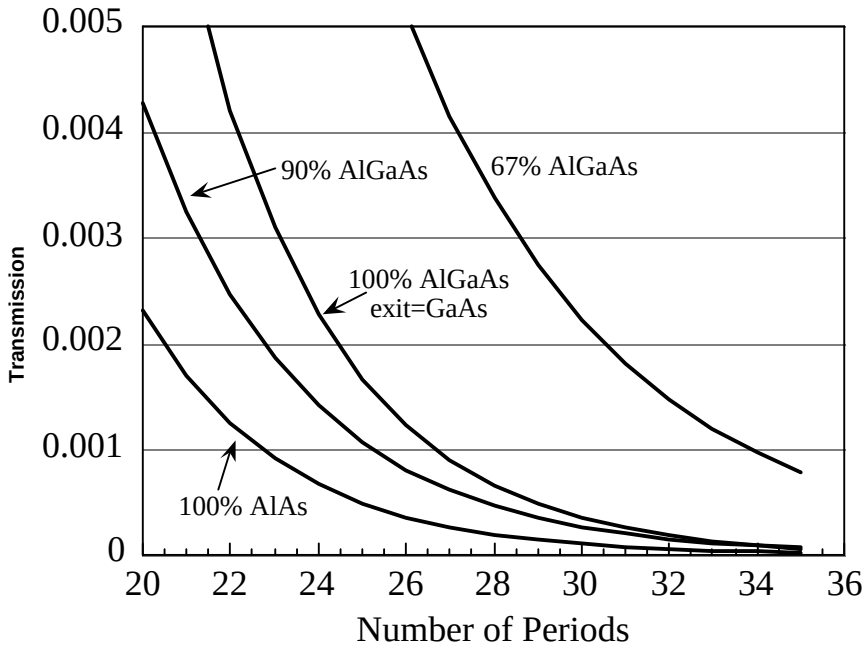

Figure 2.06. Transmission through mirror versus composition. The incident medium is InP and the exit medium is air unless otherwise stated. Wavelength of light for all cases is 1.55 μm.

One thing ignored by this formula is the possible grading of the mirror interfaces to allow for better carrier transport across the interfaces. Nevertheless, one can still use such a formula if one multiplies the refractive index difference between the two materials by a factor f. This factor is typically between .9 and 1 for most grading schemes. Figure 2.07 plots the effect of this factor for several values of f. The incident medium is InP and the exit medium is air.

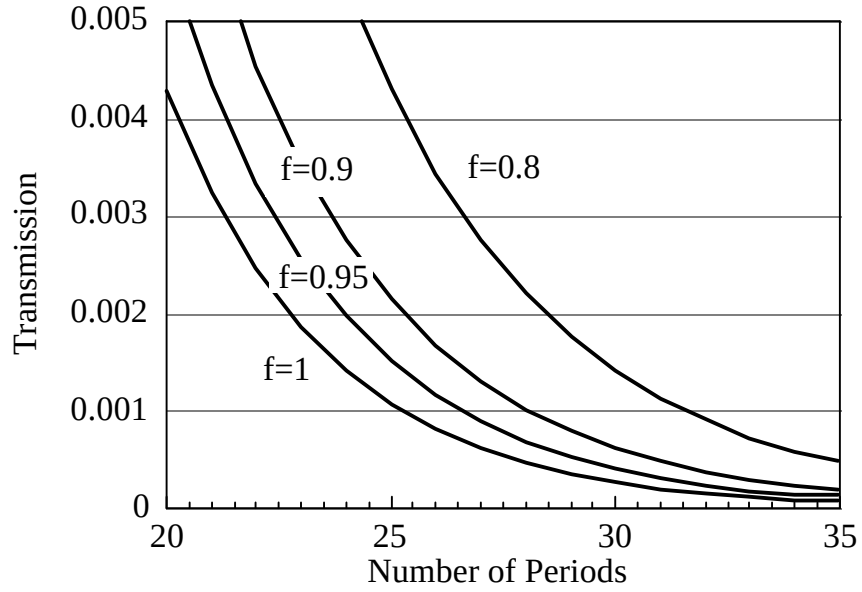

Figure 2.07. Effect of grading interfaces on mirror reflectivity/transmission. 90% AlGaAs/GaAs stack used.

Now that we have investigated the ideal case we can now also consider absorptive losses in the mirrors. In the case of a uniform absorptive loss in the mirror, an analytical formula have been developed by Babic to quantify the round-trip loss through a DBR. This formula assumes the optical wave penetrates a certain distance into the quarter wave stack, constant up to that penetration depth, and zero past it. Of course, this is nowhere near the case in reality, as can be seen in Figure 2.02. To make the formula accurate the loss penetration depth is chosen such that the same amount of loss occurs in this penetration as in the real structure. The formula for this penetration depth is given below in Equations 2.07.

$$l_{pent.} = \left(\frac{l_o}{4n}\right)\Lambda$$
$$\Lambda = \frac{q}{1-p}\,\frac{(1+a^2 p^{m-1})(1-p^m)}{(1+q^2 a^2 p^{2m-2})} \qquad (2.07)$$

So the loss from this penetration depth is then simply given *by* $L=1-\exp(2al_{pent}) \approx 2al_{pent}$. This is a fairly simple formula for the loss from a mirror, but the penetration depth formula can be simplified with some approximation even further. For most VCL structures the reflectivity from the mirror is quite high.

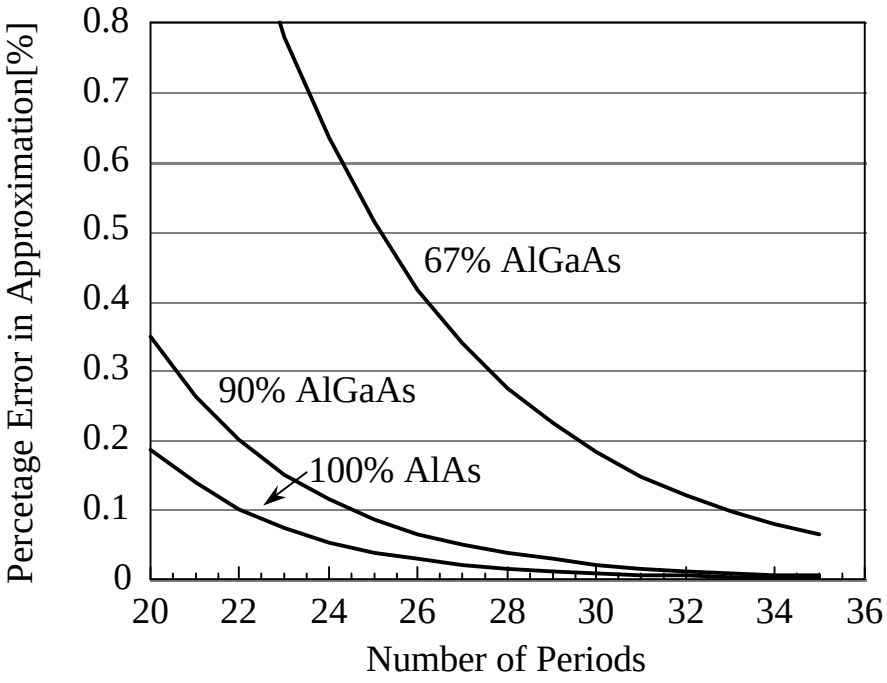

Figure 2.08. Error in penetration depth approximation vs. number of periods.

In this case, one can approximate the penetration depth as simply $l/4Dn$, where Dn is the index difference between the two materials. This formula shows the direct relationship between the loss in a mirror and the refractive index difference between the two material used. One can ask how closely the simple formula matches the more complicated one. Figure 2.08 plots the percentage error in the penetration depth for several compositions as a function of number of mirror period.

Evidently, for high reflectivities the error in using this second approximation is quite small. One certainly does not know the loss in the layers to within 1% accuracy. It is also interesting to plot this error versus the transmission through the mirror. Figure 2.09 plots this error versus the transmission through the mirror (changing the number of mirror periods to vary the reflectivity). Note that all three cases plotted in Figure 2.08 fall on the same line when plotted in this fashion. So we can conclude that this approximation does not depend on the refractive index of the high material, but rather on the total reflectivity from the stack. Again, one sees that for any reasonable parameters, the error in such a formula is quite small. This formula is intended for use when the loss in the stack is uniform. If one wants to have different loss levels in the two materials, or even have nonuniform loss in one material, then

one needs to do the overlap integral of the loss with the standing-wave pattern. In this way, one can get the average loss through a period and use it in the simple formula above.

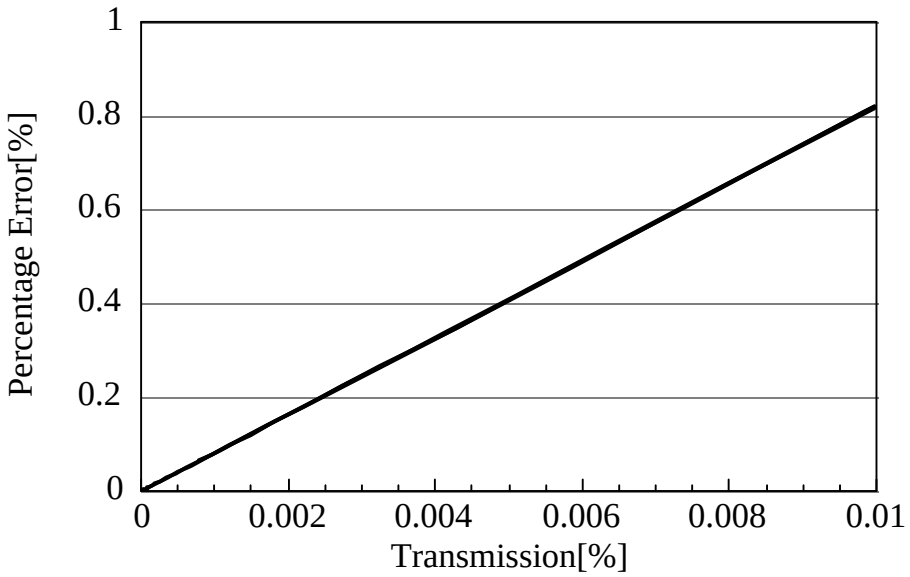

Figure 2.09. Error in formula versus transmission through mirror.

2.03 Absorptive Loss in GaAs/AlGaAs/InP

With a good idea of how to calculate loss in a VCL, we can get into specific loss values for our design. Table 2.01 summarizes the work done by Babic and others[5,6] on the absorption loss in GaAs and InP at different wavelengths of interest. These losses are normalized to 10^{18} cm^{-3} doping level.

	0.98 μm	1.3 μm	1.55 μm
p-GaAs	10	15	25
p-InP	-	15	15
n-GaAs	5	6	6
n-InP	-	5	5

Table 2.01. Absorptive losses in cm^{-1} per 10^{18} cm^{-3} doping level.

One can easily discern that the p-type material is more absorptive than n-type for the same doping level. In addition, much less doping is needed for the same resistance level using n-type material. This means that for the same resistance level the p-type material is much more absorptive than n-type material. One also sees that this absorption level becomes much higher for longer wavelength. This is because the primary contribution to this absorption is intervalenceband absorption. For this reason, much of the focus on reduction of loss has been in the p-type mirrors. Later in this chapter, an investigation of p-type mirrors which allow for low-doping level mirrors with reasonable resistances will be described.

Region	Material/ doping cm^{-3}	Length of interaction [nm]	Absorptive loss [cm^{-1}]	Percent Loss[%] Round-trip
n-mirror	AlAs/GaAs $2\ 10^{18}$	7800	12	0.19
n-cladding	InP $5\ 10^{18}$	3000	25	0.15
MQW	InGaAsP nid	1750*	50	0.17
p-cladding	InP $1\ 10^{18}$	3000	15	0.09
p-mirror	$Al_{0.67}Ga_{0.33}As$/ GaAs $5\ 10^{17}$	12000	12.5	.3
Total				**0.9**

Table 2.02. Broad-area losses in Babic double-fused VCL.

The high-carrier densities in the active region may cause an increased absorption[7] so that the absorption in this region may be anywhere from 30-100 cm^{-1} depending on the carrier density at threshold. Table 2.02 summaries the absorptive losses in the double-fused devices fabricated by Babic which operated to 33°C cw.

Of course, material losses are not the only type of loss in a VCL. There are other losses which depend on the 2-D structure of the VCL. Such loss include scattering losses off sidewalls or diffractive losses in unguided regions.

* actual MQW thickness ~1000 nm, but must multiply by gain enhancement factor.

The difference between the material absorptive losses and these other type of losses is that material losses do not vary with the diameter of the devices, thus such losses are many times referred to as the broad-area loss. As described in Chapter 1, different VCL structures have different size-dependent losses. Hegblom and Thibeault have shown both theoretically and experimentally[8,9] that such size-dependent losses are usually extracted from the differential efficiencies of similar devices of diverse diameters. Equation 2.08 shows the relationship between the differential efficiency, the injection efficiency, the broad-area loss, and the size-dependent loss.

$$h_d = h_i \frac{T}{T + L_{BA} + L(d)}$$
$$L(d) = \frac{h_i}{h_d} T - T - L_{BA} \qquad (2.08)$$

Notably, the injection efficiency may have a size dependence which must be considered when doing such an analysis. As shown in Chapter 5, for the device we have fabricated, such a dependence is very weak such that one can consider the injection efficiency a constant. However, it is still an important concern when calculating total loss since the differential efficiency is directly proportional to it. Babic resolved this uncertainly by creating a new term which was the round-trip loss divided by the injection efficiency.

With this, one can examine the total loss in the 33°C Babic structure and see where improvements would be possible. One of the strongest losses in an etched-pillar device, for small diameters, is scattering loss of sidewalls. The highest temperature CW device for Babic was an 8-μm device. Yet, one can see from plot 7.10 in Babic dissertation that the round-trip loss for the 8-μm device is almost double the broad-area round-trip loss of 1%. With an oxide-confined device the scattering loss at 8 μm diameter is extremely small. This means we can get almost a factor of two reduction in loss by going to an oxide-confined device rather than an etched-pillar structure. This shows one of the primary benefits associated with oxide-confined devices. The other heating/voltage benefit shall be discussed later in this chapter as well.

One can also reduce the broad area loss in the structure by changing the doping levels in the different layers or by going to different composition mirrors. In the final generation of devices fabricated in this work, several improvements were made to reduce the loss. The first was the elimination of doping in the n-mirror by using an n-intercavity structure. The second was the move to 90% AlGaAs mirrors to reduce the penetration depth into the p-mirror, and the third was the optimization of doping in the p-mirror. This optimization will be discussed in further detail in this chapter, but, in short, it involves lowering the doping for mirror periods near the active region and

raising it for periods far away from the active region. Table 2.03 summarizes the absorptive losses in the final generation structure. One can see the broad-area round-trip loss is about 33% lower in the top-emitting structure. In addition, in the top-emitting structure, the transmitted power does not go through the n-doped substrate so that the effective differential efficiency is about another 30% higher. This means we expect about a two-fold improvement in the differential efficiency for broad-area devices over the Babic structure devices, and about a 4 fold improvement for devices on the of 8-μm diameter.

Region	**Material/ doping cm^{-3}**	**Length of interaction [nm]**	**Absorptive loss $[cm^{-1}]$**	**Percent Loss[%] Round-trip**
n-mirror	AlAs/GaAs nid	7800	2	0.03
n-cladding	InP 5 10^{18}	3000	25	0.15
MQW	InGaAsP nid	1750*	50	0.17
p-cladding	InP 1 10^{18}	3000	15	0.09
p-mirror	$Al_{0.9}Ga_{0.1}As$/ GaAs 4 10^{17}	9000	5	.1
Total				**0.55**

Table 2.03- Expected round-trip loss from top-emitting structure.

2.04 Grading and Doping in P-mirrors

One can see that a great deal of the loss in the original Babic fused-VCLs came from the p-mirror. Improved design of this mirror can eliminate much of this loss. However, this design is constrained by two counterbalancing effects: (1) reducing the doping in the mirrors to give lower loss but (2) increasing the doping in the mirror to reduce the resistance. The resistance of the p-mirror can be quite high due to the many heterojunction interfaces between GaAs and AlGaAs and the low p-mobility in AlGaAs. For example, the excess resistance in the Babic structure was equally distributed in the fused junction and the p-mirror, with only minimal excess voltage drop in other regions. The height of the heterointerface barriers depends on the Aluminum composition in the low-index layers. As the aluminum composition is reduced, these barriers become lower, but this improvement in resistance is at the sacrifice of increased loss with a higher penetration depth. This problem is specific to the p-mirror and not the n-mirror due to the smaller loss and much higher mobility in n-type GaAs/AlGaAs.

To balance all the different effects in the p-mirror, one needs to design the mirror very carefully so as to minimize loss where possible without

---

[*] actual MQW thickness ~1000 nm, but must multiply by gain enhancement factor.

incurring a large voltage penalty. One well developed method in the design of p-mirrors is band-engineering to lower the barriers between the interfaces. There has been much work on such subjects both theoretically and experimentally[10,11,12]. The basic idea of band-engineering is to grade the junction between the two materials and dope this interface such that there is little or no barrier to current flow. With increased loss at 1.5 μm, the doping level used in such schemes must be lowered relative to GaAs based VCLs. This lower bulk doping means the interface doping must be reoptimized to reduce resistance. This reoptimization usually involves doping the interfaces very heavily. To prevent heavy accumulation of holes at the interfaces(causing loss), n-type doping can actually be inserted into the p-mirror to reduce the accumulation of holes in certain spatial regions. One can also optimize the doping relative to the position of the standing wave. This can mean putting lower doping in mirror periods closer to the active region where the standing wave is larger, and it can also mean optimizing the doping within a specific mirror period to reduce loss. For instance, one can allow hole accumulation at the standing-wave nulls, but must minimize the holes at the standing-wave peak. Finally, one can also optimize the doping relative to the penetration depth of the optical wave.

The band-engineering designs are usually characterized by the type of grading used between the two interfaces. The two types of grading schemes used for the mirrors in this thesis are the double parabolic and the uniparabolic grade[11,13]. The Babic structure used the double-parabolic grading scheme, developed by Peters *et al.*, which is characterized by an upward facing parabola meeting a downward facing parabola at the midpoint. Figure 2.10 shows the typical characteristic doping of a double-parabolic grading scheme. The goal of such schemes is usually to achieve a flat valance band.

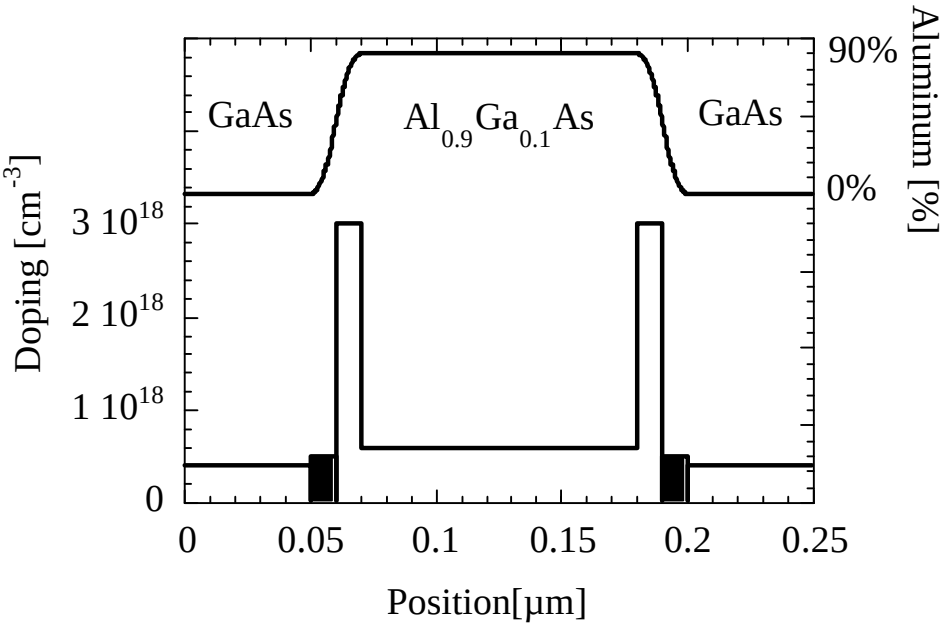

Figure 2.10. Double-parabolic grading scheme along with doping levels. Black regions represent n-type doping instead of p-type.

One can see that, in this grading scheme, one dopes the AlGaAs side of the parabola with very high doping, and the GaAs side of the parabola usually has very little or no doping. In fact, in the example of Figure 2.10, n-type doping is placed in the GaAs half of the parabola. The reason for such an asymmetry in the doping is that the natural affinities or band lineup of the GaAs/AlGaAs interface cause an accumulation of holes on the GaAs side and a depletion on the AlGaAs side. To counteract accumulation and depletion, the doping profile is engineered for uniform hole concentration.

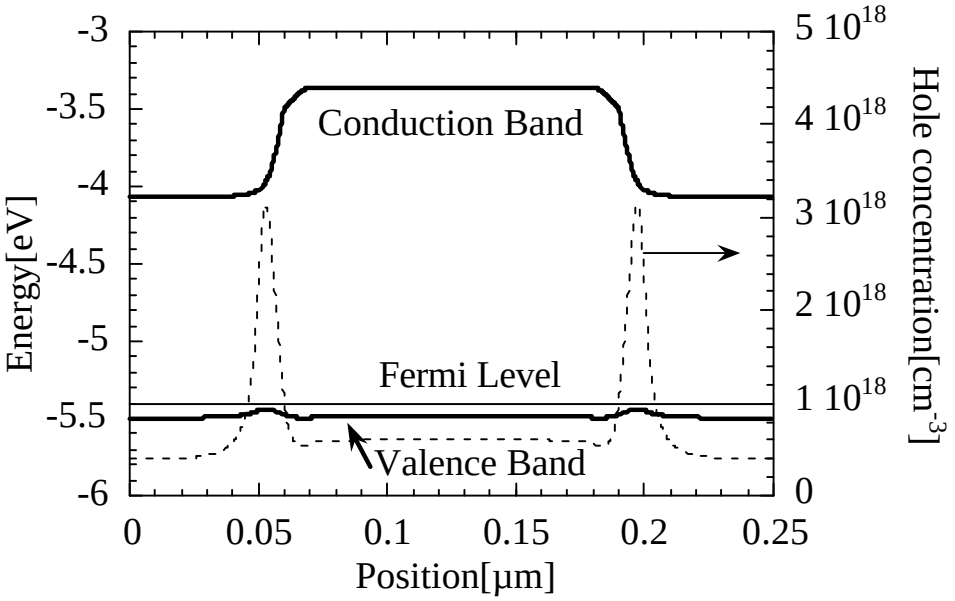

Figure 2.11. Band structure and hole concentration of doping and grading profile shown in Figure 2.10.

Figure 2.11 shows the resultant band structure and hole concentration for the doping profile in Figure 2.10. The valance band is nearly flat with no barriers to hole transport. One sees in the hole concentration that there are no regions with hole depletion. In fact, there is a hole accumulation at the two interfaces. It is important to note that the accumulation is actually occurring where there is n-type doping and not where there is a large p-type doping spike. To reduce this accumulation, one would need to increase the n-type doping at these positions.

This grading scheme allows for very low resistance interfaces as long as the approximate dopant profile in Figure 2.10 is maintained. However, the problem with this scheme is that such a profile is difficult to realize with Be as a p-type dopant. Be very easily diffuses at high temperatures, such that the very sharp peak seen in Figure 2.10 gets smeared out. The other problem with Be doping is that it has very poor incorporation into high Aluminum containing alloys. This is clearly a problem with this grading scheme, in that the very high-doping spike at the interface is in the high Al containing region. Thus it becomes very difficult to get the necessary high peak of Be for these concentrations of Al. If, however, one uses carbon doping instead of Be doping, this scheme works well. But, if carbon is not an option, one can lower the composition of Aluminum in the mirrors to increase the Be incorporation.

In the Babic structure, only 67% Aluminum was used in the mirror at the sacrifice of increased loss.

The uniparabolic grading scheme first proposed by Lear[13] overcomes much of the problems associated with the double-parabolic grading scheme. The uni-parabolic scheme is defined by a single parabola going all the way from one side of the heterojunction to the other. The dotted line in Figure 2.12 depicts the designed grading and doping scheme for the uniparabolic grade. One can also achieve flat band condition with this grading scheme, as with the double-parabolic scheme but with three important differences. First, the Be is spread over twice as thick a layer as in the double parabolic case, reducing the effect of Be diffusion. Second, spreading the doping over twice as thick a layer, with the total doping charge kept the same, means the peak doping only needs to be half as high, reducing the amount of Be that is intended to be incorporated. Finally, because much of the high-doping spike necessary for flat-band is actually in the low Al concentration region, one can use a high Al percent layer and still incorporate Be at the interfaces.

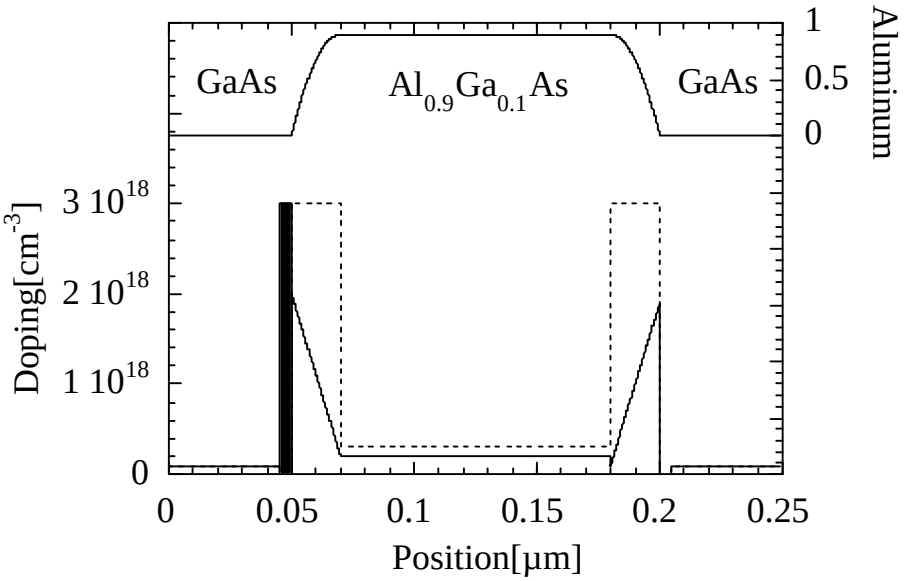

Figure 2.12. Uni-parabolic grading scheme along with doping levels. Black regions represent n-type doping instead of p-type.

The solid line in Figure 2.12 shows the approximate actual dopant profile measured from Secondary Ion Mass Spectroscopy(SIMS). One can see that even with the uniparabolic scheme, there is still a very large deviation between the intended doping profile and the actual doping profile. In reality, though, the lower incorporation is partially compensated with a excessive intended doping profile. Another interesting feature in Figure 2.12 is the use of an n-type compensating spike on only one of the interfaces in a period. The compensated interface sits at the standing-wave peak where loss is very important, but the other interface is at the standing-wave null where loss is reduced. Effectively, one can overdope the standing-wave null since the loss there is insignificant.

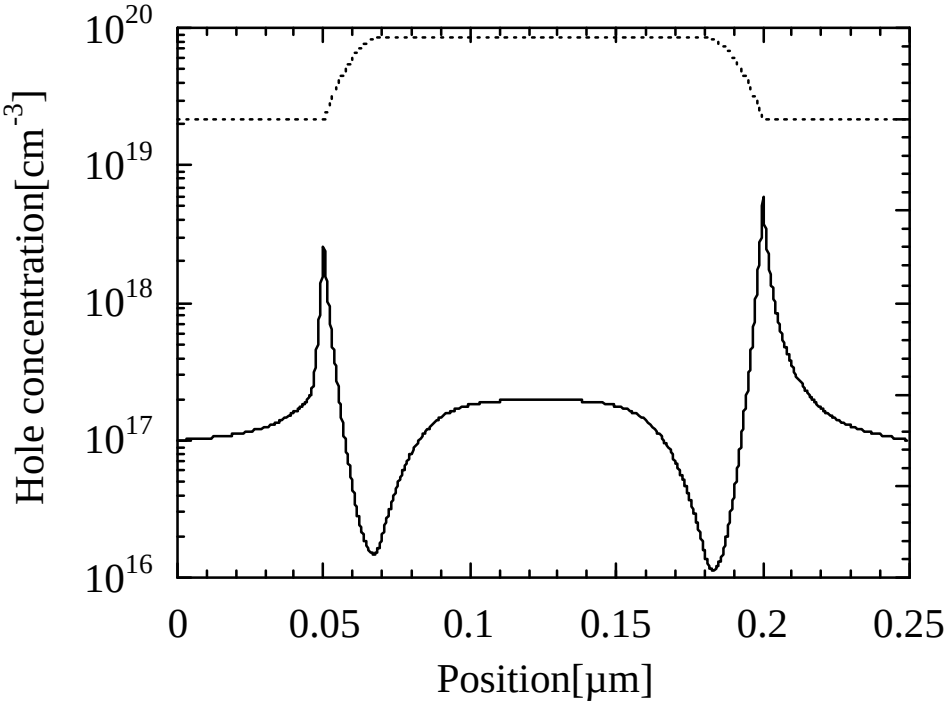

Figure 2.13. Simulated hole concentration using uni-parabolic grading scheme with measured doping concentration depicted in Figure 2.12. Dotted line shows the position of the interfaces.

Figure 2.13 shows the calculated hole concentrations using the actual doping measured as shown in Figure 2.12. One can see that there are regions of accumulation and slight depletion. The reason for the depletion is the low Be incorporation relative to the intended design. One can see that the interface with the n-type spike has about half the amount of hole accumulation at the peak relative to the other interface.

Figure 2.14 shows the loss in the structure with and without considering the standing-wave factor using the simple formula of 25 cm^{-1} per

10^{18} cm^{-3} holes. One can see that the effective loss is actually double at the left interface(the peak), and the effective loss at the right interface(the null) is almost zero.

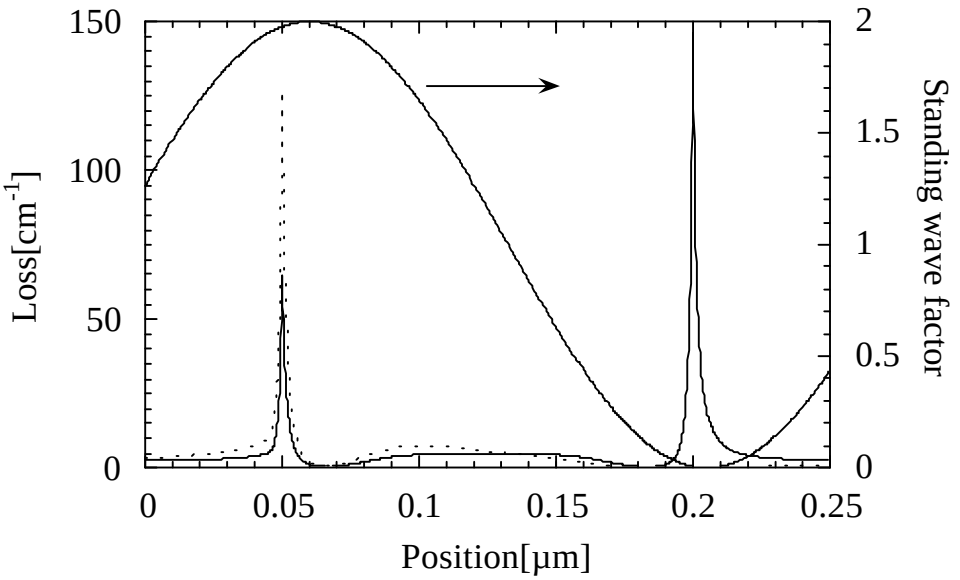

Figure 2.14. Solid line shows absorptive loss without considering standing-wave factor. Dotted line shows the effective loss with the standing-wave factor.

To get the average absorption through a mirror period one can integrate the effective loss in Figure 2.14 and divide by the length. If we integrate the actual material loss rather than the effective loss, we can get an idea of the impact of the standing wave. Doing this integration the average loss is 4.5 cm^{-1} for the actual case and 5.7 cm^{-1} if we ignore the standing wave. By placing the loss asymmetrically more at the null than the peak we get a reduced average effective loss.

The final important factor in the design of the p-mirror is the electrical resistance of the design. We first consider only the perpendicular flow of current to the interfaces. Later one sees that one has to consider both parallel and perpendicular flows of current in oxide devices.

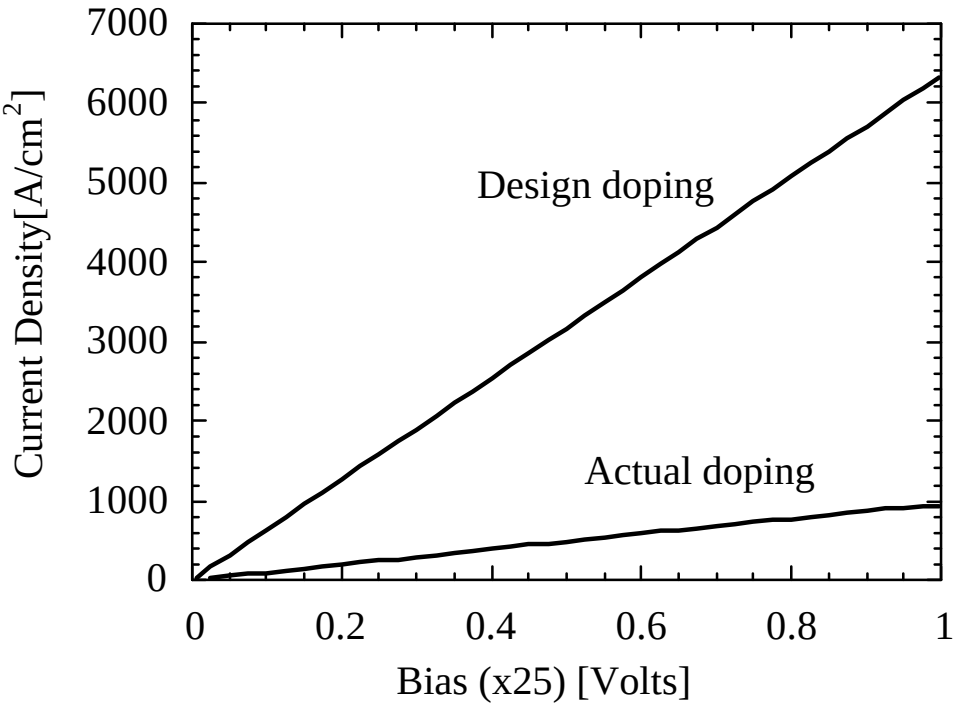

Figure 2.15. J-V curves through a 25-period mirror composed of the uni-parabolic grading and doping described in Figure 2.12. Simulation done using WinSim[14].

The simulated J-V curves through a single period of the uniparabolic mirror structure is shown in Figure 2.15. The x-axis is multiplied by 25 to show the voltage that would occur on a 25-period mirror. We see a very large

difference, more than a factor of six, in resistance between the actual doping profile and the intended doping profile. The effective average conductivity in the perpendicular direction for the actual doping can be calculated as 0.65 1/(Ohm cm). We will see in the next section that this is about twice the nominal values expected from the conductivities of the individual layers, suggesting that there remains a significant heterobarrier contribution to the resistance. However, this resistance level is still quite low for such a minimal doping/loss level.

2.05 2-D Design

The focus of the design so far has been on the 1-D design of the VCL structure, namely the epitaxial layers that comprise the VCL. But, the 2-D design of the VCL has important implications on device performance as well. In Chapter 1, quite a bit of time was spent discussing the importance of scaling the active region diameter. In this section I will show some of the scaling laws involved in designing small diameter devices. As alluded to earlier, the key development that allows for higher performance at smaller diameters is the use of the oxide confinement.

Figure 2.16 shows a schematic comparison between an oxide-confined device and an etched-pillar device. In both cases, the active region is the same diameter. Yet, in the oxide-confined case, the regions surrounded by the dotted line is filled with semiconductor, and in the etched-pillar case it is empty with air. The two important dimension scales in this figure are the active region diameter and the oxidation depth. If the oxidation depth goes to zero, then one has an etched-pillar device rather than an oxide device. The oxide-confined device must be better than the etched-pillar in terms of both electrical and thermal resistance. Clearly, the thermal and electrical conductivities of doped semiconductor are always better than in air.

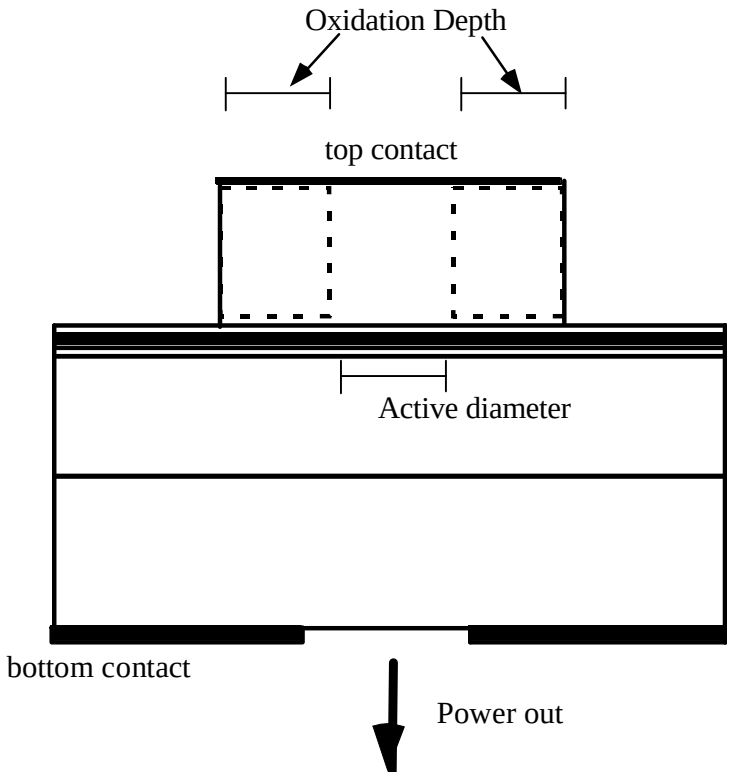

Figure 2.16. Schematic demonstrating difference between oxide-confined and etched-pillar device.

In the case of the oxide-confined device, current and heat can flow through the dotted region, but cannot flow there in the etched-pillar device. The amount of improvement depends on several factors, two of which are the actual oxidation depth and the active region diameter. Due to the aspect ratio, the improvement for very large active region devices will be less than for small active region diameters, as well as reduced with smaller oxidation depths.

To get an exact calculation on the resistance for different structures, one needs to model the structure with over a hundred layers for all the different layers in the epitaxial structure. This in itself is very time consuming, but to really get an accurate picture one would also have to take into account the grading and doping schemes at all the interfaces. Furthermore, mirror periods have different resistances in the parallel and perpendicular directions which further complicate the modeling. It is impractical to do a full simulation with thousands of layers to get general trends in behavior. Instead, one has to simplify the modeling to a reasonable computational level while hopefully maintaining most of the important trends. One way to do this is to convert the many mirror periods into one layer with an effective conductivity. This effective conductivity can have separate conductivity in the parallel and perpendicular directions.

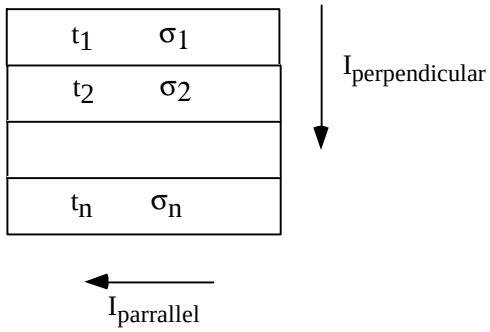

Figure 2.17. Multilayer current flow schematic.

To get the correct conductivities in both directions one must examine the current flow separately in both directions. Figure 2.17 show the two types of current flows. When the current flow is in the perpendicular direction the different layers add up in series. By contrast, in the parallel direction, the resistances add up in parallel, as would be in a classical resistor network. To get an average conductivity for a set of layers one has to do the average correctly, taking into account if current flow is in series or in parallel. In the perpendicular direction, the layers are in series so that one has to average the resistivities of the layers. In the parallel direction the layers are in parallel(electrically) so that one has to average the conductivities rather than the resistivities.

$$s_{parrallel} = \frac{1}{t}\int_0^t s(z)dz$$

$$s_{perpendicular} = 1/r = \frac{1}{\frac{1}{t}\int_0^t r(z)dz} = \frac{1}{\frac{1}{t}\int_0^t \frac{dz}{s(z)}} \qquad (2.09)$$

The parallel conductivity is always higher than or equal to the perpendicular one just as resistors have a lower resistance in parallel than in series. The large difference in mobility between GaAs and AlGaAs layers means that typically the parallel conductivity is significantly higher than the

perpendicular one. This same argument can be made for the thermal conductivities, but there is not nearly as great a difference in thermal conductivities between AlGaAs and GaAs as there is in their electrical conductivities. Figure 2.18 shows the conductivity and hole concentration for the uni-parabolic case as discussed earlier. Even though the hole concentration is higher by a factor of 2 for the AlGaAs the conductivity of the layer is much smaller. Doing the integration as described above for this case, one gets a perpendicular average conductivity 1.3 $(\text{Ohm cm})^{-1}$ and a parallel conductivity of 9.7 $(\text{Ohm cm})^{-1}$. There is more than a factor of seven difference between the two directions. This perpendicular conductivity is still twice as high as one would expect from the J-V curves in Figure 2.15. Yet, as discussed before, this discrepancy is due to the voltage drop on the heterointerfaces.

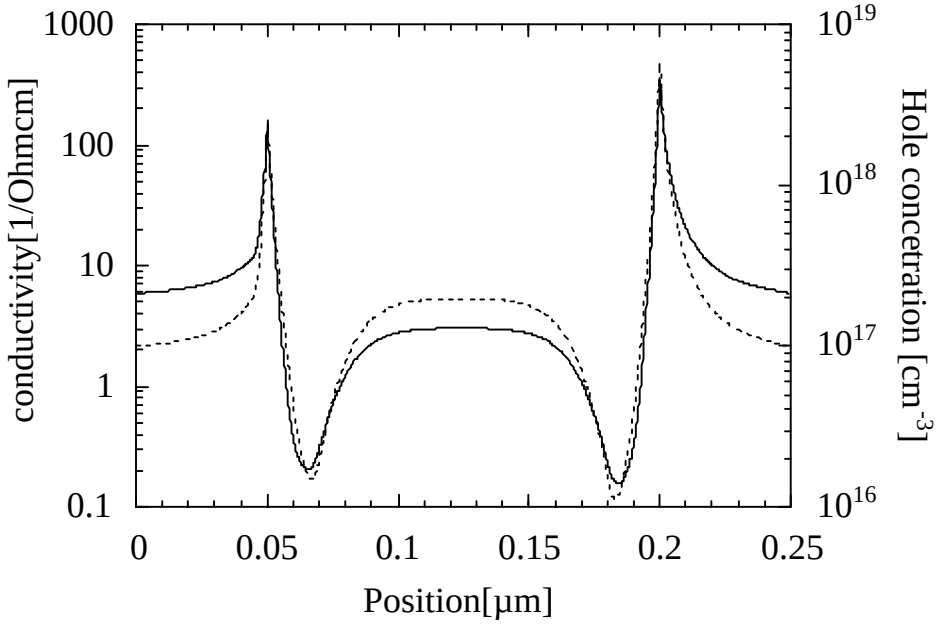

Figure 2.18- Hole concentration and electrical conductivity for uni-parabolic grading scheme. Solid line is conductivity and is read on the left axis. Dotted line is hole concentration and is read on the right axis.

We can now try to simplify the problem of solving the current flow in the p-mirror using this knowledge. In fact, if one had a finite-element, current-solving program that would determine the current flow with different conductivities in the perpendicular and parallel directions, the problem would be very simple. One could use a single material for the whole p-mirror with different conductivities in the two directions. Regrettably, such a program was not available at the time.

To work without such a program, one needs to use effective layers that would act like different conductivities in the two directions. To accomplish this, we use several layers with different conductivities similar to the real VCL case. The difference is that we use a much smaller number of layers, and we do not include the heterobarriers or grading region. The effective conductivities in the parallel and perpendicular direction take care of this discrepancy. The values of conductivities in the two different type layers are adjusted so that one gets a specific resistance vertically through the whole mirror stack. For this simulation, we will use the measured perpendicular resistance as the measure from the Babic structure, to see what improvements in voltage can be made using the oxide-aperture structure. The Babic p-mirror passed 1 kA/cm^2 at a 1 Volt bias across the p-mirror. Through some simple calculations, one can derive that the average conductivity of the layers is about 0.7 $(\Omega cm)^{-1}$. In the case of no oxidation, as in the Babic device, the difference in parallel and perpendicular conductivities does not matter, since all the current flow is vertical. In the case of the oxide-aperture device, the ratio of the two conductivities is very important. Even without heterobarriers, we saw that the ratio of parallel to perpendicular conductivities can be as high as 10 to 1. Including the heterobarriers ,this factor may be even larger. To get an idea of the effect of this ratio, we do the simulation with three value of the ratio: 5, 10,

20. The 5 value is a low estimate with little heterobarrier contribution, and the 20 is a high value with significant heterobarrier contribution to the current flow. Figure 2.19 shows the schematic of the model used to calculate the resistances in Figure 2.20. The layer conductivities are adjusted such that the total vertical resistance of the stack with no oxidation remains the same. This means that when we increase the parallel conductivity, we must decrease the perpendicular conductivity in the other layers to keep the same total vertical resistance.

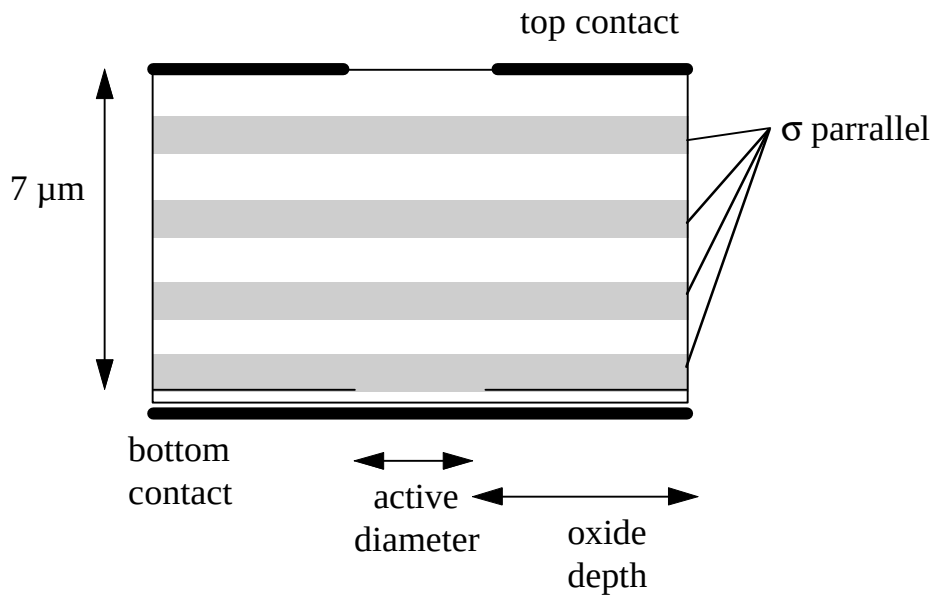

Figure 2.19. Schematic of model used to calculate mirror resistance.

Figure 2.20 shows the result of the current solving simulations. The plot is of the total bias across the mirror necessary for 10 kA/cm^2 current density into the aperture. Two active region diameters were investigated,

namely, 6-μm and 12-μm. It is in this range that we will see the highest performance devices exist. We first notice that all the curves meet up when the oxidation depth is zero. This is because we have normalized to current density, so that with only 1-D vertical flow of current all the cases are equivalent. The three lines for each of the active region diameters represent different values of parallel to perpendicular conductivity is the mirror. We kept the total vertical resistance constant, so that without oxidation, the three cases are equivalent. The triangles represent a ratio of 5 of parallel to perpendicular conductivity. This is on the low end of the spectrum as to the value of this ratio. This case can also be though of as the case with very little heterointerface resistance. The squares represent the opposite extreme, in which the ratio is 20. In this case we expect a significant heterobarrier contribution, limiting vertical conductivity.

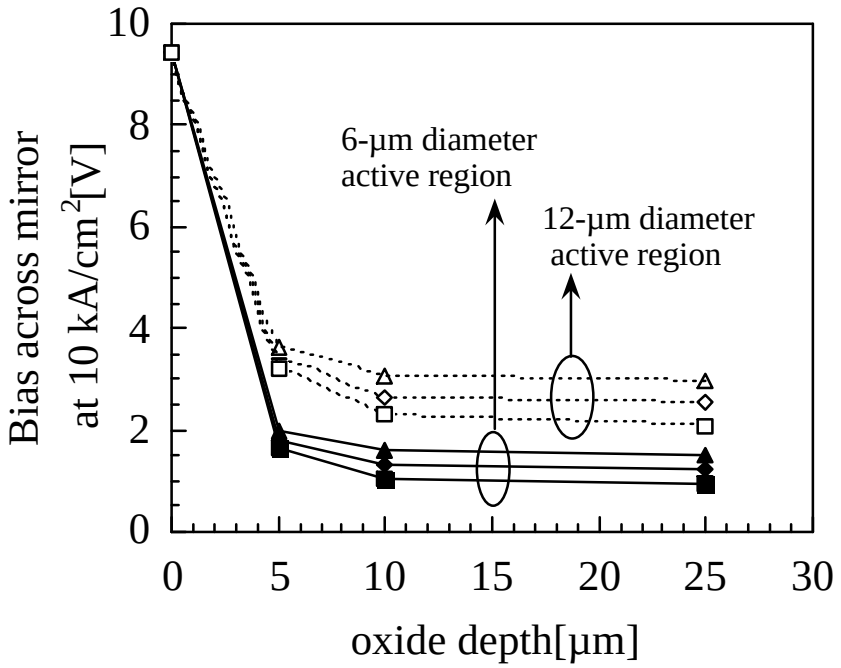

Figure 2.20. Simulation results from model depicted in Figure 2.19. Two different active region diameters are simulated(12-μm dotted lines, 6-μm solid lines). The three lines for each diameters represent different ratios of parallel to perpendicular conductivities(triangles ratio is 5, diamonds ratio is 10, squares ratio is 20).

What we see is for all the cases, even a meager oxidation of 5-μm allows for a great reduction in resistance. The improvement is quickly saturated beyond 10-μm oxidation depth. We also see that with a higher ratio of parallel to perpendicular conductivity there is a greater reduction in resistance with the oxidation. Finally we see for a given current density(not current), the smaller active region means a reduction in mirror voltage. The smaller active region

diameter allows for a greater relative lateral current flow when the oxidation is introduced.

2.06 General Device Scaling

One of the most important factors in a high performance device is its self-heating. If one wants to make a high-temperature cw device, the heating at threshold and above threshold must be minimized. As indicated, the device diameter plays a significant role in a number of relevant factors such as the thermal resistance and electrical resistance. One could argue that as the device is shrunk down, the thermal resistance increases dramatically causing the heating to be worse. Alternatively, the threshold current decreases with device diameter, so the heating should be reduced. Their two effects act in opposite directions, so one has to conduct a relatively simple analysis to figure out which is more dominant.

Clearly, the exact answer depends on the specific structure considered with factors such as the oxidation depth or composition of the mirror layers playing a role. A particularly revealing analysis would find scaling laws for devices without considering the specifics of individual structures. In such a case, one could not use specific values for parameters, but find scaling laws for each parameter. We will try to determine an approximate relationship between

heating at threshold and device diameter. Let's first start with the very simple linear relation for heating at threshold.

$$\Delta T_{thres.} = \Theta_{therm.} P_{thres.} = \Theta_{therm.} I_{thres.} V_{thres.} \qquad (2.10)$$

where Q is the thermal resistance of the structure. Next we try to determine more explicit relationships of these parameters on the device diameter. The first parameter to consider is the thermal resistance. One cannot give a general expression for all structures for the thermal resistance. What we can say, however, is that for most devices the thermal resistance is inversely proportional to the device circumference. The reason one can make such a general statement is that for most practical structures, the heat is mostly extracted from the perimeter of the device. The simplest representation of a VCL, in term of thermal resistance, is a disk-shaped heat source(the active region) on an infinite half-space(the substrate) of conductivity k. In this case, the analytical expression for the thermal resistance has been derived as $\Theta_{th} = \frac{1}{2kd}$ [15]. This formula has the classic inverse relationship of the thermal resistance to device diameter. For etched-pillar devices, I have measured this dependence as Equation 6-3 in Babic's thesis[4] and reproduced the fit to the data here as Equation 2.11.

$$\Theta_{th} \approx 1520\left(\frac{12}{d[\mu m]}\right)^{1.16} \frac{K}{W} \qquad (2.11)$$

There is not an exact inverse relationship with device diameter, but it is quite close to the simple law. Theoretical simulation of such a structure by Piprek did suggest an exact inverse relationship should hold. In any case, for our approximation analysis, we can take the following for the thermal resistance $\Theta_{th} \propto 1/d$.

The next parameter to consider is the relationship of the threshold voltage to device diameter. The problem with this parameter is that it explicitly depends on another parameter in our heating equation, namely the threshold current density. To get purely its contribution to the scaling, one would have to consider the current density versus device diameter as well. To get the dependence of voltage on current density as well as diameter, one usually writes the voltage at threshold as some turn on diode voltage plus the threshold current time a linear resistance. As show in the above analysis, this resistance can vary with device diameter.

$$V_{thres.} \approx V_D + V_{fusion} + I_{thre.} R(d) = V_D + V_{fusion} + p\left(\tfrac{d}{2}\right)^2 J_{thre.} R(d)$$

(2.12)

The device resistance has a different scaling law, depending on if the device is an oxidized or an etched-pillar type.

$$R(d) \propto \frac{Length}{Area} \propto \frac{L}{d^2} \qquad \text{etched-pillar} \qquad (2.13)$$

$$R(d) \propto \frac{Length}{Circumfrence} \propto \frac{L}{d} \qquad \text{oxidized devices} \qquad (2.14)$$

When one puts this dependence into the threshold voltage equation, one see that for the etched-pillar device the voltage is independent of device size(for a given current density). The behavior will be confirmed in the results chapter of the thesis. For oxidized devices, the threshold voltage can actually decrease with device size. However, for either case, if the threshold current density is reasonably small, the voltage is dominated by the combination of the diode turn-on voltage as well as the fused junction voltage. If the derivation was for the heating behavior at higher biases, as would be the case in actual operation conditions, then the linear resistance term becomes more important. In such a case, the oxidized devices would reduce heating for smaller devices due to their reduced series resistance. Thus for our heating at threshold analysis, the voltage is independent of device diameter. This is to say, the J-V curve remains approximately the same at smaller diameters.

With this information we can derive an approximate scaling law for heating at threshold versus device diameter.

$$\Delta T_{thres.} \propto \left(\frac{1}{d}\right)\left(V_{thre.}\right)\left(\frac{p}{4} d^2 J_{thre.}(d)\right) \propto d \cdot J_{thre.}(d) \qquad (2.15)$$

One can see from Equation 2.15 that the heating at threshold is proportional to the diameter times the threshold current density. In an ideal laser with no size dependent losses, such as carrier diffusion or sidewall scattering losses, the threshold current density would be a constant with device diameter. Here, the smaller the device, the lower the heating at threshold, i.e. smaller is better. Unfortunately, in real devices, there are many size dependent losses. The minimum heating in such a case occurs when the threshold current density starts to increase linearly or superlinearly with device diameter.

2.07 Spreading Current

In Chapter 5, we will see that spreading current causes the greatest deviation from the ideal constant current density in the oxide-confined, double-fused vertical-cavity lasers. In this section, we will examine the effects and scaling involved with current spreading around the oxide-aperture. Hegblom and I jointly developed a simple approximate analytical model to describe current-spreading around an aperture[16]. This model is very useful is seeing the general trends that occur when one has on aperture placed a certain distance above an active region.

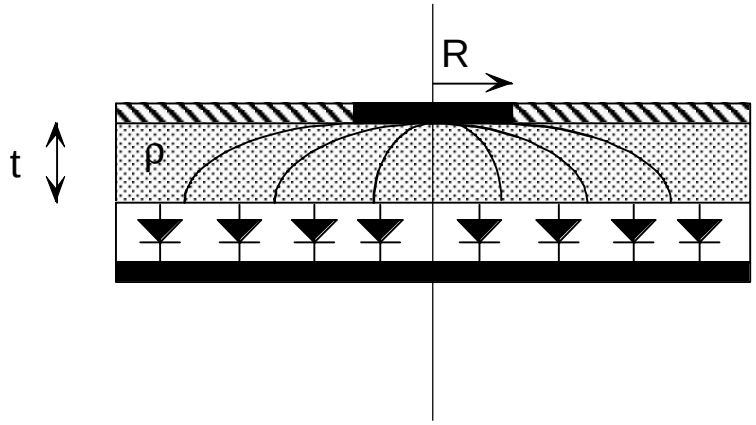

Figure 2.22. Schematic of model used to solve current spreading problem.

To treat the current spreading problem, we consider a simplified version of the problem in which the region below the circular aperture is modeled as resistor network on top of a diode. This approach was first used for in-plane lasers to determine the increase in threshold due to spreading[17,18,19]. However, it has not been pursued to the same extent for VCLs[20]. By solving this problem we can determine the relevant factors contributing to increased threshold current. In addition, through this analysis, we find that the differential efficiency is only weakly affected by this kind of current spreading. In Chapter 5, this finding will be confirmed by experiment results.

Figure 2.22 shows a schematic of a portion of the VCL structure. Current flows through an aperture of radius, R into a layer of sheet resistance ρ_s ($\Omega/\square$)= ρ/t and through a layer with a diode J-V characteristic. (r is the

resistivity and *t* is the thickness of the layer). The additional current necessary to reach threshold may be estimated by assuming a uniform voltage across the aperture opening and then determining the current which flows beyond the aperture edge given the voltage, V_{IN}, at $r=R$.

As the current moves radially outward through a small annulus (of width, *dr*), it encounters a voltage drop due to the resistive layer.

$$dV = -\frac{r_s dr}{2pr} I(r) \qquad (2.16)$$

And the lateral current decreases due to current being sunk vertically by the diode.

$$dI = -(2pr)drJ_D(V(r)) \qquad (2.17)$$

$J_D(V) = J_O\left(\exp[qV/(hkT)]-1\right)$ is the J-V characteristic of the diode layer. We can generalize the problem a bit by modifying the value of r_s. For two (or multiple) resistive layers of resistivity r_1 and r_2 and thickness t_1 and t_2, we use the parallel sheet resistance of these layers,

$$\frac{1}{r_s} = \frac{t_1}{r_1} + \frac{t_2}{r_2} \qquad (2.18)$$

as was the case with the mirror stacks. In the case of two apertures, one below the active and one above, we need to consider the voltage drop through the upper resistive layer and the lower resistive layer in Equation 2.16. So we

simply have to use a sheet resistance which is the series combination of the resistance of the upper and lower layers

$$r_s = \frac{r_u}{t_u} + \frac{r_l}{t_l} \qquad (2.19)$$

where r_u and r_l are the resistivities and t_u and t_l are the thicknesses of the upper and lower layers, respectively. We see that due to the large difference in resistivities between an n-doped layer and a p-doped layer that putting two apertures does not curb spreading current much. The p-doped low-resistivity layer usually dominates.

Equations 2.16 and 2.17 have been solved for several geometries including circular[21]. Once the boundary conditions are applied that I=0 as$r \to \infty$, and that $V(R) = V_{IN}$, one can determine the total lateral current, I_{OUT}, at r=R.

$$I_{OUT} = 2pJ_{IN}\left(RL_s + L_S^2\right) = I_o/2 + \sqrt{I_O I_{IN}} \qquad (2.20)$$

We define a characteristic spreading length and characteristic spreading current as

$$L_s = \sqrt{\frac{2hkT/q}{r_s J_{IN}}} \text{ and } I_o = 8p\,\frac{hkT/q}{r_s} \qquad (2.21)$$

Rather than writing the current in terms of V_{IN}, we have expressed it in terms of $I_{IN} = pR^2 J_{IN} = pR^2 J_D(V_{IN})$ which is current injected within the aperture $r<R$ if the resistive drop in the center was neglected. The total current injected into the device is the sum of the current flowing within the aperture ($r<R$) and the spreading current: $I_{TOTAL} = I_{IN} + I_{OUT}$.

We have intentionally written the solution in two forms to reveal the scaling of the spreading current vs. device radius. When $R=2L_S$, over half the total current is lost due to spreading, or alternatively, when $I_{IN}=I_O$, over half (3/5) of the total current is lost due to spreading. The above solution was found with the approximation that the -1 is dropped from the diode characteristic. Although that approximation will incorrectly predict the current and voltage *distribution* at radii much larger than the device radius (where the currents are small), a numerical solution of the original equations shows the error on the *total* lateral current is negligible when the diode at $r<R$ is biased above turn-on (as is the case at threshold).

With an estimate for the current injected in the center of the device at threshold one obtains the excess contribution to threshold current from spreading simply from Equation 2.16. To find the change in the differential efficiency due to spreading, we must examine the *additional* current that one

must inject for $r>R$ relative to the *additional* current injected within the aperture.

Thus we have,

$$h_i = \frac{h_{io}\, dI_{IN,r}}{dI_{IN,r} + dI_{OUT}} = \frac{h_{io}}{1 + (dI_{OUT} / dI_{IN,r})} \qquad (2.22)$$

where h_{i0} is the differential efficiency in the absence of spreading. Inside the aperture, the diodes are clamped so we cannot neglect the voltage drop due to the resistive layer above them, which yields Equation 2.23.

$$\frac{dI_{IN,r}}{dV} = \frac{pR^2}{rt} \qquad (2.23)$$

Outside the aperture (where the diodes are not clamped) we need to inject an additional current found from differentiating Equation 2.16.

$$\frac{dI_{OUT}}{dV} = \sqrt{\frac{I_o}{I_{IN}}}\,\frac{dI_{IN}}{dV} = \sqrt{\frac{I_o}{I_{IN}}}\,\frac{I_{IN}}{2V_T} = \frac{I_{OUT}}{2V_T} \qquad (2.24)$$

$$\frac{dI_{OUT}}{dI_{IN,r}} = \frac{dI_{OUT} / dV_{in}}{dI_{IN,r} / dV_{in}} = \frac{1}{R}\sqrt{\left(2t^3 r J_{IN}\right) / V_T} = \frac{R_h}{R} \qquad (2.25)$$

Then the internal quantum efficiency above threshold is given by Equation 2.26.

$$h_i = \frac{h_{io}}{1 + R_h / R} = \frac{h_{io}}{1 + D_h / D} \qquad (2.26)$$

Where we can rewrite,

$$R_h = \sqrt{2rt^3 \frac{J_{in}}{V_T}} \text{ and } D_\eta = 2R_\eta \qquad (2.27)$$

R_η (D_η) is the characteristic device radius (diameter) at which the internal quantum efficiency drops by 50%. To get a feel for the sizes, we can plug in some numbers typical for the InGaAs based 980 nm VCLs at UCSB: t=600Å, hkT/q=0.05 volts, J=500A/cm^2 (a good current density at threshold for a 3QW device) and $r = 1/(qmn)$=0.3 Ω-cm for an $Al_{0.3}Ga_{0.7}As$ layer p-doped 2 10^{17} cm^{-3} with mobility μ=100 cm^2/(V sec). Then we find D_η=0.02μm.

Using the same numbers, we find the diameter, $2L_S(1+\sqrt{3})$, at which half the threshold current is lost due to spreading, is 3.5 μm. Comparing this to D_η=0.02μm, we see the effect of current spreading on the differential efficiency is really a second-order effect because the additional current injected above threshold spreads very little in comparison to the current that it takes to reach threshold. Essentially, the reduction in external quantum efficiency due to current spreading is an immeasurable amount. This conclusion is supported by the data presented in Chapter 5. The physical reason why the differential efficiency does not decrease is that the differential resistance of the diode(which causes the current spreading) becomes negligible above threshold as compared

to well below threshold. Some attempt was made at solving this problem analytically with the fused junction voltage as a parameter in the model, but no solution was found. In addition, the uncertainty in parameters around the fused junction such as mobility or band diagram would make any analysis very difficult. We will see however, in Chapter 5, that this model is very useful in estimating the spreading current at threshold.

2.08 Summary

In this chapter, the basic design of VCLs was analyzed. We determined that there are many parameters that contribute to a high-performance design. We began with a simple 1-D model in Section 2.01, where we examined the effect of the standing wave has for the VCL design. The standing wave in the cavity creates regions which are very sensitive to loss and region where loss has a minimal effect. In Sections 2.02 and 2.03 we examine the specific loss mechanisms in the double-fused structure. To reduce the round-trip loss in our cavity, we presented in Section 2.04 special designs to reduce the absorptive loss in the p-mirror, without significantly increasing the device resistance. A general analysis was also conducted on the scaling of oxide-aperture VCLs. The introduction of the oxide-aperture proved very valuable in reducing device

resistance. We also found though some simple scaling law analysis that the heating at threshold was proportional to the current density times the active region radius. This means that to achieve high temperature cw operation, the scaling of devices to small dimensions becomes an important goal. In Section 2.06 we present an analytical model that helps analyze one of the components in the increase of threshold current density, namely current spreading. We will later learn that this current spreading is one of the critical elements in determining device scaling. In the next chapter, an analysis of the fused junction is presented, as it turns out that it plays a critical role in the device scaling.

2.09 References

1 H.A. Macleod, *Thin-film optical filters*, Adam Hilger Ltd, Bristol(1986).

2 S. W. Corsine, “Design of vertical-cavity surface-emitting lasers with strained and unstrained quantum well active regions”, Ph.D. Dissertation, University of California, Santa Barbara, ECE Tech. Rep. #93-09(1993).

3 L. A. Coldren, S.W. Corzine, *Diode lasers and photonic integrated circuits*.,Wiley, New York, (1995).

4 D. I. Babic, “Double-fused long-wavelength vertical-cavity lasers”, Ph.D. Disseration, University of California, Santa Barbara, ECE Tech. Rep. #95-20(1995).

5 D. I. Babic, J. Piprek, K. Streubel, R. P. Mirin, N. M. Margalit, D. E. Mars, J. E. Bowers, and E. L. Hu, "Design and analysis of double-fused 1.55-µm vertical-cavity lasers.", IEEE J. Quant. Elect., vol.33, 1369 (1997).

6 H. C. Casey and P. L. Carter, "Variation of intervalence band absorption with hole concentration in p-type InP.", Appl. Phys. Lett., vol.44, 82 (1984).

7 S. Seki, K. Yokoyama, and P. Sotirelis, "Theoretical analysis of high-temperature characteristics of 1.3- mu m InP-based quantum-well lasers.", IEEE Journal of Selected Topics in Quantum Electronics, vol.1, 264 (1995).

8 E. R. Hegblom, D. I. Babic, B. J. Thibeault, and L. A. Coldren, "Scattering losses from dielectric apertures in vertical-cavity lasers.", IEEE Journal of Selected Topics in Quantum Electronics, vol.3, 379 (1997).

9 P. D. Floyd, B. J. Thibeault, E. R. Hegblom, J. Ko, L. A. Coldren, and J. L. Merz, "Comparison of optical losses in dielectric-apertured vertical-cavity lasers.", IEEE Photonics Technology Letters, vol.8, 590 (1996).

10 M. G. Peters, B. J. Thibeault, D. B. Young, J. W. Scott, F. H. Peters, A. C. Gossard, and L. A. Coldren, "Band-gap engineered digital alloy interfaces for lower resistance vertical-cavity surface-emitting lasers.", Appl. Phys. Lett., vol.63, 3411 (1993).

11 D. I. Babic, G. H. Dohler, J. E. Bowers, and E. L. Hu, "Isotype heterojunctions with flat valence or conduction band.", IEEE J. Quant. Elect., vol.33, 2195 (1997).

12 M. G. Peters, D. B. Young, F. H. Peters, J. W. Scott, B. J. Thibeault, and L. A. Coldren, "17.3% peak wall plug efficiency vertical-cavity surface-emitting lasers using lower barrier mirrors.", IEEE Photonics Technology Letters, vol.6, 31 (1994).

13 K. L. Lear and R. P. Schneider Jr., "Uniparabolic mirror grading for vertical cavity surface emitting lasers.", Appl. Phys. Lett., vol.68, 605 (1996).

14 D. W. Winston, SimWindows32 version 1.4.2 software.

15 S. S. Kutateladze,and V. M. Borishanski, *A Consice Encyclopedia of Heat Transfer*, Pergamon Press, Oxford (1966).

16 E. R. Hegblom, N. M. Margalit, B. J. Thibeault, L. A. Coldren, and J. E. Bowers, "Current spreading in apertured vertical cavity lasers.", Proceedings of the SPIE - The International Society for Optical Engineering, vol.3003 176 (1997).

17 W. P. Dumke, "Current thresholds in stripe-contact injection lasers.", Solid-State Electronics, vol.16, 1279 (1973).

18 W. T. Tsang, "The effects of lateral current spreading, carrier out-diffusion, and optical mode losses on the threshold current density of GaAs-Al/sub x/Ga/sub 1-x/As stripe-geometry DH lasers.", J. Appl. Phys., vol.49, 1031 (1978).

19 H. Yonezu, I. Sakuma, K. Kobayashi, T. Kamejima, M. Ueno, and Y. Nannichi, "A GaAs-Al/sub x/Ga/sub 1-x/As double heterostructure planar stripe laser.", Jpn. J. Appl. Phys., vol.12, 1485 (1973).

20 N. K. Dutta, "Analysis of current spreading, carrier diffusion, and transverse mode guiding in surface emitting lasers.", J. Appl. Phys., vol.68, 1961 (1990).

21 W. B. Joyce and S. H. Wemple, "Steady-state junction-current distributions in thin resistive films on semiconductor junctions (solutions of grad/sup 2/v=+or-e/sup v/).", J. Appl. Phys., vol.41, 3818 (1970).

Chapter 3

Wafer Fusion

3.01 Introduction to Wafer Fusion

Semiconductor optoelectronic components are often the key elements for fiber optic communications. The efficiency and compact nature of such devices has allowed them to be incorporated into an extensive variety of applications. Improvements in expitaxial growth over the last couple of decades have allowed for a wide range of materials to be used to create ever more complex and effective device designs. However, one fundamental constraint limiting the design of semiconductor components has been lattice matching within the structure. Non-lattice matched growth, past a critical

thickness, results in strain relief by defect formation, degrading crystal quality. To overcome this barrier one can use the relatively new technique of wafer fusion to break the condition of lattice matching throughout a structure. Using wafer fusion one can combine two materials not necessarily of the same lattice constant, without degrading the crystal quality away from the interface. Materials such as GaAs, InP, and Si can be combined into a single device. Each section of a device can be optimized using the material best suited for its function. In this thesis we describe a combination of InP based active regions with GaAs based mirrors to create long-wavelength VCLs. Below, I will discuss wafer fusion as it relates to the VCLs, as well as include a general discussion on the issues of wafer fusion.

Wafer fusion is a process in which two wafers are combined to form a single unit without the use of any intermediate layer such as epoxy or metal. When one uses a intermediate layer the process is usually referred to as wafer bonding instead of wafer fusion. Although there may be many specifics to each fusion system, the basic process goes as follows. Two epitaxial surface are cleaned/passivated such that there are minimal contaminants on the surface. Then the two expitaxial surfaces are placed together in intimate contact, usually under pressure. The wafers can be placed in contact with a liquid between

them, called wet fusion, or without liquid, called dry fusion. In case of the wet fusion, any liquid trapped between the wafers must be removed before the fusion process is completed. Many times channels are etched into one of the wafers in order to allow for an escape path of the liquid. With the wafers in contact, one heats up the wafers to near the growth temperature of one of the materials. This allows atomic redistribution to occur at the surface, filling in any deviations from the ideal, atomically smooth surfaces. Wafer fusion has also been done as low as room temperature, but the quality of such an interface has not been as thoroughly characterized[1]. In either case, pressure is applied to the wafers so that any nonuniformities or voids are filled in during the fusion process. After cooling the wafer down, the two wafers should be strongly bonded. To access the epitaxial region between the two substrates, one of the substrates must be removed. This is usually done with a selective etch-stop layer, previously grown into the epitaxial structure. The substrate is wet etched up to this layer, at which point the etch-stop layer is removed. At the completion of this process, one has essentially transferred the epi from one substrate onto the epi from another substrate regardless of lattice constant. Ideally, the inherent crystal defects arising from the mismatch in lattice constant would be edge defects localized exactly at the junction. In reality, wafer

orientation and thermal mismatches may introduce other types of defects[2,3]. Two integral questions then arise. How localized do the defects remain, and at what distance is the material quality very high? K. Black *et al.* have investigated the issues related to these effects using quantum wells placed close to the junction and measuring their low-temperature photoluminescence[4]. These studies suggest that the material a given distance away from the junction, usually 100-300 nm, is of very high quality. In this chapter, we will investigate some of the material and electrical properties of the fused junction and adjacent material.

3.02 Practical Wafer Fusion

Before one starts to examine the microscopic issues involved with wafer fusion, it is useful to get a detailed look at the wafer fusion process itself. One of the first issues to consider with wafer fusion is the uniformity of the process. The results can be very nonuniform or completely fail if the correct procedures are not done. One of the critical elements in proper wafer fusion is the cleaning

procedure. Any large scale contamination on the surface can destroy the uniformity of the wafer fusion process completely. I will discuss in this section some of the cleaning and preparation procedures for InP to GaAs wafer fusion. With the correct procedure and reasonably smooth material, one can consistently get complete coverage of wafer fusion.

One of the most prevalent contaminants on a wafer surface can be organic molecules. These contaminants come from wafer handling, photolithographic resist, glassware contamination, or possibly even deposits from the air. Under a medium-power microscope, one can usually see this contamination on the wafer surface as a slight discoloration looking like photoresist residue. All such contamination must be removed if the wafer fusion process is to be uniform. The first step to eliminate this contamination is to insure that the glassware and the tweezers being used are very clean, as many times they are the source of greatest contamination. To clean the glassware, as well as the wafer surface, a solvent cleaner is used. In this process, one leaves the wafers in a successive baths of acetone and then isopropanol. One can heat up the solvents slightly, being careful not to ignite the acetone(it has a low flash point). The wafers are blown dry very quickly with nitrogen. If the solvent is let to dry slowly on a wafer, then all the contaminants in the liquid deposit back

on the wafer. Doing a thorough solvent clean, one should not see any visible discolorations on the wafers. If contaminants persist, a slight rubbing with a Q-tip with acetone may help. The cleaning should always end with isopropanol and a nitrogen dry. We have found that a water rinse tends to increase contamination because it cannot be blown dry as effectively.

Once the large scale contamination is removed, one has to deal with the invisible layer of hydrocarbons that solvent cleaning is know to leave on the wafer. To get rid of this layer the wafers are usually placed in a oxygen plasma to burn off these residues. Typically, we have used 10 minutes of a 100 Watt plasma with a pressures of 300 mT. One can go directly into an oxide removing solution after the plasma to remove the oxide formed during this step. The preferred chemical solution we have used here has been concentrated ammonium hydroxide since it can be kept quite clean. With this step complete, one can either proceed to the final steps of placing the wafers together, or go through the further cleaning of another oxygen cleaning step. For the second oxidation we usually place the wafers in a UV ozone machine for at least 30 min. to insure no hydrocarbons remain on the surface. At this point, the wafer should have a thin oxide and minimal contamination on the surface. Many oxide removal steps have been tried as the final step before wafer fusion. These

will be discussed later in this chapter, but for now the default oxide removal shall be concentrated ammonium hydroxide.

The wafers are both placed in the same container with NH_4OH and are transported to the fusion system(5 min. walk). The wafers are then flipped on top of one another with both epi-sides in contact, remaining both in solution. The wafers are pressed together until some tension is felt between the wafer. They are then taken out of solution, slightly dried, and placed in the fusion fixture. The fixture is tightened to press the wafers together, and placed in the fusion furnace.

Next to organic contamination, the second leading cause of non-uniform fusion is uneven pressure on the wafers during the fusion. To avoid uneven pressure, the fusion fixture must be carefully designed to apply even pressure. Several research groups have developed different fusion fixture to insure uniform pressure between the wafer. Lo *et al* has developed a fusion fixture that uses the thermal expansion of Aluminum to apply even pressure to the wafers[5]. Figure 3.01d shows the design we have chosen to use. It consists of essentially two graphite plates pressed together with screws. The amount of pressure applied is proportional to the amount of torque used to tighten the screws. A variable torque wrench is used to adjust pressure. The half-dome

shape in between the wafers and the top plate is critical to uniform pressure. It compensates any tilt between the top plate and the bottom plate. Figure 3.01b shows an exaggerated picture of what could happen if the half-dome shape was not used to compensate tilt. The second important aspect to the half-dome is that it partially compensates for bending of the two plates. Figure 3.01c shows an exaggerated picture of the effect plate bending can have on pressure uniformity.

One can identify problems with non-uniform pressure by looking at the pattern of fused versus unfused area. If the unfused area appears to be randomly distributed, then the problem is most likely contamination, however if there seems to be a definitive pattern to the unfused area(e.g., the center is fused and the outer edges are not, or vice versa), then the fixture is probably the problem. Occasionally, even a well-designed fixture will deform and lose its flatness, and in this case a specific region will always come out poorly unfused. One then has to polish the surface of the fixture to a flat condition again.

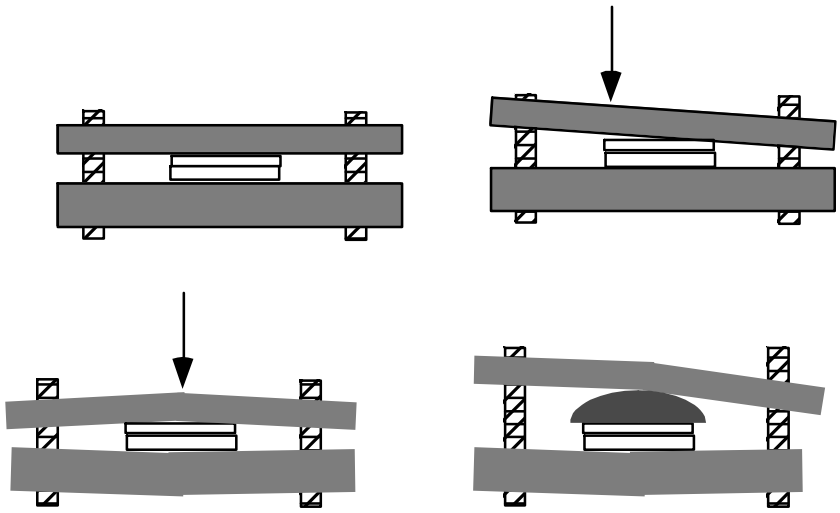

Figure 3.01(a,b,c,d). a) Simple parallel plate wafer fusion fixture.
b) Tilt in parallel plate causes non-uniform pressure.
c) Bending of plates also cause non-uniform pressure.
d) Half-dome shape compensated tilt as well as bending.

The fusion furnace we are using at UCSB is a simple modification to an LPE growth tube. In fact, any furnace that runs hydrogen or nitrogen and can be heated up to the appropriate temperatures could be used as a fusion system. The graphite fusion fixture is place on a quartz boat and placed near the center of the furnace. The furnace usually is maintained in a nitrogen atmosphere. With the fixture in place, the chamber is sealed and evacuated to a pressure of about 10 mT. We have also experimented with fusion where the evacuation was only to 50 Torr and could find no substantial difference in the fusion

quality. The chamber is then back filled to atmospheric pressure with either hydrogen or nitrogen. Finally, the temperature is ramped up to about 630°C and kept there for about 30 minutes. The ramp up to 630°C usually takes about 18 minutes. At the end of the fusion time the temperature is ramped back down to room temperature. We have not investigated the dependence of the fusion quality on the ramp down time. It can vary from 1 hour to 3 hours depending upon whether the furnace is retracted at 400°C or left to room temperature.

3.03 Surface Preparation

Among the most thoroughly investigated issues we have examined in our studies of fusion is the surface preparation directly before fusion. The oxide removal step used by Babic was an ammonium hydroxide dip followed by a methanol bath in which the wafers were placed together. This allowed for uniform fusion, but was not characterized in terms of the contaminants or electrical characteristics. One of the goals of the fusion investigation was the characterization of the fusion interface with different cleaning procedures. We found that to get uniform fusion the cleaning steps above were always necessary. So, the primary parameter to vary in our experiments was the final

oxide removal step. We investigated many preparations, including fusion in other furnaces, to asses the techniques to ensure fusion uniformity. One must remember that the results point to general trends and not absolute statements as to whether one process is effective or not.

One of the first questions to consider when choosing an oxide removal solution is whether it leaves the surface hydrophobic or hydrophilic. To complicate matters, a single solution may leave one surface hydrophobic while leaving the other hydrophilic. In general, we found that fusion using at least one hydrophilic interface improves the large scale fusion uniformity. Figure 3.02 shows a picture of a wafer fused with a hydrophilic surface. One can see that the channels in the contrasts as the epi above the channels, is slightly bowed.

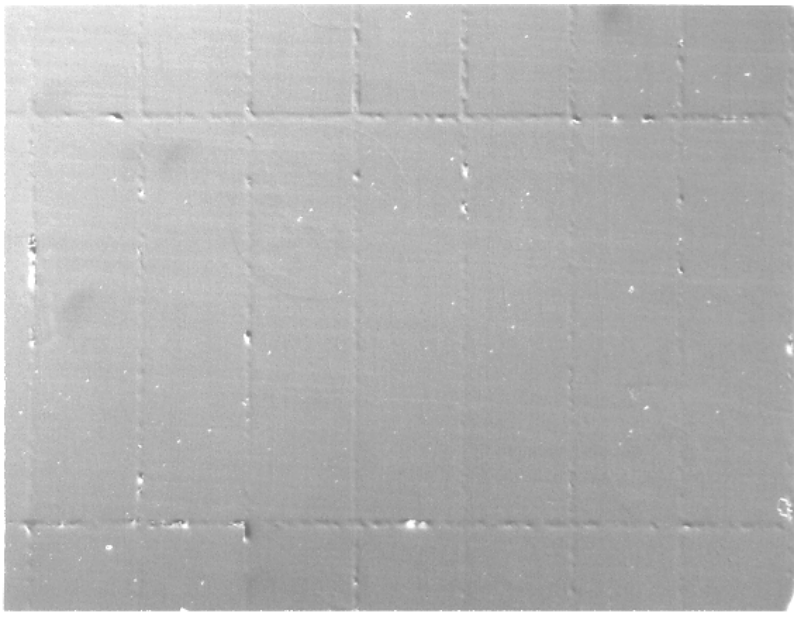

Figure 3.02. Uniform wafer fusion using a hydrophilic interface. Channel spacing is 150 μm. Picture is after substrate removal looking at the fused epi.

Figure 3.03 shows a typical fusion with both hydrophobic interfaces. One can see large-scale non-uniformities, appearing as bubbles in the fusion. These "bubbles" are believed to be caused by trapped liquid/gas that does not escape along the channels, but further investigation must be done to confirm this. Interestingly, however, if the channels are placed close enough together then these non-uniformities do not form, even if the channel do not offer a direct path to the outside environment. One can see that the closed frame of channels in Figure 3.03 toward the bottom of the picture is not connected to the rest of

the channel pattern. Yet the region of material in this box is fused uniformly. This raises the question as to whether the true value of the channels is a path for liquid to escape through, as there is no escape path out of this pattern. One possibility is that the volume of material that remains trapped is so small that even a closed channel pattern can accommodate the excess.

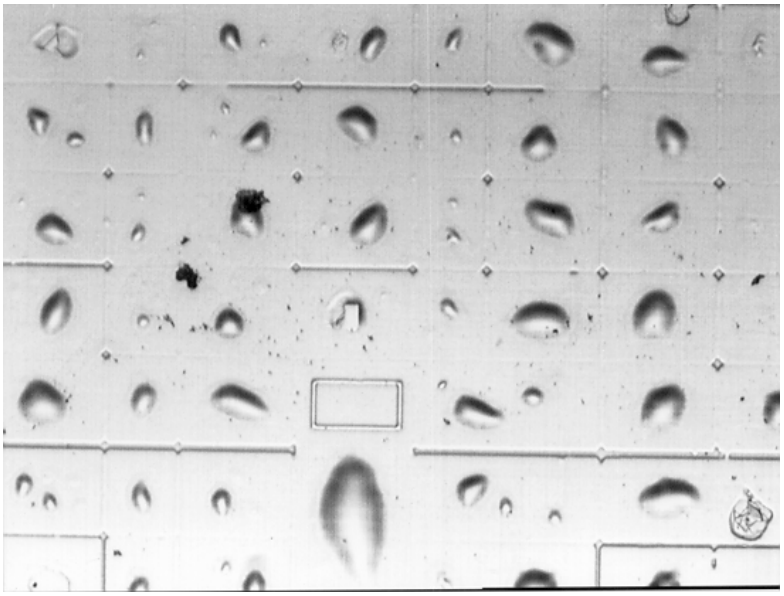

Figure 3.03. Wafer fusion using hydrophobic interface, same scale as 3.02.

Without a detailed investigation, one can only speculate on the true nature of the channels in wafer fusion. However, there is no question that in both hydrophilic and hydrophobic conditions the channels were found consistently to

help macroscopic fusion uniformity. Sections of the wafer with a lower density of channels had worse fusion than ones with higher density channels. A consistent uniformity could be reached with a hydrophilic interface and channel spacing of about 200 μm. With a hydrophobic interface one needed a channel spacing of about 100 μm to achieve uniform fusion. In all cases, the channel widths were 5 μm and the channel depths were about 300 nm.

The final issue with the hydrophobic/hydrophilic interface is how one achieves one type of condition versus the other. Conventional wisdom says that if one has an oxide on the surface of the semiconductor, then the surface is hydrophilic, due to hydroxide-hydroxide interaction. In Si processing the hydrophilic/hydrophobic condition of the surface tells whether SiO_2 is present on the surface. This test can also be used in GaAs/InP processing if the correct chemicals are used. When using HCl or HF based solutions, it is generally true that when the surface turns hydrophobic the oxide is removed. The exception to this rule of thumb is using buffered HF, which contains NH_4F as a buffering solution. The reason for this exception is that solution containing ammonium group usually terminates the surface with ammonium. The ammonium termination is hydrophilic, so that even when all the oxide is removed the surface remains hydrophilic. For this same reason the NH_4OH solution leaves

the surface hydrophilic even with no oxide. With these guidelines one can determine if the surface should be hydrophilic or hydrophobic when the oxide is removed.

3.04 Analysis of the Fused Junction

There are several desired characteristics from the fused junctions. These include good optical, electrical, and thermal properties. Each of these parameters can affect laser performance dramatically. The first parameter to consider is the optical losses at the fused junction. Examining the fused junction under a scanning electron microscope, one generally does not see any nonuniformities at the junction. Figure 3.04 shows the typical double-fused structure over a large scanning area. Even with poor fusion which gives rise to small microbubbles in the fusion, the bubbles are much smaller than the wavelength of the light in the material. This suggests that they would have minimal impact on the transmission through the junction.

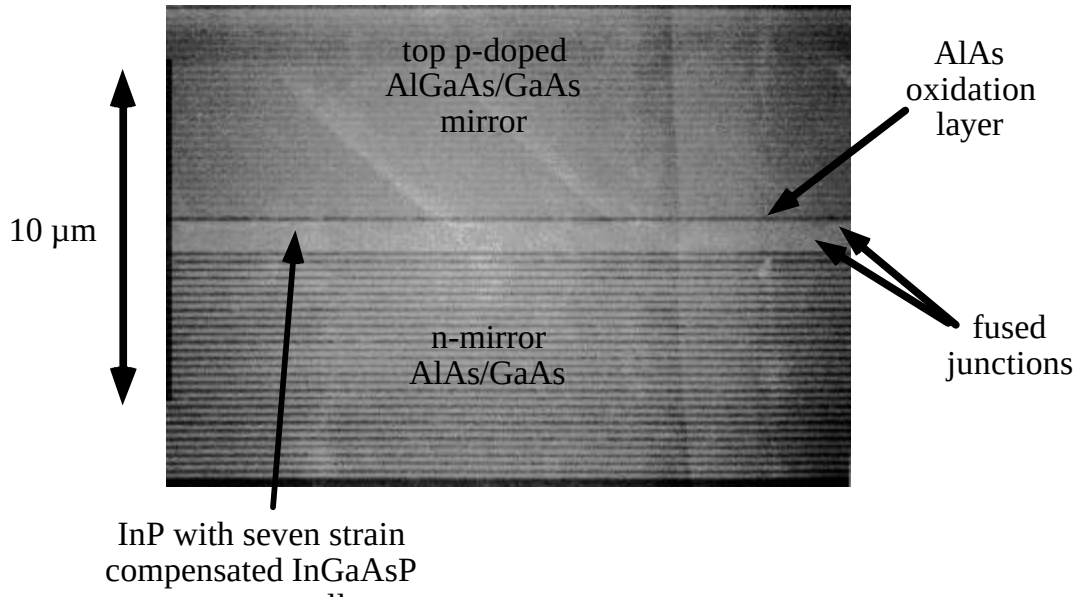

Figure 3.04. Scanning electron microscope image of fused junction over a

10-20 μm. Fused junction is not visible with SEM picture.

The very smooth fused-junction interface suggests that there would be virtually no optical scattering loss from the interface. As pointed out in the first and second chapter, the vertical-cavity laser is sensitive to extremely small amounts of optical loss. Luckily, we can take advantage of the standing-wave pattern to reduce dramatically any effective loss arising from the fused junctions. We do this by placing the junction near a standing-wave null as discussed in Chapter 2. In many cases, though, the fused junction cannot be placed exactly at the standing-wave null, due to growth inaccuracies or cavity adjustments. In this case, it is interesting to note how much loss the fused junction contributes to the loss in the device. The problem with measurement of the fused-junction loss is that one needs extremely high sensitivity to get even an estimate of the loss. Even a 0.1% transmission loss would be significant in a VCL, and this kind of accuracy is almost impossible to achieve with standard instruments. Nonetheless, one way to get this kind of sensitivity is in the high Q cavity of a VCL. The differential efficiency is very sensitive to even such levels of excess loss. The problem with using this method is that one has to have a very good estimate of all the other losses in the cavity as well as an accurate value for the injection efficiency. The fused-junction loss must be a significant portion of the

total loss for this method to be valid. As will be seen in Chapter 5, we do not have an exact value for many of these numbers. We could simply say that any loss that we have not taken into account is due to the fused junction, but this does not necessarily give any more information. Another method to get an estimate of the fused-junction loss is to place the junction in a waveguide and measure the excess loss it introduces. In this method, one extends the interaction length with the optical mode to hundred of microns instead of a couple nanometers. This, however, does not give an exact description of how the optical mode is traveling in a VCL. The k-vector is in the direction of the junction instead of perpendicular to it. If the loss is primarily absorptive, then this will not be a problem, but if it is refractive, then this method would not be accurate. Liu *et al.* have carried out such waveguide measurements using InP to InP fusion[6]. Waveguides were made with and without fused junctions present. The excess loss of the waveguides with the fused junctions was found to be about 0.5 cm^{-1}. One must assume an interaction length of the fused junction in order to translate this into round-trip VCL loss. This interaction length will fall out of the calculation since it will be multiplied again to give the per-pass loss in a VCL. We assume this length to be about 20 nm, which gives an optical confinement factor of about 0.5%. So if we assume all the loss is

confined to the 20 nm region, the absorptive loss from this region would be 100 cm^{-1}(0.5/.005). This sounds like an extremely large amount of loss, but one has to remember that it is confined to a very small region. The per-pass loss through the fused junction in this scenario is only 0.02%. Going through two fused junctions twice as in the double-fused VCL, the total round-trip loss would still only be 0.08%. With the fused junctions near a null, this contribution would be negligible. The waveguide measurements suggest that the fused junction does not contribute much loss to the VCL. With further knowledge of other losses in the devices this may be confirmed by the differential efficiencies of the VCLs.

The electrical properties of the fused junction play an important role in device performance as well. In the laser design, for instance, the current must pass through the fused junction because this allows the current confinement to be done using lateral oxidation in the GaAs/AlGaAs mirror. This is a vital consideration as there isn't yet an equivalently effective confinement scheme in the InP system. Previous results have shown very low-resistance conduction from n-InP to n-GaAs[7], although this is not as important as the conduction between p-GaAs to p-InP. As discussed in the final part of the Chapter 2, the current-confinement layer must be on the low mobility p-side to avoid excessive

current spreading. There has been a least one report on low-resistance p-InP to p-GaAs fusion, but the doping levels in this report were much too high for VCL use ~ 10^{19} cm^{-3}[8]. We have found that it is very difficult to get a low-resistance p-InP to p-GaAs fusion using reasonable doping levels consistent with VCL design.

Investigation of the fused-junction resistance were done using a structure as depicted in Figure 3.05. The reasons an p/n MQW active region was used are three-fold. First, the use of a n-InP layer allowed for very low-resistance ohmic contacts to be used, without the need for high-temperature alloying of contact. This prevented any interaction between the metal contact and the fused junction. If one uses alloyed contacts, one has to be very careful not to allow the metal alloy to get to the fused junction and complicate the measurement.

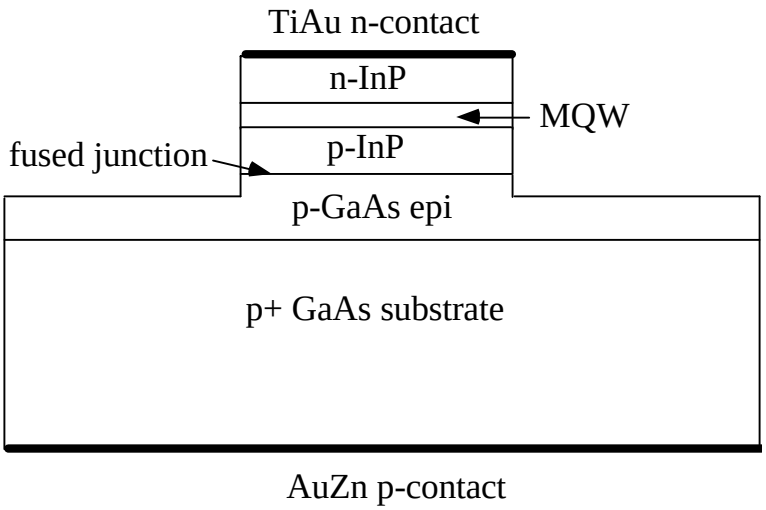

Figure 3.05. Schematic of structure to measure p-InP to p-GaAs resistance.

The second reason we used the structure depicted above was that one could eliminate any false positive results. We could do this by testing the reverse bias breakdown of the junction. If in some way the junction was shorted, through lithography or other means, the reverse breakdown of the diode would also be shorted. If the diode maintained a high reverse bias breakdown voltage then there could be no possibility of the device being shorted. The forward voltage of the fused junction could be determined from subtracting the total voltage by the theoretical diode turn-on voltage. Furthermore, this subtraction is not really necessary since, in the real VCL devices, the active region and fused junction are also in series. The voltage on the test structure would be equivalent to the

voltage on the fused junction and active region in the real device. The third and least obvious reason to employ to the depicted structure is that there can actually be an interaction between the fused junction and the active region. For this reason, we used actual MQW active regions grown for laser structures. This interaction gives rise to very strange I-V curves as will be described shortly.

One of the most obvious parameters to vary in such a study is the doping of the layers adjacent to the fused junction. A second parameter we varied is the oxide removal step before fusion. The fusion time and temperature were kept constant for most of the experiments, but were occasionally varied to see what effect this might have. We found that under the conditions that we were using, the time, temperature, or preparation procedure did not significantly change the I-V characteristics of the junctions, but rather only changed the fusion uniformity. The range of temperatures used were 600-650°C, with fusion times between 20-40 minutes. Most experiments were done at 630°C for 30 minutes at peak temperature. Hydrogen was primarily used as the atmosphere gas during the fusion. Some experiments were performed with Nitrogen with no noticeable difference. Significant noise was present in the

results of these experiments such that conclusions could only be drawn through the use of numerous fusions.

Measurement of the I-V curves were done through the use of a HP4145A semiconductor parameter analyzer, which takes data points at fixed biases. A typical I-V curve is shown in Figure 3.06.

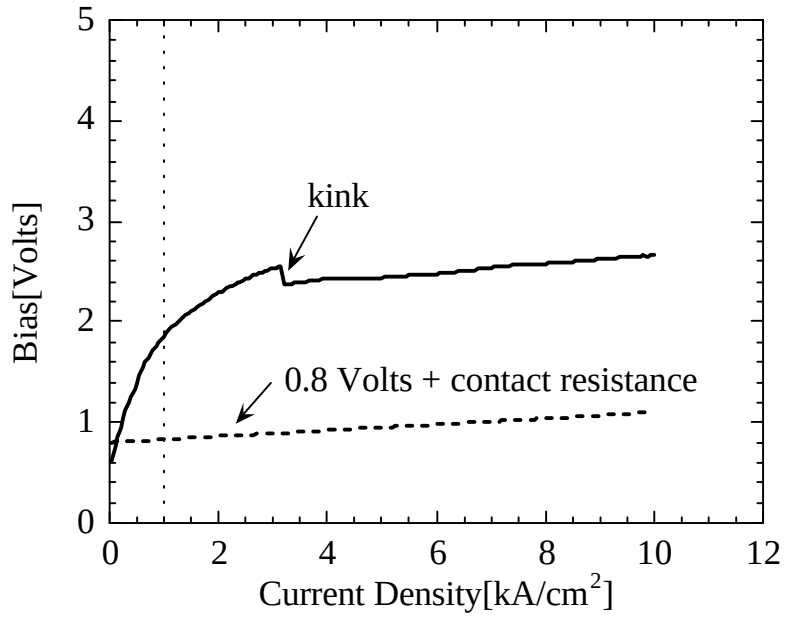

Figure 3.06. typical J-V curves of structure depicted in Figure 3.05.

Surprisingly, the kink seen in the I-V curve is present on almost all devices. The kink occurs at different current levels many times from even a single device. At first this was suspected as some sort of measurement error, but

indeed this kink persisted on tens of generations of wafers. A different picture arose when one measured the same device with a scope I-V current tracer. These devices sweep the voltage up and down in a continuous fashion such that one can see hysteresis more easily.

Figure 3.07 shows a typical trace of the I-V curve directly taken from the curve tracer. One easily discerns a region of negative-differential resistance. This I-V curve is very similar to what one would expect from a poor thyristor device.

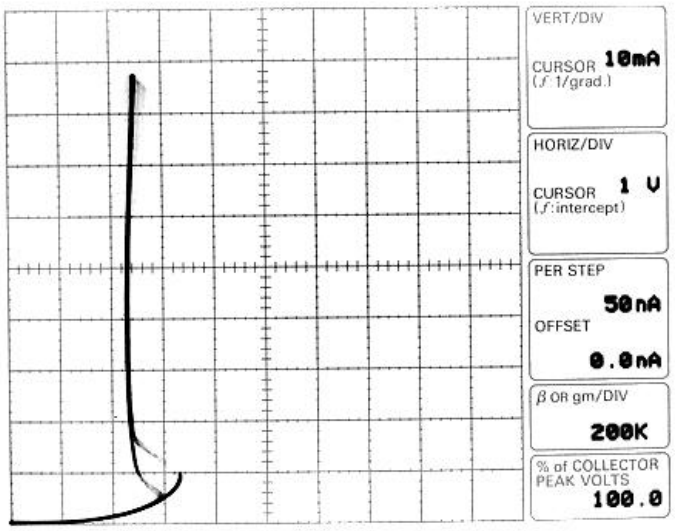

Figure 3.07. I-V curve trace showing negative-differential resistance of fused junction in series with active region.

A thyristor is a semiconductor device many times used as a voltage switching element. In Chapter 5 we will investigate more closely the behavior of a thyristor. For now, the basic structure of a thyristor is an n/p/n/p doping profile. In the fused- junction structure, we only have a n/p/'fused junction'/p. If the fused junction/active region structure is to act like a thyristor, the p-p fused junction must in some way be acting as an n-region. Indeed, the hole barrier at the fused junction acts in a similar fashion to an n-region. As will be seen in Chapter 3, there are large amounts of contaminants at the junction such as oxygen. One possibility is that Oxygen acts as a mid-gap state possibly pinning the Fermi level in GaAs.

Figure 3.08 shows the band diagram of the device with and without Fermi-level pinning at the junction. Clearly holes have a significant barrier to traverse to get to the active region, giving rise to a large resistance for holes to go past the junction. As the device is biased, most of the voltage drop is across the fused junction. At high enough bias, the fused junction starts to pass some current causing the active region diode to begin to turn on. As the bias is turned higher, there begins to be some overflow of electrons from the active region diode which traverse the p-InP spacer layers towards the fused junction. Since there are no barriers for electrons at the fused junction, they can traverse

it with little voltage drop and recombine with holes in the GaAs. In this situation there is little resistance at the fused junction, which means a greater amount of the bias is being applied to the active region, which in turn means more electron leakage. This avalanche effect leads to a switching of the I-V curves from the condition of high resistance at the fused junction to a low resistance at the fused junction. At first glance, this appears to be a good situation since the total resistance is lower. However, on closer inspection, one sees that this is very bad for a laser design. All the recombination now is occurring at the fused junction instead of the active region. This means no lasing can occur past the switching point of the thyristor. If lasing does occur before the switching action the carrier density at the active region will be relatively constant, reducing the increase in electron leakage at high current densities. Unless the fused-junction resistance is reduced, electron leakage can be very detrimental to this design. Electron leakage at 1.3 μm is indeed worse so that it is even more important to reduce the fused-junction resistance for lasers of this wavelength.

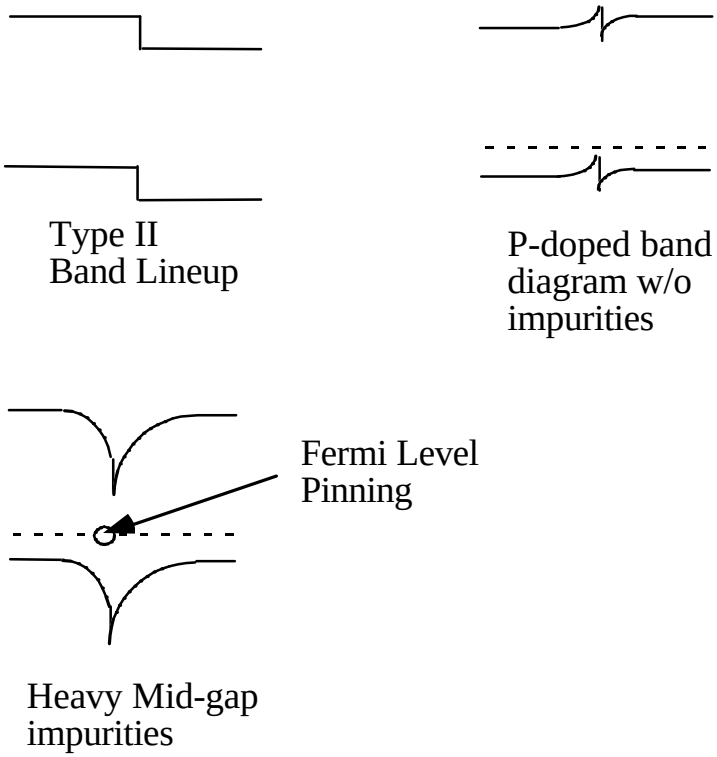

Figure 3.08. Band diagram of fused junction with and without pinning.

Table 3.01 summarizes the results of I-V testing of the fused junctions. As stated, the only consistent parameter that altered the fused-junction voltage was the doping in the adjacent layer. The first two entries(A and B) show there is little to no difference in changing the GaAs doping for 1 10^{18} to 5 10^{18} cm^{-3} in the last 30 nm closest to the junction if the InP doping is kept at 10^{18} cm^{-3}. Entry C shows that the change in Carbon doping with everything else held constant does not alter the result. Entry D shows that even if the doping

level is cut to $2\ 10^{17}$ cm^{-3}, the turn-on voltage still remains the same. The conclusion to be drawn from entries A-D is that as long as the InP doping level is 10^{18} cm^{-3} and is Zinc doped, then the turn-on voltage is between 1.2-1.5 Volts for the fused junction. The next three entries try to explain what happens when the doping level in the InP is cut to $3\ 10^{17}$ cm^{-3}. In the case of the high Be doping, the turn-on voltage remain relatively constant, but in both cases of the Carbon doping the voltage was significantly higher.

Run#	GaAs doping	InP doping	Turn on voltage
A	$1\ 10^{18}$ Be	$1\ 10^{18}$ Zn	1.2-1.5 V
B	$1\ 10^{18}$ /5 10^{18} Be	$1\ 10^{18}$ Zn	1.2-1.5 V
C	$1\ 10^{18}$ /5 10^{18} C	$1\ 10^{18}$ Zn	1.2-1.5 V
D	$2\ 10^{17}$ C	$1\ 10^{18}$ Zn	1.2-1.5 V
E	$1\ 10^{18}$ /5 10^{18} Be	$3\ 10^{17}$ Zn	1.2-1.5 V
F	$2\ 10^{17}$ C	$3\ 10^{17}$ Zn	5-6 V
G	$1\ 10^{18}$ /5 10^{18} C	$3\ 10^{17}$ Zn	5-6 V

Table 3.01. Turn-on voltage versus doping profile for p-p GaAs/InP fusion.

We believe the reason for this disparity is the higher diffusion of Be relative to Carbon. This allows the Be dopant to accumulate at the interface. In the case

of the high Zn doping on the InP side, the dopant that can accumulate at the interface is Zn; therefore it is irrelevant what happens on the GaAs side. If, however, there is not much Zn on the InP side, there must be Be on the GaAs side to diffuse and dope the junction. The diffusion of dopants to the interface can be seen in the SIMS data presented in the next section.

3.05 Fusion Impurities

The fusion process may introduce many impurities at the junction. One would suspect that different preparation procedures would result in different amounts of impurities incorporated at the junction. In this work, we focused on two impurities, namely oxygen and carbon, tracking the concentration of such impurities through numerous fusion procedures. Oxygen was chosen since it is known to cause problems with current flow, and carbon was chosen as an indication of contamination at the surface. We generally found very high levels of oxygen at the junction regardless of cleaning and deoxidizing procedure, but the carbon level was consistently different with different procedures. We used a Secondary Ion Mass Spectroscopy(SIMS) characterization on the interface, relying correct calibration by Charles Evans & Co., which performed the

measurements. We could get reliable data from the carbon scans, but the oxygen reading was usually saturated when the fused junction was reached, indicating a concentration greater than 5 10^{21} cm^{-3}. This makes difficult comparisons of oxygen concentration among different samples. The variation from run to run was also quite large, so that quantitative values were not very accurate. Figure 3.09 shows a typical SIMS scan for oxygen. In this case, the detector was obviously saturated so that all that could be said is that the level is above 5 10^{21} cm^{-3}.

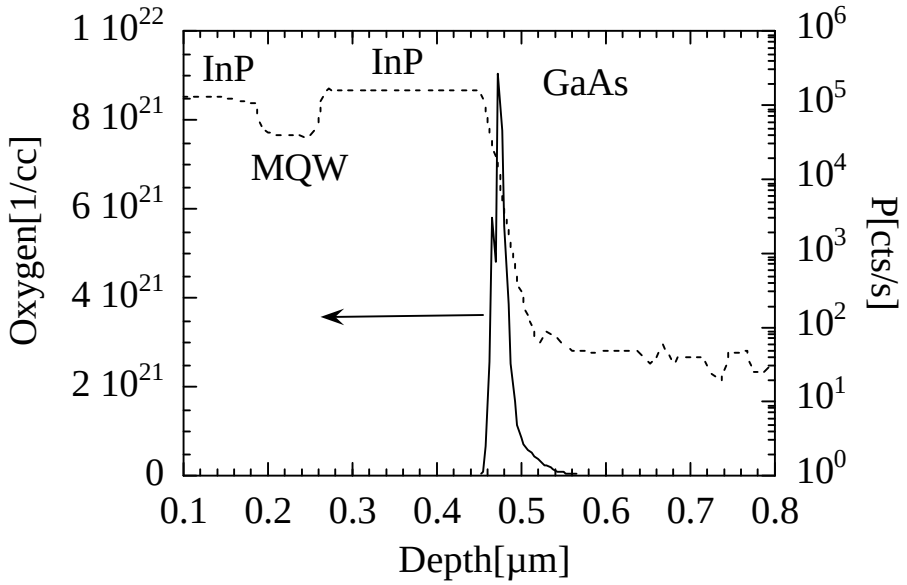

Figure 3.09. SIMS scan of fusion interface showing saturated oxygen peak.

In Table 3.02 we use the following descriptions for the amount of contamination of oxygen: $>3\ 10^{21}$ cm^{-3} is high, $\sim 10^{21}$ cm^{-3} is medium, $<10^{20}$ cm^{-3} is low. Carbon contamination was quite a bit lower. Thus we used the following designations: 10^{21} cm^{-3} is very high, 10^{20} cm^{-3} carbon is high, $<10^{19}$ cm^{-3} carbon is low. The table summarized all the different procedures used on the wafer before inserting into the fusion furnace. We include the resultant impurity concentrations, as well as a qualitative estimate of the fusion uniformity. Good uniformity implies more than 95% of the wafer is usually fused. Average uniformity means that the fusion has some sort of consistent problem which makes fusion of greater than 80% of the area rare. Bad uniformity means that only about 50% of wafer is usually fused.

Process	Uniformity	Carbon	Oxygen
NH_4OH direct	good	low	high
NH_4OH ->methanol	good	low	high
NH_4OH ->isopropanol	good	medium	medium/high
HF/HCl -> H_2O-> NH_4OH	good	high	medium
HCl/H_2O	bubbles	not tested	not tested
conc. HF	average	high	medium
conc. HF/glove box	good	high	low
Buffer HF	good	medium	medium
NH_4S wet solution	bad	not tested	not tested
NH_4S dry passivation	very bad	not tested	not tested
Sb dry passivation	no fusion?	not tested	not tested

Table 3.02. Clean procedure affect on fused junction.

Some general rules can be drawn from the table. The use of NH_4OH is not as effective as HF in removing oxide. However, the use of HF significantly increases the carbon contamination at the interface. The fused-junction voltage

seems to be the same in either case, so it is unclear which is better to use. The HF preparation leaves the surface hydrophobic which causes some problems with uniformity. An alternative we have recently discovered is the use of Buffered HF which gives equally good uniformity and should remove the oxide like concentrated HF. Putting the wafers in a solvent such as methanol or isopropanol does not seem to make much of a difference, although the use of isopropanol seems to increase carbon contamination slightly. The dry passivation techniques gave very bad fusion uniformity, for which we do not have an explanation.

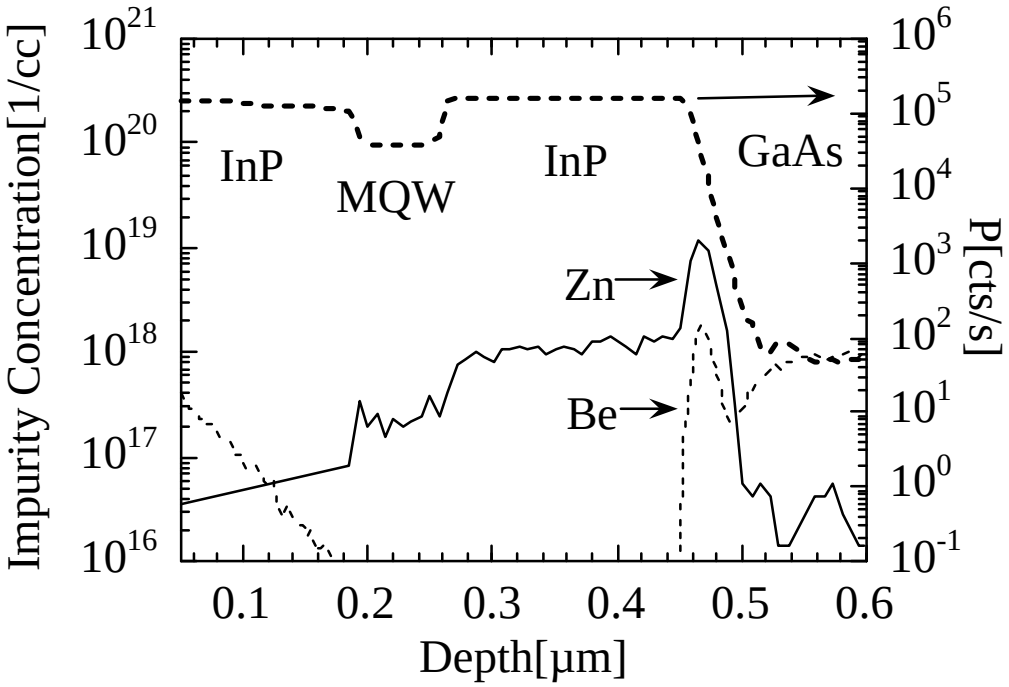

Figure 3.10. SIMS scan showing accumulation of Zn and Be at the junction.

Different doping levels were also tried with different cleaning procedures resulting in a very large matrix of experiments. For some runs the doping profiles were also scanned to give an indication of the accumulation or depletion at the junction. Figure 3.10 shows a typical doping scan of the junction showing significant accumulation of Zn at the junction. This is consistent with earlier conclusions that Zn can accumulate at the junction, somewhat lowering the fused-junction resistance. We can also see that some of the Zn has diffused into the quantum-wells. We found that the range of

cleaning procedures that we had attempted had little affect on the turn-on voltage. The most likely reason for this lack of improvement is that we did not lower the oxygen level below the level at which the Fermi level was no longer pinned, or the Fermi level was being pinned by some other factor. Other steps which will be discussed in the next section must be taken to reduce the oxygen level below the 10^{19} cm^{-3} level where there may be an appreciable difference in voltage.

3.06 Oxygen Desorption During Fusion

The big question that arises when doing these fused-junction experiments is why such a large amount of oxygen remains at the fused junction. After all, regrowth techniques in InP and GaAs are such that only a minimal amount of oxygen is left at the regrowth interfaces. The same procedures are used to prepare the samples in both cases, yet in the fusion case several orders of magnitude more oxygen is present at the end. Similar times and temperatures are used as well. In the fusion case, one expects overpressure of group V elements to be provided by evaporation of these elements off the surface. Less apparent is the difference between regrowth and fusion. In the

fusion case, both group V and group III elements are present during the mass transport. In the case of regrowth, one can apply only the group V element to the surface while trying to desorb the oxide. This means no regrowth occurs until the group III elements are applied. One can raise the temperature without degrading the surface to let the oxide desorb from the surface. In the case of wafer fusion where the two wafer are placed together and heated up simultaneously, the rate of oxide desorption and mass transport are determined by the same factors of time and temperature.

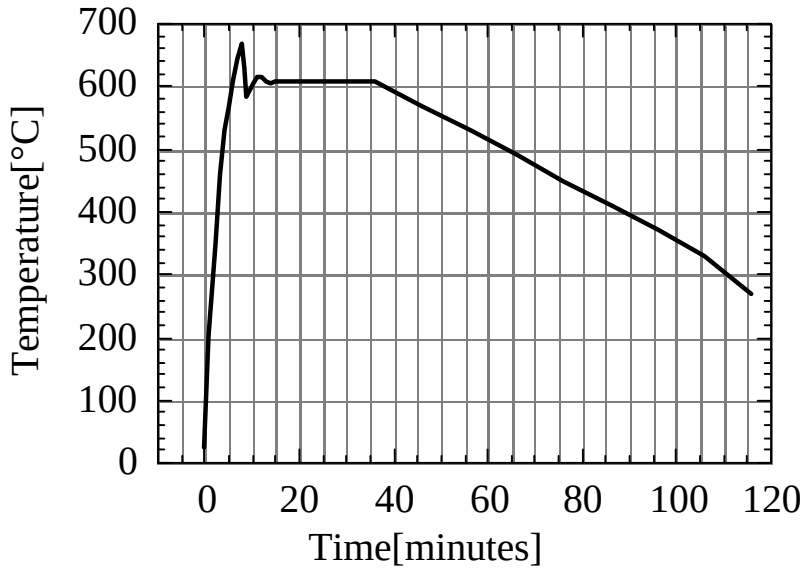

Figure 3.10. Very fast ramp-up of temperature in fusion furnace.

Since so much oxygen is present at the junction, one must assume the fusion process occurs before the full oxide desorption process occurs. This may mean much of the fusion is oxide assisted. Once the fusion process is in effect, there in no way for the oxygen to escape the junction, as all the microvoids, leading to the outside environment, are sealed by the fusion process. Here one needs preferential desorbtion of oxide rather than of the group V elements during the fusion process. We attempted to ramp up the temperature in many different ways to achieve a differential absorption of oxygen versus group V elements. These schemes involved the use of either a very slow ramp in temperature or a very fast ramp. No method seems to give the proper differential between the oxide desorption and fusion process. Figure 3.11 shows the fastest ramp up rate we could achieve with our fusion furnace. The idea here was to raise the desorption temperature before much mass transport could occur to seal in the oxide. This sample, however, still had a very high oxygen peak. In the final chapter, I will describe a possible system to remove the oxide from the fused junction. This system required the wafers to be placed together at high temperature making the design and implementation of such a system somewhat complex.

3.07 Summary

This chapter reviewed many of the issues involved with wafer fusion. We started with a general discussion of the fusion process, and then gave a summary of the practical aspects involved with this process. In Section 3.03 the cleaning procedure for fusion was reviewed with Section 3.04 detailing the surface preparation before fusion. This preparation is one of the most important aspects in achieving uniform fusion. Section 3.04 began the analysis of the fused junction and explored the optical and electrical properties of the junction. A detailed investigation of the electrical properties revealed that the fused junction offered a 1 Volt barrier to hole transport. In Chapter 5, we will look again at the fused-junction voltage, and see what impact it has on device performance. A chemical analysis of the fused junction revealed a large oxygen concentration at all our junctions. Simple band-diagram estimations reveal that this oxygen concentration may be the source of the excess voltage drop. In the final chapter, this voltage drop will be addressed again. The chapter immediately following will describe the steps needed to complete the VCL processing after the wafer fusion is complete.

3.08 References

[1] C. Taek Ryong, N. Hosoda, T. Suga, and H. Takagi, "1.3 mu m InGaAsP/InP lasers on GaAs substrate fabricated by the surface activated wafer bonding method at room temperature.", Appl. Phys. Lett., vol.72, 1565 (1998).

[2] R. J. Ram, J. J. Dudley, J. E. Bowers, L. Yang, K. Carey, S. J. Rosner, and K. Nauka, "GaAs to InP wafer fusion.", J. Appl. Phys., vol.78, 4227 (1995).

[3] G. Patriarche, F. Jeannes, J.-L. Oudar, and F. Glas, "Structure of the GaAs/InP interface obtained by direct wafer bonding optimised for surface emitting optical devices.", J. Appl. Phys., vol.82, 4892 (1997).

[4] A. Black, A. R. Hawkins, N. M. Margalit, D. I. Babic, A. L. Holmes Jr., Y.-L. Chang, P. Abraham, J. E. Bowers, and E. L. Hu, "Wafer fusion: materials issues and device results.", IEEE Journal of Selected Topics in Quantum Electronics, vol.3, 943 (1997).

[5] Z. H. Zhu, F. E. Ejeckam, Y. Qian, Z. h. a. n. g. Jizhi, Z. h. a. n. g. Zhenjun, G. L. Christenson, and Y. H. Lo, "Wafer bonding technology and its applications in optoelectronic devices and materials.", IEEE Journal of Selected Topics in Quantum Electronics, vol.3, 927 (1997).

[6] B. Liu, A. Shakouri, and J. E. Bowers, "Fused vertical directional couplers.", Conference Proceedings. LEOS '97, 10th Annual Meeting. IEEE Lasers and Electro-Optics Society 1997 Annual Meeting (Cat. No.97CH36057), 205 (1997).

[7] H. Wada, Y. Ogawa, and T. Kamijoh, "Electrical characteristics of directly-bonded GaAs and InP.", Appl. Phys. Lett., vol.62, 738 (1993).

[8] A. V. Syrbu, J. Fernandez, J. Behrend, C. A. Berseth, J. F. Carlin, A. Rudra, and E. Kapon, "InGaAs/lnGaAsP/lnP edge emitting laser diodes on p-GaAs substrates obtained by localised wafer fusion.", Elect. Lett., vol.33, 866 (1997).

Chapter 4

Device Fabrication

Processing and fabrication play crucial roles in achieving packagable high performance device. Having already dealt with wafer fusion in the previous chapter, I will continue here to describe all of the other processes involved in the fabrication of such devices. This device fabrication has gone through many iterations of optimization as well as designs, but ultimately the steps involved are all very similar. For brevity, I will focus on the fabrication of the final design of the top-emitting structure. The emphasis in this chapter will be on the best process for each step, along with avoidance of problem areas.

4.01 Pre-processing Analysis

Before actual processing of devices begins, one can take several measurements that later become very useful. One of the first steps is to record the photoluminescence for the active region sample. This can be done directly on the wafer sample since the quantum wells are only buried 300 nm below the surface. The PL intensity is a good indication of the quality of the active region. The PL peak wavelength is one of the most important parameters to measure, as it is a relatively good indicator for the approximate peak-gain wavelength. As will be discussed in the results chapter, it is important to have the correct alignment between the peak gain and mode position. The peak-gain wavelength is usually slightly blue shifted relative to the peak PL wavelength due the higher injection densities in an actual electrically pumped device. The blue shift is estimated to be on the order of 5-10 nm[1].

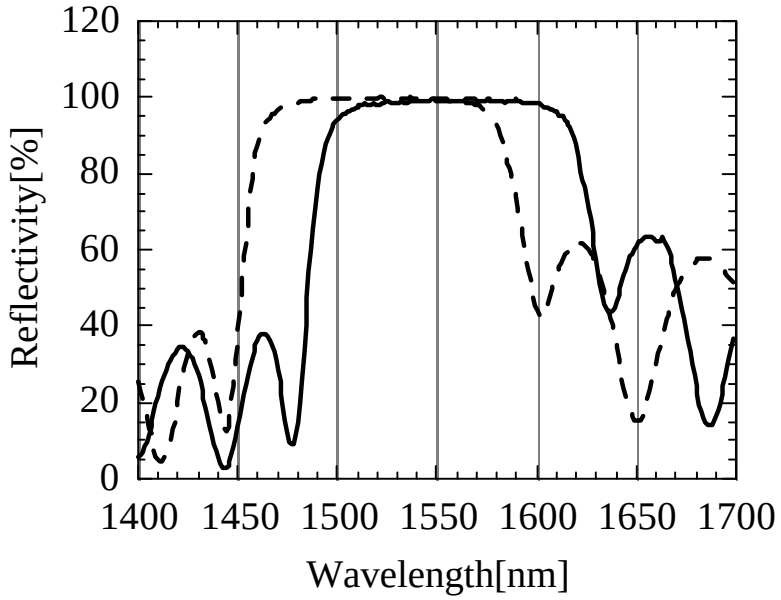

Figure 4.01. Example of non-uniformity in expitaxial growth of the mirror samples. Dotted line represents a measurement 1 cm from the edge of a 2-in. wafer and solid line represents measurement from the center of the wafer.

Also of great importance is measurement of mirror reflectivities before beginning device processing. The absolute value of the mirror reflectivity is difficult to measure, but the shape of the mirror reflectivity versus wavelength is relatively easy to measure. The measurement is done with a Lamba-9 spectrometer. Both mirror stopbands are measured. One distinctive feature of fusing relatively small pieces is that one can choose different regions of the larger epitaxial wafer for different properties. This allows one to use the natural non-uniformities of the growths for ones advantage. If a mirror was grown at too long a wavelength for a specific laser design, one can cleave a piece near

the edge of the wafer where the growth rate can be as much as 3% shorter. This flexibility can allow for significantly different results for the same epitaxial growth. Figure 4.01 shows the lateral variation of the mirror reflectivity across a two-inch wafer. By choosing pieces from the edge or center, one can get as much as 50 nm(3% growth rate variation) of play for the same growth. To start the fabrication, 8x8 mm pieces of the active region, p-mirror, and n-mirror are chosen and cleaved according to the desired final wavelength.

4.02 Etching Channels

The first step of the VCL process is etching channels. As decribed in the last chapter, channel etching is critical in achieving uniform wafer fusion. Channels possibly allow for escape paths for the trapped liquids between the two wafer surfaces. With this interpretation of the channels function, it is clear that in order for the channels to be effective they must extend to the wafer edge. Normally, this would not be any problem, except that photoresist is usually quite thick at the wafer edge. If one does a normal exposure and developing, the wafer edge is usually not developed all the way through. There are two options to over come this. One can severely overexpose the channel pattern or do an edge-bead removal before doing the lithography. Either way is

effective, but the edge-bead removal is preferred in that one can obtain a much sharper pattern for the channels. Figure 4.02 shows a picture of the typical channel pattern after etching. A selective etch that stop on the quantum wells is used so that the channel depth is approximately 300 nm.

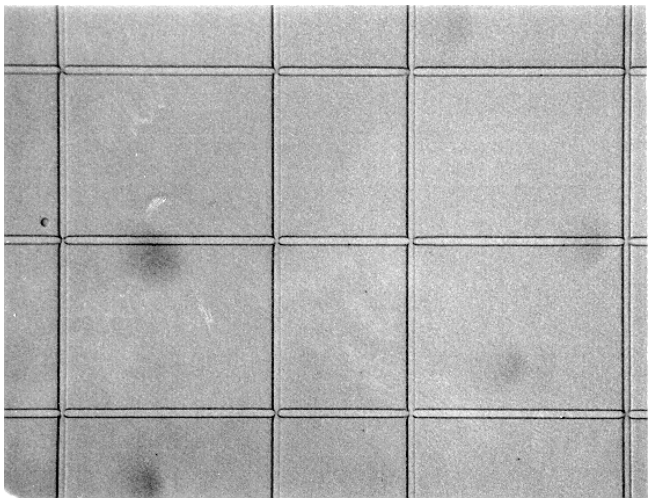

Figure 4.02. Picture of InP wafer with channels before fusion process. Horizontal lines are 200 μm apart.

Figure 4.03 shows a Dektak profile of an etched channel. The flat bottom of the channel indicated that the etch has reached the quantum wells. The quantum wells act as an etch-stop layer for the InP channel etch, resulting in a uniform flat bottom. This etch depth is very useful in determining the cavity length of the active region. The Dektak gives about +/- 100 Å accuracy

for this etch depth and scan length. This is not enough accuracy to determine the cavity mode exactly, but allows for a very good estimate(+/- 15 nm).

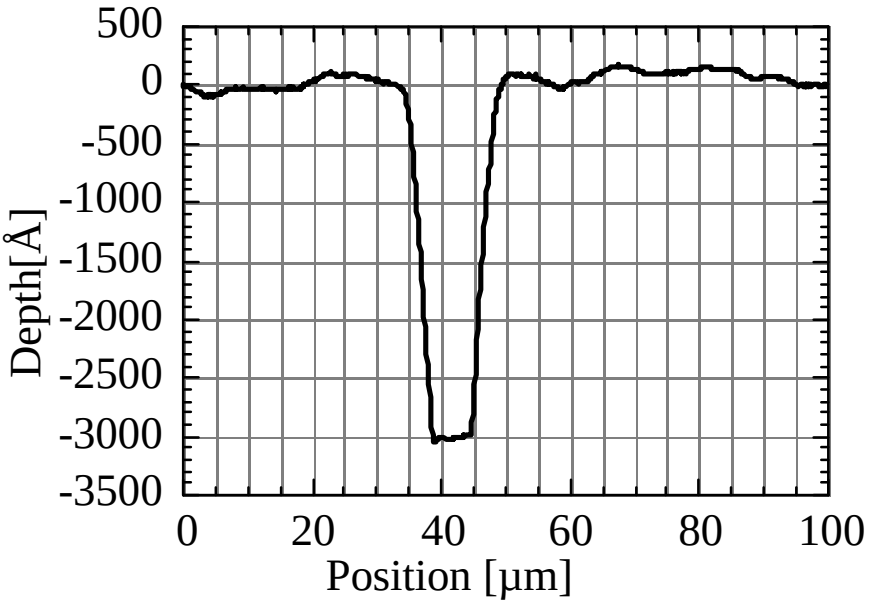

Figure 4.03 - Dektak profile of etch channel in MQW active region

In cases where the cladding is too thick for a specific laser design, it may be necessary to etch the InP to get the correct cavity mode wavelength. This etch can be rather tricky as several parameters are required. Firstly one wants the etch to be very slow and reproducible. This allows one to adjust very thin amounts. Secondly one wants the etch to have high selectivity over the quantum wells to use the wells as a reference to the etch depth. Finally, the etch has to be relatively smooth so that there will be negligible impact on the

fusion quality. The etch that seems to fit these parameters best is 1:9 $HCl:H_3PO_4$. The etch is very selective over quaternaries and is relatively smooth for very small etch depths. The surface begins to roughen if one tries to etch farther than 500 Å. The etch rate is a bit fast ~50 Å/sec, but further dilution of the etch results in very erratic etch rates. For example, increasing the phosphoric content to 15 from 9 would result in the etch rate dropping between a factor of 2-10. Depending on the temperature or the amount of mixing, one gets very different results. Using 1:9 gives relatively reproducible results for small etch depths(<500Å). One can also do adjustment of the n-side of the active region after the first fusion. In this way, one can change the thickness of the active region by as much as 25%. However, it is highly preferable to have the correct active region thickness grown without need for adjustment, so every effort should be made to grow the correct thickness.

4.03 Substrate Removals

Once channels are etched, one can fuse the InP/InGaAsP active region to the GaAs/AlGaAs p-mirror as described in Chapter 3. With the first fusion complete, one needs to remove the InP substrate up to the InGaAs(P) etch-stop layer. This process is accomplished by wet chemical etch of the InP with 3:1

$HCl:H_2O$. This solution etches InP quite violently, with vigorous bubbling of the etch products. This vigorous bubbling many times causes a problem with the substrate removal, namely the bubbles block further etching. Portions that have bubbles attached to them leave what appear to be pyramid-type shapes of unetched InP, even when other sections of the wafer are completely etch-to-the-etch stop. These pyramids can sometimes be as high as 50-100 μm. Since the etch-stop layer has only a finite length of time that it can remain in solution before the etch breaks through, one cannot simply leave the sample in solution until the residual InP is etched away. If pyramids do form, one needs to somehow remove them so that further planar lithography or a second fusion can be done. This is usually done by either cleaving that portion of the wafer off, or scrapping this material off with a diamond tip scribe. Usually these pyramids form very close to the edge of the wafer making this first option feasible.. The second is less attractive, but is also effective. The best way to address these pyramids is to prevent their formation. Stirring does not seem effective in preventing the bubbles from sticking to the wafer. However, vibration of the solution is. Vibration can be done either by a very slight ultrasonic blast every 5 minutes of etching or even by a tapping of the etch container at such intervals. This knocks the bubbles off and allows for uniform etching. The use of vibration appears to be a very effective way to deal with this problem.

With the substrate removed, the etch-stop layer is etched with 3:1:50 H_3PO_4:H_2O_2:H_2O. This process can take between 5-10 minutes depending on the exact etch-stop layer composition. Important to the laser design is that the etch-stop layer be completely removed, so overetching of this layer is usually done. With this layer removed, the second fusion can proceed. This second fusion is done under the same condition as the first, with the only difference being that no channels are etched into the InP. The reason no channels are needed for the second fusion is that the channels from the first fusion still provide an escape path for material. This is because the material over the channel from the first fusion is very thin so that it actually bends down, forming effective channels for the second fusion.

With the second fusion complete, one of the GaAs substrates must be removed. It should be clear from the processing point of view that it is just as easy to make p-down devices as p-up devices. One just has to choose which substrate to remove. For all the devices in this thesis, the p-substrate was removed leaving p-up devices. Indeed, one has to be careful here not to remove the wrong substrate, as they can look identical. The GaAs substrate removal is done in a standard spray etcher which can remove an entire 500 μm substrate in 3 hours. The etch solution is 30:1 H_2O_2:NH_4OH and is very selective between GaAs and Al(Ga)As. The etch-stop layer thickness is

typically between 100-150 nm and has an Al composition above 67%. These types of numbers afford about half an hour of time from when the first portion of the etch-stop layer is exposed to when the etch-stop layer breaks. Since the whole substrate takes about three hours to etch, one can calculate that you need about one part in six etch uniformity over the whole substrate to insure no breaks in the etch-stop layer. This etch uniformity is not very difficult to achieve on a 8x8 mm sample. When the etch is nearly done, one sees a small section of the wafer start to get very smooth. This smooth section slowly expands to cover the entire wafer in about 10 minutes, completing the substrate removal. The etch-stop layer is immediately removed before it becomes entirely oxidized. The Al(Ga)As etch-stop layer is removed in about 10-15 seconds using 1:1 HF:H_2O.

Once the etch-stop layer is removed, much of the processing proceeds similarly to GaAs VCL processing. In fact, Ko *et al.* managed to use the same mask developed for the fused VCL to make record 850 nm AlInGaAs VCLs[2]. The first step is always to measure the mode position of the VCLs. This is done in the Lambda-9 very much like the mirror reflectivity measurement. One sees a characteristic dip in the mirror reflectivity near the center of the stop-band. This dip corresponds well to the final lasing mode of the VCL.

4.04 Pillar Etching and Contacts

There are several different ways to process the wafers. By definition, each generation of devices is processed in a slightly different way. So, to keep the fabrication section of reasonable length, I will focus on the top-emitting VCL processing employed in the final two generations of devices(later described as generation D and E).

For the top-emitting devices, the first step of the process is depositing p-metal contacts what will eventually be on top of the pillars. The first-layer mask is composed of rings of different diameters as well as TLM patterns. Lithography is done through a the standard 5124 IR process. This is a very reliable and reproducible process. Ti/Pt/Au contacts are evaporated in an e-beam evaporator and lifted off. Ti/Pt/Au was chosen as the contact scheme because these contacts can survive the extended high-temperature exposure of the oxidation furnace. For several sets of devices, these contacts were left exposed during the oxidation process. This method allowed for reasonable contact resistances, but the metal had a very rough black tint to it after coming out of the furnace. This made probing more difficult and could not be well integrated with the final generation bond pad metal. To prevent this metal degradation, 150 nm of PECVD grown SiN_x was deposition on the whole wafer

before further processing was done. This SiN_x protects the metal during the oxidation process.

Once the SiN_x deposition is complete, a mask must be applied for the definition of the pillars. Several types of masks were investigated for the Cl_2 based RIE etching. These include PECVD SiO_2, PECVD SiN_x, e-beam evaporated SiO_2, and e-beam Ni masks. The Ni was not compatible with the oxidation process and could not be removed easily. The PECVD SiN_x did not offer enough protection through the very long RIE etch. E-beam evaporated SiO_2 did work well for straight sidewalls, but as much as 600 nm was require to protect the 7 μm of GaAs/Al(Ga)As etching. With the oxidation process incorporated into the devices, there was no need for vertical sidewalls any more. In fact, several research groups were using wet-etching to define the pillars[3]. However, we found that wet-etching gave excessively slanted side walls which could contribute to device capacitance. The process that was finally incorporated was to use a thick photoresist as an etch mask. This did not give perfectly vertical sidewalls, but was much better than wet-etching, and gave very fast processing times. AZ4330 resist(3 μm thick resist) was patterned over the metal ring(which were covered by SiN_x). The alignment at this point must be quite accurate to avoid ring contact blocking the light output. Some tolerance should be designed into the mask so that this does not occur.

Plus or minus 3 μm provides enough tolerance so that this is not be a problem. With the resist patterned, one needs to first etch through the SiN_x protection layer. This can be done through wet-etching or, preferably, through CF_4 plasma-etching.

At this point, one needs to do the RIE etching of the pillars. Our etching was done in a Plasma-therm RIE etching machine. The etch gases' flow rates were 5:2.5:25 of $SiCl_4$:Cl_2:BCl_3. The pressure for the etch chamber was 5 mTorr and the microwave power was 60 Watts. This gave an etch rate of 0.5 μm per minute. Our RIE machine also has a lock chamber so that pumpdown to 3 10^{-6} only took 10 minutes. Figure 4.05 shows an example of the sidewalls under these etch conditions. This etch profile appears to be acceptable, so these etch conditions were used for several generations of devices. For the last two generations of devices, this etch profile was problematic due to the slight overhang of material at the top of the ridge. This made it very difficult to deposit metal on the side of the ridge in order to make an interconnect from the top ring to the p-bondpad. To eliminate this overhang, different etch conditions were used. For straighter sidewalls, pure Cl_2 was used at a flow of 10 sccm at a pressure of 3 mT. In addition, the RF power was increased to 200 W. This gave an etch rate closer to 1 μm/min. Figure 4.06 shows the results of using these etch conditions.

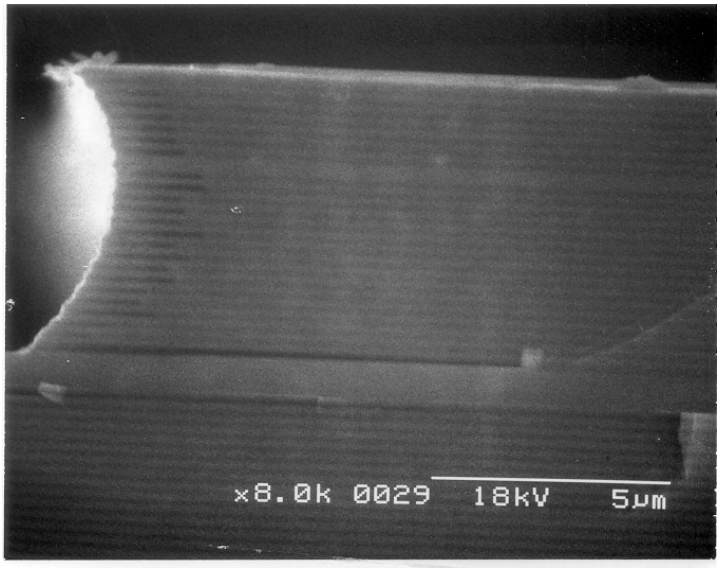

Figure 4.05. Sidewall profile of etch pillars using photoresist as etch mask and etch gases of 5:2.5:25 $SiCl_4$:Cl_2:BCl_3.

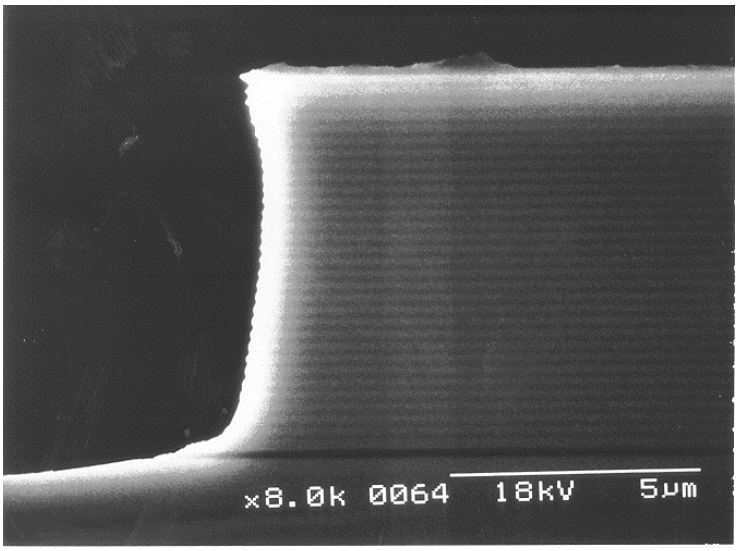

Figure 4.06. Result of etching sidewall in pure Cl_2 gas.

In either case, the etch was monitored with a HeNe laser reflection. A typical trace of the etching is shown in Figure 4.07. One can clearly see the periodicity of the reflection, corresponding to the periodicity of the mirror. At this etch power and chemistry, etching of InP is substantially slower than GaAs/Al(Ga)As. Conveniently, the reflectivity goes nearly to a constant value when one reaches the p-InP cladding.

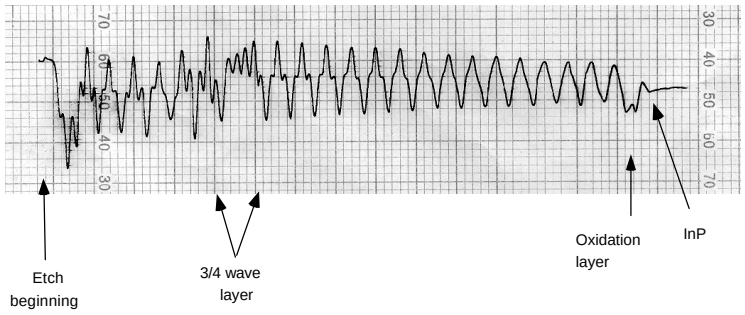

Figure 4.07. Laser monitor power for RIE etch.

For the n-intercavity design, one needs to eventually to expose the n-InP cladding layer. This can be done through a separate wet-etching step with a separate mask or directly in the RIE by changing the etch conditions. If one uses the same gas flows for the $SiCl_4$:Cl_2:BCl_3 etch chemistry, and increases the RF power to 300 Watts then InP and InGaAsP are etched at ~100 nm/min. This allows for a very simple method to get to the n-InP layer. If, however, one

wanted to fabricate photodetectors or LEDs in the same fabrication steps, one would use a separate mask for the etch through the p-InP and MQW. One can make such devices by leaving portions of the active region unetched in the field. If one places a metal contact in these areas of the field, which will be done anyway for the VCLs, then one can make detectors by reverse-biasing these contacts, or LEDs by forward-biasing. Either way, there must be a section of the field next to devices that have the n-InP exposed so that a contact can be placed there later. We found, though, that it is highly preferable to reach the n-InP layer through continued etching in the RIE machine because the latter allowed for much more reproducible oxidation depths as described in the following section.

4.05 Lateral Oxidation

Once the photoresist is removed for the etch step, one needs to do the lateral oxidation whereby nitrogen is bubbled through a heated bath of water before being injected into the modified furnace. The idea behind this step is that AlAs can be oxidized at certain temperatures and conditions, resulting in a high quality stable oxide[4]. The oxide turns out to be more structurally stable if the original layer is not pure AlAs but, rather, contains a small percentage of

Gallium[5]. This small percentage of Gallium also results in a much reduced oxidation rate, about half the rate for every 2% of Gallium introduced[5]. The original double-fused laterally-oxidized devices did not have Gallium incorporated into the oxidation layer, resulting in a very difficult control of the oxidation depth. All the subsequent generations used a $Al_{0.98}Ga_{0.02}As$ layer for oxidation. Even with this step, for most of the device generations, the oxidation process was the least controllable and reproducible process. In the last two generations, we were able to control the oxidation process with a change in the pillar etching. Typically, calibration of the oxidation rate could be done with a portion of the p-mirror. One simply cleaves a portion of the p-mirror from the same epi growth as the sample. The sample with the fresh cleaved interface is then placed into the furnace. Several times and conditions can be calibrated to get the desired oxidation depth. Since the oxidation layer is so close to the surface and causes such a large index change, one can directly see the oxidation in a optical microscope and therefore measure the oxidation depth. The oxidation depth versus time usually gives a linear relationship with reasonably shallow oxidation depths(<30 μm). Past a certain depth, the oxidation depth starts to take on a squareroot dependence with time[6]. Figure 4.08 shows a typical plot of the oxidation depth versus time in furnace.

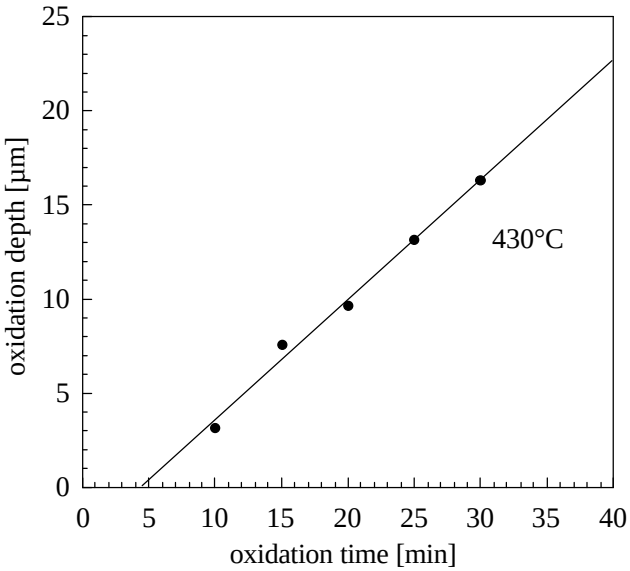

Figure 4.08. Typical oxidation depth versus time in furnace. Water temperature was 80°C, and flow was 5 sccm of N_2.

Interestingly, the oxidation rate versus time line usually does not intersect the origin. There always appears to be some significant turn on time before the oxidation begins. The origin of this turn on time is likely to relate to some chemical reaction on the surface of the oxidation layer. There may be some native oxide that must be broken through before the "good" oxidation proceeds.

Using the test samples, one gets relatively reproducible curves of the oxidation depth versus oxidation time. The problem that continually arose was that the oxidation depth in the real VCL samples did not match up to the calibrated curve. Many times, this resulted in too little oxidation of the pillars.

The next chapter describes generation C devices where exactly this phenomenon occurred. If one tries to compensate for too little oxidation in the real sample, there is a risk that all the devices will be closed off by the oxidation, destroying the sample.

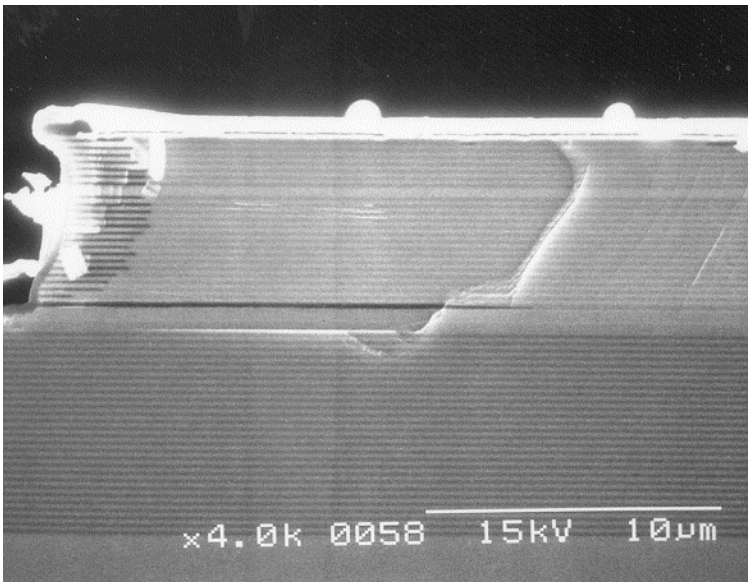

Figure 4.09. Example cross-section SEM to measure oxidation depth.

There have been several runs where as much as a factor of two times difference in the oxidation rates was observed. For earlier generations, the real double-fused samples usually oxidized slower than the calibration samples. One may attribute the reduced oxidation rate to the fusion process, but for some runs there was a match with the calibration curves. One option for calibration was to use a portion of the real laser sample. However this resulted in a large loss

of area to an already small sample of 8x8 mm. And, in processing two identical sets of samples with very similar processing procedures, you do not always get the same oxidation depth in the two samples.

These issues were further complicated by the challange of determining the oxidation depth on an actual laser sample. Unlike the fused sample, the oxide in the calibration samples is buried below the thick p-mirror preventing the use of a standard optical microscope. One alternative technique is to use an infra-red microscope to see through the mirror, but it is often very difficult to see the oxidation front, especially with very thin oxide layers. Another method is to probe the devices electrically and see which diameter devices do not pass current. To do this, though, the SiN_x on top of the p-metal must be removed in order to probe. Finally, the most reliable method to determine the oxidation depth is to cleave across a bar on the wafer, and look for the oxide through cross section SEM. An example of this can be seen in Figure 4.09. Doing cross section SEM also forces the wafer to be cleaved into smaller pieces, but to reliably get the oxidation depth this method was necessary.

A commonly posed solution to combat the oxidation problem is to do the oxidation in small increments until one gets the correct depth. Unfortunately, this idea does not work, because once a sample has been in the oxidation furnace, the results of further exposure are unpredictable. Many

times the wafer will not oxidize any further regardless of how long it is in the furnace, and other times it will continue to oxidize at the normal rate. There have been several papers on this effect[7]. For the first several generations, we were at a loss as to how to control the oxidation depth. The only effective method I found to combat this problem was to have a large array of device sizes, such that there were a wide range of oxidation depths that resulted in reasonable size devices. To this end, the mask I designed had pillar diameters varying from 30 μm to 66 μm in steps of 1 μm (36 different diameters). This, of course, took up more area on the wafer, meaning less devices of the best diameter per wafer. It was only in the final two generations that we began to understand the problem with the oxidation reproducibility.

As described in the RIE etching section, one can choose to etch the device pillar all the way to the top p-InP layer, or change RIE etch conditions and go all the way to the n-InP layer. For all the earlier generations, the etch was stopped on the p-InP layer(we did not know yet that we could change the etch condition to etch InP as well). The oxidation layer was very close to the layer the RIE etch stops on, namely the p-fused junction. Due to nonuniformities in the RIE etching, a shoe formed at the bottom the pillar. In the first several generations, the oxidation layer was right at the base of this etch shoe. The chemistry of the shoe layer may block or slow down the lateral

oxidation for some samples. Note that the shoe layer may be different for different samples depending on the exact etch times used. This might explain the variations between what were supposed to be identical samples. In the final two generations, the RIE etching was taken all the way to the n-InP layer. In this case, the oxidation layer was 40-60 nm away from the final layer of the etch. This distance is larger than the typical etch shoe height. For the last two generations of devices, the oxidation depth was quite controlled and matched up well with calibration samples. Further study must be done before one can definitely say that the etch shoes was the problem, but it seems highly likely that it is at least a contributing factor.

4.06 Bondpad Metal Formation

With the oxidation process complete, the next step is to remove the SiN_x from the top of the pillars. This can be done directly without any mask using CF_4 etching of the SiN_x. One can then probe the p-metal to test for the contact resistance. This is done using a TLM pattern with variable gap spacings where typical contact resistances are on the order of $5\ 10^{-5}\ \Omega cm^2$.

At this point, there is an optional processing step to reduce the capacitance of the final device. If the bottom mirror is semi-insulating, then it

will reduce the p-bondpad capacitance significantly if one etches away the doped n-InP below the pad. If one simply uses SiN_x as the isolation of the p-bondpad to the n-InP, then the result will be a large capacitance to the device. The etching is accomplished by masking off everything but the region of the p-bondpad, using AZ4330 resist, and wet-etching the InP to the GaAs layer. A thick resist is used to make sure the sidewall of the pillars are completely covered and are not etched during this process. If the bottom mirror is doped or one is not interested in very high speed modulation, there is no reason to do this step. To save time and to minimize error, this step was usually omitted.

To allow for a connection from the p-bondpad to the top of the pillars some sort of isolation/bridge layer must be used. There are several possibilities for such a bridge including a PMGI or air bridge. Since the lead from the bondpad to the pillar will cover a relatively small area, the bridge layer does not need to have an ultra low capacitance per unit area. Low capacitance can be achieved by having a thick layer of a low dielectric material. In all the relevant device generations, SiN_x was used as the bridge layer as it was determined that it would allow the easiest and most robust fabrication. PECVD deposited SiN_x has a relative dielectric constant of about 4-5, which is reasonably low. One, however, cannot deposit very thick layers of SiN_x without cracking. To avoid cracking and pinholes, two separate depositions of 200 nm each were applied to

the wafer. Openings must then be etched in the SiN_x layers in order to make contact to the device. AZ5214 resist is used to mask off the areas where SiN_x should remain. The etching of the SiN_x is done in CF_4 plasma as described earlier. With the holes in the SiN_x etched, the resist is removed, and one can begin the lithography for the final metal deposition.

The final deposition of metal serves three purposes: 1) the p-metal bondpad 2) the connection bridge between the p-metal and bondpad metal, and 3) the n-metal contact. One can choose from a relatively wide variety of metals to make Ohmic contact to n-InP. We choose Ti/Au for this function because Ti/Au can also be used as a bondpad metal as well as a good interconnect metal. The proper execution of this deposition and liftoff can be difficult as there are several complications to this lithographic and deposition process. The most obvious problem is the need for the metal to go up the pillar sidewall to act as an interconnect layer. Uniform coverage of the sidewall of the pillar can be achieved with an angled fixture. In this way, the deposition metal is directed at an angle to the substrate. Of course, if one wants to cover all different angles of the pillar, as would be necessary with a round pillar, rotation of the fixture is necessary. We used an angled rotation stage in an e-beam evaporator to fabricate the device with bondpad metal. Yet, the problem with this angled evaporation is that it makes liftoff much more difficult. This

problem can be seen in Figure 4.10. An angled evaporation does not allow for a clean break of the metal pattern. This liftoff problem is exacerbated by the fact that a relatively thick metal must be evaporated. Typically, this metal must be a least 500 nm thick to allow for ease of wire bonding.

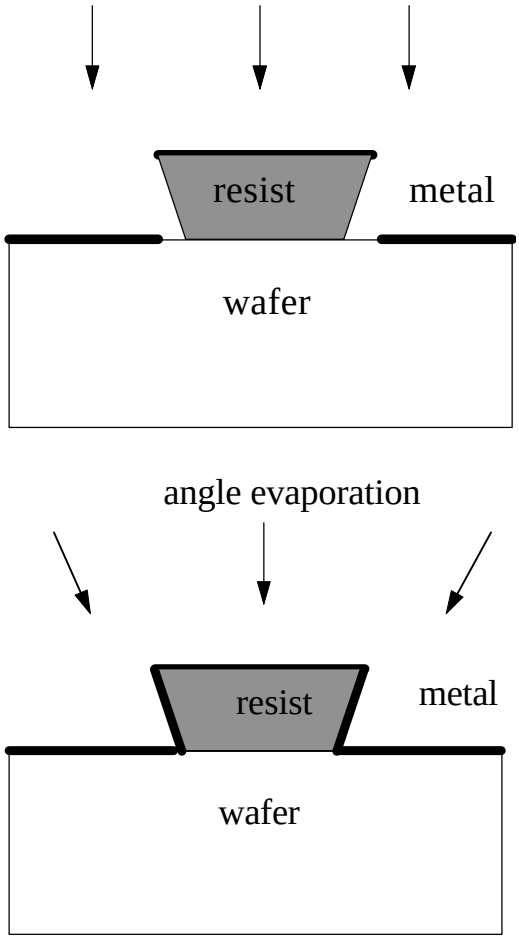

Figure 4.10. Liftoff using angle and regular evaporation of metal.

In order to achieve a clean liftoff with these conditions, the resist profile must be tailored to have a large undercut. To do this, one can use a two-layer resist pattern. The bottom layer is exposed everywhere while the top layer is exposed only where one wants the metal. The developer penetrates the top layer only in selective areas, and then starts to develop the bottom layer which is exposed everywhere. This results in an undercut as depicted in Figure 4.11. This simple two-layer resist process works well on a planar surface, but we have the further complication of the 7-μm tall pillars. Metal needs to be lifted off in the field as well as on top of the pillars(so that power can get out the top). The natural resist profile on top of tall pillars is contrary to the resist profile necessary for liftoff. But we have found that if the mask is designed such that the areas around the edge of the pillars are developed, then the liftoff can still be accomplished. To do this, the interconnect layer must go all the way around the edge of the pillar, rather than the simple wire connection.

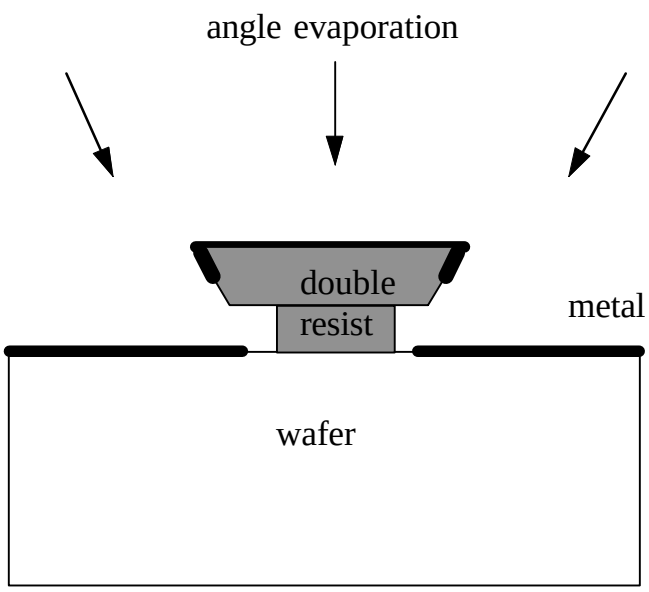

Figure 4.11. The use of a double-layer resist may facilitate liftoff of an angle evaporated metal.

The final trick necessary to making this process reliable is reducing the evaporation angle from the standard 45° to closer to 20°. In doing so, one allows for easier liftoff due to the reduced deposition on the sidewalls of the resist. This, of course, also reduces the thickness of the interconnect metal on the pillar sidewall. However, one only needs a thick metal in the field and not on the sidewall. For example, if one chooses a 20° angle evaporation and wants 500 nm in the field for bonding, there is still 180 nm(500 nm * tan(20°)) of metal on the sidewall. The reduced angle evaporation greatly improved the yield of devices after it was incorporated. Reducing the angle of evaporation can cause open circuit devices if one is not careful. If the sidewall profile of the

pillar is such that there is an overhang of material, the metal interconnect layer can be disconnected. In the RIE section of this chapter, we discussed methods to achieve a straight sidewall profile such that there is no significant overhang.

Finally, Figure 4.12 shows an SEM image of a completed device, and Figure 4.13 shows the schematic structure of this device. This final structure evolved over several generations of processing to this final point. In the next chapter, we will go over the device characteristics that drove the design towards this structure.

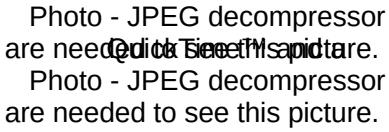

Figure 4.12. SEM picture of completed double-fused top-emitting long-wavelength VCL.

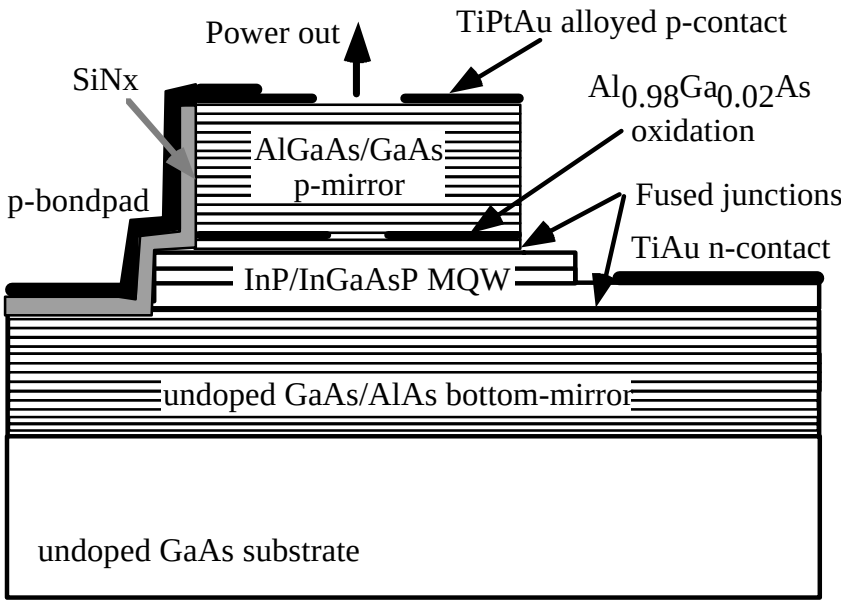

Figure 4.13. Schematic diagram of final generation of 1.5 μm VCLs.

4.07 References

[1] J. Piprek, Y. A. Akulova, D. I. Babic, L. A. Coldren, and J. E. Bowers, "Minimum temperature sensitivity of 1.55 μm vertical-cavity lasers at -30 nm gain offset.", Appl. Phys. Lett., vol.72, 1814 (1998).

[2] J. Ko, E. R. Hegblom, Y. Akulova, N. M. Margalit, and L. A. Coldren, "AlInGaAs/AlGaAs strained-layer 850 nm vertical-cavity lasers with very low thresholds.", Elect. Lett., vol.33, 1550 (1998).

[3] M. Grabherr, R. Jager, R. Michalzik, B. Weigl, G. Reiner, and K. J. Ebeling, "Efficient single-mode oxide-confined GaAs VCSEL's emitting in the 850-nm wavelength regime.", IEEE Photonics Technology Letters, vol.9, 1304 (1997).

[4] J. M. Dallesasse, N. Holonyak Jr., A. R. Sugg, T. A. Richard, and N. El-Zein, "Hydrolyzation oxidation of Al/sub x/Ga/sub 1-x/As-AlAs-GaAs quantum well heterostructures and superlattices.", Appl. Phys. Lett., vol.57, 2844 (1990).

[5] K. D. Choquette, K. M. Geib, C. I. H. Ashby, R. D. Twesten, O. Blum, H. Q. Hou, D. M. Follstaedt, B. E. Hammons, D. Mathes, and R. Hull, "Advances in selective wet oxidation of AlGaAs alloys.", IEEE Journal of Selected Topics in Quantum Electronics, vol.3, 916 (1997).

[6] R. L. Naone, E. R. Hegblom, B. J. Thibeault, and L. A. Coldren, "Oxidation of AlGaAs layers for tapered apertures in vertical-cavity lasers.", Elect. Lett., vol.33, 300 (1997).

[7] H. Lim Dae, G. M. Y a n g, K. Jong-Hee, Y. K. Lim, and J. H. Lee, "Sealing of AlAs against wet oxidation and its use in the fabrication of vertical-cavity surface-emitting lasers.", Appl. Phys. Lett., vol.71, 1915 (1997).

Chapter 5

Device Results and Analysis

5.01 Introduction

In this chapter I go over many of the results from several generations of device designs. Progressive generations are differentiated by major structural changes. Thus, a single generation or fabrication run can have several distinctive permutations. Through the generations presented, one gains an overall picture of the tradeoffs involved in the design of long-wavelength VCLs. Throughout this chapter I build the argument that wafer fusion is critical to device performance. This contention stands in stark contrast to early thoughts that the fused junction plays a very minimal role in the final device performance. I have chosen to present the device generations in chronological order to provide the strongest evidence for the final conclusion in this chapter. At the

end, I also include a short overview as to what was learned from each relevant generation. The ultimate goal of our research was to achieve a VCL that best matched the conditions outlined in Chapter 1 for a commercial device. The extent to which this goal has been met can be determined by this chapter as well as Chapter 6.

5.02 Generation A -- the First 64°C cw Operation

The first project that I embarked upon was to take the Babic laser structure that lased to 33°C cw, and to make an incremental improvement by introducing an oxide aperture into the device. This seemed like a relatively modest goal in that I could just take the p-mirror designed by Babic and add an oxidation layer for current constriction. This was done by simply replacing the last quarter-wave layer of AlGaAs with AlAs. This would reduce the scattering losses from the pillar sidewalls, allowing for much smaller low-threshold devices.

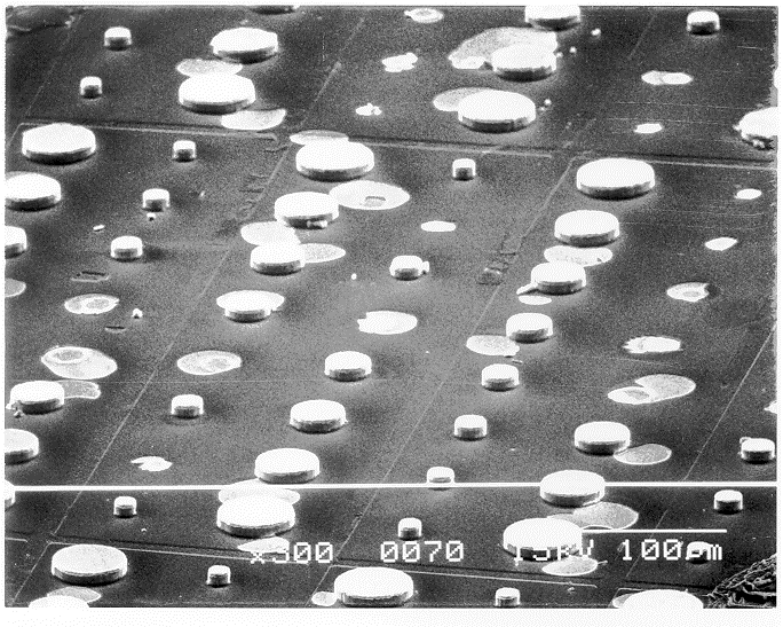

Figure 5.01. SEM picture of first working oxide VCLs showing many devices missing.

Of course, seemingly simple steps may become complicated. The Ti/Au top metal reflector was destroyed in the oxidation furnace. To overcome this problem, the process had to be rearranged such that this metal layer would be placed at the end instead of the beginning of the fabrication process. This meant using a dielectric etch mask instead of the usual Ni one. This also allowed for the alloying of the n-contact separately from the p-contact(a minimal improvement). However, this minimal improvement of alloying the n-contact removed nearly half the devices on the wafer. Figure 5.01 shows a typical picture of the wafer. The new oxide layer made the pillar unstable

during high-temperature processes. In addition, the oxidation process was incredibly difficult to control as the oxidation rate was very fast. With trial and error, though, some devices were eventually made.

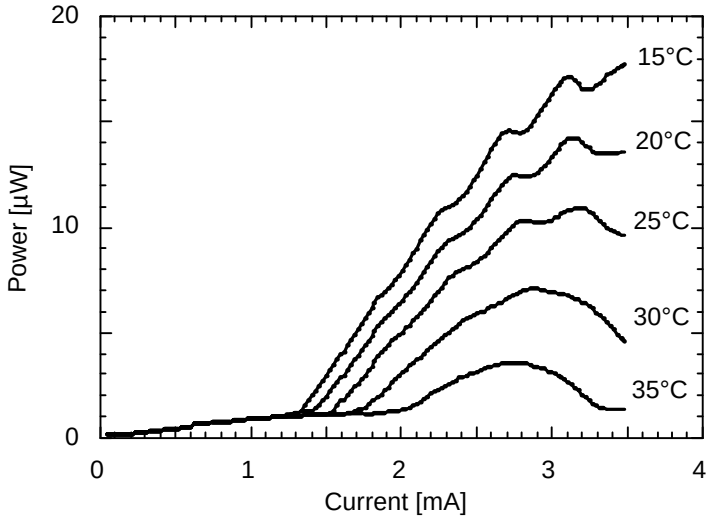

Figure 5.02. L-I curves from the first working 1.5 µm oxide confined VCLs.

The performance offered an incremental improvement over previous devices in terms of threshold currents(1.3 mA cw) and maximum cw operating temperature(39° C)[1]. Figure 5.02 shows the best L-I curves taken from this wafer. The efficiency from these devices was quite small ~1%, and the threshold voltage was quite large ~ 6 V. With no other explanation in sight, the low efficiency was blamed on scattering loss from the aperture, and the high voltage was blamed on poor mirror growth.

These original laterally-oxidized lasers offer a lead-in to explaining what was done with the first set of important devices(Generation A). The basic lessons learned from this first set of devices was that we needed a more stable oxide, a more controllable oxidation process, and reduced index perturbation by the oxide. These were all elements that appeared to be easily fixed. Through interaction with several sources, it became clear that using some Ga in the oxidation layer significantly reduced the oxidation rate, as well as improved the structural stability of the oxide. This was later written up in a paper[2]. To this effect, we decided to use a 98% Al layer instead of a 100% Al layer as the oxidation layer. We were still concerned about the scattering losses that might occur due to oxide, as described by Hegblom[3]. As demonstrated in this APL by Hegblom, one could reduce the impact of the oxide by either making the oxide very thin, or by placing it near a standing-wave null. We had not yet considered the impact of too little index perturbation, so we did both, resulting in an effective index perturbation as described by Hadley[4], of Dn=0.002. This is an extremely small value for a guiding index. These lasers were probably gain-guided instead of index-guided. The final result of these discussions was to design the p-mirror very similarly to the one before, but using a thin oxide, near a null, as the oxidation layer. Figure 5.03 shows the basic device structure, whereas Figure 5.04 shows a cross section SEM of this structure.

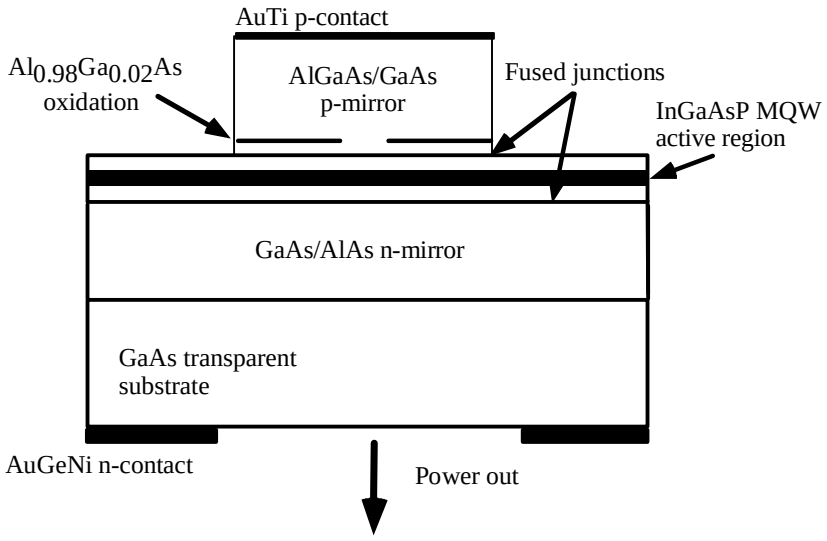

Figure 5.03. Schematic of generation A devices.

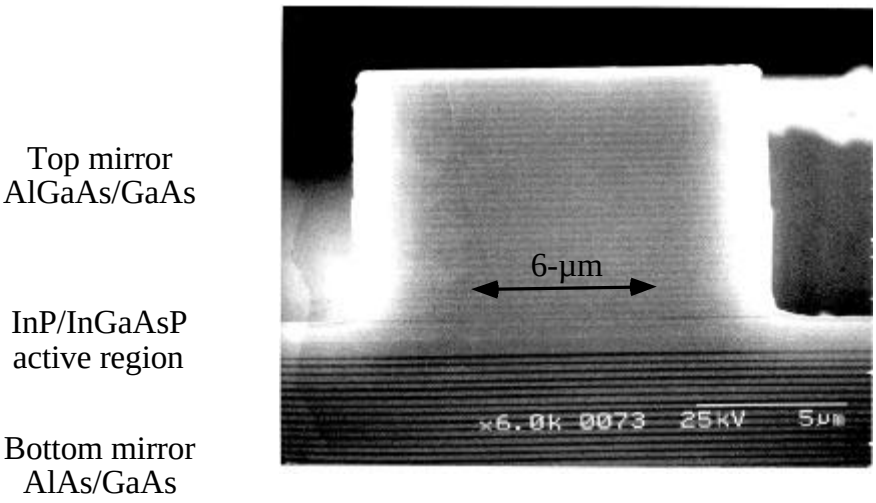

Figure 5.04. Cross section SEM of generation A devices.

Surpassing our expectations, these steps resulted in substantial improvements. The devices performed much better than any devices had

performed before. Ironically, these devices, in a couple of respects, are still better than the many subsequent device generations. The maximum cw operating temperature was 64°C, as is shown in Figure 5.05. The lowest threshold currents were below 1 mA as shown in Figure 5.06.

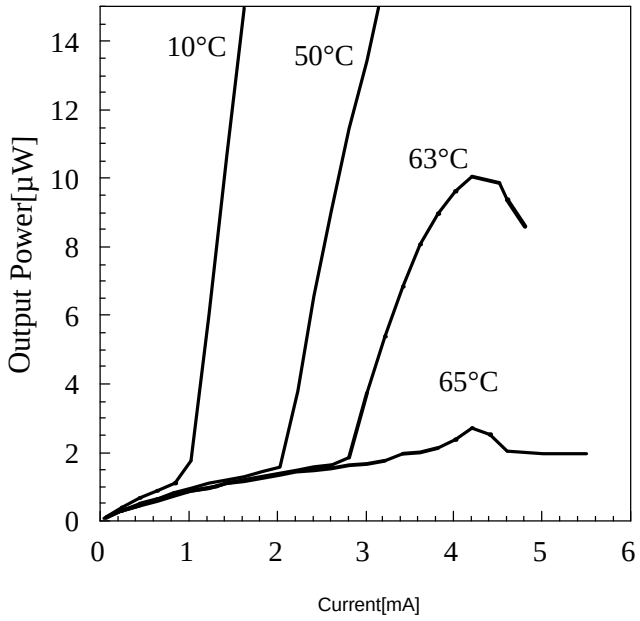

Figure 5.05. L-I curves showing 64°C cw operation.

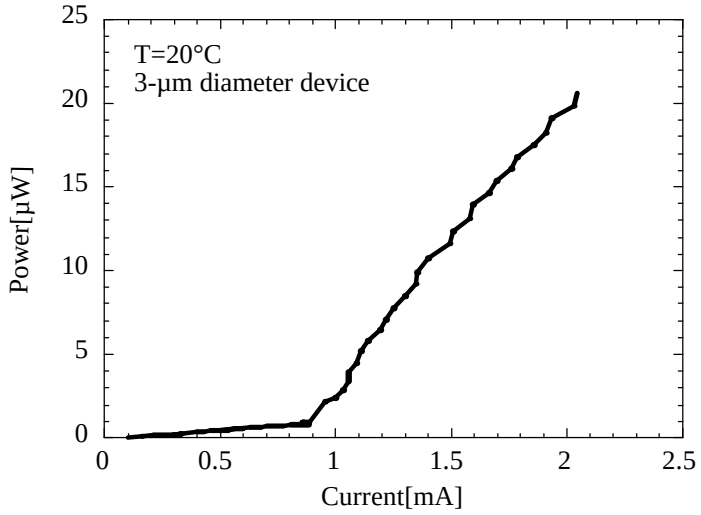

Figure 5.06. Submilliamp pulsed threshold currents as low as 0.8 mA.

There were other important characteristics of the devices that were very encouraging. We were back at the 4-5% range of differential efficiency that we expected for non-oxidized devices[5]. Even more interesting was that we had kept the same differential efficiency for device sizes as low as 3 μm to as high as 30 μm. This was indeed a very significant result in that this meant we had virtually no size dependent scattering losses. We had hoped that by eliminating these scattering losses that the threshold current would also scale with the oxide aperture. These measurements were taken before we had done the analytical work on leakage current. We thus concluded, very logically, that if the differential efficiencies were constant then there could not be much current lost around the aperture. We had not yet considered the possibility that the leakage

current could be clamped at threshold. It was later, with these results, that Hegblom and I tried to calculate the contribution of leakage current below and above threshold, leading to the analysis described in Chapter 2. Figure 5.07 shows the measured room-temperature pulsed threshold current versus oxide-opening diameter. We also plot on this graph what the threshold current would be for a constant 1 kA/cm^2 threshold current density. The placement of the constant current density line very much depends on the oxidation depth. If the oxide depth is 2 μm larger or smaller than anticipated then the line would be shifted over by that amount. For this reason, it was vital to determine the correct oxide depth. With such a low index perturbation, one could not determine this depth from the mode spacing, or use an infrared microscope. In addition, with relatively low powers, it would be very difficult to align a near-field measurement. The chosen method that gives the highest accuracy was the use of cross-section SEM as described in the fabrication chapter. This, of course, destroyed much of the sample as several attempts were needed to cleave through a center of a device. This process was done after all the testing was complete, and the resultant oxidation depth we measured was 4 μm +/- 0.5 μm. This was a relatively shallow oxidation, which we will later see becomes a defining feature of this generation of devices. However, even with no knowledge of the oxidation depth, the threshold current did not scale very well

with the device area. On a log-log plot, proper scaling of threshold current density clearly would be a straight line with a slope of 2. To explain this lack of scaling, we introduced the leakage current problem, and thus the leakage current model.

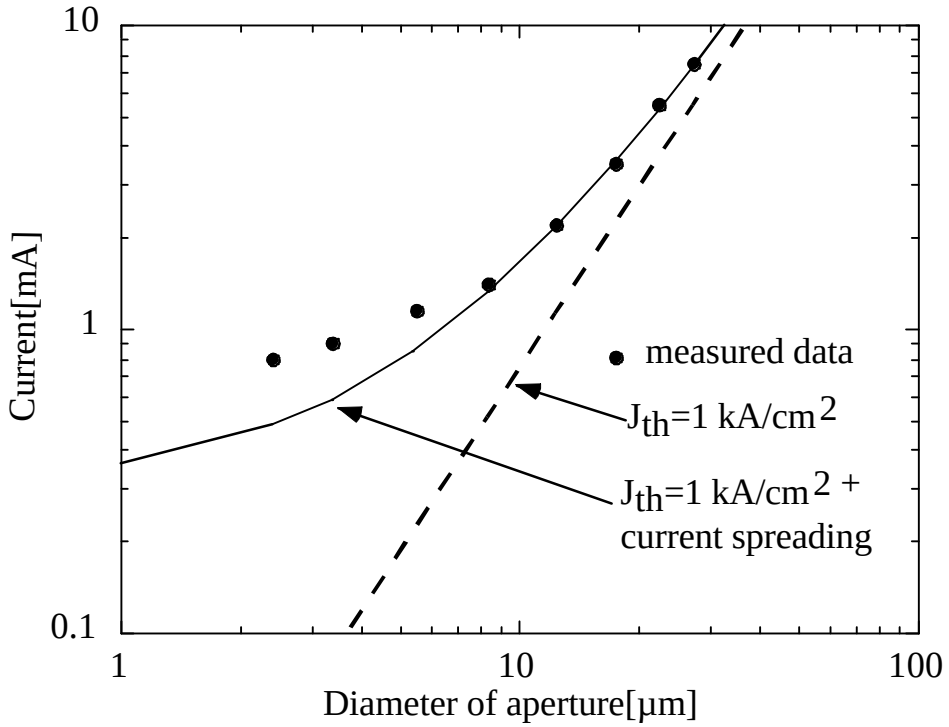

Figure 5.07. Pulsed threshold current versus oxide-opening diameter.

Figure 5.07 also shows a fit to the threshold currents using the leakage current model described in Chapter 2. The leakage current parameter I_0 for this fit is 400 μA. This appeared to a good fit, especially for larger diameters. We tried to estimate this leakage current parameter to see if it would be reasonable for

the aperture we had. Indeed, if one assumed all the leakage occurred in the much thicker InP region, then one could extract from the fit an effective mobility of 60 cm^2/Vs for the current spreading layer. This mobility is about 30% lower than the normally quoted value of 10^{18} -cm^{-3} p-doped InP. This value was reasonable, as one would expect the fused junction to reduce the mobility in the adjoining layers. This analysis, though, depended on the seemingly innocent assumption that most of the current spreading was in the InP region. It turned out that this surmise was fairly accurate for this generation of devices, because of the very shallow oxidation depth, but in subsequent generations this assumptions would be invalid. The data from the generation A devices provides the strongest evidence for the conclusions of the leakage current model, namely that the leakage current is clamped above threshold. How else could the efficiencies of the devices remain the same for all sizes, with clearly more relative current spreading for smaller devices? The difference between the dotted line in Figure 5.07 and the solid line represents the amount of current leakage there is at threshold for each device.

However, using this model, there still remained a very large deviation at very small diameters. This was a mystery, as we had no good explanation how the differential efficiencies of these devices remained high, yet the threshold current would not scale, even when taking into account leakage current. One

explanation could be that the leakage current model was not really describing the correct physical system. Nowhere in the model is there a fused junction, and even if it could be included, there were no measurements of the fused junction characteristics at the time. This explanation did not seem to be consistent with the fact that the model seemed to fit so well at the larger diameters. The next generation of devices gave the answer to this problem when near-field pictures were taken of the modal shapes.

With all of the good qualities of devices from this generation, there were still several problems that needed to be dealt with to make better devices. The first of these was that the output was still very low, even though it was significantly better than the previous best devices. Typical devices put out about 120-150 μW cw output power at room temperature. The Babic devices could only put out about 30-40 μW at 15°C. There was a two-fold effect that allowed for this increased output power. The most obvious one was that these lasers could operate at higher temperatures and therefore could be taken higher above threshold. The second effect was that the smaller diameter devices maintained the same differential efficiency as the larger devices, as discussed previously. This meant we had a high differential efficiency for the smaller devices which were the ones that could operate to higher temperature. The high-temperature cw Babic device was a relatively small device of 12 μm, of

which the differential efficiency was only 2%, compare to 4% for broad-area devices. These two effects, of course, were tied together. The higher efficiency, with the same output mirror, meant the losses were lower in the oxidized device. Lower losses meant there was less gain necessary, allowing for operation to higher temperature. Thus in this generation, with the shallow oxidation, the electrical and thermal resistance benefits of the oxidation were minimal. Instead, the reduction in loss played a great role.

Figure 5.08 shows the threshold voltage for the mean threshold voltage for generation A devices. The shape of the electrical I-V curves of these devices were nearly identical to the regular etch pillar devices of Babic. The threshold voltages were all between 3-4.5 Volts. The shape of this graph shows a decrease in threshold voltage with smaller diameter for the larger devices. This would seem contrary to the plot of threshold current density which shows a monotonic increase in threshold current density for smaller devices. This is where the oxide plays a role in reducing the voltage across the mirror. As the pillar gets smaller, for the same oxidation depth, the relative importance of the oxidation depth increases. The larger effective pillar reduces the resistance of the p-mirror. Eventually, of course, this improvement is swamped by the very rapid increase of threshold current density a very small diameters.

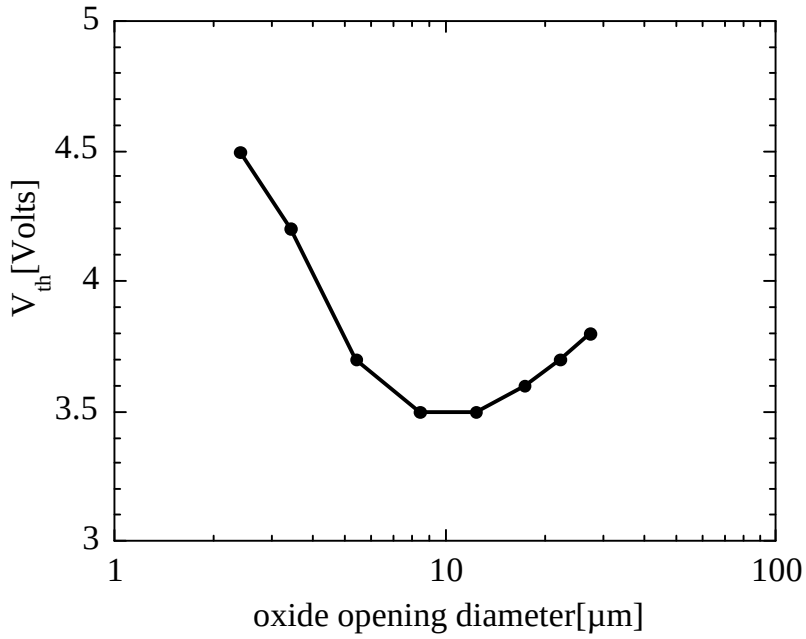

Figure 5.08. Mean threshold voltage versus diameter for generation A devices.

From the results in the fused junction chapter, one could conclude that about 1-2 Volts were across the mirror at threshold, with the rest across the fused junction and the active region. When analyzing these devices, however, we did not have the fused junction data yet, so all the excess voltage was assumed to be across the p-mirror. Increasing the oxide depth seemed like a great opportunity to greatly reduce the resistance of the device. Indeed, in subsequent generations, with deeper oxidation depths, the portion of voltage across the p-mirror became practically insignificant. The larger oxidation depth would also solve a practical problem with these devices, namely the very small

pillars were very difficult to probe. With pillar diameters of only 10 μm, many times the sharp probe would destroy the top mirror surface. This made much of the analysis very difficult and made system characterization almost impossible. So going from generation A devices to generation B devices, there were three primary goals. Number one was to increase the output power to useful levels. Number two was to reduce the voltage across the device. And, number three was to make the devices more "probe-able".

5.03 Generation B-- High-Power Devices

In many ways, generation B devices are very similar to the generation A devices. Both use the same top mirror, same active region, and same structure. There are, nevertheless, two primary differences that significantly affect the device analysis and performance. The first is that the oxidation depth was increased to 14 μm from 4 μm, and the second is that the output mirror allowed for much larger transmission. The idea behind these two steps was to increase the cw output powers. The increased oxidation depth would reduce the electrical and thermal resistances, and the higher output mirror transmission would increase the differential efficiencies. Indeed, both of these improvements came into play as the output powers were greatly increased. But there seemed

to be some new effect greatly increasing the threshold currents. Figure 5.09 shows the plot of threshold current for generation A and B devices. We will next try to understand what caused this increase in the threshold currents going to generation B devices.

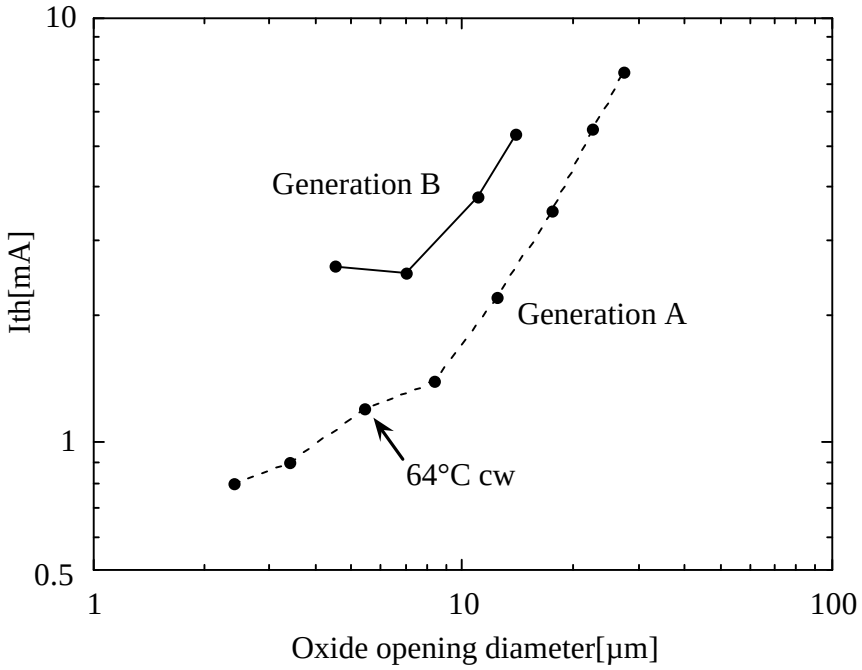

Figure 5.09. Room-temperature pulsed threshold current for generation A and B.

Table 5.01 shows a detailed comparison of the two device generations. Looking down the table one sees that the increased transmission has dramatically increased the differential efficiencies of the devices, and also increased the threshold gain value. Could this be the reason for the increase in threshold currents? At first glance, one might think so, yet a simple analysis

reveals otherwise. Since these two generations use the same epitaxial wafer as the Babic structure, we have significant information on the gain curves from these active regions.

	Generation A	**Generation B**
p-mirror	30.5 period $GaAs/Al_{0.67}Ga_{0.33}As$	same epitaxial wafer
Active region	7 strain-compensated InP/InGaAsP QWs	same epitaxial wafer
n-mirror	28 period AlAs/GaAs	24 period AlAs/GaAs
Oxidation depth	4 μm	14 μm
Mode wavelength	~1548 nm	~1542 nm
PL wavelength	~1550 nm	~1550 nm
Max. cw operation	64°C	52°C
Threshold voltage	3.5-4.5 Volts	2.7-3.5 Volts
Lowest threshold current	0.8 mA	2 mA
Best cw power @15°C	150 μW	1 mW
Typical cw power @15°C	100 μW	400 μW
Transmission through mirror	0.07 %	.25 %
Transmission through substrate	70%	70%
Internal efficiency-- η_i	~80%	~80%
External efficiency-- η_d	~4%	~12%
$G_{th}=L+T=\eta_i/\eta_d *T$	1%	1.15%
Round-trip Loss-- L	0.93 %	0.91 %

Table 5.01. Detail comparison of generation A and B devices.

Equations 5.01 show the gain current density relationship measured in Babic's thesis for the same quantum well in generations A and B. These equations are by no means exact and they depend on many factors such as the gain peak, mode position, and temperature, but they do provide a rough estimation of the gain curve for the conditions we are interested in.

$$G \approx G_o \ln\left(\frac{J}{J_o}\right) \approx 1.5\% \ln\left(\frac{J[kA/cm^2]}{0.5 \cdot kA/cm^2}\right)$$
$$J_{th} \approx 0.5 \cdot kA/cm^2 \exp\left(\frac{G_{th}}{1.5\%}\right) \qquad (5.01)$$

We can analyze what happens to the threshold current density as the threshold gain goes from 1% to 1.15% as in the case from generation A to B. In this case, the threshold current density increases from ~1 kA/cm^2 to ~1.1 kA/cm^2. This is only a 10% change in the threshold currents. What is actually observed is over a 100% increase in threshold currents. Clearly, even if our calculations

are only estimates, the increased mirror transmission could not account for such a large increase in the threshold currents.

So the question remains as to what causes the increase in threshold currents from generation A to B. The epi-layers are essentially the same. If the new mirror had a higher loss, this would be seen in the differential efficiency. Before addressing this mystery, let us first look at a comparison of the *J-V* characteristics of the two generations. Figure 5.10 shows the measured *J-V* characteristics of 7 and 8 μm oxide-opening devices from generations A and B. Generation A device is only oxidized 4 μm in from the sidewall, so its pillar diameter is 16 μm. Generation B device(7 μm opening) is oxidized 14 μm, so the pillar diameter is 35 μm. The currents are divided by the aperture area to give current densities. What we first see is a huge improvement in the *J-V* characteristics of the deeper oxidation. Indeed, if one wants high-power devices what is relevant is not what the voltage is at threshold, but rather at the peak power point. The peak power point is many times above threshold, where we have the most improvement. At 4 Volts bias the shallow oxidation is only at 2 kA/cm^2 whereas the deeper one is all the way at 10 kA/cm^2.

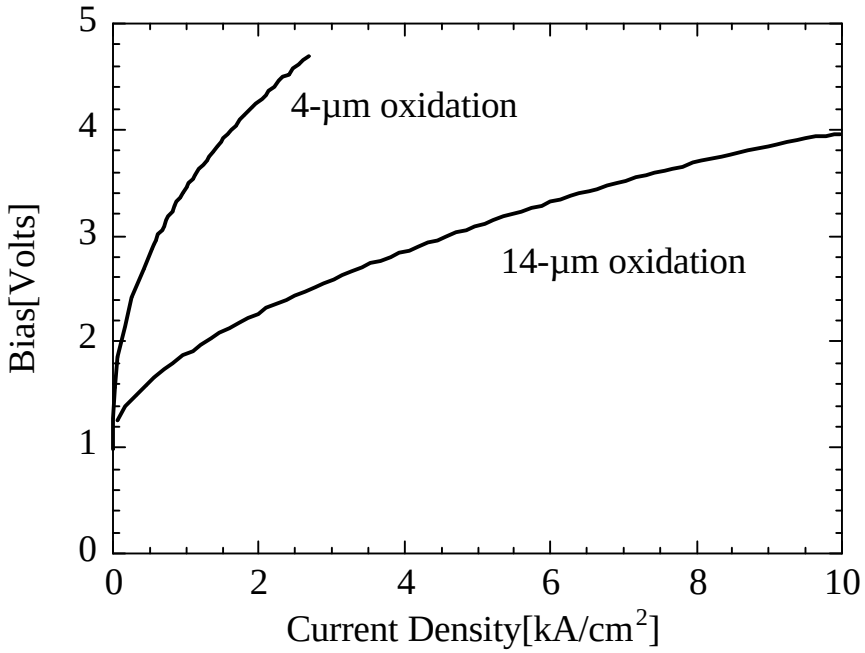

Figure 5.10. Comparison of J-V characteristics of deep versus shallow oxidation.

The reason for the improved *J-V* characteristics is simply the effect described in Chapter 2, in which deeper oxidation allows for a greater area for the current to flow through. When one looks closely at the *J-V* curve shown in Figure 5.10 for the 14 µm oxidation, something strange should be evident. The *J-V* curves in this plot are better than any of the curves described in the fusion chapter. It appears as if the turn-on voltage of the fused junction/active region combination is only about 1.4 Volts. Did somehow the laser run have a better fusion than all the tens of fusions we had tested? The answer, obviously, is no.

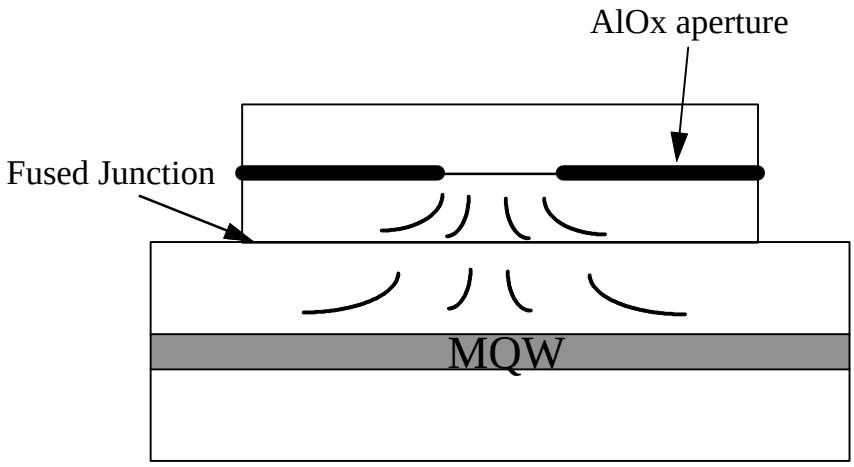

Figure 5.11. Schematic close up of area near oxide aperture.

Figure 5.11 shows a schematic close up of the area near the aperture in the VCL. One can see that there is a region between the aperture and the fused junction where current can spread. The high resistance of the fused junction to holes forces the current to spread past the aperture. This means that the effective current density at the aperture and at the fused junction are not necessarily the same. Since the current spreads to a larger area, the effective current density is lower than simply dividing the total current by the aperture area. As the current density gets larger, and the device eventually lases, the differential resistance of the fused junction/MQW diode becomes very small. This means no extra current spreading is occurring. This is how the differential efficiencies are maintained. The *J-V* curve shown must be distorted to get the

real *J-V* curve of the 1-D fused junction and active region. At low-current densities, the area is actually larger, effectively compressing the x-axis. If one draws a straight line from the region of high-current density to the y-axis, you get a turn-on voltage of about 2 Volts, consistent with the results in Chapter 3.

We can now return to the question of why the threshold currents in generation B devices were so much larger than in generation A. The big difference between the two generations is the oxidation depth. With the generation A devices the oxidation depth was only 4 μm, so the current could only spread 4 μm out before being forced to cross the fused junction. Some further spreading can occur in the InP, but since the current is already somewhat spread out, this effect is limited. In the case of the generation B device the current could spread out to 14 μm past the aperture before being forced to cross the fused junction. This is indeed a very big effect. Let us assume a 8 μm active region diameter, then the ratio of the pillar area between the two cases is a factor of 5 meaning there is five times more area for the current to spread in the case of the generation B devices. This explains the much larger thresholds in this case. How much, however, can the current really spread? This is difficult to estimate as there is great uncertainty as to what the band diagram and mobilities look like very close to the fused junction.

One way to get a qualitative idea of how much current spreading is occurring is to look at the near-field patterns below and above threshold. With this set of lasers the output powers are quite high so that aligning a near-field camera to the devices was not difficult. Figure 5.12 shows a typical near-field scan of the generation B devices above threshold. To get a scale as to how big the spot size is, we can look at the near-field pattern below or at threshold. Figure 5.13 shows the near-field pattern at threshold. We see that there is a bright central region where the lasing profile will occur, and we also see a fainter region of spontaneous emission around the central lobe. In fact, there is spontaneous emission all the way to the pillar sidewall. This could mean that significant carriers are spreading around the aperture and recombining radiatively all the way to the pillar sidewall.

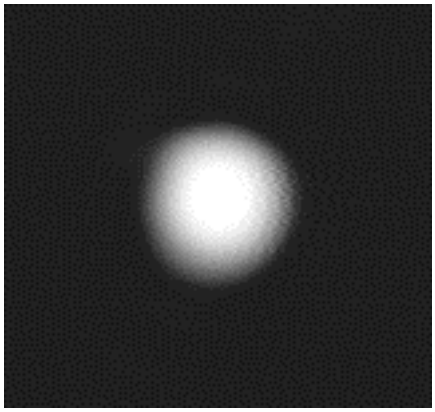

Figure 5.12. Near-field pattern well above threshold.

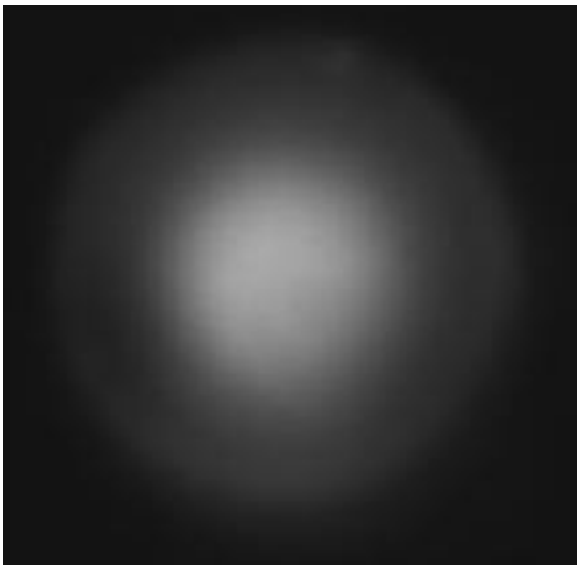

Figure 5.13. Near-field pattern at threshold.

One does not see the spontaneous emission in the Figure 5.12 because the camera is adjusted to the much higher power of the lasing mode. It does not have the dynamic range to both not saturate the lasing mode and still see the spontaneous emission. Many times in the near-field pattern we could see the pillar sidewall where we could pick up a greater angular spectrum of the spontaneous emission. This meant that we could get a relatively accurate scaling factor for the near-field pictures. We could now compare the near-field pattern to the aperture diameter. What we observed was a very interesting phenomena. The near-field patterns of the smaller devices did not scale with aperture diameter.

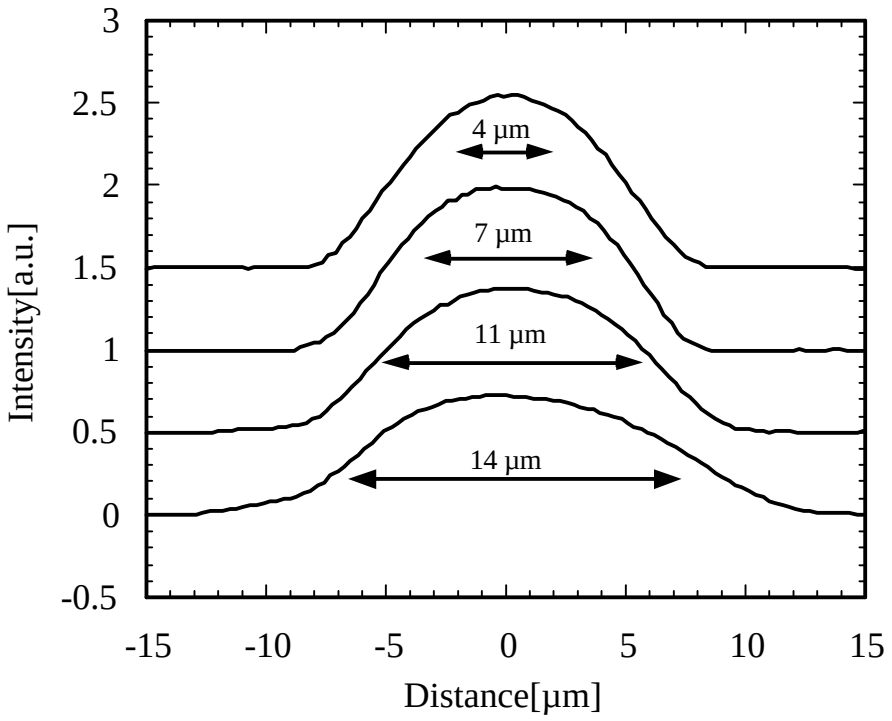

Figure 5.14. Near-field comparison of four device sizes of generation B devices.

Figure 5.14 summarizes the results of the near-field experiments. We see that the mode full width at half maximum diameter does not get smaller than about 8 µm. Also observed was that the smaller devices were decidedly single-mode, whereas the larger were typically multimode. This issue will be taken up in the next chapter.

The obvious question arises as to why the near-field diameters do not scale with the oxide-opening diameters. The answer to this goes back to the description of the oxide thickness and position explained in the generation A

devices. These generation B devices also had the thin 20 nm oxide layer placed just 20 nm away from the first standing-wave null away from the fused junction. This oxide structure provides a very small index perturbation to the mode of only 0.002. The oxide does not confine the optical mode at smaller diameters. How does this lack of confinement affect the threshold current and efficiencies of these devices? What we know from in-plane laser analysis is that a reduction in the optical lateral confinement factor does not affect the differential efficiency of a laser. Indeed, we do not see such a reduction in our devices. What affects the efficiency of the devices is only the internal efficiency along with the ratio of loss to transmission of the mode. In our smaller devices the optical mode is nearly identical to the larger diameter openings, meaning the diffractive losses of the modes are very similar. The scattering losses for such a weak perturbation are very small so that each of the optical modes shown have very similar optical losses. The transmission through the mirror is also equal, so that if the injection efficiency is the same, then the differential efficiency should be uniform across the different device diameters. There is, however, a penalty for a reduced gain mode overlap. The modal gain from the active region is reduced by the optical confinement factor. The reduced modal gain must be compensated by an increased material gain to achieve lasing. The higher material gain means a higher threshold current density. These two effects that

come into play in determining the threshold current. Assuming a fixed optical mode diameter, a reduction in the current aperture diameter means a reduced area to pump a given current density, but, opposingly, it also means an increase in the threshold current density. This suggests that there is an optimum aperture to give the lowest threshold current. We can do a simple analysis to determine what that optimum might be.

Let us assume we have a fixed optical mode size of radius R and a current aperture of radius r_{ox}. The optical mode can be approximated by a cosine function since this best fits with the near-field data. For our analysis there is gain G present inside the aperture and none outside the current aperture. We also assume a logarithmic gain function as described earlier. The optical confinement factor G_{xy} is the overlap of the optical mode and the gain in the radial direction. We define a new symbol a which will be the ratio of the optical mode radius to the current aperture radius. The optical confinement factor can thus be written as follows...

$$\Gamma = \frac{1}{p^2 - 4} \int_0^{a_{ox}} a Cos^2\left(\frac{ap}{2}\right) da \qquad (5.02)$$

This integral has a relatively simple analytical solution that can be worked out. Figure 5.15 plots the confinement factor versus different values of a.

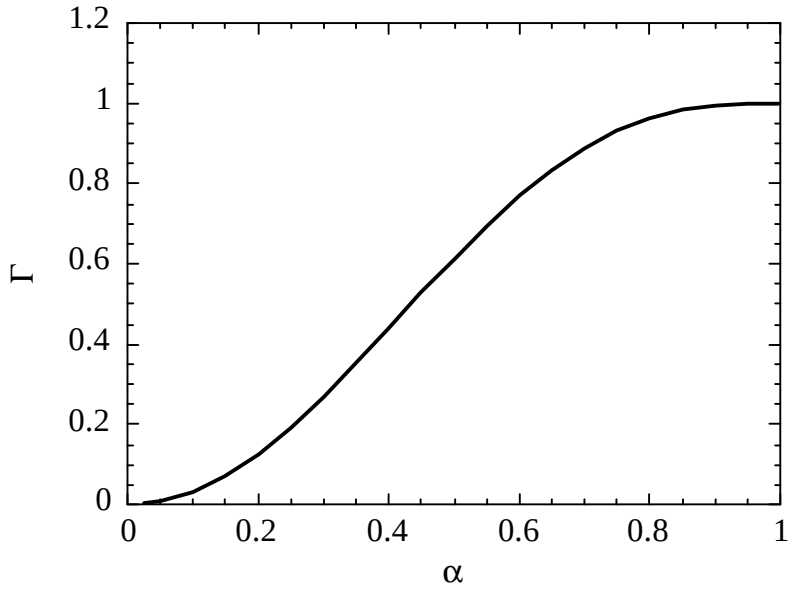

Figure 5.15. Plot of radial confinement factor versus current to optical mode ratio.

With the confinement factor determined we can analyze the threshold current for different cases. Let us again look at the logarithmic gain curve, this time including the confinement factor. In addition, we define a new factor *b*, for this analysis, which is defined as the ratio of the threshold gain G_{th} to the gain parameter G_o. This parameter essentially defines the point on the gain curve that the laser lases.

$$J_{th} = J_o \exp\left(\frac{G_{th}}{\Gamma G_o}\right) = J_o \exp\left(\frac{b}{\Gamma}\right)$$
$$I_{th} = J_{th} p r_{ox}^{\ 2} = J_{th} p R^2 a^{\ 2} = \left(J_o p R^2\right) a^{\ 2} \exp\left(\frac{b}{\Gamma}\right) \tag{5.03}$$

We see from these equations that the threshold current scales with the size of the optical mode times the factor accounting for the reduced current aperture. In this equation, when G equals one, the threshold current is simply the threshold current density times the aperture/mode(they are the same in this case) area. Using these equations, we can now plot the result for the optimum aperture diameter for a fixed optical mode size. We normalize the results to the threshold current of the G=1 case, where aperture and mode diameter are the same. Our results only depend on the normalized factor b which is the ratio of threshold gain to the gain parameter G_o. At room temperature, for this generation of lasers this b parameter is about 0.6-0.7, from the studies done by Babic[6]. At higher temperatures where we expect to have reduced gain and higher losses, this b factor can be significantly larger. If we assume the gain parameter decays exponentially with temperature with a characteristic temperature of about 60°C, then at 80°C the b factor will be larger by approximately a factor of 2.7 than at room temperature. Later in this chapter we will also see the loss increases at higher temperature due to increased free-carrier absorption. This usually has a larger characteristic temperature of about 100°C. This means that the losses will increase by a factor of about 1.8 at 80°C. Putting these two effects together gives us a total fractional increase in b of about 5 going from 20°C to 80°C. This gives a range of b from 0.6 to about

3 of interest. Figure 5.16 plots the results of this analysis. One sees that there is indeed an optimum aperture radius for a fixed optical mode radius. The reduced area of the aperture translates into lower threshold currents at first, but eventually there is a large increase in threshold current density due to the higher necessary material gain. The logarithmic nature of the gain means that eventually the increase in threshold current density overwhelms the decrease in area.

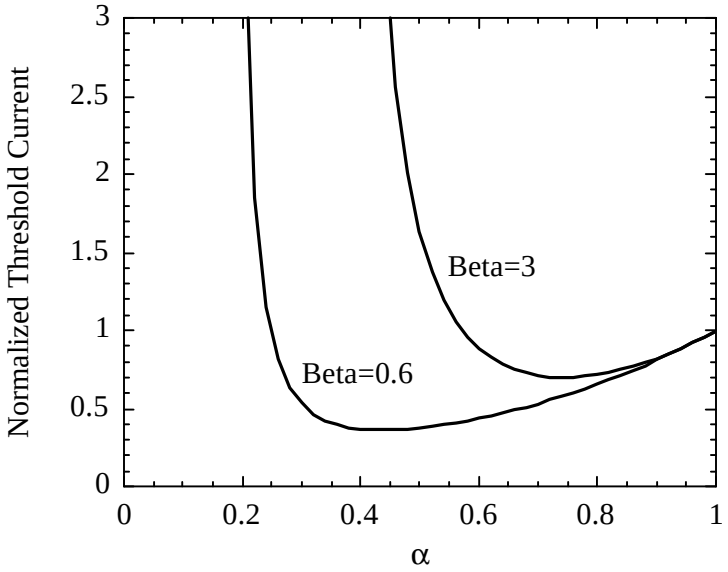

Figure 5.16. Plot of normalized threshold current for the room-temperature case of b=0.6 and high-temperature case of b=3 versus relative aperture radius.

For higher b values there is less relative gain available, so this domination occurs at much larger values of a. Note that there is a different optimum value for a for different temperatures. If one choose a value of a=.4(aperture radius

is about half the mode radius) then at room temperature the threshold current would be less than half the case of a=1. But, this same condition would mean that at 80°C your threshold would be more than three times higher than it need be. The farther along the gain curve a laser operates, the less benefit there is to shrinking the aperture below the mode diameter.

One has to be careful as to the conclusions that can be drawn from this analysis. Remember that we assume a constant optical mode diameter. This case appears to be accurate for generation B devices, but will not be generally true. It is always better to shrink the optical mode and aperture diameter versus just shrinking the aperture diameter by itself(assuming no other effects are considered). To verify this we do the same analysis, but now keeping the aperture diameter fixed, while changing the mode diameter. We retain the same definition for α, the ratio of current aperture radius to mode diameter radius.

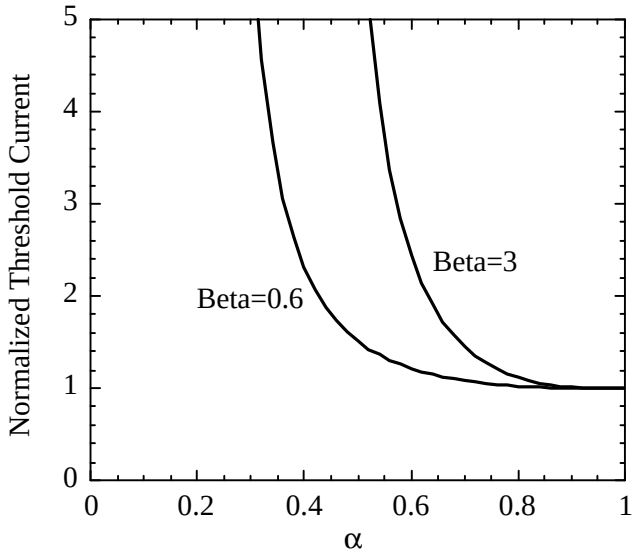

Figure 5.17. Effect of increasing optical mode with constant aperture area.

Figure 5.17 summarizes the results from this analysis. Keeping the aperture size fixed we can see that it is always better to have the optical mode as small as it can be, at least in terms of threshold currents. Having the mode diameter slightly larger than the aperture diameter has little impact, however, if the mode gets too much larger than the aperture then the threshold currents are dramatically increased. Once again, the higher along the gain curve, the worse the effect.

Returning back to the analysis of generation A devices, we left unanswered the large increase in threshold current for very small diameters. In our fit of the threshold currents, we assumed the optical mode was the same

size as the current aperture. We see that this is not the case for the thin oxide aperture. We did not measure the near-field pictures of these devices before they were cut up, so we might assume the near-field patterns would be similar to the ones in generation B devices. Yet this cannot be the case due to the shallow oxidation in generation A devices. Using the nearfields in generation B devices, the optical mode would be past the pillar sidewalls. We assume instead that the optical mode is limited in generation A devices by the pillar sidewall. In this case, the α factors for the two smallest devices of diameter 3 and 5 μm would be 0.375 and 0.55 respectively. We see on our plot that indeed this is in the correct range to seriously affect the threshold currents. For the generation B devices, directly taken from the near-field pictures, the α factor are approximately 0.28,0.5,.78, and .95 for the four different device sizes.

Figure 5.18 shows what happens if you superimpose the measured threshold currents with the results obtained in Figure 5.16. In this plot, I normalized the threshold currents of the smaller devices by threshold current of the largest device. Thus, both for the theoretical plot and for the actual data, the threshold is normalized to the case of the oxide aperture diameter and mode diameter being the same. There are no fitting parameters on this plot. The β we use of 0.6 is from a separate analysis of the quantum wells as described

earlier. We see that there is a reasonable agreement with the theory considering that there are no fitting parameters.

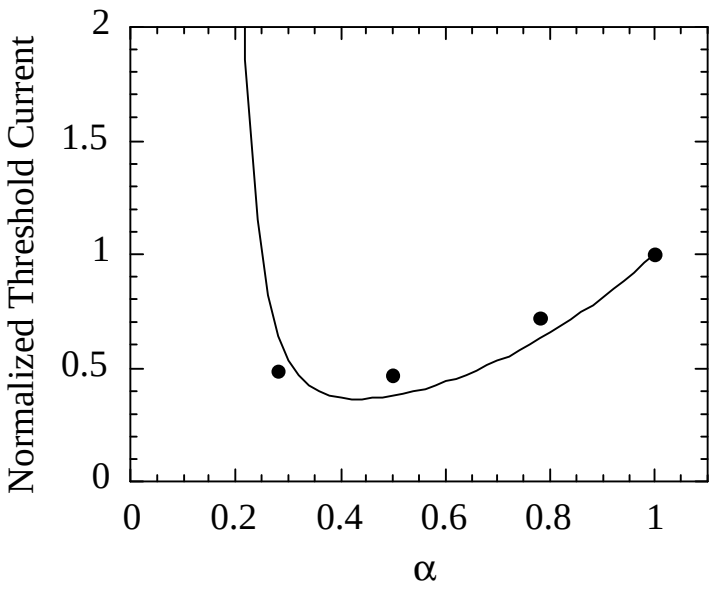

Figure 5.18. Line is theoretical plot as described in Figure 5.16. Dots represent measured data as shown if Figure 5.09.

We appear now to have two different explanations for the increase in threshold currents from generation A to generation B devices. First, we had the current spreading, which was caused by the increased oxidation depth, and second, we had the large optical mode, which reduced the confinement factor. Both explanations are based upon direct measurements of the devices. In reality, only a combination of these models can give the correct picture of what is really occurring in the devices. For larger devices of about 12 μm diameter,

the optical mode is essentially the same size as the current aperture, so that current leakage is the primary effect. This can be seen in Figure 5.09 where we observe that the largest device of generation B which has an α near 1, still has a threshold current about twice the amount of the equivalent generation A size device. In the generation A plot of threshold currents, we see that for very small devices, the leakage current model is not enough to explain the increase in threshold current density. In reality, of course, the two effects can interact somewhat with each other. The current spreading can provide some gain outside the aperture effectively increasing the a factor. We can also have an effect in the other direction, where a low a factor increases the threshold current density, hence increasing the spreading current. Both effects are important and must be considered when analyzing device behavior.

Despite these characteristics, the device performance from generation B was quite good. All of the transmission experiments discussed in the next chapter were done using such devices. In Chapter 6, the dynamic characteristics of these lasers will be discussed. The goal of this generation of devices was to increase the output power to levels useful for transmission experiments. Indeed, this was accomplished with typically 300 μW cw output power that could be coupled into a single-mode fiber. There were also several hero devices that set the standard for power output for a long-wavelength VCL.

Figure 5.19 shows such a hero device that was able to output 1 mW at 15°C. The diameter of the device was 11 μm and had a multimode output spectrum. Typical L-I-V curves from this generation will be presented in the next chapter.

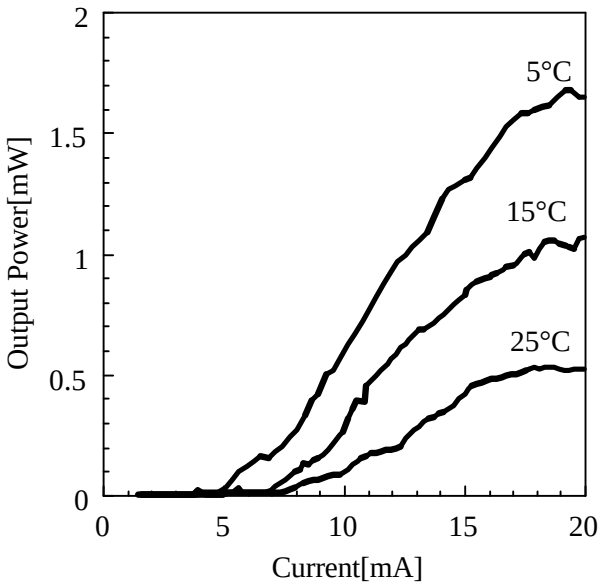

Figure 5.19. Highest cw power achieved from a long-wavelength VCL.

The 7-μm devices exhibited the best high-temperature characteristics. This may be because at this dimension the confinement factor was still large, and the threshold current was relatively small. Figure 5.20 show the threshold currents and differential efficiencies, both in pulsed and cw versus temperature. These devices could operate to 50°C in cw mode, and all the way to 100°C in pulsed mode(a record at the time). In the next generation of devices, we look at the effects that contribute to the temperature behavior of the VCLs.

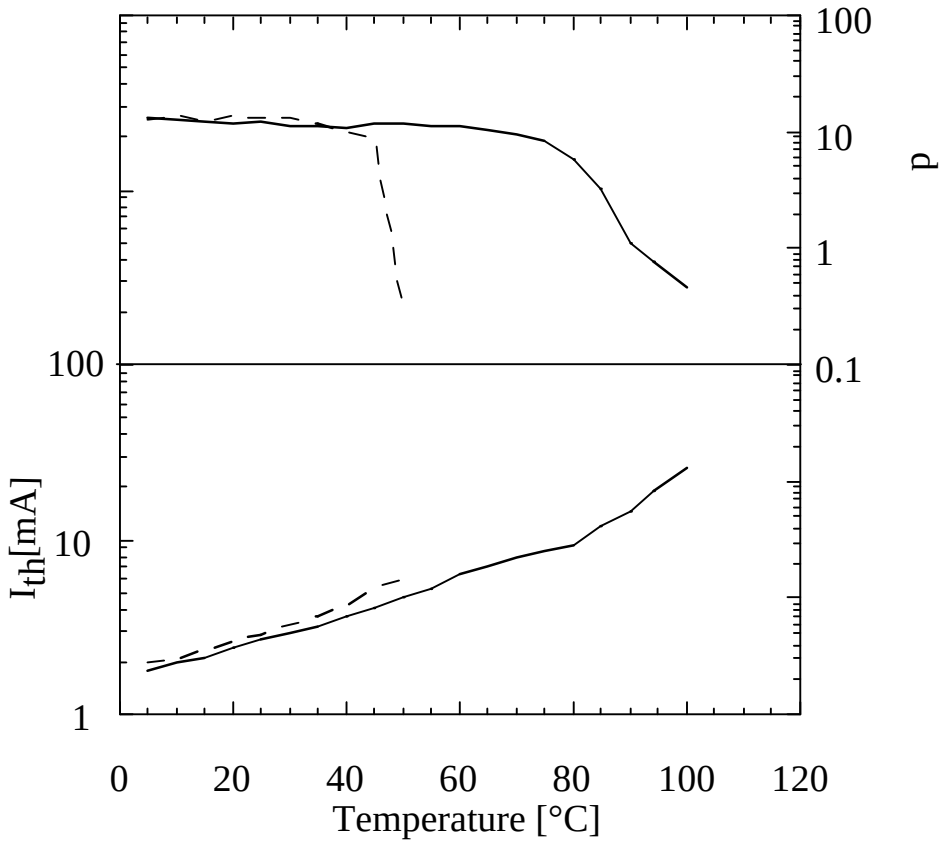

Figure 5.20. Temperature behavior of generation B devices. Dotted line is cw operation, and solid line is pulsed operation(.5% duty cycle).

5.04 Generation C -- 120°C Pulsed Operation

For the generation C devices, we try to focus our analysis on the temperature behavior of our device rather than the device scaling. There are at least a couple of design features that were changed in this generation versus

generation B. The first major change was to make the n-contact an intercavity contact. Instead of using the bottom mirror to provide electrons to the active region, the n-InP cladding region was used for this purpose.

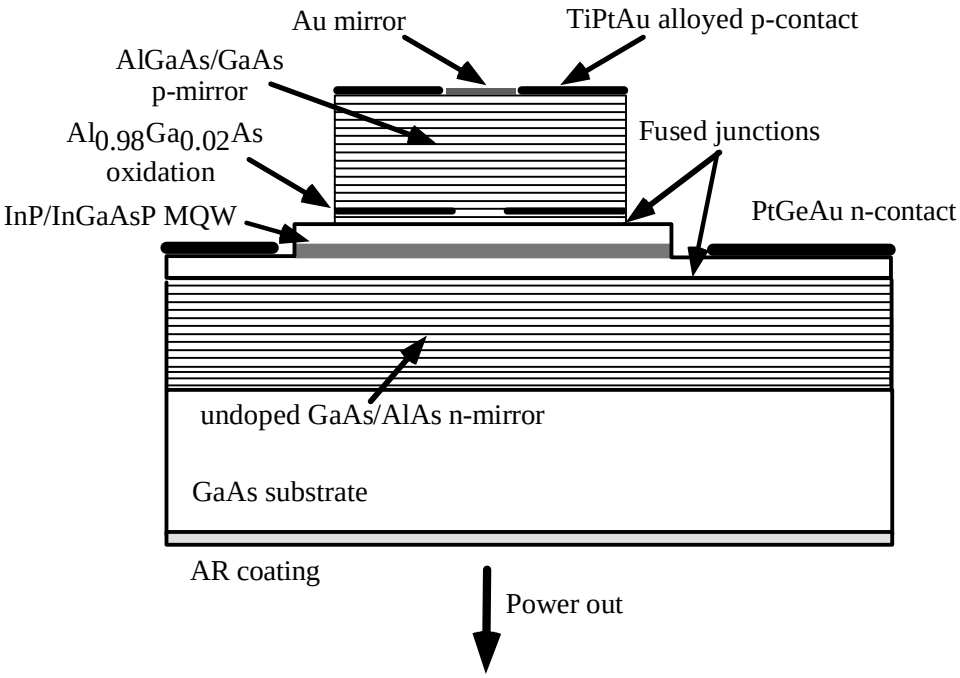

Figure 5.21. Schematic diagram of structure for generation C devices.

In this way, the loss due to the n-doping in the mirror could be eliminated. As you may remember for the design chapter, this loss accounted for about 20% of the total loss. In addition, the bottom mirror could now be grown on a semi-insulating substrate. This greatly reduced the absorption of the power going through the substrate. This effect should increase the differential efficiency by

more than 40%, and to balance it, the number of output mirror periods could be increased. The threshold gain should now be lower, allowing for higher temperatures, while still giving reasonably high differential efficiencies. The number of output mirror periods chosen was twenty-eight. This, ideally, would give a transmission of 0.67% as in the generation A devices. Figure 5.21 shows a schematic diagram of the devices in generation C. What one sees is that there is also another structural change in the devices. The top metal mirror, which was before a Ti/Au mirror uniformly placed on top of the pillar, is now a combination of metals. In the center of the pillar there is a pure gold mirror, which gives a higher reflectivity that a Ti/Au mirror. The outer ring of the pillar has a Ti/Pt/Au contact, which has very low relative reflectivity, but makes for very good Ohmic contacts. Ideally, the oxidation is such that the mode is confined to the area where there is only the pure gold mirror. Maximum reflectivity can be achieved without sacrificing Ohmic contact. If, however, the oxidation does not confine the mode to the area where there is a pure gold reflector, then there will be increased loss in the device. In fact, in this processing run there was a major problem with the oxidation of the device. For reasons described in the processing chapter, the oxidation depth turned out to be only 10 μm, instead of the intended 18 μm. This meant that our smallest devices were now 16 μm in diameter, a very large value. The consequences of

this will be discussed later. In addition, the short oxidation now gave problems with the metal reflector scheme. The short oxidation meant that the gold reflector did not cover the whole oxide opening on all the devices. The metal reflector was designed to have a 3 μm tolerance to the center of the pillar if the oxidation was deeper than 13 μm. That tolerance was eliminated by the short oxidation depth. This means that some devices had a centered reflector and some did not, depending on the lithographic alignment of the oxide opening and the gold reflector.

On the bright side, this error in oxidation could potentially be used to analyze the gain curve of the devices. Since we had a varying loss among the devices, we would now plot the threshold gain versus threshold current density. There was, however, one complication. There is not a direct translation between the differential efficiencies of the devices and the loss in the devices. One needs to know the injection efficiency of the device in order to make this translation. At the time there was no standard way to get injection efficiencies from individual VCLs. In order to make this measurement, I developed a new technique to estimate the injection efficiency from individual VCLs.

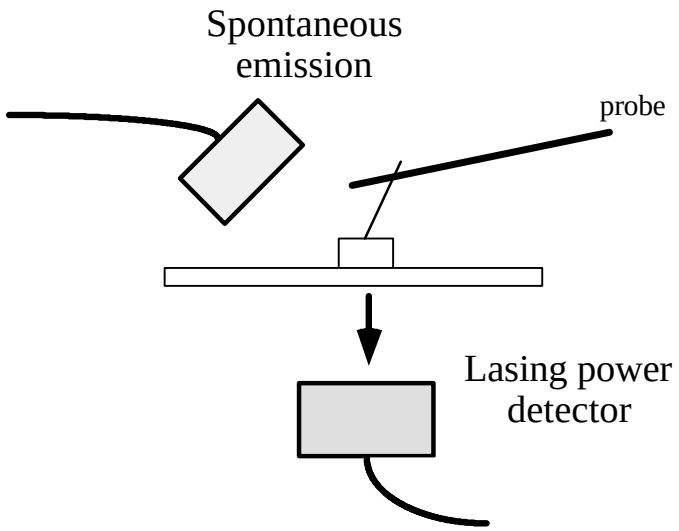

Figure 5.22. Schematic of test setup for measuring injection efficiencies.

The measurement involved detecting the spontaneous emission efficiency above and below threshold. Ideally, if the injection efficiency of a device is 100%, then the spontaneous emission power should be completely clamped at threshold. However, with a reduced injection efficiency, the carriers that never make it into the active region can recombine optically, increasing the spontaneous emission above threshold.

Figure 5.22 shows the schematic of the test setup to measure the injection efficiency of individual VCLs. One needs a separate power meter for the spontaneous emission and the lasing power. It turns out, that in a bottom-emitting VCL, the separation of the two powers is rather easy. The lasing power is localized in a small angular spectrum out the bottom of the device. If

one places another detector on top of the device, this detector only measures the spontaneous emission power. In practice, one has to make sure that no reflections occur that would divert the lasing power to the top detector. One could also use a spectrum analyzer to separate out the lasing wavelength and the spontaneous emission if the spatial separation was difficult. The key to the measurement, however, is that it is not important to get the absolute value of the spontaneous emission, but rather the relative slopes above and below threshold. Figure 5.23 shows a example measurement of a device with an 80% injection efficiency.

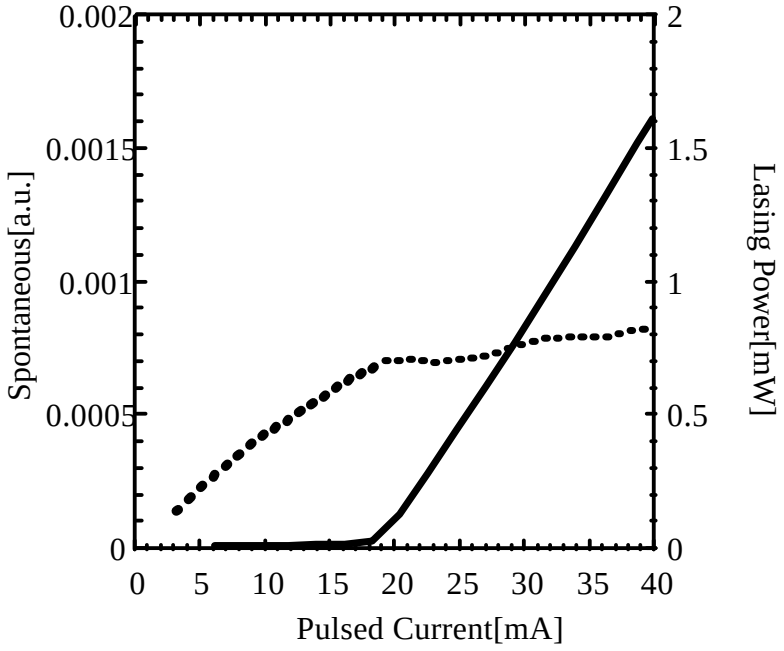

Figure 5.23. Example measurement of injection efficiency.

The injection efficiency is simply given by one minus the ratio of above and below threshold spontaneous emission power slope. This same measurement was done on 980 nm VCLs by Hegblom, giving a value of 90% injection efficiency. This value agreed well with the expected value from measurement of in-plane lasers, with similar active regions.

Once one has the injection efficiencies and the differential efficiencies of devices, then one can plot a number of interesting parameters of the lasers. Figure 5.24 shows a plot of the differential efficiencies of generation C devices versus the measured injection efficiencies of the devices.

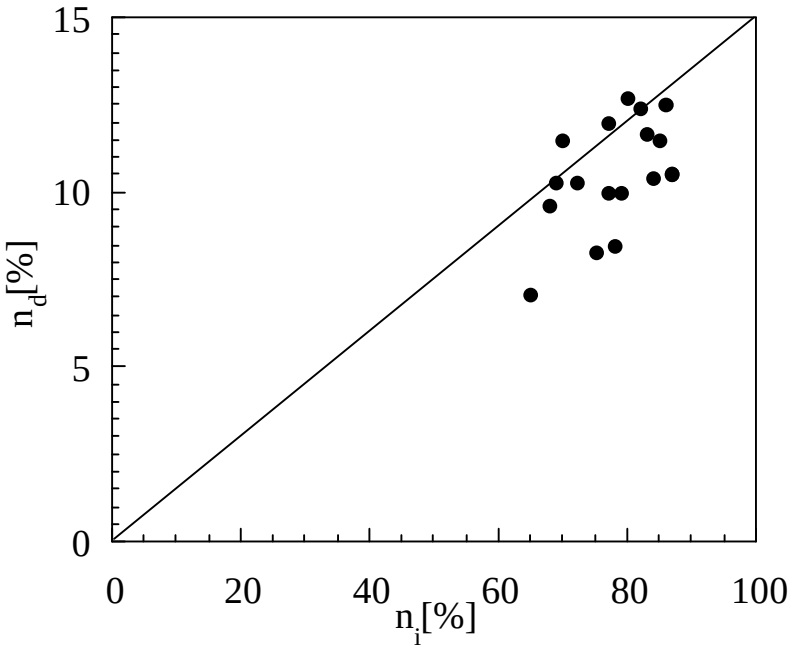

Figure 5.24- Plot of differential efficiencies versus injection efficiencies for generation C devices.

If the round-trip loss of the devices was constant, then all the points should fall on a straight line, intercepting the origin. Yet we know, however, from the problems with the oxidation, that the round-trip loss of the devices are expected to vary quite a lot. We can see from this plot that the injection efficiencies of the devices vary from about 60-85% which is quite normal for such a seven quantum-well structure. Most of the variations in the output efficiencies are due to changes in the loss rather than changes in the internal efficiencies. One also sees that some of the efficiencies on the devices are quite large, especially considering a 28 period output mirror, which before gave only 4-5% efficiency. In fact, these efficiencies are too good to be true if the transmission through the mirror was the nominal 0.067%. This would mean an unbelievably low round-trip losses of 0.38%. When one measures the mode wavelength of the lasers, the explanation for these high efficiencies arises. The lasers were intended to lase at 1540 nm as in previous generation. This means that both mirrors and the PL were centered at this wavelength. The actual lasing wavelength, however, was only 1520 nm, due to the cavity being too short. The mirror transmission at 1520 nm is 0.1% instead of 0.067% at 1540 nm. This means that the efficiencies of the devices will be higher relative to what is expected. The mismatch of the intended wavelength and the actual lasing mode also has a significant affect on the gain as will be seen later. With knowledge of the

transmission through the output mirror, we can now do a histogram plot of the round-trip loss of the devices to see the effect of the metal mode mismatch. Figure 5.25 shows such a plot. We see that the average round-trip loss through the device is about 0.7-0.8%. We expected about a 0.2% improvement from previous devices by removing the doping from the n-mirror. We also expected to get a slightly lower loss with the use of the higher reflectivity pure gold mirror. This low round-trip loss should also improve the high-temperature operation.

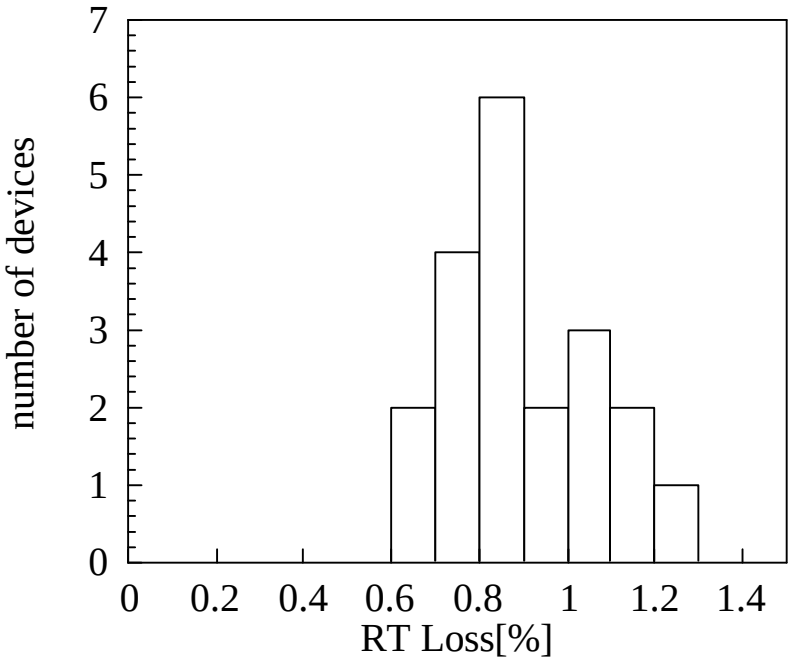

Figure 5.25. Histogram of round-trip losses of devices.

By knowing the losses plus transmission for each device, we can determine the threshold gain for the device. In addition, we can separately measure the threshold current density of the devices. Since our smallest size is 16 μm, we can put aside issues such as current spreading and gain mode mismatches. Figure 5.26 shows a plot of the gain versus current density for the generation C devices. We see significant scatter from the usual logarithmic gain curve. This scatter may be due to variations in the material quality of the active region for different devices. We can, however, fit the best case gain curve to these devices using a logarithmic fit, which should give the relevant gain curve for the highest performance devices.

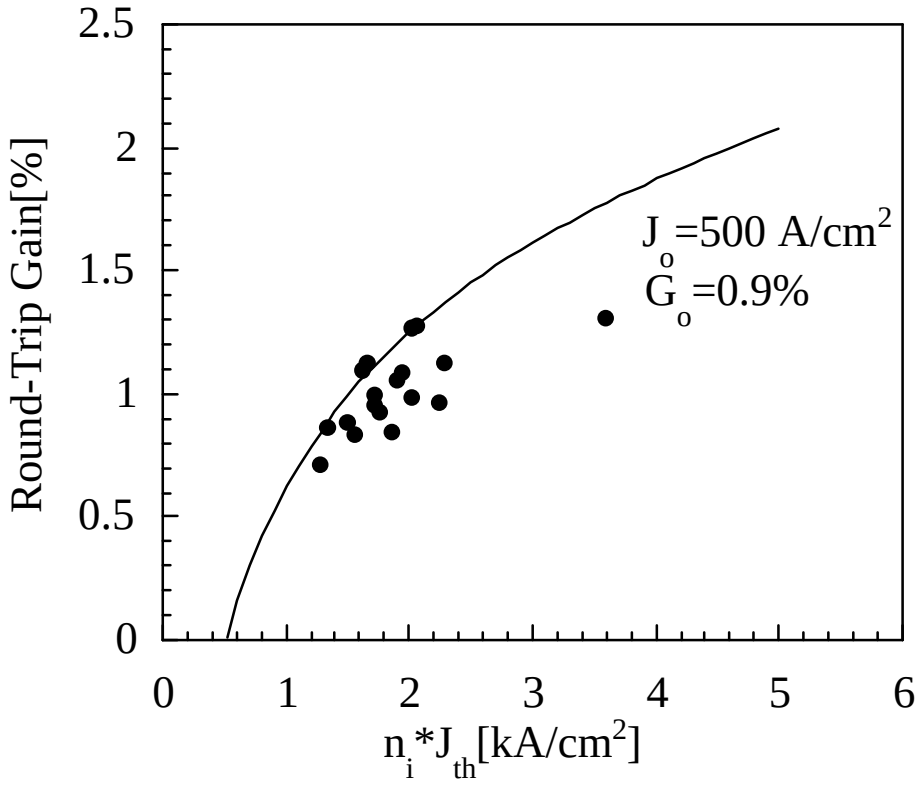

Figure 5.26. Room-temperature gain curve of generation C devices.

What we see from the fit is that our gain parameter G_o is significantly worse than in previous devices, and that our transparency current density J_o is pretty similar to previous devices. The reason for this can be explained by the large difference between the gain peak and the lasing mode of the devices. According to this data, a 20 nm offset from PL peak to lasing mode results in a 40% reduction in G_o but a minimal change in the transparency current density.

We can, of course, do some of these measurements at higher temperatures. This can give us an idea as to what degrades at higher temperatures. Figure 5.27 shows a plot of several of the relevant parameters versus temperature. The plot only goes to 60 °C because the measurement of injection loses accuracy as the efficiency of the device is decreased. From room temperature to 60°C, we get a clear picture of what degrades the most in the laser. We can clearly see that the injection efficiency remains almost constant in this temperature range. This is consistent with the literature which suggests a degradation of injection efficiency only at about 70°C[7]. With knowledge of the injection efficiency and the differential efficiency, we can also plot the round-trip loss in the device. We do not expect the transmission through the mirror to change much in this narrow temperature range. We see that the increase in loss in the device has a characteristic temperature of about 100 °C. This loss is most likely due to free-carrier absorption in the active region due to carrier spill over into the well[8]. This phenomenon is well documented in in-plane lasers. Finally, we also plot in Figure 5.27 the current density times the injection efficiency. This value should represent the carrier density in the active region. We see that the carrier density necessary for lasing increases with a characteristic temperature of only 53 °C. The losses increase at a much lower rate than the threshold current density. This means that for an equivalent loss

value the gain at higher temperatures is worse. Auger recombination and carrier spillover are well known to increase the threshold current of long-wavelength lasers at these temperatures[7]. The decrease in gain at higher temperatures is the primary factor for the increase in threshold current of the laser at higher temperatures. The increases in loss, however, play the primary role in the reduction of the differential efficiency with temperature. These two statements are the result of the minimum change of the injection efficiency in this temperature range.

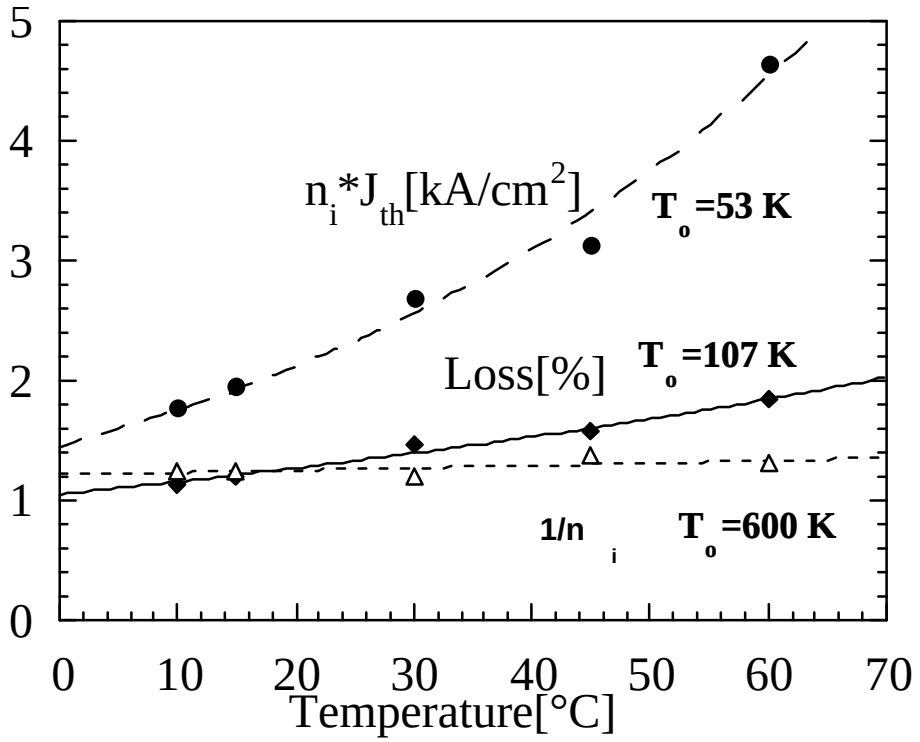

Figure 5.27. Characteristic temperatures of parameters in the long-wavelength

VCL. T_0 of threshold current is 49 K, and T_{nd} of differential efficiency is 92 K.

We can, at last, compare the threshold currents of generation C device with generation A and B devices to see if any improvement in this area has been achieved. We have already demonstrated that the threshold gain of the generation C devices are quite a bit lower that the other two generations. We also know that the oxidation depth of these devices was about 10 μm. Previously, we determined that the oxidation depth plays a critical role in the threshold currents of small diameter devices. For the generation C devices, the oxidation depth is in between generation A and generation B devices. The intended oxidation depth was much larger, so that the minimum diameter devices were 16 μm. We cannot, therefore, expect too low a threshold current. Furthermore, we have shown that the 20 nm offset between the lasing mode and PL peak causes a significant degradation in the gain curves of the device. These three effects balance out to give threshold current between generation A and generation B device. Figure 5.28 shows the comparison plot of the three generations.

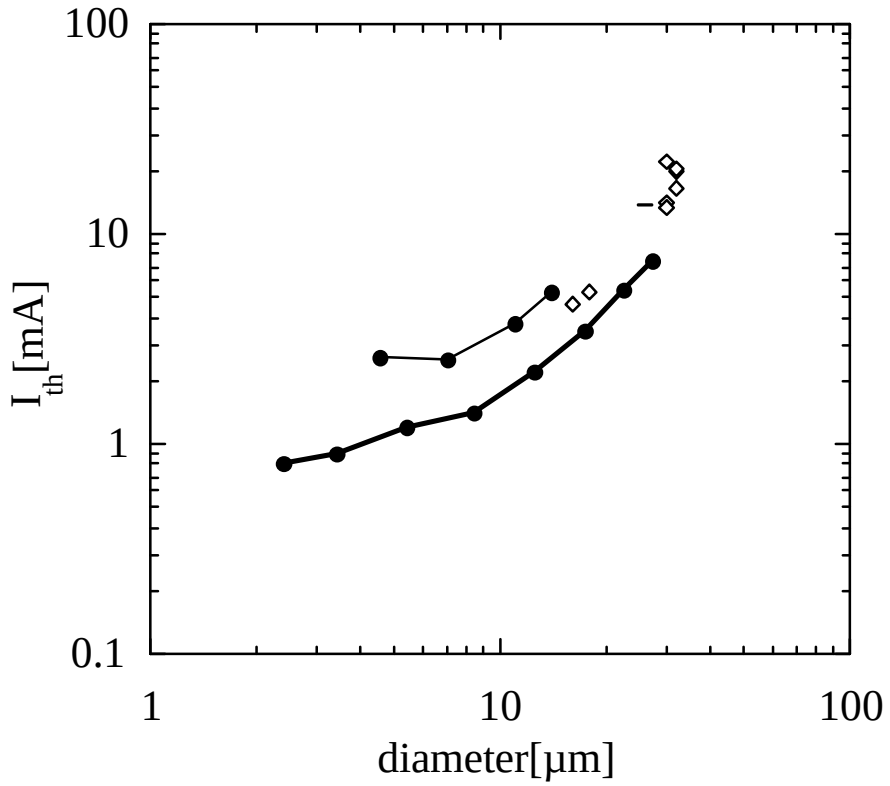

Figure 5.28- Open dots show threshold currents of generation C devices. Black dots show generation A on bottom and generation B on top.

We clearly see that since there are no small devices, the lowest threshold currents are too large to work for higher temperature cw operation. Thus the highest temperature cw operation was only in the 50 °C range. In pulsed operation where heating is minimal, though, these devices performed exceptionally well. In fact, we measured pulsed operation up to 121°C. This may not even be the limit of the devices, as higher temperatures could not be achieved without destroying the thermo-electric cooler on the stage. This

device had a reasonable threshold current of about 4 mA at room temperature, but as the temperature is raised, the threshold current becomes quite large. This large threshold current generates much too much heat in cw operation. A 30 mA threshold current would generate 90 mW of power if we assume 3 Volts at threshold. We can estimate that the thermal resistance of such a device is about 0.6 K/mW, so that the temperature rise would be about 55 °C. Subtracting the 55 °C heating from the 105 °C pulsed L-I curve, we determine that this laser would have similar characteristics at 50 °C in continuous-wave operation as at

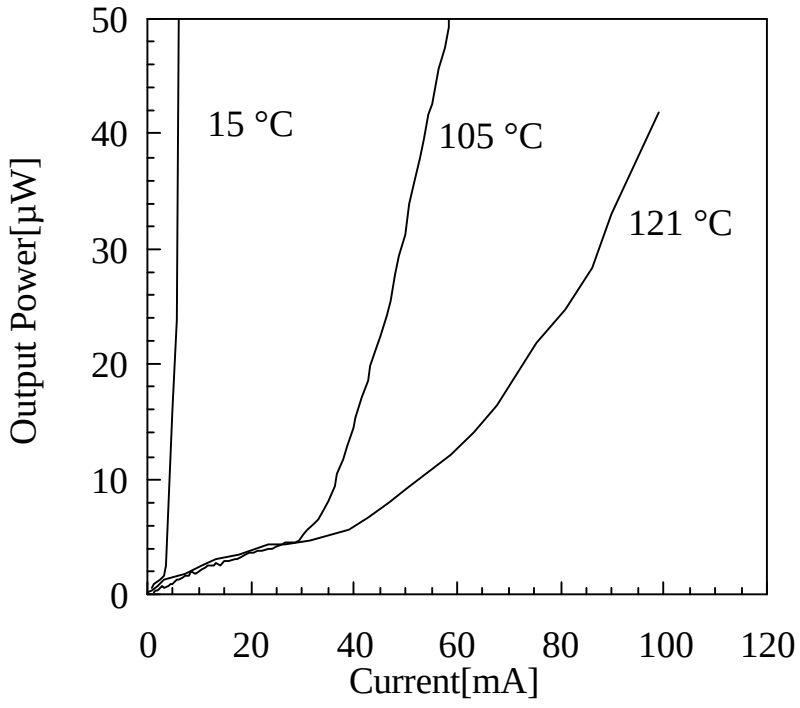

Figure 5.29. Record pulsed operating temperature from a long-wavelength VCL.

Generation C devices showed the potential for reduced loss in the lasers, as well as the positive implication to high-temperature operation with this reduced loss. To achieve new, record high-temperature cw operation, one needs the proper threshold current scaling as discussed in the generation A and B devices, along with the reduced loss in the generation C devices. The heating at threshold is not so significant at room temperature. However, the room-temperature threshold current has a direct correlation with the threshold currents at elevated temperatures. With a typical characteristic temperature of 50°C, the threshold current increases by almost an order of magnitude going from room temperature to 120°C. A 0.5 mA threshold at room temperature would translate to only a 5 mA threshold at 120°C. This means reduced heating at the higher temperatures, and ultimately higher cw operation temperatures. On the other hand, if one starts with a 5 mA threshold current at room temperature, at 120°C this current would be as large as 50 mA, if the device lased at all. Trying to increase the characteristic temperature of the laser is another means to reduce the impact of heating at higher temperatures. Nonetheless, this approach probably still requires the reduced loss to achieve the higher characteristic temperature.

5.05 Generation D -- First Top-Emitting Devices

The high-temperature pulsed operation from the generation C devices was very promising for high cw temperature operation. The gain-mode offset could be improved to give increased gain, and smaller devices could be fabricated with better control of the oxidation process. Furthermore, a new top-emitting structure was developed to make the devices more practical. Figure 5.30 shows the structure of the new top-emitting design. The bulk of the fabrication chapter was dedicated to the processing of this type of structure. In many ways, the structure is very similar to the generation C devices. With the generation D devices, there is no gold reflector on top of the pillar, and the bottom mirror has 31.5 periods instead of 28. This forces the light out the top rather than through the bottom. The phase of the top surface reflection was also adjusted to be phased matched to air rather than gold. This air reflection boosts the reflectivity of the top mirror significantly so as to minimize the number of periods needed to be grown. Thirty-one periods of 67% AlGaAs/GaAs were used for the top mirror, which nominally should give a transmission of 0.2%. Since one could no longer probe directly on top of the pillar(this would now block the light), a metal line was needed to connect the top-ring with a field bondpad. SiNx was used as the isolation layer for the field.

As discussed in the fabrication chapter, one could also etch the layer underneath the bondpad to reduce capacitance for high speed operation. However, this step was not done on this generation of devices to save time and to minimize fabrication errors.

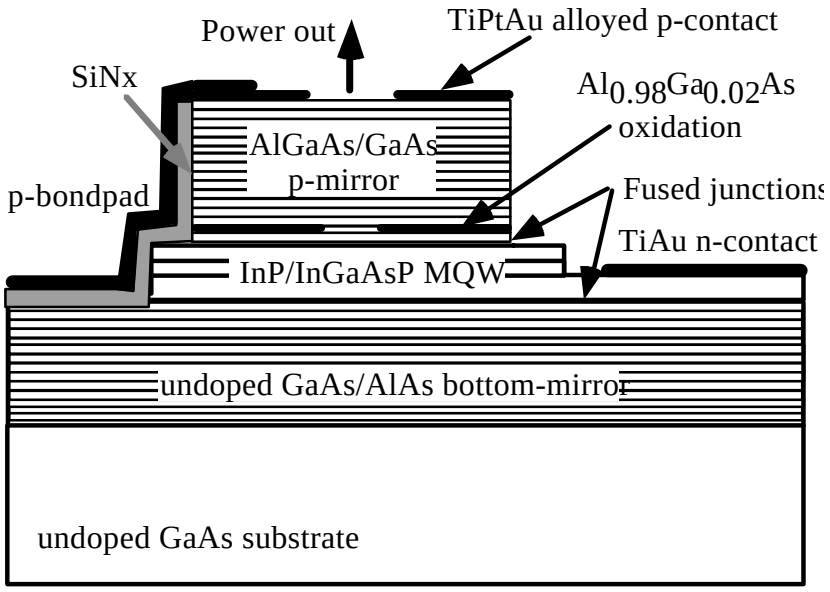

Figure 5.30. Top-emitting design for VCLs.

This generation of devices was expected to achieve high-temperature cw operation for reasons described above. Nevertheless, as occurs many times, a new problem arose with this generation. The fusion with the new p-mirror gave significantly higher threshold voltages, as high as 6-8 Volts. At first indication, one would suspect that the mirror was poorly designed, thus resulting in a large resistance. However, independent measurements(ohmic

contacts on the mirror itself) of the mirror resistance showed that the resistance through the mirror was minimal. This suggested that the fused junction was the cause of the high voltage. There was also the possibility that the high-temperature processing of the mirror through the fusion might cause dopant interdiffusion and increase the mirror voltage. To test this theory, we fused a piece of this mirror to an InP active region and then removed the InP substrate and epi to which the fusion was done. We then put contacts on this piece and tested its resistance. Indeed, the mirror resistance did increase, but was still orders of magnitude less resistive than what we were seeing in the VCL case. In addition, the turn-on voltages of the lasers were nearly independent of device diameter, also suggesting the fused junction to be the problem.

This new p-mirror was fused to several different InP active regions, always giving the same high voltage result. No lasing was observed in these laser structures for several runs. We concluded that something in the p-mirror design or growth was causing a large barrier for holes at the fused junction. As explained in the fusion chapter, a 1-1.5 volt barrier is to be expected, but in this design the voltage was substantially higher. It was also still unclear why this high voltage was preventing lasing from occurring. Device heating alone could not account for this phenomena. To understand why we were not getting lasing, one has to note that electrons do not have a significant barrier to cross

the fused junction. This means that the electrons that are spilled over the quantum well active region will drift past the fused junction and recombine in the GaAs region. When electrons traverse the fused junction, there is an effective current flowing through the junctions. The current flowing across the junction reduces the voltage across the junction. For a fixed applied voltage, the reduced voltage across the junction gets applied to the active region. The increased bias across the active region results in increased electron leakage to the junction. One can see that this can lead to an avalanche switching effect, such as in a thyristor. At first glance, one might think that this switching effect is a good thing. After all, once the switching has occurred, there is significantly less voltage across the junction. However, a closer inspection reveals that most of the recombination is occurring at the fused junction and not at the quantum wells. This, of course, would prevent any lasing from occurring.

To insure that increase voltage was not dependent on some anomaly in the growth, a mirror was grown again with essentially the same design. However, the same high voltage was present in the new mirror. One might speculate that somehow our fusion system had degraded or was contaminated, but this theory could be debunked since epi samples again gave similar results. In addition, we sent a piece of this mirror to be fused at KTH, using their fusion procedure and system[9]. The results were identical to our own system. The

overriding question was, what was different about this design from other designs. The three differences that could be discerned were that the oxide layer was closer to the fused junction, the mirror was grown on a p-type substrate versus a s.i. substrate, and that the uni-parabolic grading scheme(as described in the design chapter) was used. The reason that the oxide was placed closer to the fused junction was to reduce the leakage current around the aperture. P-doped substrates were used to test independently the resistance of the mirror. This independent test of the mirror resistance suggested that the grading scheme was not the problem. So, we hypothesized that the closer oxide was causing some problem with the fusion. In the new design, the oxide was only 70 nm from the fused junction, whereas in the previous samples the oxide was about 150 nm from the junction.

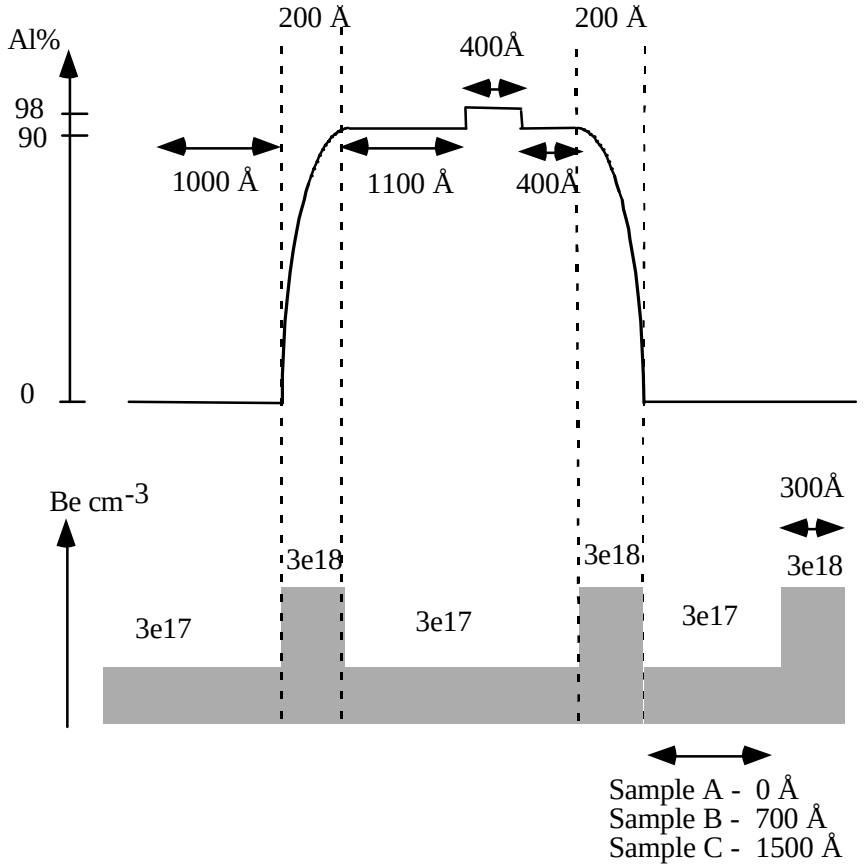

Figure 5.31. Design of mirror near the fused junction.

Test samples were grown on a p-type substrate simulating the final period of the new mirror design. The distance of the oxidation layer to the fused junction was varied from 50 nm to 200 nm. Figure 5.31 shows the design near the fused junction for these samples. Sample A reproduces the design as in the actual mirror. One can see that to get the oxide aperture closer to the fused junction, the phase of the first GaAs/AlGaAs interface is not in phase with the rest of the

mirror. This slightly lowers the reflectivity but has minimal other adverse effects.

The three samples were fused to an active region, and processed for I-V measurements. No oxidation was done on any of these samples. Unfortunately, the results of the I-V testing were inconclusive. All three samples had about a 3 Volt turn-on or 2.2 Volts across the fused junction. This is quite a bit larger than the usual 1.2 Volts across the junction, but was still much better than the 5-7 Volts in the real laser samples. Thus, no definitive conclusion could be made from this experiment.

One way to stop the fused junction from acting like a thyristor is to reduce electron leakage over the active region. This would force holes rather than electrons to traverse the fused junction. Abraham *et al.* had been working on incorporating an electron stopping barrier in 1.5 μm active region to achieve high To lasers[10]. This scheme involved using a InGaP region on the p-side of the active region. The InGaP layer has a type II interface with InP. This introduces a barrier for electrons, but not for holes. This barrier for electrons is estimated to be about 30 meV. This may not seem like a major barrier, but simulations of the active region by Abraham suggest that the T_o of the laser can be improved from 60 to 130°C. We fabricated VCLs with this active region and the infamous problematic p-mirror. The resistance of the junction was once

again terrible, but this time we could achieve lasing in the devices. Indeed, these lasers could be considered quite good despite their high voltage. Figure 5.32 shows L-I-V curves at several temperature operating in cw operation. The highest cw operation from this sample was from 12-μm devices which lased up to 65° C. More typical were devices that ran up to 60°C cw. The differential efficiencies from the devices varied rather randomly from about 7% to 20%. This variation could be due either to changing losses or to injection efficiency. There was no reason to suspect that there should be different losses in different devices. The injection efficiencies, however, could be suspect due to the high fused junction voltage. When measured by the techniques described earlier, the injection efficiencies were, in fact, quite scattered. The values varied from 20-60%, quite a bit lower than in previous generations even at the high end of 60%. The differential efficiencies of the devices were still among the highest that had been fabricated. These high efficiencies were achieved by the combination of the high transmission through the mirror(0.25%) and the low loss in the cavity. The scatter in the data made very difficult any systematic analysis of the round-trip loss in the devices. The lower values of the round-trip loss were in the range of 0.5%. This significantly lower loss could be attributed to the low doping in the uniparabolic grading scheme as described in the design chapter. In addition, 90% AlGaAs was used in the p-mirror rather

than the usual 67%, which lowered the penetration depth into the p-mirror(reducing loss). Going from 67% mirror to 90% AlGaAs mirror reduced the penetration depth and loss by 20%. Looking at the design chapter discussion of loss in the device, we can see that 0.5% round-trip loss is a reasonable value. This high efficiency gave maximum room temperature output powers of about 400 μW, and at 50° C could still provide 100 μW of cw power. This is a marked improvement over the previous high power generation B device which stopped lasing at 50°C cw. Furthermore, the characteristic of the lasers improved to about 90°C, consistent with the use of the electron stopping InGaP layer.

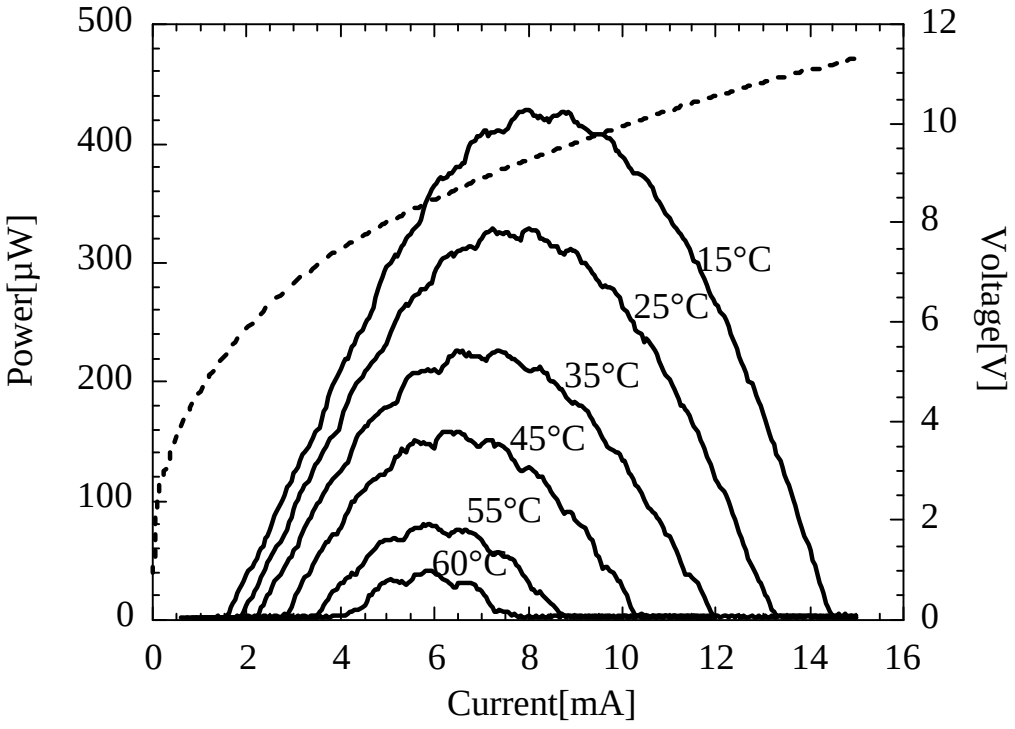

Figure 5.32. High-temperature, high-power lasing from generation D device.

What we see in Figure 5.32 is that despite the very high voltage in the device, causing excessive heating, the device operates to very high-temperature cw. The heating in a device is equal to the thermal resistance times the power dissipated. Figure 5.33 plots the electrical power dissipated at threshold as well the electrical power at the point at which the device stops lasing(past roll over) for several ambient temperatures. The reason the device stops lasing past certain current levels is that the active region is heated so that the internal

temperature is past the maximum temperature of operation. If we assume that for each of the points on the plot the maximum internal operating temperatures are the same, then all the maximum operating points should fall on a straight line. Indeed, we see in the figure that this is the case. The extrapolation of the line to the origin should give the maximum pulsed temperature operation, since this point corresponds to the maximum temperature without any internal heating. This plot also allows one to calculate the thermal resistance as the inverse of the slope of the line. Figure 5.33 shows that the device in Figure 5.32 has a thermal resistance of 0.5 °C/mW and a maximum pulsed temperature operation of about 95°C. The maximum pulsed operation of the laser is significantly lower than in the generation C devices. The round-trip loss of both device are about the same, suggesting that the active region is not acting as well in the generation D devices. The likely cause of this poorer performance is the fused junction affecting the active region. We have already measured that the injection efficiency at room temperature of the devices is lower than expected. At very high temperatures, electron leakage becomes more pronounced. Thus, it is likely that at very high temperatures the electron leakage is causing the fused junction to stop the device from lasing. This statement, however, is somewhat speculative and needs further confirmation with experimental evidence.

Looking at Figure 5.33, we have a graphical representation of the high-temperature performance of a laser. We can see that cw operation occurs between the top line and the bottom line, whereas pulsed operation occurs anywhere below the top line. Reducing heating at threshold moves the bottom line down. Improving the T_o of the device reduces the curvature of the bottom line, effectively increasing the area of cw operation. The point of maximum pulsed operation acts as a pivot point for the top line. Increasing the point of maximum pulsed operation, through reduced loss or higher gain, moves the top line to the left. Doing so again opens up the "eye" between the top and bottom line on the plot. Finally, reducing the thermal resistance of the device increases the slope of the top line. It is clear that if the pivot point of the line is the x-axis, then increasing the slope of the line(reducing the thermal resistance) results in a larger region of cw operation. The maximum pulsed temperature operation should not change with a change in thermal resistance.

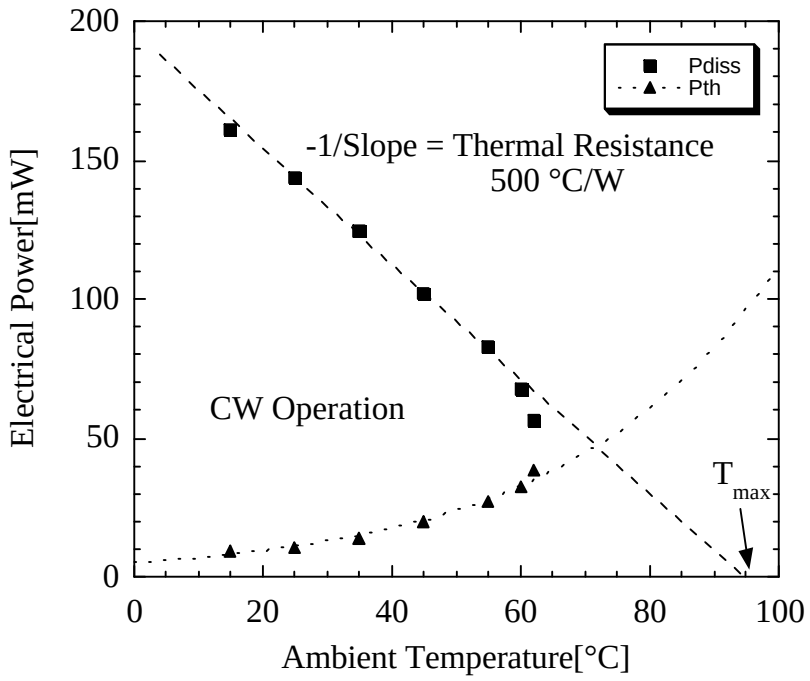

Figure 5.33- Plot of electrical power dissipation at threshold and at rollover.

The goal of making high-temperature, high-power lasers is accomplished by opening the "eye" between the bottom line and top line. The larger the distance between the two lines, the more power the device can put out. The point of maximum output power occurs approximately at the midpoint between the two lines. This plot highlights the effect several strategies have in improving high-temperature cw operations.

Once one has the thermal resistance of the device, it is very easy to get the internal temperature of the device at any point. Figure 5.34 shows the

internal temperature of the device running cw, with an ambient temperature of 15°C.

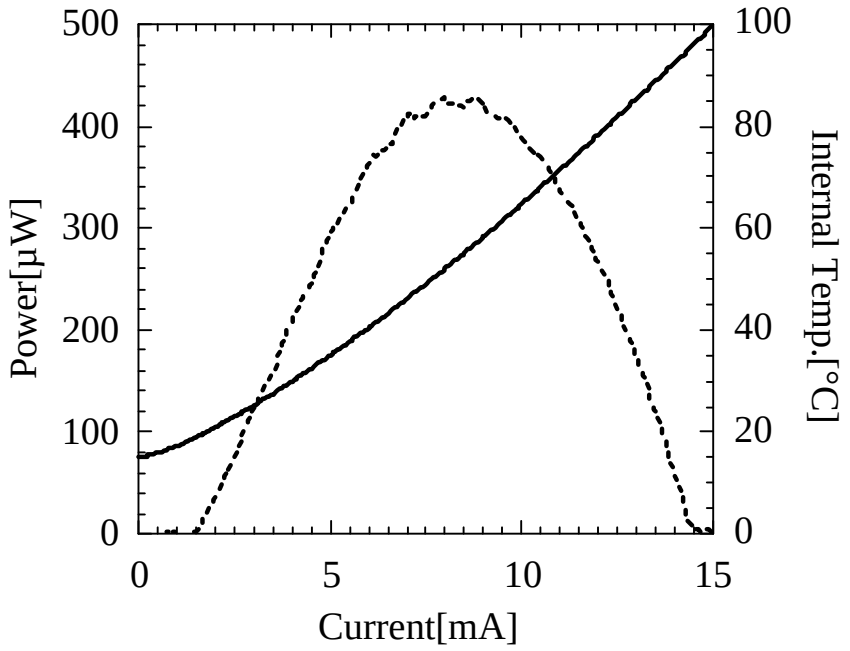

Figure 5.34. Plot of internal temperature of a device under cw operation. Dotted line is output power, and solid line is internal temperature.

The technique of using the rollover point to determine the thermal resistance and maximum pulsed temperature has one drawback. To roll over the device completely near room temperature many times requires huge current densities. In the plot above, 15 mA corresponds to a current density over 15 kA/cm^2. This has potential for damaging the device. One way to get around such high-current densities is to use only relatively high ambient temperatures for the

device. For example, if we would only use the points above 45°C in Figure 5.30 then the current density at rollover would not pass 10 kA/cm^2. No damage appeared to be induced in the lasers while doing this test.

5.06 Generation E-- Hybrid Carbon-Beryllium Mirror

After the very large resistance of generation D, the final generation of devices discussed in this thesis, generation E, were designed to reduce the electrical resistances of the VCLs. The fabrication structure was identical to generation D. The difference in this generation was in the p-mirror doping design. As discussed in Chapter 2, to get a low mirror resistance one would like to use Carbon doping at the interfaces due to better incorporation and reduced diffusion of the dopant. In the fusion chapter, however, we found that carbon can be a problem with the fused junction voltage. On the other hand, Beryllium does do well at the fused junction, but has difficulty at the GaAs/AlGaAs interfaces. Generation E devices allowed for a hybrid design, with most of the mirror doped with Carbon, but with the GaAs layer doped with Beryllium. If the MBE machine that we used had both sources, this would be trivial to implement, but this was not the case. Instead, we needed to grow most of the mirror in one machine, and then take the wafer out of the machine

and regrow a Be doped GaAs cap layer in another machine. We also increased the intended average doping to 5 10^{17} cm^{-3}, about twice the value of generation D devices. This was to demonstrate the lowest voltage that could be achieved in the device. The Be cap on the device was 30 nm and was doped at 5 10^{18} cm^{-3}.

The Carbon doped growth of mirror structures was only recently optimized by Hegblom *et al.* at UCSB(Peters first developed the carbon source at UCSB). Using a solid Carbon source, the mirror structures grown at UCSB had, for a long time, very rough surface morphology. However, recently, Hegblom found that by using a high-temperature growth on 700°C, one could achieve smooth surfaces even with the mirror thicknesses need for a 1.5 μm VCL. The mirror grown for the generation E devices was among the first to come from the new growth technique. Unfortunately, the doping calibration was not accurate at the time, so that the mirror was grown with twice the intended doping level. This introduced a large amount of loss into the device as discussed in the design chapter. In turn, this large amount of loss limited high-temperature operation in this generation to only 45°C cw. Figure 5.35 shows a typical L-I-V curve from laser of this generation.

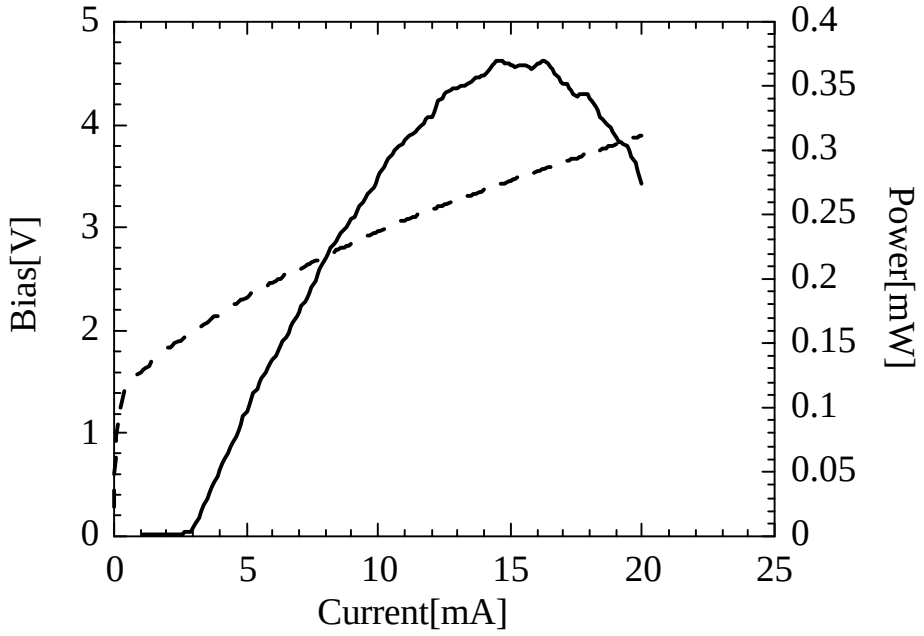

Figure 5.35. L-I-V characteristics of generation E devices. Solid line is power.

Again, we can see reasonable output powers of about 400 μW. The efficiency of the devices were quite low at about 5% due to the large loss in the mirror. The reasonable output power was because of the reduced voltage above threshold. Even all the way to the peak output power, the voltage of the device was still below 4 Volts. The differential resistance of the device was 80 Ohms, quite a low value for a 8-μm diameter device. The threshold voltages of the devices were typically about 2 Volts, with the best threshold voltage of about 1.7 Volts.

We attempted to package devices from this generation onto TO headers. This process was not very successful as the adhesion of the bondpad

metal to the semiconductor was quite poor. Wire bonding the samples resulted in pulling off the bondpad metal. The wire bonding process resulted in the destruction of most of the devices. We managed to complete the packaging process on several devices, but only two of the packaged devices performed reasonably well at the end of the process. Both devices were biased at 6 mA for 4 days. The current density at 6 mA for 8-μm devices is 12 kA/cm^2, a very large value for degradation tests. No degradation was observed in the L-I-V characteristics of the devices at the end of four continuous days. It was decided to severely stress one device for a short period of time, while the other one would be directly placed on a makeshift life-tester. The stressed device would be biased at 20 mA for 1 minute. This rapid degradation resulted in reduction of about 10% in the maximum cw output power. The other devices L-I-V characteristics are shown in Figure 5.35. Both devices were left at room temperature and biased to 6 mA. The cw output powers under these conditions were approximately 100 μW. The power would fluctuate with temperature as the stage was not temperature controlled. There appeared to be no degradation with time as the devices were polled periodically for power output. The stressed device, however, quickly decreased in power from 100 μW to not lasing at all in a period of a couple of days, 1500 hours into the test. The unstressed device lasted almost three times longer to 4200 hours, with a similar

death. This may seem discouraging for reliability of such devices, but the current densities applied were quite high and the devices had significantly higher losses than typical devices. The packaging procedure must be improved to give us many devices to say anything definitive about the reliability of the devices.

5.07 Summary

We have now gone over five generations of devices. In each device generation, a different aspect of the device physics was emphasized. Less emphasized was the evolution of the device structure from a very simple bottom-emitting device to a rather complex top-emitting device with an n-intercavity contact and complete bondpads for packaging. The later structures improve the output power of the devices, but also very importantly make the final device more practical for real use. In the next chapter, we will go over some of the system tests we have tried to do using such devices. In this chapter, the primary emphasis was on the device physics that were limiting the maximum performance operation. In generation A the scaling of the device to small dimensions was the primary focus. Even though the differential efficiency of the devices scaled very nicely to small dimensions, the spreading current around the aperture did not allow the threshold current density to scale well

with oxide aperture diameter. In generation B devices, a new aspect of the devices was introduced--the optical confinement factor. The very weak index perturbation of the oxide aperture in this case allowed the optical mode to be larger than the current aperture. We shall see in the next chapter that this effect may be useful in getting single-mode operation from the VCLs. We also determined the penalty in threshold current for a given mismatch in the aperture and optical mode. In generation C devices, the primary focus was on the internal losses in the device. By lowering the internal losses, the maximum pulsed temperature was raised to above 120°C. An error in the oxidation depth limited the maximum cw operation of these devices. Generation D devices were the first to work with the full top-emitting device structure. In this generation, we encountered severe problems with the fused junction. The exact cause of these problems could not be isolated, but we were able to still fabricate high-temperature cw devices. By using an electron-stopping layer, the recombination at the fused junction was minimized. Even with 8 Volt threshold voltages some devices could operate to 65°C cw. In this generation, we also showed a very simple scheme to measure the thermal resistance of the device, as well as the maximum internal temperature. With this information, we could directly plot the internal temperature of the lasers. Finally, in generation E, we showed the lowest threshold voltage lasers we had even made. By using

a custom doping near the fused interface we showed threshold voltages as low as 1.7 Volts. However, even in this generation, most of the excess voltage across the device was due to the fused junction. Each generation had its problems and its virtues. By eliminating the problems with each of the devices, we potentially could come up with “the perfect device”. In reality, however, as each problem is solved new problems typically arise. One can only try to address the problems that one sees before him/her. The primary problem with the double-fused long-wavelength laser at this stage is the fused junction voltage. The impact of this voltage is firstly current spreading around the aperture, and secondly excessive Joule heating. A reduction in this voltage would greatly improve device performance. The other aspects that are important to remember when designing or fabricating such devices are the optical confinement factor, current spreading in the InP cladding, and proper matching of the gain peak, mirror stopbands, and mode position. The next chapter presents some of the issues involved with the dynamic and system behavior of the devices. These issues are crucial to achieving a commercially viable device.

5.08 References

[1] N. M. Margalit, D. I. Babic, K. Streubel, R. P. Mirin, D. E. Mars, J. E. Bowers, and E. L. Hu, "Laterally oxidized long wavelength cw vertical-cavity lasers.", Appl. Phys. Lett., vol.69, 471 (1996).

[2] K. D. Choquette, K. M. Geib, H. C. Chui, B. E. Hammons, H. Q. Hou, T. J. Drummond, and R. Hull, "Selective oxidation of buried AlGaAs versus AlAs layers.", Appl. Phys. Lett., vol.69, 1385 (1996).

[3] E. R. Hegblom, D. I. Babic, B. J. Thibeault, and L. A. Coldren, "Estimation of scattering losses in dielectrically apertured vertical cavity lasers.", Appl. Phys. Lett., vol.68, 1757 (1996).

[4] G. R. Hadley, "Effective index model for vertical-cavity surface-emitting lasers.", Optics Letters, vol.20, 1483 (1995).

[5] N. M. Margalit, D. I. Babic, K. Streubel, R. P. Mirin, R. L. Naone, J. E. Bowers, and E. L. Hu, "Submilliamp long wavelength vertical cavity lasers.", Elect. Lett., vol.32, 1675 (1997).

[6] D. I. Babic, “Double-fused long-wavelength vertical-cavity lasers”, Ph.D. Disseration, University of California, Santa Barbara, ECE Tech. Rep. #95-20(1995).

[7] S. Seki, K. Yokoyama, and P. Sotirelis, "Theoretical analysis of high-temperature characteristics of 1.3- mu m InP-based quantum-well lasers.", IEEE Journal of Selected Topics in Quantum Electronics, vol.1, 264 (1995).

[8] S. Jong-In, M. Yamaguchi, P. Delansay, and M. Kitamura, "Refractive index and loss changes produced by current injection in InGaAs(P)-InGaAsP multiple quantum-well (MQW) waveguides.", IEEE Journal of Selected Topics in Quantum Electronics, vol.1, 408 (1995).

[9] F. Salomonsson, K. Streubel, J. Bentell, M. Hammar, D. Keiper, R. Westphalen, J. Piprek, L. Sagalowicz, A. Rudra, and J. Behrend, "Wafer fused p-InP/p-GaAs heterojunctions.", J. Appl. Phys., vol.83, (1998).

10 P. Abraham, work to be published.

Chapter 6

Dynamic Performance and System Experiments

6.01 Introduction

In the previous chapter, the emphasis of the analysis was placed on the DC performance of the lasers. The DC performance would be enough if the laser was modulated by an external modulation, but for direct modulation links, the dynamic behavior of the lasers is also of importance. In this chapter, I will emphasize some of these dynamic characteristics, as well as some practical considerations in using long-wavelength VCLs in link experiments. Issues such as modulation bandwidth, side-mode suppression ratios(SMSRs), polarization switching, and linewidth will be examined. The focus of the analysis will be on

generation B devices, as described in the previous chapter, because these devices were the best available devices at the time these experiments were conducted. In this generation's devices one could achieve reasonable fiber-coupled cw output powers, desirable for link experiments. Single-mode and multimode devices were also available on the same wafer enabling analysis of the differences in performance when using single-mode versus multimode. I begin the chapter with the general motivation of why we expect a high bitrate-distance product using 1.5 μm VCLs in contrast to using more conventional GaAs based VCLs. However, before proceeding, I would like to acknowledge the major role Sheng Z. Zhang played in making most of these experiments.

6.02 Overview of VCL Transmission Experiments

Transmission experiments with VCLs have been reported with laser wavelengths of 0.67 [1], 0.85 [2], 0.98 [3,4,5], and 1.5 μm [6]. The problems and advantages of each wavelength were discussed in Chapter 1. Here, to emphasize the importance of using 1.5 or 1.3 μm lasers, we plot in Figure 6.01 the theoretical dependence of maximum transmission distance on the bit rate for different operating wavelengths. On this same plot we also show some of the reported transmission experiments with VCLs. The solid lines show the

dependence of the loss-limited transmission distance as a function of bit rate for different wavelengths while the dashed lines show the dispersion-limited distance.

Multimode fiber (MMF) systems are usually preferred over single-mode systems for short distance data communication links for reasons of packaging, reliability, and cost. For this reason, most of the transmission experiments with laser wavelengths shorter than 1.0 μm were performed with multimode fiber. Intermodal dispersion is usually the dominant limiting factor in these systems. As a result of intermodal dispersion, modal noise, which is exhibited as fluctuations of the speckle patterns observed in the multimode fiber, strongly degrades the system performance. Modal noise is formed by the interference of the modes from a coherent source when the coherent time of the source is greater than the intermodal dispersion time within the fiber. The conditions that give rise to modal noise are: 1) a coherent source with a narrow spectral width and 2) disturbances or mode selective loss along the fiber. Multimode lasers are much less coherent and thus are less sensitive to mode selective loss in the fiber.

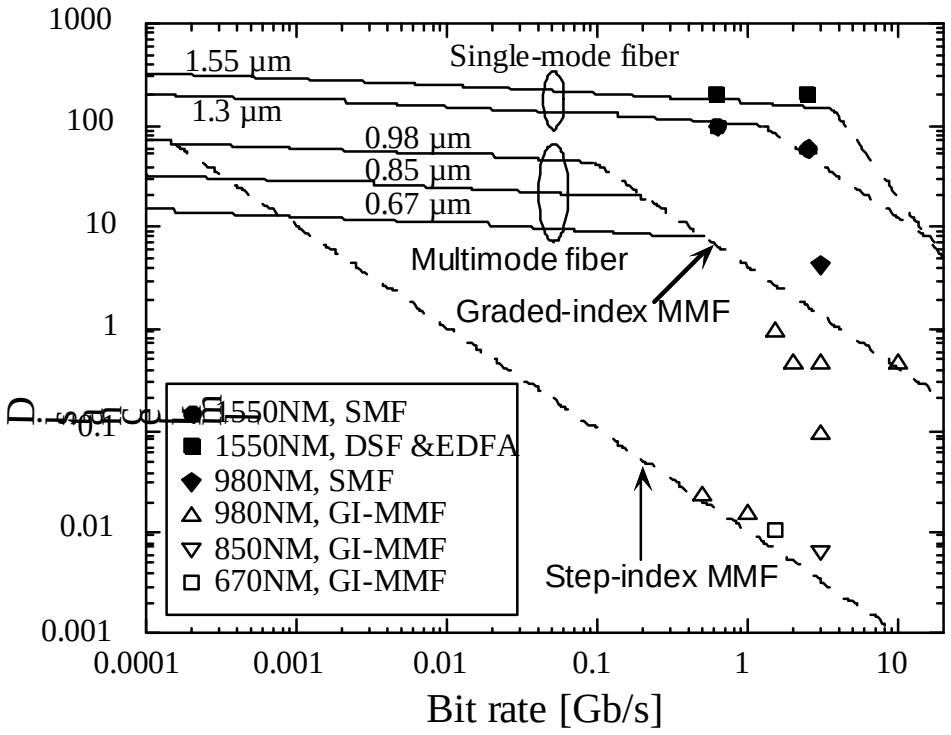

Figure 6.01. Theoretical and experimental plot of maximum transmission distance versus bit rate. Points are taken from literature.

As shown in Figure 6.01, intermodal dispersion starts dominating over fiber loss for bit rates higher than 100 Mb/s in multimode fiber systems. The maximum achievable distance with step-index multimode fiber is limited to 10 and 1 meter for bit rates of 1 Gb/s and 10 Gb/s, respectively, which excludes the use of step-index fiber for such high-speed applications.

Considerable improvement can be achieved by using graded-index multimode fiber, in which maximum transmission distance can be several

hundred meters to several kilometers for bit rates of 10 Gb/s to 1 Gb/s. The longest distance demonstrated with graded-index MMF is 1.0 km at 1.5 Gb/s [3], while the reported largest bit rate-distance product is 5 Gb/s km [5]. The intermodal dispersion can be further reduced by using single-mode fiber. However, the intermodal dispersion still exists for GaAs based lasers if one uses standard telecom single-mode fiber(SMF). This is because standard SMF was designed for longer wavelengths, and it guides two modes even at 980 nm(longest wavelength achievable in GaAs based lasers). This has limited the maximum reported transmission distance at these wavelength to 4.3 km [4]. There is no such limit for 1.5-μm VCLs, in which we now discuss transmission over 200 km of single-mode fiber.

6.03 Digital Transmission Experiments

We begin this section with a general description of the 2.5 Gb/s digital transmission experiments conducted using the long-wavelength VCLs. In the subsequent sections, we will go over some of the device characteristics that allowed for such a transmission experiment, as well as some of the limitations on the devices to higher bit rate performance. Figure 6.02 shows the schematic diagram of the experiment set-up for testing link performance.

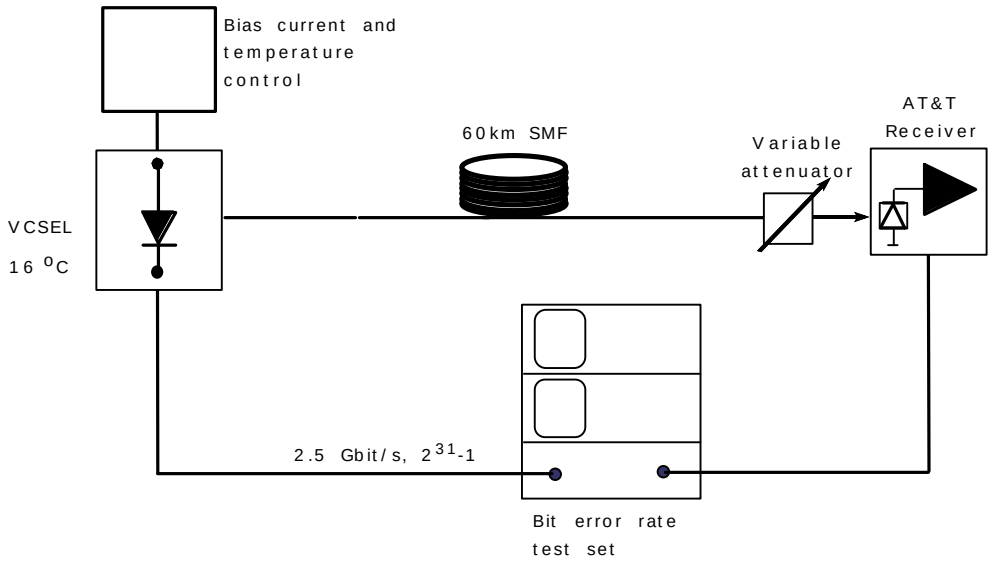

Figure 6.02. Schematic diagram of 2.5 Gb/s transmission experiment.

The devices were mounted on a temperature controlled brass plate at 16°C. A Rucker-Koll probe was used for contacting the p-contact on top of the pillars. The bottom-emitted light was coupled into an angle-polished single-mode fiber through a hole in the stage. The maximum coupling of light into the single-mode fiber was accomplished by use of a Graded Index(GRIN) lens. The 7-μm diameter generation B devices were used for the single-mode transmission experiments. Figure 6.03 shows the light versus current characteristics of the laser diode used in much of the experiments. The plot shows that a 70% coupling efficiency could be achieved into the fiber. We also plot the power

through a grin with the use of an isolator. No isolator was used in the actual experiments, the reason for which will be explain later.

In each of the experiments, the coupled light was put through some distance of optical fiber followed by an optical attenuator and a digital receiver. The optical attenuator was used to control the average received power at the detector. In this way, plots could be made of bit-error rate versus average received power. The AT&T(Lucent) 1319B Lightwave receiver was used, with a bandwidth of 2.5 GHz. The signal from the receiver was put through a 1.87 GHz low-pass filter to "clean" the eye diagrams. The resultant signal was placed either into a sampling scope, or the bit-error rate tester(BERT). The signal from the BERT was a pseudo-random bit sequence(PRBS) of 2^{31}-1 at 2.5 Gb/s. The signal was used to modulate the laser through the use of a high frequency bias-tee.

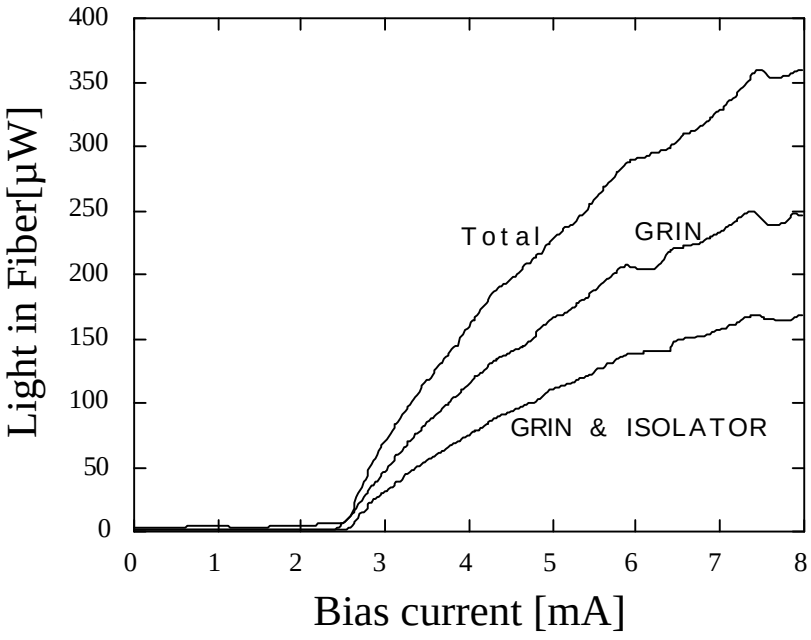

Figure 6.03. Light versus current characteristics using GRIN lens for coupling.

6.04 System Results

In achieving long-distance transmission through fiber, some of the most important factors are the conditions of laser operation. The bias point for the lasers, as well as the depth of modulation, become critical to achieving maximum performance operation. These factors directly affect the maximum transmission distance that can be achieved with a given bit error rate(BER). Figure 6.04 shows a schematic L-I curve for a laser, with labels for some of the key terms. The extinction ratio is the ratio between the power in the off-state

and the on-state. Since BER diagrams plot the BER versus average received power, and not modulated power, there is an inherent power penalty with a lower extinction ratio. Only if the off-state power is zero(an infinite extinction ratio) is there no inherent extinction ratio penalty. The extinction ratio penalty has a simple formulation for systems using a pin receiver as we are using. Equation 6.01 expressed this formula as such[7]:

$$d_{ex} = 10 \log_{10}\left(\frac{1 + r_{ex}}{1 - r_{ex}}\right) \qquad (6.01)$$

The modulation depth is the ratio of the modulated optical power to the high level optical power. An infinite extinction ratio would correspond to a modulation depth of 100%. Due to the extinction ratio penalty, the larger the modulation depth, the less average optical power is necessary at the receiver. To reduce this penalty, one could place the bias point close to threshold, or increase the modulation current such that the low-power state is near threshold. However, as will be seen later, to achieve a certain modulation frequency from the laser, the bias point must be placed well above threshold. To achieve low extinction ratio penalty as well as a large modulation frequency, one can bias the device well above threshold and increase the modulation current.

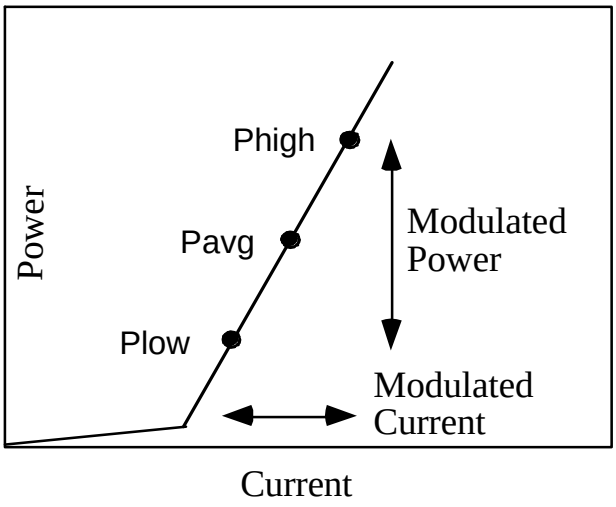

Figure 6.04. Schematic showing average bias and modulation depth.

There is, although, another penalty that comes in to play when one has a large modulation depth. This penalty is associated with the frequency shifting of the device with current modulation. This shifting is called chirp and makes the laser linewidth wider than would be expected ordinarily. Going through a dispersive medium such as in fiber, frequency chirping broadens optical pulses, causing a power penalty. The amount of chirp with which a laser is associated is called the linewidth enhancement factor a. This a can be different for different lasers, and will be discussed in a subsequent section of this chapter. However, the frequency chirp of any semiconductor laser can be expressed as Equation 6.02[7]:

$$\Delta n(t) = \frac{a}{4p}\left(\frac{d}{dt}\ln P(t) + kP(t)\right) \qquad (6.02)$$

Increasing the extinction ratio will increase the “adiabatic” frequency chirping(*kP(t)* term) between the on- and off-states. The extinction ratio penalty and chirp penalty counterbalance to give an optimum modulation depth for maximum transmission distance.

Figure 6.05 shows the bit-error rate versus received average power while transmitting over 0-,30-, and 60-km standard SMF. The power penalties at 30 and 60 km were 1.4 and 3.2 dB, respectively. The optimum bias current and modulation voltage were 4.4 mA and 0.47 V, respectively for the 60 km transmission case. These conditions gave an extinction ratio of 1.8:1, yielding an inherent power penalty of 5.4 dB.

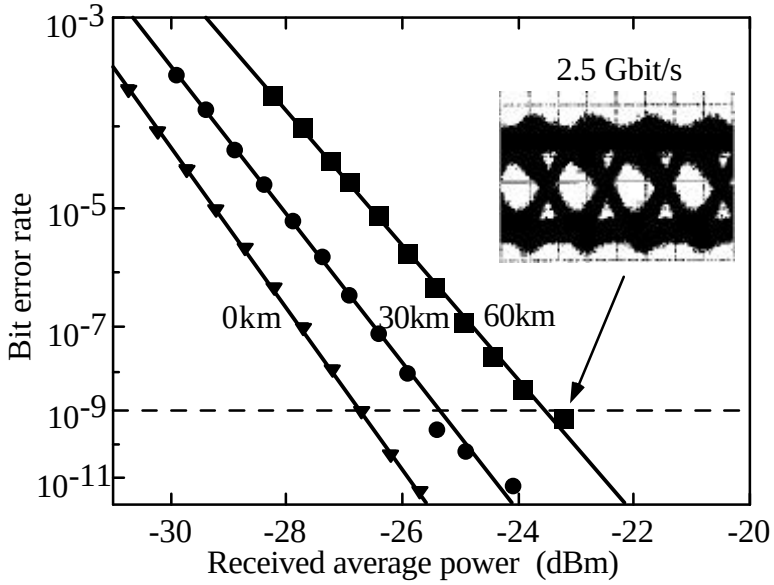

Figure 6.05. Bit-error rate versus received power for 2^{31}-1 PRBS data.

Using a higher extinction ratio causes a greater power penalty, suggesting that dispersion is critical to limiting transmission distance. The inset of Figure 6.05 shows the eye diagram at 10^{-9} BER after 60 km of dispersive fiber. To confirm that dispersion plays an important role in the transmission system we conducted another experiment with dispersion-shifted fiber. In this case, transmission over 75 km of fiber with dispersion minimum at 1.56 μm was accomplished. Figure 6.06 shows the bit-error rate as a function of the received average power while transmitting over 0 km and 75 km dispersion-shifted fiber, with the triangles and circles representing the BER at 0 km and 75 km, respectively. A bit-error rate better than 10^{-10} was achieved at a received optical power of -28.4 dBm

after 75-km transmission. A bias current of 4.4 mA and a modulation voltage of 0.6 V(corresponding to 2.2:1 on-off ratio) were used.

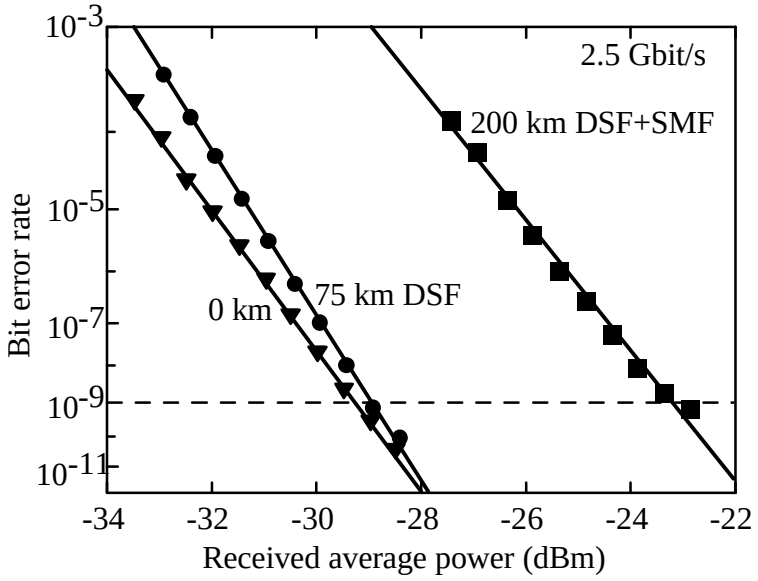

Figure 6.06. Using DSF longer distance transmission can be achieved.

The power penalty after 75-km DSF was only 0.3 dB. We see in this case that the optimum extinction ratio was much larger. In addition, the power penalty with this extinction ratio was quite small. This low-power penalty with dispersion-shifted fiber shows that with standard SMF we were indeed experiencing a dispersion power penalty.

Additional measurements were done with the use of an optical amplifier. Transmission at 2.5 Gb/s over 200 km was observed with a BER less than 10^{-9}. The erbium-doped fiber amplifier(EDFA) with a gain of about 30 dB

was inserted after 70 km of fiber and was followed by a 3-nm optical band-pass filter. The 200-km fiber consisted of 60, 40, and 100-km single-mode fibers successively with dispersion zero wavelengths of 1.31, 1.54, and 1.56 μm. The rectangles in Figure 6.06 show the BER versus the received average power. We see the power penalty was 6.1 dB after 200-km of fiber. The BER was limited by the available optical power, as the attenuator was set to zero to achieve the 10^{-9} BER at 200-km. The use of EDFA with VCLs is contrary to what was discussed to in the first chapter as EDFAs are very expensive. So, solely investigative reasons motivate such a long-distance experiment.

6.05 Modulation Response

As was shown in the previous section, the modulation response of a laser plays an important role in transmission experiments. One would like to use a high extinction ratio, which means modulating the device closer to threshold, but if one gets too close to threshold, the laser will not have the necessary modulation response.

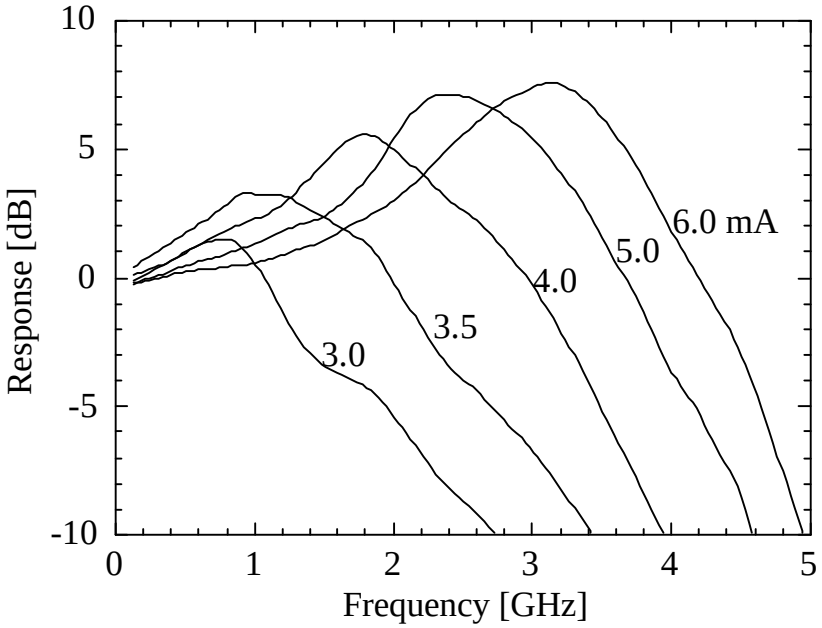

Figure 6.07. Small signal modulation response from VCL.

Figure 6.07 shows the small-signal(0 dBm) modulation response of the laser used in the digital transmission experiments. We see that we get multi-gigahertz operation for relatively small bias currents, as was discussed in the Chapter 1. In the absence of gain compression and device heating, one would expect the bandwidth of the device to scale as the square root of the current above threshold. Solving the single-mode photon and carrier density rate equations, one gets the familiar formula[7]:

$$w_R = \left[\frac{\Gamma v_g dG(I - I_{th})}{q} \right]^{1/2} \qquad (6.03)$$

where w_R is the relaxation oscillation frequency, dG is the differential gain, G is the confinement factor, v_g is the group velocity and q is the electronic charge. The 3-dB bandwidth of a laser is usually 1.55 times its relaxation oscillation frequency[8].

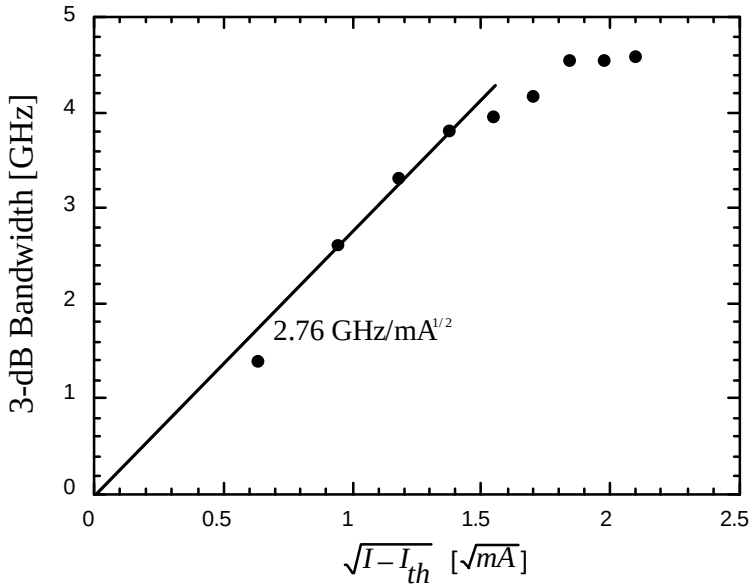

Figure 6.05. Measured 3-dB bandwidth from VCL.

In Figure 6.05 we plot the 3-dB bandwidth versus the square root of current above threshold. According to Equation 6.03 the points should fall on a straight line. The slope of this line is call the modulation current efficiency factor(MCEF). This specific laser has an MCEF of 2.76 GHz/mA$^{1/2}$, and the maximum 3-dB modulation frequency is 4.8 GHz. This maximum-modulation frequency limit could be coming from several factors not inherent to the device,

including bondpad capacitance and inductances with the current probe. One way to examine the inherent bandwidth in a laser is to measure the peak in the relative intensity noise(RIN) from the laser. In doing so, one excludes all capacitances and probe problems, but keeps transport and heating issues limitations. Figure 6.06 shows the calculated 3-dB frequency of the laser from the RIN measurements. We see that indeed the inherent bandwidth of the device is larger than the 4.8 GHz measured.

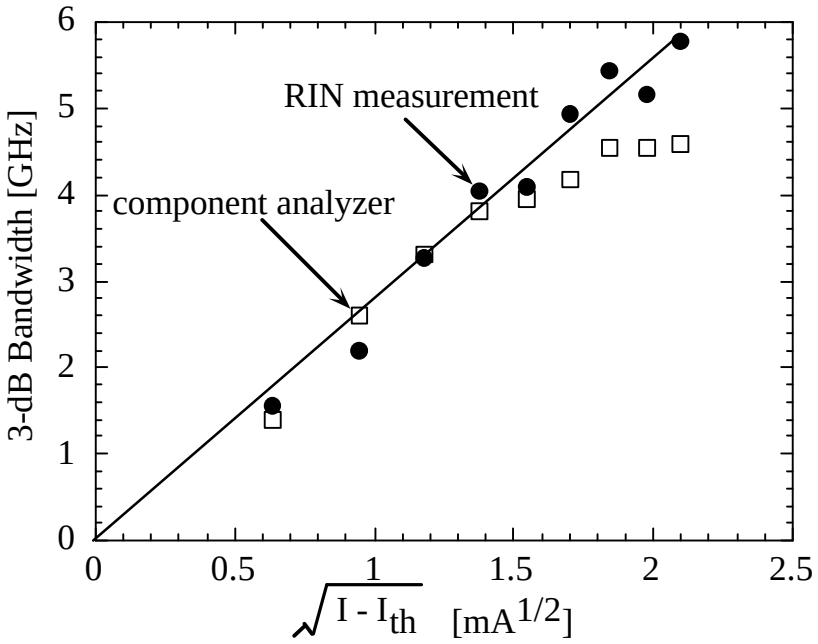

Figure 6.06. Inherent bandwidth of VCL higher than measured bandwidth.

The limiting factor in the modulation bandwidth is believed to be due to the ground connection of the coax probe used to bias the device. The reason the probe is blamed is two-fold. One is that this type of probe is not specified to be used at such high frequencies. Only by shortening the ground connection to a 2 mm length could we even get to 5 GHz. The second reason is that the original oxidized double-fused lasers were also measured using the same type of probe. The frequency response of these lasers are plotted in Figure 6.07. Yet again we see that the characteristics of the devices are quite different. Only 3.5 mA is necessary to reach maximum frequency. We also see again, however, a very strong dip at 4.8 GHz. It is possible that these two very different lasers have exactly the same frequency response, but this seems very unlikely. The common factor in the two experiments is the coax probe.

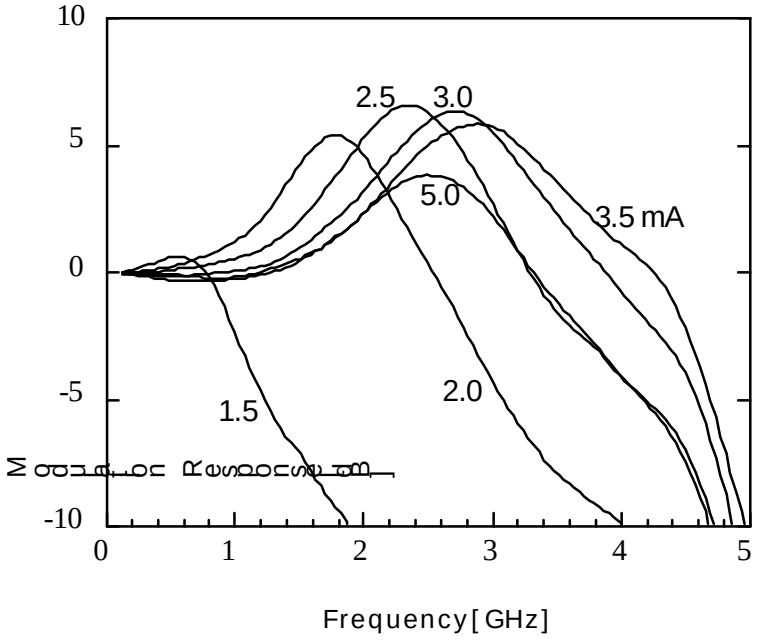

Figure 6.07. Original oxide VCLs modulation response.

To get a better idea of some of the characteristics of the devices we can fit the modulation response to a general transfer function[9].

$$|M(f)|^2 = \frac{1}{1+(f/f_L)^2} \cdot \frac{f_0^4}{(f_0^2 - f^2)^2 + (g/2p)^2 \cdot f^2} \qquad (6.04)$$

where *M(f)* is the normalized ratio of the small signal light output to the modulation current, *f* is the modulation frequency, f_0 is the resonant frequency, f_L is the parasitic roll-off frequency, and *g* is the damping rate. The K-factor, defined as $g = K \cdot f_0^2 + g_0$ with g_0 a constant, was found by fitting to be 0.37 ns, indicating an intrinsic bandwidth of 24 GHz ($f_{\max} = 2p\sqrt{2}/K$). This bandwidth

does not represent issues related to heating of the device but does include issues such as transport and gain compression. We can now go on to the other important issue limiting the transmission experiment, namely the spectral width of the source.

6.06 Optical Spectrum

As discussed in the previous chapter, generation B offered highly single-mode device as well as multimode devices. Figure 6.08 depicts a typical spectrum of the device used in the transmission experiments. The spectrum is shown under DC bias and also under 60% modulation at 2.5 Gb/s. We see that the high SMSR of over 50 dB is maintained through dynamic modulation. The reason for the high SMSR is the very weak index guiding of the oxide aperture. The very weak guiding means the confinement factor for the fundamental mode is reduced, as discussed in the previous chapter. The reason for the high SMSR is that the higher order modes have even a lower overlap with the gain region. The overlap with the center of the device where gain is present is much lower for higher order modes. In larger devices, the confinement factor for the modes goes to one so that the differential between higher order mode gain and fundamental mode gain is lost.

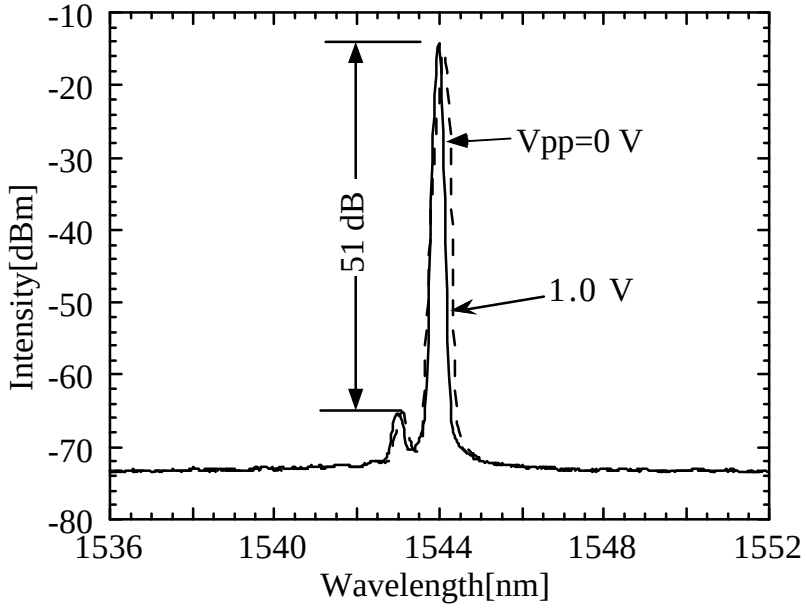

Figure 6.08. Stable high SMSR under 60% optical modulation.

Figure 6.09 on the next page shows a typical spectrum of one of the 14-μm device in generation B. We see that the spectrum is clearly multimode. These devices are multimode throughout the entire L-I curves. These spectrums were measured through light coupled into a single-mode fiber, as used in the transmission experiments. The high SMSR of the smaller devices used in the transmission experiment show that we probably do not have a power penalty due to multimode interference in the laser. A 50-dB SMSR is more than enough to conduct high-speed long-distance links.

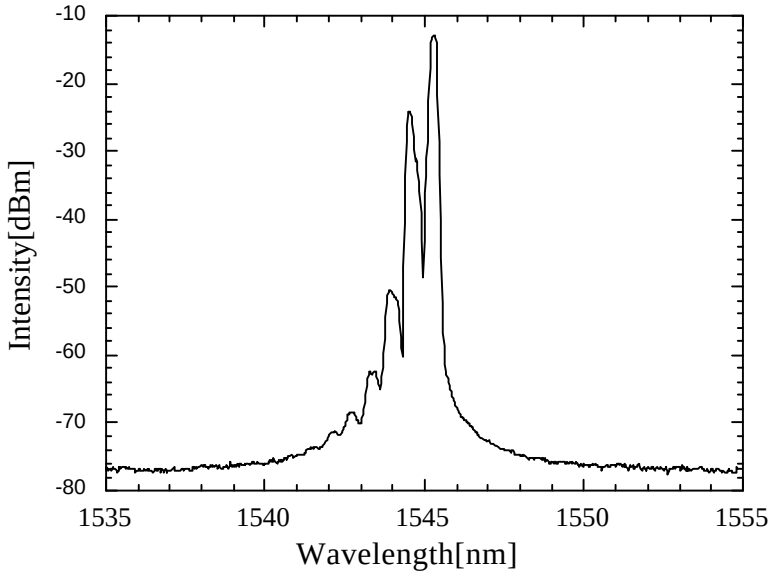

Figure 6.09. Multimode spectrum of largest devices of generation B.

6.07 Frequency Chirp

To get the spectral width of a single-mode laser, we need its linewidth, as well as its linewidth enhancement factor. For high bit-rate transmission, one of the most important parameters for a directly modulated laser is the chirp parameter, or linewidth enhancement factor a. An easy and accurate method for measuring laser chirping parameter is by using an HP8703 network analyzer to measure the frequency response of a dispersive single-mode fiber upon the chirped optical pulse [10]. To cancel the bandwidth contributions of the laser feeding circuitry, the modulation response of the laser, and the response of the

receiver, a calibration measurement was first performed by recording the frequency response curve of the whole link without the dispersive fiber. All subsequent frequency responses with the dispersive fiber are then divided by this reference curve. An erbium doped fiber amplifier (EDFA) was inserted before the fiber to increase the signal level. Resonance frequencies show up as sharp peaks in the frequency response. The u^{th} resonance frequency f_u and the chirp a of the laser follows a simple relation[10] :

$$f_u^2 L = \frac{c}{2Dl^2}(1 + 2u - \frac{2}{p}\arctan(a)) \qquad (6.05)$$

where u = 0, 1, 2, … is the order of the resonance frequency, L is the length of the fiber, D is the dispersion of the fiber, c is the speed of light, and l is the wavelength of the laser. Figure 6.10 shows the resonance frequencies of the fiber with a VCL source.

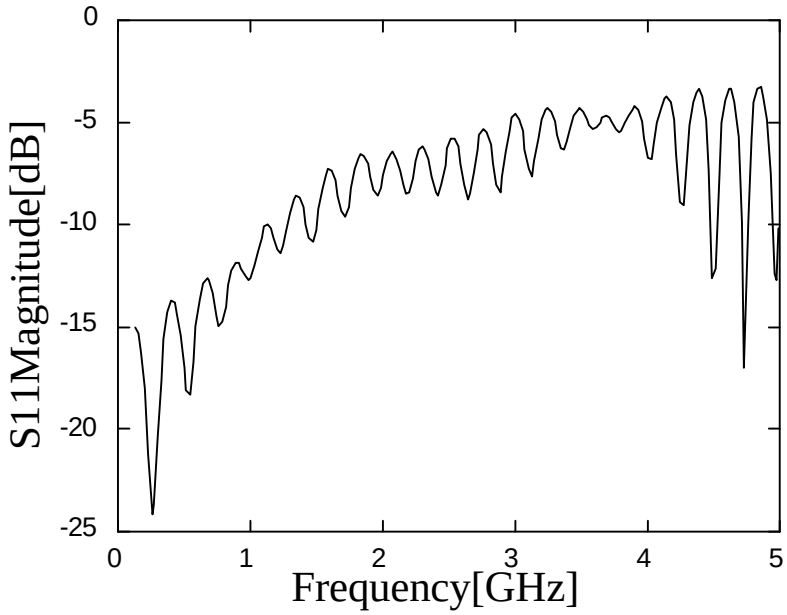

Figure 6.10. Measurement of linewidth enhancement factor.

By fitting the measured $f_u^2 L$ product as a function of $2u$, both the dispersion and the linewidth enhancement factor can be obtained. Figure 6.11 shows the result of this fitting at different bias levels of the laser. We can read from the plot, the a parameter was 4.0±0.1, while the dispersion D was 16.0 ps/(nm km) at 1.543 μm. This a factor is comparable to a good DFB laser diode.

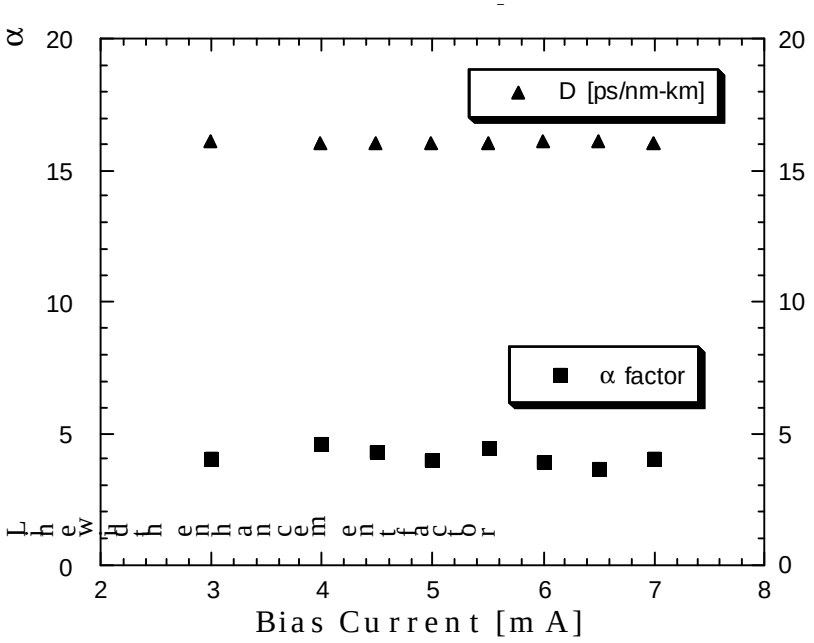

Figure 6.11. Result of linewidth enhancement measurement.

6.08 Linewidth and Polarization Switching

The final important factor to measure to get a idea of the spectral width of the laser is the cw linewidth of the laser. This factor was measured with a self-homodyne measurement [11]. Figure 6.12 shows the measured laser cw linewidth as a function of the inverse of the total optical power. The minimum linewidth was as narrow as 39 MHz at an optical power of 270 μW. This minimum linewidth is comparable to 980 nm VCLs [12]. The fluctuations of the linewidth around the straight line is due to the cross-coupling between two

competing lasing modes of orthogonal polarization, which is also the cause for the relatively high residual linewidth.

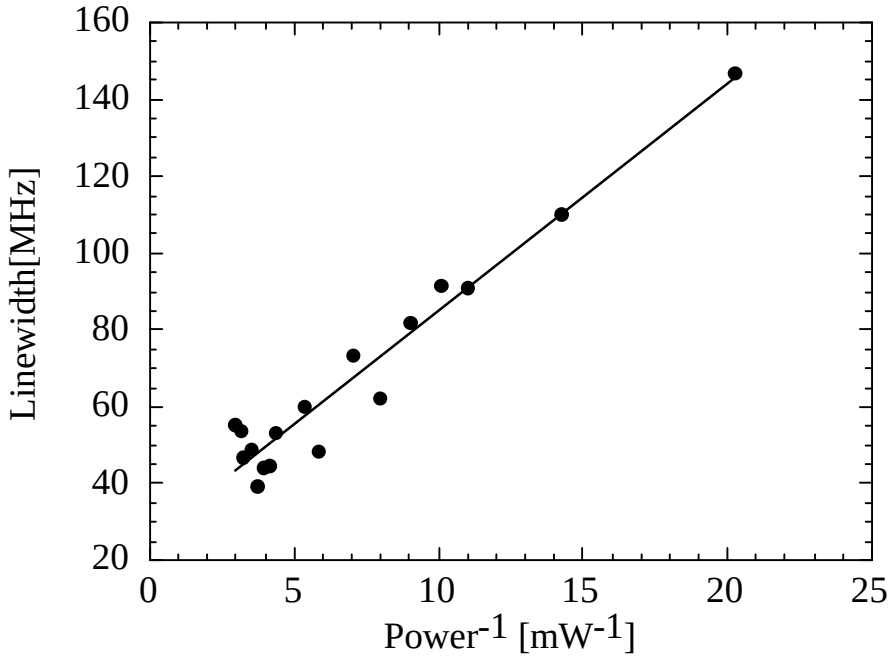

Figure 6.14. Linewidth of device used for 2.5 Gb/s experiment.

In a circularly symmetric laser such as a VCL even if one has only a single longitudinal mode, two orthogonal polarization modes can arise due to the circular symmetry. There has been significant research effort in breaking this symmetry for GaAs based lasers[13,14]. These efforts include making non-circular devices and introducing a polarization selective loss elements. Due to the very similar structure between our long-wavelength laser, and GaAs based structures, it is likely that an effective solution for polarization stability in the

GaAs based lasers will also work in our case. As of yet, we have not incorporated these techniques to stabilize the polarization. Figure 6.15 shows a polarization resolved L-V curve of the VCL used in the transmission experiment. We see regions where one polarization is completely dominant and regions where the other polarization is completely dominant. The switching between the two modes caused low frequency noise in the laser, seen in the linewidth measurement. Such noise could cause problems for the transmission experiment. To avoid this problem, we did not have any elements that were polarization selective in our link experiment.

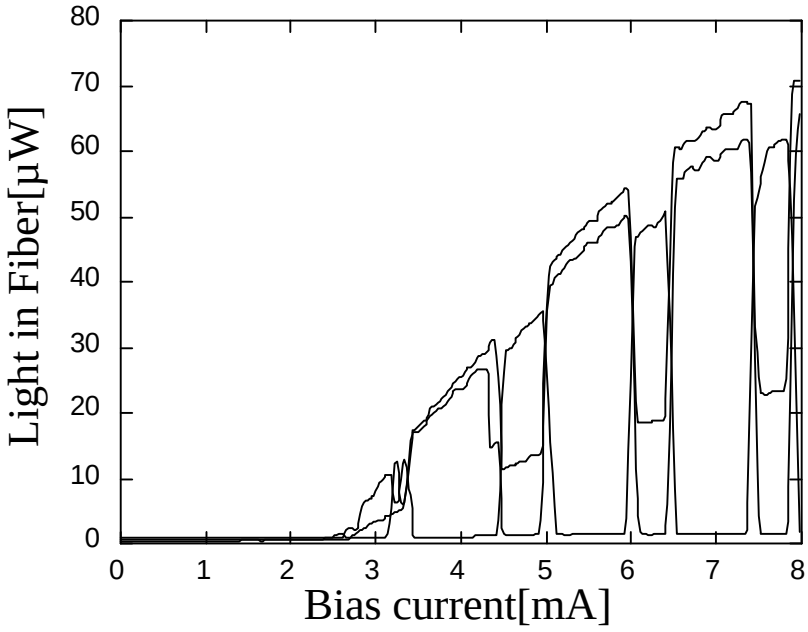

Figure 6.15. L-I curve at 0,45,90 degrees polarization for VCL.

Since our isolator was polarization sensitive, we needed to remove it to achieve maximum performance. We did not have available at the time a polarization insensitive isolator, but such devices are quite common. We might expect further improvements by using such a device, or by stabilizing the polarization of the laser.

6.09 Summary

The link experiments in this chapter represent the possibility of using long-wavelength VCLs in high-speed, medium-distance links. We demonstrated an unamplified link of 60 km at 2.5 Gb/s. As device performance improves, one would like eventually to complete an equivalent transmission experiments over the full temperature range of 0-70°C. This would mark a great development in VCL research. These devices performed on an equivalent level to a competing DFB laser diode at room temperature. The SMSR available and chirp of the VCLs were found to be very similar to a good DFB laser. However, more output power from the VCL would help improve the maximum transmission distance. In the final chapter, we will examine what can be done to further improve device performance.

6.10 References

[1] D. M. Kuchta, R. P. Schneider, K. D. Choquette, and S. Kilcoyne, "Large- and small-signal modulation properties of red (670 nm) VCSELs.", IEEE Photonics Technology Letters, vol.8, 307 (1996).

[2] D. M. Kuchta, R. A. Morgan, K. Kojima, M. T. Asom, G. D. Guth, M. W. Focht, and R. E. Leibenguth, "Multiple transverse mode VCSEL's for high speed data communications.", LEOS '93 Conference Proceedings. IEEE Lasers and Electro-Optics Society 1993 Annual Meeting (Cat. No.93CH3297-9), 372 (1993).

[3] H. Kosaka, K. Dutta, K. Kurihara, Y. Sugimoto, and K. Kasahara, "Gigabit-rate optical-signal transmission using vertical-cavity surface-emitting lasers with large-core plastic-cladding fibers.", IEEE Photonics Technology Letters, vol.7, 926 (1995).

[4] U. Fiedler, B. Moller, G. Reiner, D. Wiedenmann, and K. J. Ebeling, "Proton implanted VCSEL's for 3 Gb/s data links.", IEEE Photonics Technology Letters, vol.7, 1116 (1995).

[5] U. Fiedler, G. Reiner, P. Schnitzer, and K. J. Ebeling, "Top surface-emitting vertical-cavity laser diodes for 10-Gb/s data transmission.", IEEE Photonics Technology Letters, vol.8, 746 (1996).

[6] S. Z. Zhang, N. M. Margalit, T. E. Reynolds, and J. E. Bowers, "1.54-mu m vertical-cavity surface-emitting laser transmission at 2.5 Gb/s.", IEEE Photonics Technology Letters, vol.9, 374 (1997).

[7] G. P. Agrawal, *Fiber-optic communications systems*, Wiley, New York(1992).

[8] L. A. Coldren, S.W. Corzine, *Diode lasers and photonic integrated circuits*.,Wiley, New York, (1995).

[9] R. Nagarajan, T. Fukushima, J. E. Bowers, R. S. Geels, and L. A. Coldren, "High-speed InGaAs/GaAs strained multiple quantum well lasers with low damping.", Appl. Phys. Lett., vol.58, 2326 (1991).

[10] F. Devaux, Y. Sorel, and J. F. Kerdiles, "Simple measurement of fiber dispersion and of chirp parameter of intensity modulated light emitter.", Journal of Lightwave Technology, vol.11, 1937 (1993).

[11] D. M. Baney and W. V. Sorin, "Linewidth and power spectral measurements of single-frequency lasers.", Hewlett-Packard Journal, vol.41, 92 (1990).

[12] W. Schmid, C. Jung, B. Weigi, G. Reiner, R. Michalzik, and K. J. Ebeling, "Delayed self-heterodyne linewidth measurement of VCSELs.", IEEE Photonics Technology Letters, vol.8, 1288 (1996).

[13] K. D. Choquette and R. E. Leibenguth, "Control of vertical-cavity laser polarization with anisotropic transverse cavity geometries.", IEEE Photonics Technology Letters, vol.6, 40 (1994).

[14] P. Dowd, P. J. Heard, J. A. Nicholson, L. Raddatz, I. H. White, R. V. Penty, G. C. Allen, S. W. Corzine, and M. R. T. Tan, "Complete polarisation control of GaAs gain-guided top-surface emitting vertical cavity lasers.", Elect. Lett., vol.33, 1315 (1997).

Chapter 7

Conclusions and Future Work

7.01 Overview

Through the first six chapters, we have looked at long-wavelength vertical-cavity lasers from several different perspectives. In Chapter 1, we articulated the demand for such devices based upon the vertical-cavity laser as an inexpensive source for fiber optic communications. To be commercially successful, several technical requirements had to be satisfied. The most difficult of these demands is the wide temperature range of operation. To avoid the use of thermoelectric coolers, the devices must be able to operate to the datacom

specification of 0 to 70°C, or the telecom specification of -40 to 85°C. Meeting these specifications has been a major goal of long-wavelength vertical-cavity laser research for some time. To achieve the required range of operation, the device structure must be carefully designed. In Chapter 2 we examined the design issues in making high-performance devices. These issues could be classified into two categories: 1) one-dimensional cavity issues, such as round-trip loss and gain, and 2) three-dimensional issues such as current spreading, optical confinement, and heating. Each of these issues plays an important role in the performance of fabricated devices. Before analyzing the actual generations of devices fabricated, two chapters were dedicated to the fabrication of such devices. One of these chapters was exclusively devoted to the subject of wafer fusion, since this was one of the unique elements of our structure. Here, a detailed analysis of the fused junction was presented. This analysis included chemical and electrical, as well as structural analysis of the junction between InP and GaAs. The knowledge from this chapter was later used in analyzing the overall device performance. In the fourth chapter, on fabrication, the actual process of making the top-emitting VCLs was described. With a complete description of the fabrication process complete, we moved on to the actual devices fabricated. Several generations of devices were analyzed in this chapter, with a special emphasis on particular aspects of the device

structure in each generation. With all the device generations one can gain a complete picture of the design of fused vertical-cavity lasers. Finally in Chapter 6, the devices were tested in link experiments to verify their vaibility in real systems. Dynamic characteristics of the device were investigated and measured for usefulness in high-speed digital-transmission experiments.

7.02 Contributions

This section summarizes the fundamental contributions and accomplishments presented in this thesis. The most obvious achievement was the integration of the oxide aperture into the double-fused long-wavelength VCL. This integration was at the heart of the record performance of the devices presented. This integration, however, also introduced the new problem of current spreading around the aperture. Hegblom and I worked on a simple model to describe this current spreading, which eventually yielded a relatively accurate and simple formula for current spreading in VCLs. The second contribution in this thesis was the detailed study of the fused junction. Before our work in this field, it was assumed that the fused junction voltage was negligible compared to the p-mirror resistance. In the oxide aperture VCL, with properly designed mirror layer, this assumption was not true. An extensive

analysis was undertaken to study this fused junction voltage. We found an excessive amount of oxygen in all the fused junction samples. This oxygen was believed to be the cause of the excess one volt drop across the p-InP/p-GaAs junction.

Another major advancement in this thesis is the improvement in device structure. The top-emitting structure has many advantages over the simple bottom-emitting structure of the original double-fused VCLs. First, significantly higher output powers can be realized through the elimination of the power flow through the substrate. Second, and more importantly, the new device design allows for a packagable device. The final device structure could be easily integrated into most packages, due to the simple bondpads on top of the devices, and the top-emitting nature. The devices could be directly mounted without the need for a complex flip-chip bonding process. This development should allow for extensive life-time testing of the devices in the near future.

In the analysis chapter, two new techniques were developed to extract important parameters from devices. This first was the measurement of injection efficiencies of devices through the detection of spontaneous emission power. This technique allowed for direct measurement of injection efficiencies of individual devices. With this information one could extract important

parameters such as the round-trip loss and gain in a device. If the devices had varying internal losses, one could also extract the gain curve for the active region. The second new measurement technique is used to determine the thermal resistance of a devices as well as the predicted maximum pulsed temperature. Essentially, one plots the electrical power dissipated at full rollover point versus ambient temperature. This very simple technique demonstrates graphically where improvements can be made in the maximum cw operating temperature.

Finally, numerous records for long-wavelength VCLs were reported. These include: lowest pulsed threshold, lowest cw threshold, highest cw temperature operation, highest pulsed-temperature operation, maximum room-temperature cw output power, maximum high-temperature cw output power*, highest modulation response*, maximum SMSR, longest transmission distance*, and maximum bitrate-distance product*. (The parameters with asterisks have never been reported by any other group so we have the *de facto* record in this area.) The threshold current record of 0.8 mA pulsed was achieved with the generation A devices. In these devices, we were able to get rid of size-dependent losses with a very weak oxide index perturbation. The reason for the very low threshold on these devices, in contrast to later devices, is the shallow oxidation in this generation. This shallow oxidation of 4 μm

limited the current spreading between the fused junction and the oxide aperture. Later generations were designed with a deep oxidation. The larger oxidation depths led to reduced differential and thermal resistances in the devices. This allowed for much higher cw powers to be demonstrated. In addition, the larger oxidation depths facilitated the development of the top-emitting structures. The deep oxidation allowed the top ring contact to be a reasonable 10 μm wide, without interfering with the optical mode. A shallow oxidation of 4 μm would require extremely thin rings with very precise alignment tolerances. The top-emitting structure allowed for still higher cw output powers while still maintaining a record high maximum cw operating temperature.

In the generation A devices, 64°C cw operation was achieved for the first time. This improvement was mainly due to the reduced losses in the devices relative to the 33°C cw devices fabricated by Babic *et al.* In these early devices, however, the power was quite low due to the low transmission of the output mirror. In addition, the n-substrate absorbed much of the output power. The shallow oxidation on these device meant the differential resistances and thermal resistances were also high, so that the device would quickly roll over. The maximum room temperature cw output power was only about 100 μW. Nonetheless, this was still a significant improvement over the previous record devices which would only give a maximum cw room-temperature output power

of 40 μW. In the generation D top-emitting devices, one could still achieve 65°C cw operation, but the same device could put out 400 μW of cw power at room temperature. This is an order of magnitude improvement in maximum cw output power over the Babic 33°C devices, with a 22°C improvement in maximum cw operating temperature. This generation of devices could still put out 100 μW of cw output power even at 50°C. Eventually, the important record to be established will be the maximum cw output power at 70°C. But, for now, no such record exists because no long-wavelength VCLs lase at that temperature. The maximum temperature pulsed operation from generation C devices was a record 122°C. This record may even be a bit higher as this measurement was limited by the maximum stage temperature achieved. This shows the potential of devices to work at very high temperatures. A simple analysis of this potential is presented at the end of this chapter.

Finally, we also examined some of the dynamic behavior of the devices. We measured a record 4.8 GHz 3-dB bandwidth from the devices. We also determined that this bandwidth was limited by the type of coax probe we were using. From RIN measurements the inherent bandwidth of the device is expected to be above 7 GHz. The high SMSR of 50 dB from the devices were a result of the low index perturbation of the oxide in generation B devices. This technique was useful in achieving high power single-mode devices. The

minimum linewidth of the devices was measured to be about 40 MHz, limited by cross coupling between two polarization states. The linewidth enhancement factor was measured to be around 4, a reasonable value for a good DFB laser. The distances achieved in the link experiments were records for any VCL experiments. The low fiber loss at 1.5 μm allowed for such long distances with the very meager power of 300 μW in fiber. Without amplification, the maximum distance was 60 km(75 km in DSF), and with amplification, it was 200 km. All of these records point to the effectiveness of using wafer fusion with lateral oxidation in fabricating long-wavelength vertical-cavity lasers.

7.03 Remaining Problems and Unanswered Questions

Although many of the issues limiting the device performance were brought forth and analyzed, some problems remain a mystery. Among these is the origin of the fused junction voltage possibly due, as speculated in Chapter 3, to a high oxygen concentration at the fused junction. This explanation seems quite plausible, but must be confirmed by experimental data. The only way to confirm whether oxygen is the problem is somehow to get rid of the oxygen at the interface. In the future work section below, I describe a system that may allow for a low-oxygen fused junction. The second remaining mystery is the

origin of the very high fused junction voltage in generation D devices. The use of the p-mirror in this generation consistently yielded voltages on the order of 5-8 Volts. Independent tests of the mirror voltage concluded that, indeed, the excess voltage was in the fused junction. Although several experiments were devised to determine the origin of this excess voltage, none came up with a conclusive result. It is important to determine the origin of this problem so it does not reoccur in future generations of devices. One speculation as to the cause of this voltage is that growth on a p-type substrate may lead to poor surface morphology, somehow leading to very high fused junction voltage. There is no direct evidence to show that the surface morphology plays any role in the fused junction resistance. Another crucial aspect that is, as yet, relatively unknown is the reliability of the lasers. InP based lasers are typically very reliable. However, the fused junction introduces a unique element into their design. One must figure out the contribution of the fused junction to the degradation of such lasers if indeed such a contribution exists. We have only tested two devices over extended periods of time in this thesis. Still, we achieved over 4000 hours of cw operation from one of the devices, giving a promising result for future study. In conclusion, even with the extensive study in the fusion chapter, the majority of the unknowns in these devices remain at the fused junction.

7.04 Future Work

To improve device performance, future work in this subject should be focused on two areas. The first area of these is the removal of the oxide from the fused junction. In this work, we have nearly exhausted all wet chemical passivation treatments to prevent this oxide formation. These efforts were mostly fruitless, as we did not get any appreciable reduction of the oxygen concentration. To address the issue, one would like a system that could remove the oxide in an *in situ* oxygen-free chamber. The key to achieving this goal is to have the two wafers separated when placed into the chamber. In this way, one could remove the oxide on the two wafers, and then press them together without any exposure to air. Two possible ways to remove the oxide *in situ* are through sputtering, or through thermal desorption. In the case of the sputtering, one could use Argon ion gun to remove a very small amount of material from the surface, thus also removing the thin oxide at the surface. The challenge in this arrangement is how to etch both the InP and GaAs in the same chamber, as the two epi surfaces would be facing one another. The other challenge in designing such a system is to have a mechanical mechanism to apply pressure to the two wafers after oxide removal. In the case of thermal

desorption of the oxide, one would need a growth source to maintain the surface integrity during the high temperature desorption. This growth source could be an Arsenic flux, or a growth gas such as Arsine or Phosphine. In either case, the inclusion of such toxic sources considerably increases the complexity in building such a system. Figure 7.01 shows a schematic picture of a fixture that allows the wafers to be put into contact *in situ*. Figure 7.02 shows a load-locked system to apply pressure to the two wafers. The fusion fixture is placed on a cart which rolls along rails. The heating comes from an infra-red or resistive heater on the bottom of the chamber. The vacuum pump and gas sources can come from the top of the chamber. After the load-lock chamber is pumped down, the load lock door can be opened. An arsine or phosphine flow can then be started, and the wafers would be heated up above the oxide desorption temperature. With the oxide removed, the pushrod would be activated, pushing the wafers together. The pushrod would then apply the specified pressure between the two wafers. Figure 7.03 shows the fusion system in the fusing configuration.

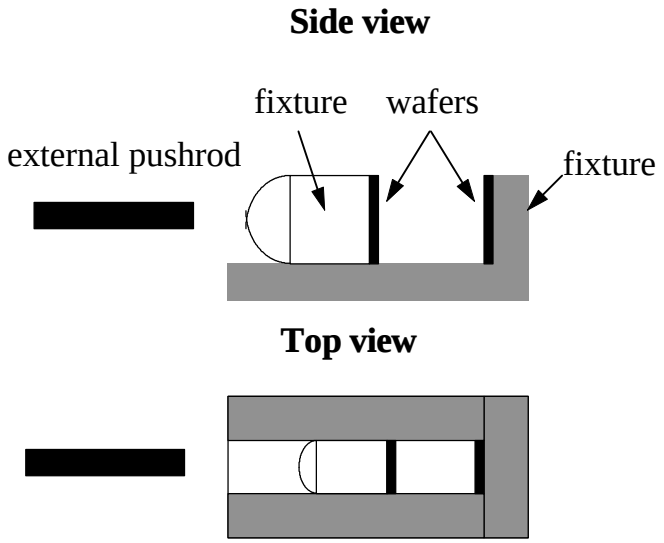

Figure 7.01. Schematic diagram of proposed fusion system.

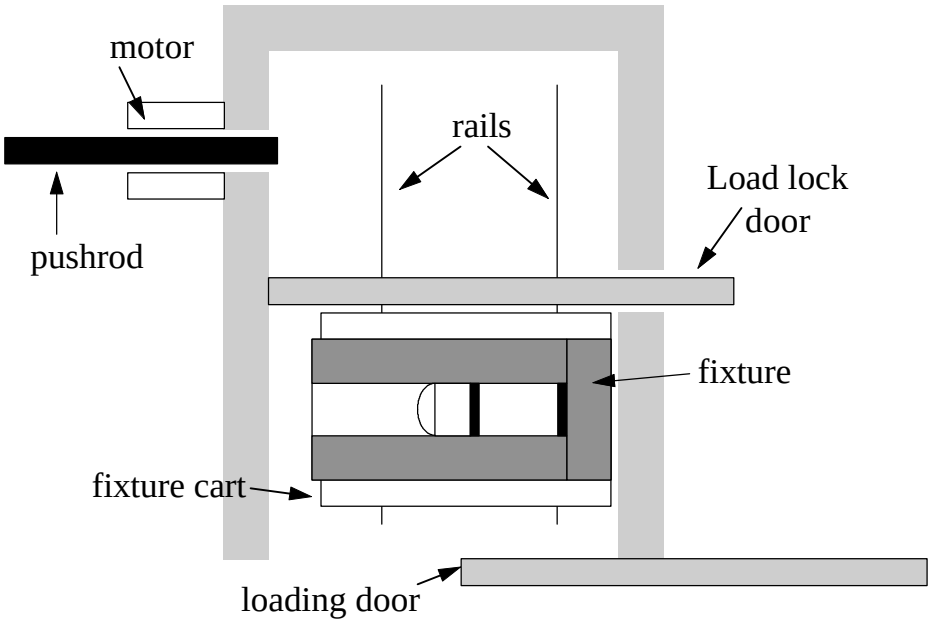

Figure 7.02. Load-locked fusion system.

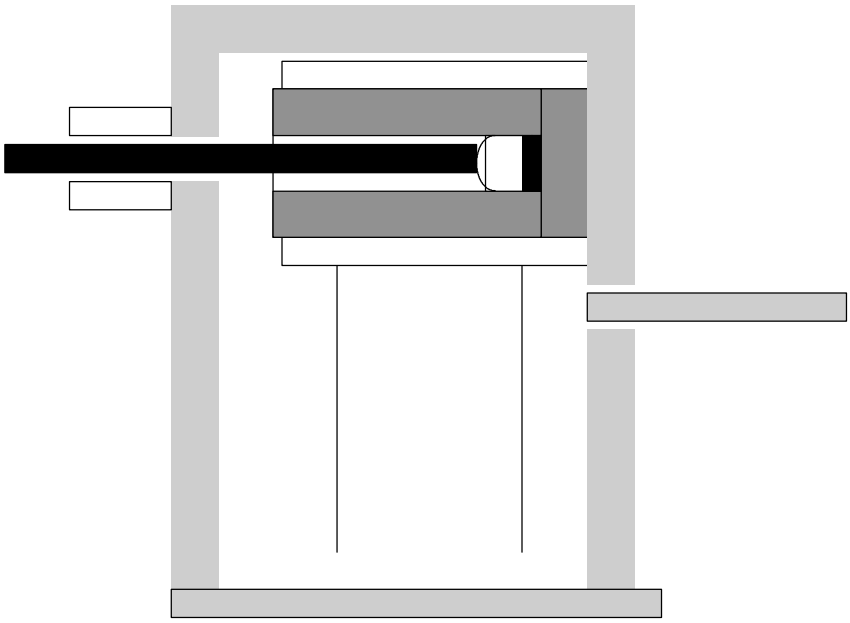

Figure 7.03. Proposed fusion system in the fusion configuration.

A second area where future work should focus is the use of better current confinement. With the current oxide aperture design it will be very difficult to get much below 1 mA threshold currents. Even if the fused junction voltage could be eliminated, current spreading in the p-InP cladding would be significant. The inherent distance required between the fused junction and the quantum wells will always allow for significant spreading. One might consider putting an oxide aperture in the InP using InAlAs oxidation[1], but such oxidation proceeds very slowly and would likely degrade the material for a significant oxidation depth. Ideally, one would want some sort of buried-

heterostructure confinement as described in Chapter 1. The reason buried-heterostructure would be so attractive is that it can eliminate both current spreading and current diffusion in the quantum wells. Since one needs so many quantum wells in the active region to get high gain, and the carrier density in the active region is typically very high, lateral carrier diffusion can be a major effect. No matter how close one puts an aperture above an active region, it cannot stop carrier diffusion. In the buried-heterostructure case, there is a lateral barrier for carriers trying to diffuse out of the lasing region. This barrier usually comes in the form of some sort of heterostructure. Significant effort has been made in GaAs VCLs to achieve carrier confinement[2,3]. So far, such efforts have had limited success due to the difficulty in forming buried-heterostuctures in this system. In the InP system, in-plane lasers are regularly grown with buried-heterostructures. One of the first successful long-wavelength VCLs by Iga *et al.* used a buried-heterostructure active region[4]. In this device, p-n-p blocking layers were grown as a barrier for current spreading and diffusion. A buried heterostructure active region could be easily integrated into that device because a deposited dielectric mirrors was used as the top mirror. The buried-regrowth may leave the surface non-planar so that it would be difficult to fused or grow another mirror onto such a surface. A dielectric mirror, however, easily conforms to the surface. Ultimately, one

would like a method to integrate a buried-heterostructure into the double-fused vertical cavity lasers.

One possible means of integrating a buried aperture into the fused VCL is through the use of “patterned” fusion. Patterned fusion consists of fusing two materials without continuous coverage between the two materials. For example, the etching of the channels may be considered the use of patterned fusion. The fusion process does not occur in areas where the wafers are not in contact. The use of patterned fusion allows one to bury an air-gap within the epi layers. The advantage of using such a technique rather than selective wet etching to achieve this undercut gap is that the patterned fusion can be precisely defined by photolithographic techniques. This reduces much of the uncertainty in the position of the gap. Figure 7.04 shows a first order idea as to the use of patterned fusion to form an aperture. One would simply etch channels as is normally done in the first fusion around the active region of the device. Etching through the active region eliminates lateral carrier diffusion in the quantum wells.

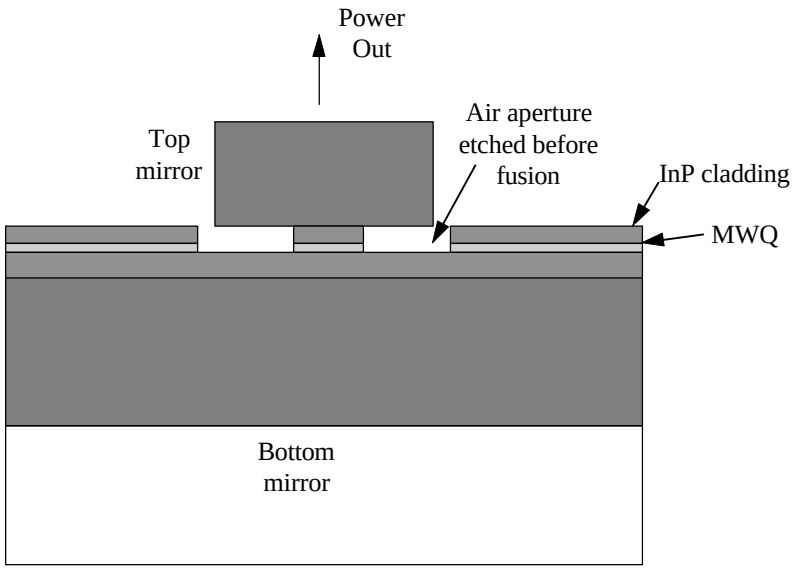

Figure 7.04. Simple aperture design using patterned fusion.

Several problems are apparent with this first order structure. The first problem, associated with etching through the active region, is that one simply trades off carrier spreading for surface recombination. Surface recombination in the InP system is quite low so this may be a worthwhile tradeoff. However, another factor plays into the reduction of surface recombination. Since the fusion process is at such high temperature, one expects mass transport to play an important role in the InP. One might expect that through the fusion process that the quantum wells would be covered over by mass transport of the InP in the cladding. Since InP has a significantly larger bandgap, one get a effective barrier for carriers diffusing out of the wells. In-plane lasers have previously

been made using this technique for burying the quantum wells[5]. The next problem with this first order structure is optical scattering loss. Such a thick air aperture directly in the cavity will cause significant scattering loss as in the etched pillar case. To address this problem, one could selectively undercut the quantum well under the cladding region. This undercut would only have to go a few microns to confine the optical mode away from the channel. In this case, one would only have an 100 nm air aperture in the cavity rather than a 400 nm one. Using formulas developed by Hegblom, one can calculate that even at 100 nm there would still significant scattering loss at small aperture diameters(<6 μm)[6]. Yet, if the air gap aperture becomes somewhat filled with InP during the fusion process, then the index difference between the aperture and the quantum wells would be very small(0.2). The index difference between quarternary material to InP and quarternary material to air is a factor of ten times smaller. This would mean a factor of ten lower index perturbation. At this level, the optical scattering loss is minimal, even for smaller devices. One would need to investigate the proper conditions to allow the undercut aperture to fill in with InP. Alternatively, one could use an oxide layer in the mirror for optical confinement of the mode.

The final problem with the simple design presented is structural stability. One essentially has a large pillar held up by a very small contact area, an

inherently unstable situation. This is fine for a research device, but would not be good for long term reliability. One could potentially fill this gap up with some insulator such as polymide to provide mechanical stability, but this may be a difficult process. In addition, it would be unclear as to the long-term stability of this arrangement. Another idea would be to etch only the current confinement channel in a ring that does not extend to the edge of the pillar. In this way, the pillar should be structurally stable. Figure 7.04 shows an example of such a structure.

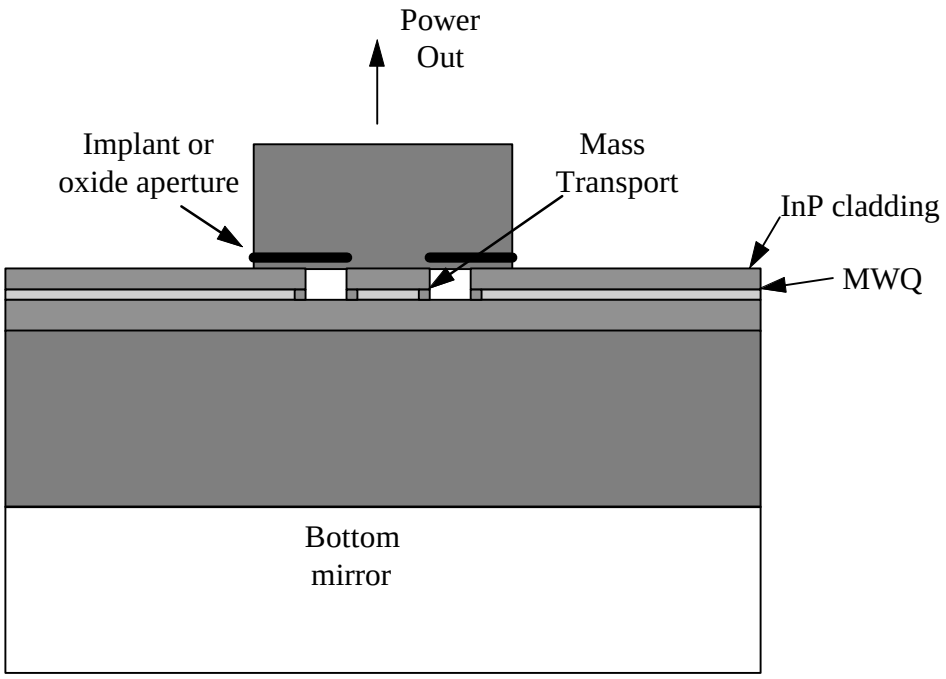

Figure 7.05. Advanced current confinement structure.

However, the problem with this design is that it offers the current another pathway through the active region. Current can flow through the area that is supposed to be providing structural stability. One could limit this pathway by using an oxide aperture again. This would not completely block this pathway, but would probably be a great improvement. The other option would be to do a proton implantation into this region to block this leakage pathway. This implantation would have to be done after both fusions, because the implantation could not survive the high temperatures of the fusion process. The implantation would therefore have to come through the thick top p-mirror. There may be difficulties with implementing such a deep implant. Thus the oxide aperture solution seems to be a better compromise between performance and feasibility.

In terms of the system research with VCLs, one could investigate the use of VCLs in wavelengthdivision multiplexed(WDM) systems. Arrays of VCLs with closely-spaced wavelengths could be used for very high data rate communications. This is especially important in multimode fiber where the distance bandwidth product of the fiber is very limited. By using multiple wavelength one can carry much more data across a multimode fiber. Each wavelength acts independently in the fiber. An array of different wavelength lasers can be coupled into the same fiber through a double-pass grating. Figure 7.05 shows a free space coupling arrangement where one could a wavelength

array into a single fiber. One could also use the technology of arrayed waveguide grating to do a similar function.

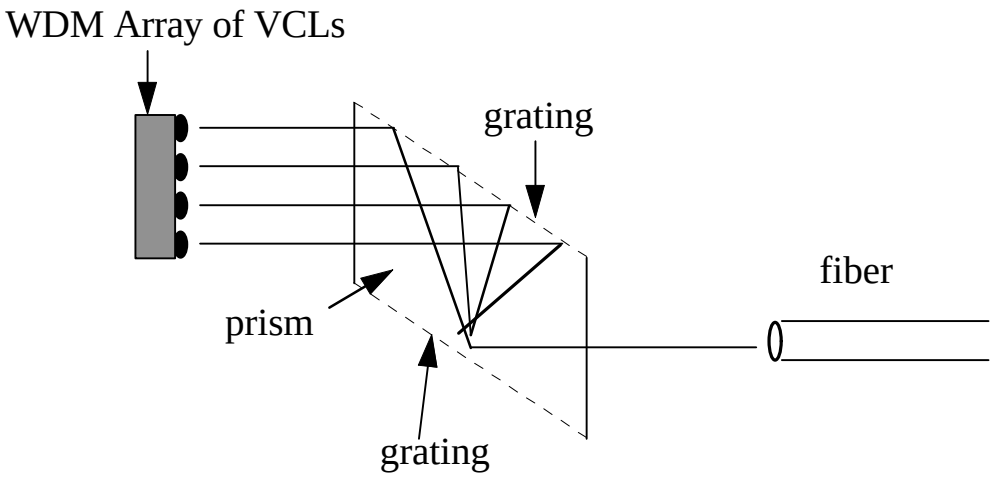

Figure 7.06. Coupling of 1xN wavelength array into a single fiber.

To get a 1xN array of different wavelength VCLs, one needs to slightly vary the wavelength of adjacent devices. This means there needs to be some difference in effective cavity lengths among the different devices. One way to accomplish this difference in cavity lengths is to etch partially the cavity in some device before fusion. This etching can be done precisely with a wet chemical etch if one uses etch-stop layers grown into the material. One could grow a superlattice of InP/1.15 Q with each layer 7.5 nm thick. One could then etch precisely at 7.5 nm intervals. Doing the effective cavity calculation on a typical structure, one sees that the lasing mode moves at approximately 5 nm per 7.5

nm of etching. In this way, we can get precise wavelength spacing for the different device in the array. One could then construct 8 wavelength layers through the use of 3 masks steps. In the first mask step, one would etch 4 layers deep, in the second 2 layers deep, and in the third 1 layer deep. Using this binary scheme, one could reach all eight layers through the combination of these three etches. The potentially problematic issue with this method would be the fusion uniformity of these quasi-nonplanar surfaces. I would expect, however, from my experience that the fusion will still be uniform with these very small deviations from nonplanarity. Seventy five nanometer of etching over 100 μm device pitch only gives an angle of $1.3\ 10^{-5}$ degrees. The use of WDM VCLs will allow for much higher traffic density per fiber, at a low cost. The high amount of data may allow for the luxury of the use of a thermo-electric cooler to stabilize the wavelength. In this case, it would not be necessary to meet the wide temperature range previously required for individual devices.

7.05 Final Comments

Long-wavelength vertical-cavity laser research has made great progress in approaching commercial level performance. The use of lateral oxidation and

wafer fusion played a key role in achieving these performance levels. For the first time, these devices were used in transmission experiments, with successful transmission of data at 2.5 Gb/s. Still, much more work needs to be done before such devices become viable in the marketplace. If successful, the future direction outlined in this chapter should allow for much higher temperature operations as well as general improvements in device characteristics. The final test of such devices will be meeting the stringent reliability standards demanded by commercial devices. If the devices fulfill these requirements, there is a good chance that long-wavelength VCLs may finally be a commercial reality, twenty years after their inception.

7.06 References

[1] H. Gebretsadik, K. Kamath, W.D. Zhou, P. Bhattacharyaa, C. Caneau, and R. Bhat, "Lateral oxidation of InAlAs in InP-based heterostructures for long wavelength vertical cavity surface emitting laser applications.", Appl. Phys. Lett., vol.72, 135 (1998).

[2] P. D. Floyd, B. J. Thibeault, J. Ko, D. B. Young, L. A. Coldren, and J. L. Merz, "Vertical cavity lasers with Zn impurity-induced disordering (IID) defined active regions.", Conference Proceedings. LEOS '96 9th Annual Meeting. IEEE Lasers and Electro-Optics Society 1996 Annual Meeting (Cat. No.96CH35895), 207 (1996).

[3] S. Y. Hu, S. W. Corzine, K. K. Law, D. B. Young, A. C. Gossard, L. A. Coldren, and J. L. Merz, "Lateral carrier diffusion and surface

recombination in InGaAs/AlGaAs quantum-well ridge-waveguide lasers.", J. Appl. Phys., vol.76, 4479 (1994).

[4] T. Baba, Y. Yogo, K. Suzuki, F. Koyama, and K. Iga, "Near room temperature continuous wave lasing characteristics of GaInAsP/InP surface emitting laser.", Elect. Lett., vol.29, 913 (1993).

[5] Z.-L. Liau and J. N. Walpole, "Mass-transported GaInAsP/InP lasers.", Lincoln Laboratory Journal, vol.2, 77 (1989).

[6] E. R. Hegblom, D. I. Babic, B. J. Thibeault, and L. A. Coldren, "Scattering losses from dielectric apertures in vertical-cavity lasers.", IEEE Journal of Selected Topics in Quantum Electronics, vol.3, 379 (1997).